UNIVERSITY OF CALIFORNIA

Los Angeles

Tuning Cyanine Dye J-aggregate Photophysics via Self-Assembly

A dissertation submitted in partial satisfaction of the

requirements for the degree Doctor of Philosophy

in Chemistry

by

Austin Daniel Bailey

2023

ABSTRACT OF THE DISSERTATION

Tuning Cyanine Dye J-aggregate Photophysics via Self-Assembly

by

Austin Daniel Bailey

Doctor of Philosophy in Chemistry

University of California, Los Angeles, 2023

Professor Justin R. Caram, Chair

J-aggregates are comprised of conjugated organic molecules that, when given the correct solvation conditions, self-assemble into a slip-stacked arrangement. In this form, not only do their absorption and emission redshift due to dipolar coupling, but many exciting properties emerge from the coherent coupling of their excitations over long distances. Namely, they boast superradiant emission from their excitonic states, leading to extraordinarily fast energy transfer and amplified radiative rates. Yet, while the optical properties of J-aggregates are unparalleled, one of the greatest challenges preventing their widespread use remains controlling their self-assembly into highly ordered nanostructures. In this dissertation, I unpack how changes to a dye's molecular structure can affect its ability to undergo J-aggregation, with regard to the design and improvement of the resulting aggregate's optical properties. Chapter one contains a historical

perspective on cyanine dyes and aggregates as colorants, as well as a short literature survey of how a dye's structure determines the optical properties of its resulting J-aggregates.

In chapter two, I explore the design of superradiant J-aggregates in different spectral windows. By elongating the polymethine chain of a well-studied cyanine dye (colloquially known as C8S3), I demonstrate the formation of tubular aggregates in the near-infrared regime. This work begins with synthesis of penta- and heptamethine derivatives of C8S3, followed by a careful screening of their J-aggregation via absorbance and cryo-electron microscopy (cryo-EM), and lastly a thorough spectroscopic characterization of each aggregate's emissive properties. While the new aggregates were considerably redshifted, they displayed different kinetics of aggregation, ultimately leading to stabilization of a morphology with decreased superradiance. To better understand those changes in superradiance, we employed a computational screening that unraveled a correlation between tube radius and disorder.

The above work opened many questions about why C8S3 organizes into highly-ordered superradiant J-aggregates while other cyanine dyes fall short. Around this time, our lab began a collaboration with Dr. Weili Zheng and Professor Edward Egelman (University of Virginia), who used cryo-EM to reconstruct the C8S3 nanotubes' structure with near-atomic resolution. Chapter three summarizes that work, which vastly expanded our knowledge of molecular packing in these systems. Prior to this work, the molecular structure of C8S3 J-aggregates had been posited from spectroscopic evidence and low-resolution cryo-electron micrographs. This result, however, unambiguously settled the long-standing dispute regarding C8S3 nanotube structure and represents an enormous advancement to our knowledge about how an individual dye organizes into a nanostructure. I contributed polarization-dependent spectroscopy and two molecules to this effort,

which primarily demonstrated how chemical modifications to the C8S3 monomer can obfuscate its self-assembly. This result inspired the full-length follow-up work, covered in chapter 4.

Chapter four investigates the role of electrostatics in the C8S3 nanotube self-assembly. This work begins from the revelation that C8S3 nanotubes feature a unique motif for self-assembly wherein the anionic sulfonate groups coordinate to the delocalized positive charge from the cyanine backbone. We tested this mechanism for self-assembly by synthesizing C8S3 derivatives with a variable number of methylene groups between the cationic cyanine and anionic sulfonate. Depending on the number of -CH_2 units, we found the dyes formed aggregates with different absorption lineshapes, and confirmed their differing morphologies using cryo-EM. Lastly, we synthesized dyes that have differently charged functional groups, thereby turning off the cation/anion interactions, and found them to exhibit significantly reduced J-aggregation. Based on these experiments, we believe that the electrostatic interaction between the alkylsulfonate and cyanine core are a significant driving force in the C8S3 self-assembly.

In chapter five, I examine the effect of a dye's steric bulk on its resulting J-aggregates. This work comprises a large-scale collaboration between many students in the Caram and Sletten labs, spanning the synthesis of new cyanines to computational screening of their self-assembly. We accomplished this goal by first synthesizing heptamethine benzothiazole dyes that differ in their 4' substitution (ranging from a phenyl ring to a 3,5-ditertbutylphenyl group). By modifying this position, we change neither the electronics nor the solubility of the dye, allowing a rational investigation of steric bulk on aggregation. Based on absorbance screening and cryo-EM, we found that these dyes form at least three J-aggregates each, all of which are extended 2D sheets (with one tubular anomaly). The addition of steric bulk was found to redshift the aggregate absorbance, while

also changing the kinetics of self-assembly and therefore leading to stabilization of different nanoscale morphologies.

In addition to these efforts, I have contributed to several other projects and conducted unpublished experiments that may inspire further investigation. Chapter six outlines these beginnings and gives direction for their future. Specifically, I discuss the potential for nuclear magnetic resonance (NMR) to offer structural knowledge on molecular aggregates and preliminary development of extremely redshifted J-aggregates in the shortwave infrared (SWIR). Taken together, these results inform the design of next-generation J-aggregated optical materials. By systematically exploring changes to the monomer chromophore, I have deduced clear structure-property relationships that serve as guidelines for making J-aggregates for applications in bioimaging, solar energy harvesting, or telecommunications. While many unsolved questions remain in J-aggregate self-assembly, this work breaks ground as a foundation for others to build upon our knowledge of cyanine dyes, their molecular aggregates, and, ultimately, their optical properties.

The dissertation of Austin Daniel Bailey is approved.

Paul S. Weiss

Yves F. Rubin

Ellen M. Sletten

Justin R. Caram, Committee Chair

University of California, Los Angeles

2023

To my Mom, who somehow ensured that I
became smarter than I had any right to be.
And to my Dad, who burned into my brain early
that there is absolutely no substitute for doing the work.

TABLE OF CONTENTS

LIST OF FIGURES

LIST OF TABLES

ACKNOWLEDGEMENTS

As I turn the page on my graduate career, I feel immense gratitude towards the exceptional instructors that helped me along my journey. Throughout my life I've had the incredible privilege of working with dedicated scholars of all levels that shaped my trajectory through academia.

Starting from the West Hartford Public School system, I was lucky to encounter many fantastic teachers, particularly in English, Latin, and math. Without their enthusiasm and encouragement, I doubt I'd have taken on the challenges I chose during college. Speaking of which, I can't mention University of Rochester without a list of world leaders in chemistry that offered me patient mentorship and rigorous training. To name a few: Dan Weix amazed me with the depth of expertise he brought to honors organic chemistry lab; David McCamant completely converted me to a physical chemist with his brimming clarity and kindness while teaching spectroscopy. And, without a doubt, Todd Krauss' brilliant teaching and unfiltered honesty taught me to appreciate the highs and lows of scientific research and discovery.

I consider myself deeply lucky to have started my graduate journey in Ellen Sletten's lab. Up to that point, my research had been mainly self-directed, having been left to my own devices to conduct air free polymer syntheses in Rochester. During my five weeks working under Ellen and Maly Cosco, I saw how an organic chemistry lab functions at the highest level and carried that experience with me for my entire Ph.D. Ellen's sheer commitment to advancing science and her unrivaled work ethic are truly humbling. I am hugely thankful for her help across all of my projects.

Lastly, I would like to thank Justin Caram for taking a chance on my success. Both of us were new to cyanine dye chemistry, as well as structure-property relationships of their resulting J-aggregates. But, after five years, I'm elated that we were able to solve these complex problems

which often required ventures into the academic unknown. During my time at UCLA I've watched our J-aggregate research operation grow enormously in sophistication, which is its own reward.

Beyond instructors, I've been blessed with fantastic collaborators to learn from. My academic work would not exist in its current form without formidable efforts from Timothy Atallah, Monica Pengshung, Arundhati Deshmukh, Cesar Garcia, Nadine Bradbury, Jill Williams, Barry Li, and John Cao. All of them contributed greatly to my Ph.D., opening me to different methods or ways of problem solving. I also owe great thanks to the fantastic friends and coworkers at UCLA who helped me navigate this treacherous journey: Ashley Shin, Zerina Mehmedovic, Stephanie Tenney, Jill Williams, Cesar Garcia, Anthony Spearman, and Roberto Chavez have all offered me enormous support. Of course, thanks to all of the Caram and Sletten lab members past and present for their help and camaraderie.

Last but not least, thank you to my friends and family. Dean and Zach were always waiting one message away, ready to fire at will. Adam performed great service in reminding me that, at the end of the day, none of this really mattered. Jeremy, a great friend and fellow Ph.D., spent many hours commiserating with me. And, most importantly, thanks to my Mom, Dad, and Liam, who set me up for success in ways that I may never fully comprehend.

Chapter one contains parts from an unpublished perspective by Austin Bailey.

Chapter two is adapted from the published paper, "Bailey, A.D.; Deshmukh, A. P.; Bradbury, N.C.; Pengshung, M.; Atallah, T.L.; Barotov, U.; Neuhauser, D.; Sletten, E.M.; Caram, J. R. Exploring the Design of Superradiant J-Aggregates from Amphiphilic Monomer Units. *Nanoscale* **2023**, *15*, 3841-3849." Experiments: ADB, APD, TLA, MP, UB, NCB; writing: ADB; editing: all authors; advising: EMS and JRC.

Chapter three is adapted from the unpublished manuscript "Deshmukh, A.P. †; Zheng, W.†; Chuang, C.; Bailey, A. D.; Williams, J.A.; Sletten, E.M.; Egelman, E. H.; Caram, J. R. Near-Atomic Resolution Structure of J-aggregated Helical Light Harvesting Nanotubes. *ChemRxiv*. †Co-first authors." https://doi.org/10.26434/chemrxiv-2022-5m8sx. Experiments: WZ, APD, ADB, JW; modeling: CC; writing: APD, WZ, CC; editing: all authors; advising: EHE, JRC.

Chapter four is adapted from the unpublished manuscript, "Bailey, A. D.; Williams, J.A.; Deshmukh, A.P.; Sletten, E. M.; Caram, J. R. Electrostatic Interactions Drive Self-Assembly of Light-Harvesting Nanotubes. *In preparation*." Experiments and data analysis: ADB, JAW, APD; writing: ADB; editing: all authors; advising: EMS, JRC.

Chapter five is adapted from the unpublished manuscript, "Bailey, A. D.†; Williams, J.A.†; Pengshung, M.; Garcia, C.A.; Deshmukh, A.P.; Cao, J.; Li, B.Y.; Bradbury, N.C.; Neuhauser, D.; Chuang, C.; Sletten, E. M.; Caram, J. R. Structural Engineering of Cyanine Dyes to Access Highly Redshifted J-Aggregates. *In preparation*." †Co-first authors. Experiments and data analysis: ADB, JAW, APD, MP, CAG, JC, BYL, NCB; writing: ADB; editing: all authors; advising: EMS, JRC.

Chapter six contains both unpublished results and work from the published manuscript "Deshmukh, A. P.; Bailey, A. D.; Forte, L. S.; Shen, X.; Geue, N.; Sletten, E. M.; Caram, J. R. Thermodynamic Control over Molecular Aggregate Assembly Enables Tunable Excitonic Properties Across the Visible and Near-Infrared. *J. Phys. Chem. Lett.* **2020**, *11*, 8026-8033." Experiments and data analysis: APD, ADB, LSF, NG, XS; modeling: APD; writing: APD; editing: all authors; advising: EMS, JRC.

BIOGRAPHICAL SKETCH

Education

2020 M.S. in Chemistry, University of California Los Angeles

2018 B.S. in Chemistry, University of Rochester

Selected Publications

1. A.P. Deshmukh.; W. Zheng; C. Chuang; **A.D. Bailey**; J.A. Williams; E.M. Sletten; E.H. Egelman; J.R. Caram "Near-Atomic Resolution Structure of J-Aggregated Helical Light Harvesting Nanotubes" *ChemRxiv* (2022). *Submitted.*

2. **Bailey, A.D**.; Deshmukh, A. P.; Bradbury, N.C.; Pengshung, M.; Atallah, T.L.; Barotov, U.; Neuhauser, D.; Sletten, E.M.; Caram, J. R. Exploring the Design of Superradiant J-Aggregates from Amphiphilic Monomer Units. *Nanoscale* **2023**, *15*, 3841-3849.

3. Deshmukh, A. P.; **Bailey, A. D.**; Forte, L. S.; Shen, X.; Geue, N.; Sletten, E. M.; Caram, J. R. Thermodynamic Control over Molecular Aggregate Assembly Enables Tunable Excitonic Properties Across the Visible and Near-Infrared. *J. Phys. Chem. Lett.* **2020**, *11*, 8026-8033.

Presentations

2023 The Optical Probes Conference: Discovery to Application, Palm Springs (Poster)

2021 Southern California Inorganic Photochemistry Meeting (Oral)

Selected Awards and Honors

2023 James D. McCullough Dissertation Award

2017 Carl A. Whiteman Jr. Teaching Award

2017 ACS Undergraduate Physical Chemistry Award

2016 DAAD RISE Fellowship

Chapter 1

Introduction to Molecular Aggregates of Cyanine Dyes

1.1. History of cyanine dyes

Since early civilization, dyes have allowed humans to bring vibrancy to the materials around them. Early colorants were sourced from plants or animals with minimal processing, and as societies became more advanced, brilliant dyes and pigments became highly traded commodities. Therefore, in 1856, when Sir William Henry Perkin prepared the first synthetic dye (mauveine), he began a now ubiquitous industry concerning the production of colored organic substances.[1]

In that same year, Charles Greville Williams published "Researches on Chinoline and its Homologues," wherein he reported the first cyanine dye synthesis.[2,3] He remarked on "a magnificent blue color," formed after heating a quinine derivative (cinchonine) with iodopentane and ammonia, yielding a dye now known as quinoline blue (Figure 1.1).

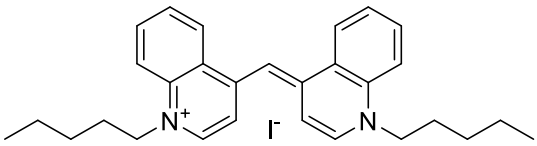

Figure 1.1. Structure of quinoline blue.

At the time, dyes were valued only in their ability to color textiles. For that reason, he decided that these compounds were impractical due to their poor photostability, despite the intense colors their salts afforded upon heating with silver oxide.

Near simultaneously with these discoveries came the advent of early photography. Before the first color photograph in 1861, photography was limited to Daguerreotypes which were produced

with silver halide emulsions. These techniques offered limited spectral sensitivity, predominantly in the UV. However, only twelve years later (1873), Hermann Wilhelm Vogel would pioneer cyanine dyes as early photosensitizers for photographic film. The addition of cyanines to the silver halide emulsion conferred vastly enhanced spectral sensitivity to the film, thereby bringing color images to life.

After that point, the burgeoning industry of photography, inextricably tied to dye chemistry, would erupt. Many widely used dyes such as ethyl red and pinacyanol were reported shortly after. In 1880 George Eastman founded what would become the Kodak company, leading to the first commercialization of a camera in 1888. Research into photography and spectrally sensitizing dyes evolved rapidly. Today, cyanine dyes are ubiquitous. These compounds enter our lives in everything from our food coloring to our favorite movies. Beyond consumer products such as hair color or textiles, cyanines have been used in solar cells, image-guided surgeries, laser systems, storage of data in CD-R or DVD-R media, and many other applications.[4]

1.2. Cyanine dye classification

Cyanine dyes are a family of organic compounds that interact strongly with light. The name "cyanine" is derived from the Greek "kyanous," which refers to a rich blue color. And, as the name would suggest, cyanine dyes useful for being both strongly colored and exceptionally fluorescent. Across their many variants, they are typically defined by a conjugated π-system between two nitrogen atoms, where only one nitrogen atom is oxidized into its quaternary form. Classifications for cyanines start by considering the nature of the two nitrogen atoms: if they both exist within an aromatic ring, the dye is referred to as a closed cyanine. Open chain cyanines (sometimes called streptocyanines) arise when neither nitrogen occurs within a ring, while hemicyanines occur when

only one nitrogen does. Merocyanines (net neutral dyes where one nitrogen atom is replaced by a carbonyl functional group) are also usually regarded within this family of chromophores, as well as many polymethine dyes more generally. Figure 1.2 displays different basic varieties of cyanines.

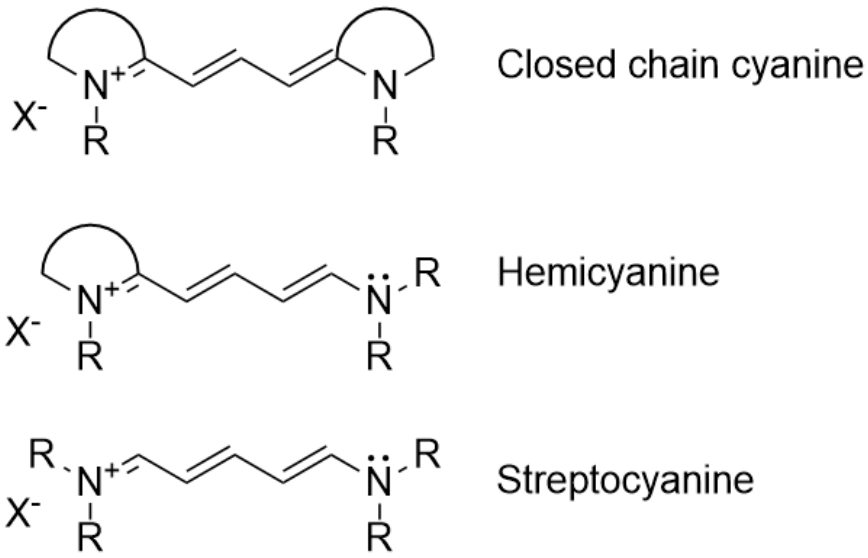

Figure 1.2. Generalized structures for open, closed, and hemicyanine dyes.

Typically, cyanine dyes used for chemistry research are of the closed form, where each nitrogen is housed within an aromatic heterocycle. Common heterocycles include benzothiazole, benzimidazole, and benzindole (carbocyanine), but other examples exist (Figure 1.3A). Another critical distinction for cyanine dyes is the length of their polymethine chain (i.e. how many unsaturated carbon atoms lie between the two nitrogen atoms). The addition of only two carbon atoms can increase the chromophore's maximum absorption wavelength by nearly 100 nanometers (~2,000 cm^{-1}), sometimes called the vinylene shift (visualized in Figure 1.3). By modulating this number of methine units, one can change the dye's color from deep blue to infrared, underscoring the enormous degree of tunability that cyanines possess.

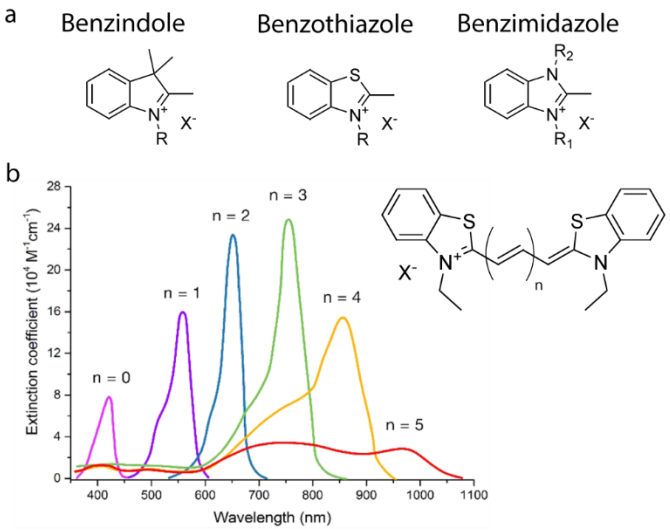

Figure 1.3. Possible heterocycles and polymethine lengths for cyanine dyes. a) Common cyanine dye heterocycles. b) Absorbance spectra showing the vinylene shift of a benzothiazole dye. Adapted from Bricks *et al*., 2018.[5]

Beyond heterocycle and length, cyanines have at least one unique substituent bound to both nitrogen atoms. Commonly, dyes possess a charged group at this position, such as sulfonate, carboxylate, or trimethylammonium, to enhance water solubility. However, many other options exist, such as N-hydroxysuccinimide (NHS) esters, which allow for facile conjugation to biomolecules.

Another critical aspect of cyanine dyes is their propensity to delocalize charge evenly between the two nitrogen atoms. While dyes are often depicted as having alternating single and double bonds, the true 'cyanine' form maintains a uniform distribution of charge (i.e. full delocalization) with all bonds having equal length.[6,7] This leads to enormous overlap between the ground and excited state wavefunctions, which is the basis for the impressive molar absorptivity of these dyes. Cyanines typically have molar absorption coefficients on the order of 10^5, which is nearly two orders of magnitude larger than many of the inorganic pigments.

1.3. Excitonic molecular aggregates of cyanine dyes

In 1936, Edwin E. Jelley, a researcher for Kodak in Harrow, England, released his work "Spectral Absorption and Fluorescence of Dyes in the Molecular State." Therein, he detailed the discovery of a molecule with "resonance radiation," or emission similar to an atomic system.[8] He noted that for cyanine dyes dissolved in polar solvents, the addition of nonpolar solvents (as well salts or changes in temperature) could drastically change the solution's color. He also remarked on the dramatic spectral narrowing of the dye's optical properties. One year later, Günter Scheibe reported a similar effect using the same dye, known as 1,1'-diethyl-2,2'-cyanine chloride (commonly known as pseudoisocyanine chloride, or PIC, Figure 1.4).[9]

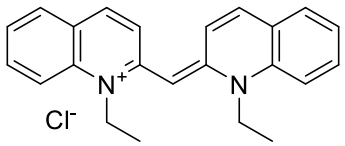

Figure 1.4. Structure of pseudoisocyanine chloride.

While Jelley and Scheibe's works were certainly groundbreaking, their observations were not well understood at the time. Over several decades, scientists came to realize that the changes to the dye's optical properties were associated with their self-assembly into aggregates, due to their noncovalent interactions. In any case, Jelley would later become immortalized through the naming of these materials as *J*-aggregates.

Since 1936, J-aggregates have become a subject of intense research in areas ranging from chemistry to photonics. Through nearly a century of research scientists have found that molecular aggregates are a unique class of materials comprised of non-covalently bound self-assemblies of highly conjugated organics. The individual dye molecules are drawn together by a combination of

π-interactions, electrostatics, solubility, and steric effects. Although this section focuses on cyanine dye J-aggregates, there are also several other common J-aggregating chromophores, such as perylene bisimides, BODIPYs, or anthracene derivatives.[10–12]

In these systems, the dye monomers stack upon each other, similar to playing cards in a deck. Depending on the geometry of stacking, the properties of the resulting aggregates will change. The two extreme cases of these arrangements result in H- and J-aggregates, ultimately yielding blueshifted and redshifted absorption, respectively. For example, fully cofacial packing (as in the case of an H-aggregate), leads to a new excitonic bright state with higher energy than the monomer. In a J-aggregate, the molecules pack in a slip-stacked fashion, which results in a bright state with lower energy than the parent chromophore, as shown in Figure 1.5.

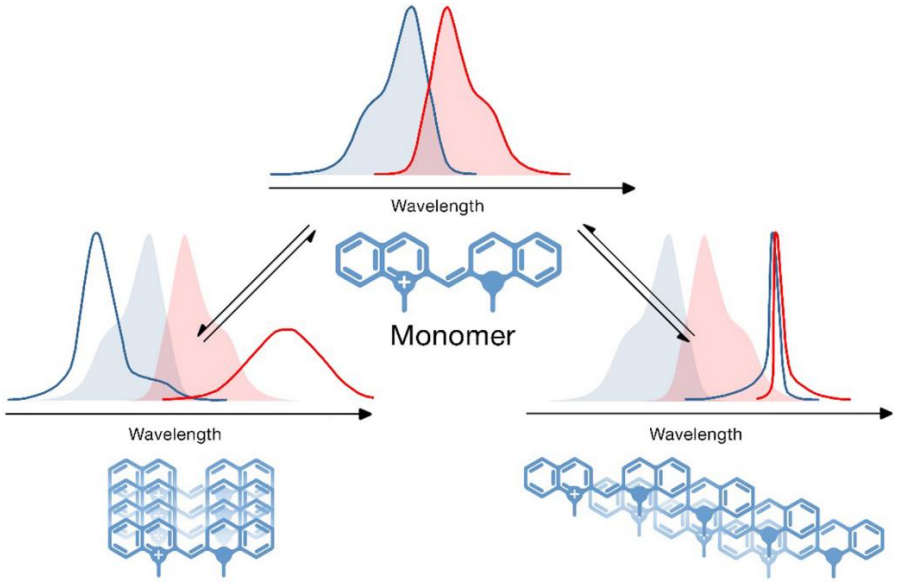

Figure 1.5. Molecular aggregation of a monomer dye, showing cofacial (left) H-aggregation and slip-stacked (right) J-aggregation. Adapted from Bricks *et al.*, 2017.[5]

The spectral changes associated with both H- and J-aggregates come from a physical phenomenon known as dipolar coupling. Within this new aggregate, the net transition dipole moment (TDM) depends on the phase relationship of the individual chromophores' TDMs. It is for this reason that the different geometric arrangements of dyes can lead to different optical properties. In addition to red-shifting and blue-shifting, the process of J-aggregation can lead to spectral narrowing, sometimes called motional or exchange narrowing.

For the case of a linear aggregate, where the molecular chain grows only in one dimension, the physics of how geometry influences an aggregate's photophysics were solved by Michael Kasha in 1963.[13] However, in addition to 1D chains of these dyes, more complicated geometries such as 2D sheets or tubular aggregates (pseudo-1D) can also exist. In these materials, the dipolar coupling and subsequent excitonic properties of the J-aggregates become significantly more complex.[14,15]

1.4. J-aggregates as biomimetic light harvesters

Much of the interest in J-aggregate research stems from the similarity between these materials and the most efficient light-harvesters found in nature. Perhaps the best example of this is the chlorosomes that occurs naturally in green sulfur bacteria.[16] These organisms live several hundred feet below the ocean's surface and survive on a flux of only 300 photons per second; in contrast, a houseplant on a windowsill has a photon flux of 10^{16} per second.[17] Because these green sulfur bacteria are evolved to harvest photons and lead them to reaction centers with unprecedented efficiency, they quickly became a subject of intense research.

Structural characterization of green sulfur bacteria has found that they contain rodlike nanostructures comprised of self-assembled chlorin molecules.[18] Researchers revealed that the

arrangement and geometry of these nanostructures mediate the exceptionally fast energy transfer between the light-harvesting chlorosomes and bacterial reaction center (Figure 1.6).[19]

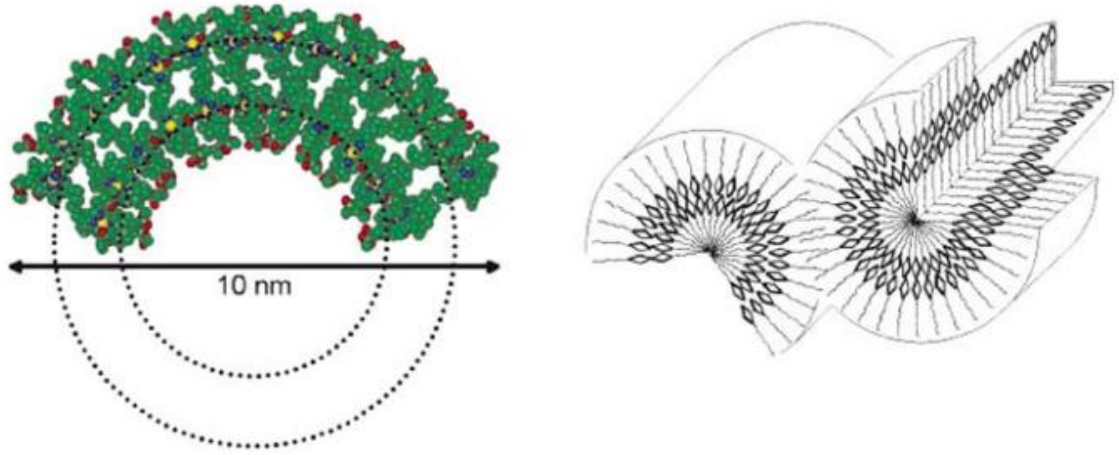

Figure 1.6. Visualization of rodlike nanostructures containing self-assembling chlorin molecules. Adapted from Chlorin Programmed for Self-Assembly.[18]

There is a clear analogy to be drawn between the chlorin nanotubes and J-aggregates of cyanine dyes. Both are self-assembled nanostructures that enable their excitations to efficiently travel over long distances. In fact, Caram *et al*. showed that certain J-aggregates can migrate their excitons over microns at room-temperature within a stabilized sugar matrix.[20]

However, what this similarity truly emphasizes is the premier feature of J-aggregates: their ability to transfer energy and charge faster than almost every other conventional material.[21] For this reason, they are highly coveted in applications where rapid movement of charge/energy is critical. Many researchers have already shown that J-aggregates can greatly accelerate energy transfer by relaying excitations between different light absorbers and emitters. [21–23]

1.5. C8S3 as a model system for studying molecular aggregates.

While J-aggregates are as varied as the cyanine dyes they assemble from, much of our knowledge concerning these materials comes from a single self-assembling cyanine dye known as 3,3'-bis(2-sulfopropyl)-5,5',6,6'-tetrachloro-1,1'-dioctylbenzimidacarbocyanine. This dye was first reported in 1997 and is oftentimes referred to as C8S3, due to the octyl (C8) and sulfopropyl (S3) chains that provide the chromophore its amphiphilic quality (structure shown below, Figure 1.7).[24]

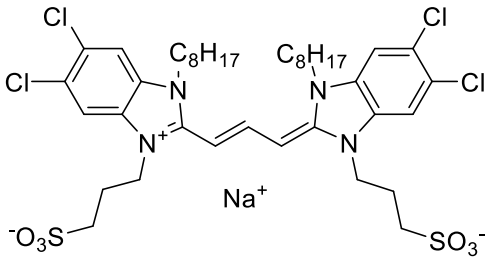

Figure 1.7. Structure of C8S3.

C8S3 is a trimethine (or Cy3) dye, meaning that the chromophore part of the molecule absorbs strongly in the visible at approximately 520 nanometers. In addition to the chromophore component of its structure, it is derived from benzimidazole heterocycles, which allows each face of the dye to possess two unique substituents. Because the two faces can be either hydrophobic or hydrophilic, C8S3 naturally self-assembles into a unique double-walled nanotube structure when given the correct solvation (methanol/water). It also features two chloro groups on each heterocycle, which help direct the self-assembly.[25] While cyanines are typically cationic, the dye possesses a net charge of –1 (due to the dual anionic sulfonate groups), and requires a positively

charged counterion (Na^+). This is because the synthesis of these dyes typically utilizes sodium alkoxides as a strong base to instigate the dye formation.[26]

As mentioned, when C8S3 molecules are given proper solvation (30% methanol:water, v/v), they self-assemble within seconds into micron-scale double-walled nanotube (DWNT) structures (Figure 1.7.a). These aggregates are also known as light-harvesting nanotubes or LHNs. Accompanied with this transition is a redshifting of the dye's absorbance and emission, as well as the appearance of distinct spectral features associated with the inner and outer walls of the material (Figure 1.8b).

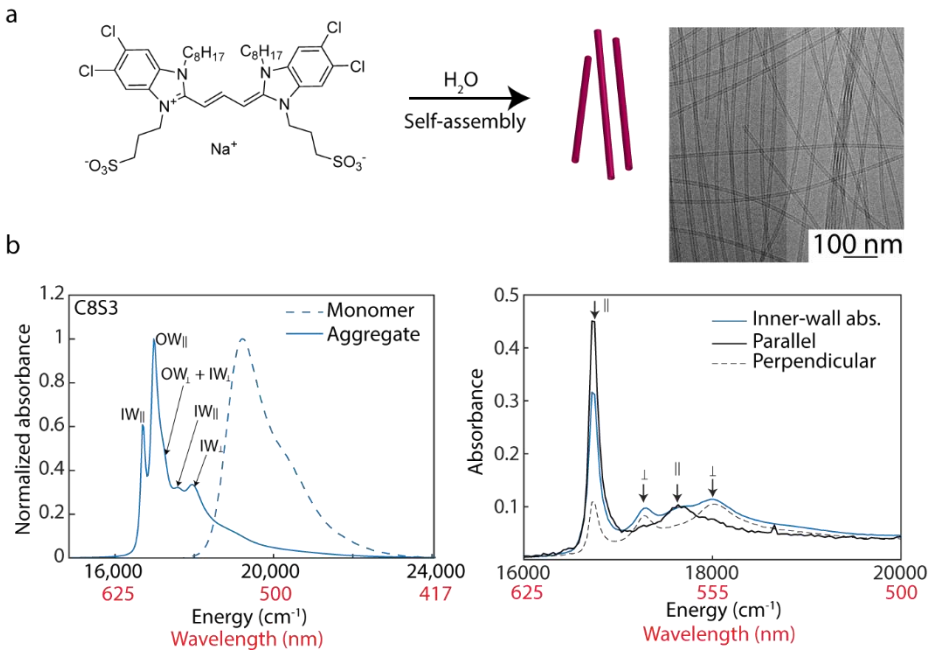

Figure 1.8. Absorption and cryo-EM characterizations of C8S3 J-aggregates. a) Scheme depicting the self-assembly of C8S3 into tubular J-aggregates and cryo-electron microscopy of DWNTS. b) Absorbance spectra depicting the C8S3 monomer and aggregate with different transitions highlighted. Adapted from Deshmukh *et al*. 2022.[27]

Within the absorbance spectrum of C8S3, there are features for both the inner and outer wall, with the outer wall being the primary absorber. Additionally, because polarization can occur across the tube's length as well as around its circumference, there are transitions (called perpendicular) that manifest as broader, higher energy shoulders to the main absorption (i.e. the parallel peaks).

However, the most important property of these C8S3 J-aggregates is their ability to delocalize excitations and transfer energy over long distances. The LHNs represent an exemplary excitonic system: their robust migration of excitations at room-temperature and band-edge emission constitutes an ideal system in nearly every aspect.

1.6. Synthetic modifications to C8S3

More recently, research on C8S3 has expanded to investigating how modifications of the parent chromophore change both self-the assembly and light-harvesting properties of the resulting J-aggregates. Typically, this type of work involves synthesizing a family of dyes with systematic changes, screening the self-assembly of each dye, and conducting a morphological or photophysical characterization. Ultimately the goal of these experiments would be to improve upon nature's light-harvesting prowess or to understand how to enable robust light-harvesting under any set of circumstances. For example, understanding how exceptionally fast energy or charge transfer can be achieved in different media or spectral windows.

Although previous efforts exist, one of the first large scale efforts towards this goal was published by Siegfried Daehne and coworkers in 2003.[28,29] They explored the effect of alkyl chain lengths on J-aggregation of benzimidazole trimethine dyes with carboxylates, sulfonates, and a second alkyl group as substituents. This work, as well several before it, was inspired by

calculations done by Knoester *et al*., as well as Kasha and McRae's models, with the intent to find three-dimensional molecular cylinders (which they termed amphipipes).[30–32] In this venture, they synthesized and screened absorption/circular dichroism (CD) of more than 20 dye's J-aggregates, generally classifying them into groups based on their absorbance lineshape and CD response. They note that C8S3 forms a different type of aggregate (type II by their nomenclature), which we now know indicated a double-walled nanotube. However, this paper also succeeded in providing a robust and straightforward synthesis for these dyes, opening the chemical space for others to contribute.

More recent examples of modifications to C8S3 include changing the monomer's halogen substitution, bridging the polymethine chain, and adding chiral substituents in place of sulfonate groups. Kriete *et al*. found that the halogen substitution (e.g. Cl vs. Br) modulates the width of the double-walled nanotube structure, which opens size tunability for these types of nanostructures.[25] In 2020, Schade *et al*. added chiral substituents (aminopropanediols) to the C8S3 monomer in lieu of sulfonate groups, and saw distinct morphological changes depending on the substituent's chirality.[33] This work similarly addresses tuning the shape and size of these materials. Lastly, in 2021, Barotov *et al*. published work on a dye that replaced its alkyl chain for a bridging unit across the cyanine, thereby eliminating nonradiative modes which contribute to decreased fluorescence efficiency. They observed an enormous increase in the monomer's dye photoluminescence quantum yield, as well as that of the J-aggregate.[34] In all cases, there is a clear trend that minor chemical modifications to the C8S3 scaffold can convey well-defined changes to the final supramolecular assembly.

1.7. Applications of J-aggregates

As optical materials, it is natural that J-aggregates serve as excellent candidates for technologies where their strong interactions with light are needed. Cutting-edge research involves these strong absorbers and emitters in areas from bioimaging to solar light harvesting. However, within this space, many competing materials exist that can offer lower toxicity or more robust photostability. Despite the strengths of their contenders, J-aggregates possess two unrivaled properties: their radiative rates of fluorescence and their spectral tunability. Dye monomers often have a radiative rate (k_r) on the order of 10^7 Hz (i.e. 10 MHz), while J-aggregates can reach 10^9 (GHz) values.[35,36] Additionally, because of the spectral tunability of the cyanine dye monomer from which a J-aggregate assembles, one can engineer aggregates in different spectral regions. Therefore, one highly anticipated application of J-aggregates lies in the telecom sector. If researchers can create a highly emissive J-aggregate at telecom relevant wavelengths (around 1300–1700 nm), these materials may find a new use as state-of-the-art information transmitters.

In addition to telecom-based applications, J-aggregates have also been employed as proof of concept for other technologies. Their extremely fast radiative rates allow them to enhance optoelectronic devices such as solar cells, luminescent solar concentrators, and OLEDs.[37–39] Additionally, scientists have used J-aggregates (typically made biocompatible by introduction of micelle or other lipid) for as exceptionally bright bioimaging agents.[40,41]

Chapter 2

Advancing Tubular J-aggregates of Cyanine Dyes into the Near-Infrared

C8S3 has proven to be a model system for studying delocalized excitons in organic nanomaterials. Here, we synthesize elongated C8S3 monomers, leading to new J-aggregates with near-infrared absorption and emission. We perform thorough characterization of these dyes' self-assembly, morphological structure, and photophysics to determine how this small change to the monomer structure influences the light-harvesting properties of the aggregates. After finding that the new dyes lead to a precipitous decrease in excitonic superradiance, we employed computational screening to gain intuition on how the minor change of structure affects the excitonic properties.

2.01. Significance of infrared optical materials

Lying just beyond human vision, the infrared (IR) portion of the electromagnetic spectrum is sometimes described as "spectrally quiet." Because there are very few naturally-occurring

materials that absorb and emit light in this region, the infrared represents an excellent spectral window for humans to transmit signal with minimal noise or background interference. Two common windows for IR technologies are the near infrared (NIR) and shortwave infrared (SWIR), which occur from 700-1000 and 1000-2000 nm, respectively. There, the reduced Rayleigh scattering ($1/\lambda^4$) of infrared light enables applications such as LIDAR (LIght Detection And Ranging), allowing humans to image through fog or smoke.[42] Similarly, the low autofluorescence of endogenous chromophores in this region allows researchers to image biological systems with never-before-seen resolution using infrared fluorophores.[35,43,44]

However, for the many advantages that infrared materials grant, the design of effective NIR or SWIR emitters is hard-earned. As small molecule chromophores shift to the infrared, their decreasing radiative rates and increasing nonradiative losses through vibrational modes create a precipitous decline in quantum yield that limits their efficacy.[45] Therefore, the redshifting associated with J-aggregation presents an attractive alternative for generating infrared emitters that can retain high brightness due to their TDM coupling. The goal for this work was to harness the exceptional photophysics of J-aggregates, and by invoking the vinylene shift (i.e. making elongated dyes), keep the exceptional light-harvesting properties but change their spectral window.

2.02. Synthesis of infrared C8S3 derivatives

In order to design a robust infrared J-aggregate, we modified the structure of an extant chromophore (C8S3), which forms tubular aggregates with superradiant emission in the visible. The traditional method for redshifting cyanine dyes and their J-aggregates is to increase the polymethine chain by one or more vinylene units, thereby inducing nearly 3,000 cm^{-1} of redshift.[46] To do this, we first synthesized the corresponding benzimidazole heterocycle and trimethine dye

as done previously (Figure 2.01).[25,28] From those molecules, we conducted several additional syntheses to obtain the pentamethine and heptamethine variants of C8S3 (**2.1a/b** and **2.2a/b**, respectively).

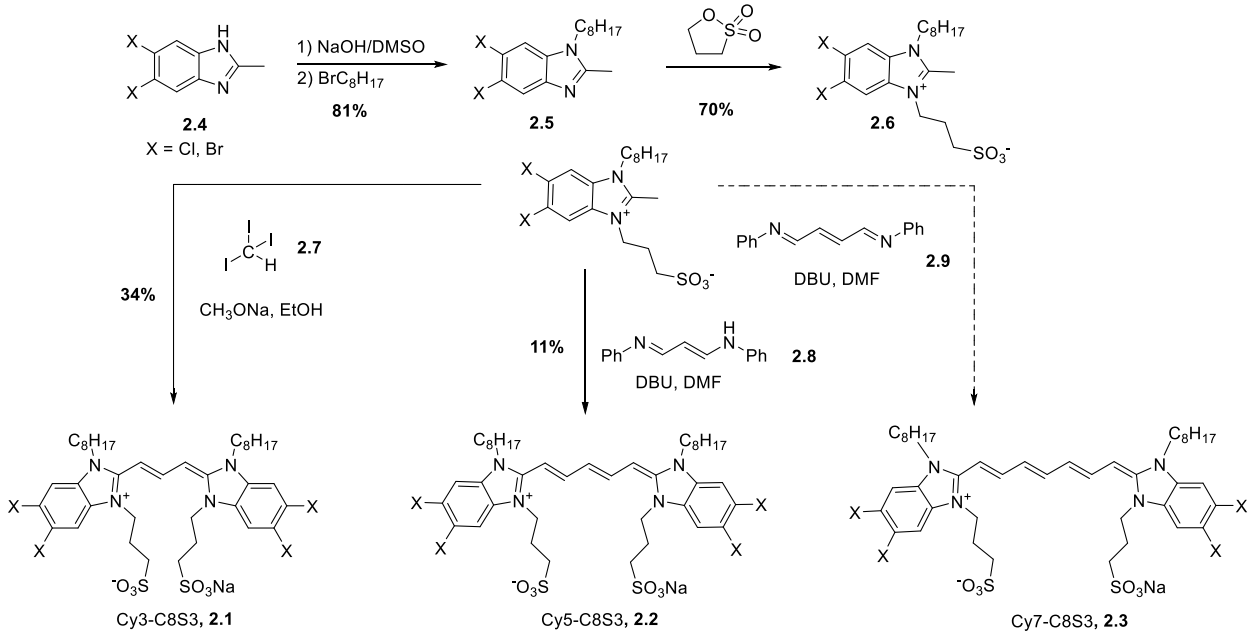

Figure 2.01. Synthesis of penta- and heptamethine C8S3 derivatives.

Figure 2.1 shows that we begin from a commercial heterocycle (5,6-dichloro-2-methylbenzimidazole) and first alkylate with bromooctane. The propylsulfonate group was then added using a neat reaction in propane sultone. This heterocycle was then heated in polar solvent with the corresponding electrophile (iodoform, malonaldehyde bisphenylimine hydrochloride, or glutaconaldehydedianil hydrochloride) for the Cy3, Cy5, and Cy7 dyes respectively. The syntheses resulted in highly colored solutions ranging from orange to purple, as shown by the absorbance traces in Figure 2.02.

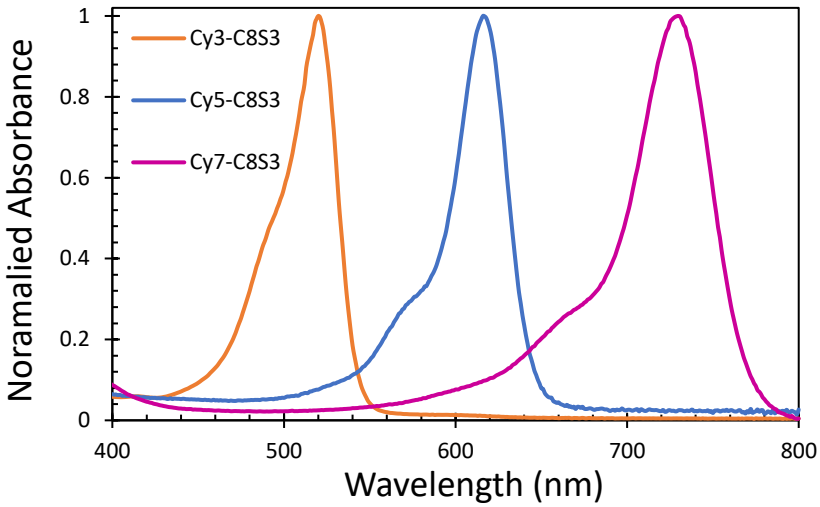

Figure 2.02. Absorption of trimethine, heptamethine, and pentamethine C8S3 derivatives in methanol.

Figure 2.2 shows the successful redshifting of the absorption λ_{max} between Cy3 (520 nm), Cy5 (620 nm), and Cy7 (730 nm) C8S3 molecules. Unfortunately, the heptamethine (Cy7) derivative was found to degrade in methanol and was not pursued. In addition to the -chloro dyes, we also investigated brominated versions of the Cy3 and Cy5 C8S3. The bromine dyes were synthesized in a similar manner, with the main difference being the lack of a commercial heterocyclic precursor. Therefore, this synthesis began by brominated 2-methylbenzimidazole using n-bromosuccinimide. After the octyl and propylsulfonate groups were installed, at the 1- and 3-positions, the dye synthesis followed identically to the chloro compounds shown in Figure 2.1. A full experimental for all compounds is found in section 2.8.

Traditionally the Cy3-C8S3 is purified through recrystallization in 1:1 DMF:H_2O, yet we found that the Cy5 and Cy7 dyes required more rigorous purification. Based on observations of other benzimidazole reactions, this is likely due to the fact that the linker molecules for these dyes

are weaker electrophiles, allowing side chemistry between the benzimidazole heterocycles. Therefore, the removal of impurities from the heptamethine and pentamethine dye reactions became significantly more challenging.

To obtain analytically pure dyes, many strategies were investigated, including recrystallization, preparative thin-layer chromatography (TLC), precipitation of the dye aggregates, HPLC, and silica column chromatography. Unfortunately, throughout the screening of many solvents and cosolvents, we did not find any combination that preferentially solubilizes the dye but not its impurities (i.e. linker or heterocyclic side products) or vice versa. Similarly, we found that thin-layer chromatography of these molecules only led to streaking and poor separation. Precipitation also did not lead to an improvement in purity.

Interestingly, when we ran HPLC samples for these dyes, which are normally a deep blue color, we found that the fractions would run clear. Fearing that the dye had gotten stuck on the column, we flushed with many solvents only to find more clear fractions. That development led to testing the pH-sensitivity of these compounds, finding that their absorption reversibly bleaches upon the addition of acid/base. We examine this observation more thoroughly in subchapter 2.11.

After extensive experimentation, we determined that among these purifications, the best option was performing multiple silica columns. This strategy seemed to work best with two columns (albeit in poor yield), where fractions were chosen based on the apparent dye concentration (i.e. color by eye). Because of differences between molar absorptivity coefficients for the dye and various impurities, UV-vis screening of column fractions did not help to reveal suitable fractions for grouping. Anecdotally, the best solution was to combine groups of 10-20 test tubes (containing ~10 mL each) by color and assess purity by ^{1}H NMR, then later combine groups of similar purity.

2.03 Degradation of Cy7-C8S3-Cl

Upon synthesis of Cy7-C8S3 (**2.3**), we attempted the standard purification of column chromatography, followed by ^{1}H NMR to assess purity. However, after noticing changes in color over time, we measured absorption of this compound across the purification timeline. We found that the dye significantly reduced its primary absorption (~730 nm) and showed increased absorption at ~620 nm after only a short time (~30 min.) in methanol, possibly due to photoblueing.[47] The changes in absorption are depicted in Figure 2.03.

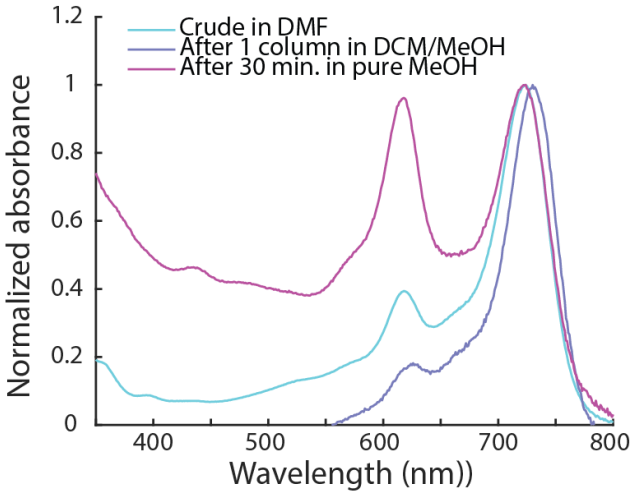

Figure 2.03. Absorbance showing degradation of Cy7-C8S3.

Although this compound degraded quickly in methanol, we attempted to observe J-aggregation several times by quickly mixing a methanolic dye solution with water, and found no redshifted absorption. Due to the rapid degradation and absence of J-aggregation, we decided to relocate efforts towards the Cy5-C8S3 J-aggregates.

2.04. Characterization of pentamethine C8S3 derivatives

Upon successful isolation of the trimethine and pentamethine dyes, we screened their absorption in methanol/water solutions of various dye concentrations as a way explore their

aggregation phase space. Aggregates of each chromophore were prepared by first weighing out a small amount of dye using a Sartorius Cubis microbalance, then adding spectroscopic grade methanol to create a stock solution of the dye. To a small volume of this stock solution was added MilliQ H_2O. The final concentration and methanol/water ratio in these solutions were varied. We then used UV-Vis to observe the different spectral signatures from distinct aggregate morphologies.

Specifically, we screened both **2.2a** and **2.2b** at varied concentrations while maintaining a constant methanol/water ratio (Figure 2.04A). We also performed kinetic time traces to watch the self-assembly unfold (Figure 2.04B). Finally, we performed non-negative matrix factorization, an algorithm which estimates the basis spectra corresponding to each species in the binary solution, to show how ratio of each aggregate (Figure 2.04C) changes as a function of concentration (Figure 2.04D).

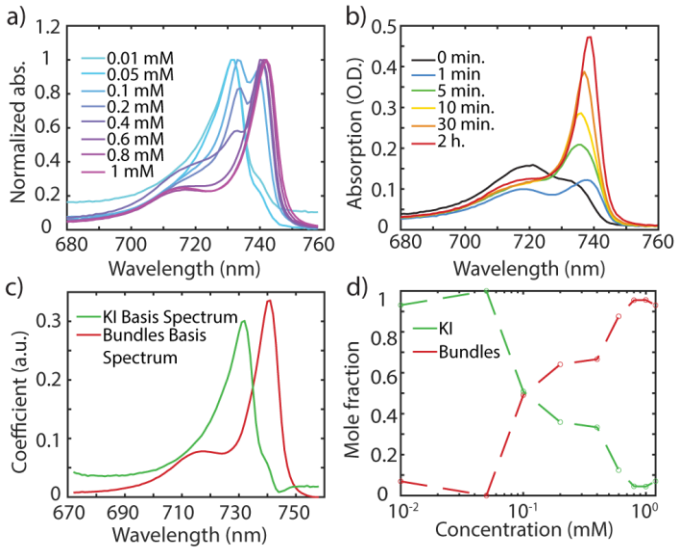

Figure 2.04. Absorption screening and modeling of Cy5-C8S3 J-aggregates.
A) Absorption screening of Cy5-C8S3-Cl at 0.01 to 1 mM. in 10% MeOH. B) Kinetic traces of Cy5-C8S3-Cl self-assembling at 0.05 mM dye, 10% MeOH. C) Basis spectra of isolated

aggregates from NNMF. D) Normalized mole fraction for the two isolates aggregates vs. concentration.

In this exploration, we found that the pentamethine dye aggregates display similar absorption lineshape to the previously synthesized trimethine dyes despite having a redshift of nearly 100 nm and form two primary aggregates each. We refer to these as a kinetic intermediate (KI) and bundles, though the analogous behavior of **2.1a** suggests that the KI are transiently formed double-walled nanotubes. The NNMF and kinetic analysis showed us that at low concentrations, the KI is favored, while at higher concentrations the KI rapidly converts to a bundled morphology. Our analysis of the mole fraction vs. concentration revealed that the two distinct aggregate morphologies can best be prepared at 0.01 and 1 mM to obtain isolated samples of each J-aggregate.

Looking at the absorbance spectra, the KI of **2.2a** shows distinct features at 740 and 731 nm, while the bundles display broad absorption around 715 nm and retain the 745 nm feature. By analogy to the existing work on C8S3, we assign these to parallel and perpendicular polarized transitions.[48] Interestingly, the 731 nm feature disappears with the increase of concentration and bundle formation; although this is consistent with the disappearance of a double-walled nanotube's inner wall, we withhold an absolute peak assignment out of caution.

After finding appropriate conditions for each aggregate with unique spectral signatures, we conducted cryo-electron microscopy (cryo-EM) to confirm their nanoscale morphologies. Figure 2.05 shows the double-walled nanotubes of **2.1a** and **2.1b**, as well as the bundles of **2.2a** and **2.2b.** Unfortunately, the aggregates prepared at 0.01 mM (stabilizing the KI aggregate) did not have sufficient sample density to determine morphology via EM. Therefore, although the short-lived

kinetic species shares several key similarities to the **2.1a** DWNTs (both in lineshape and slightly blueshifted absorbance) we do not definitively label it as the DWNT morphology.

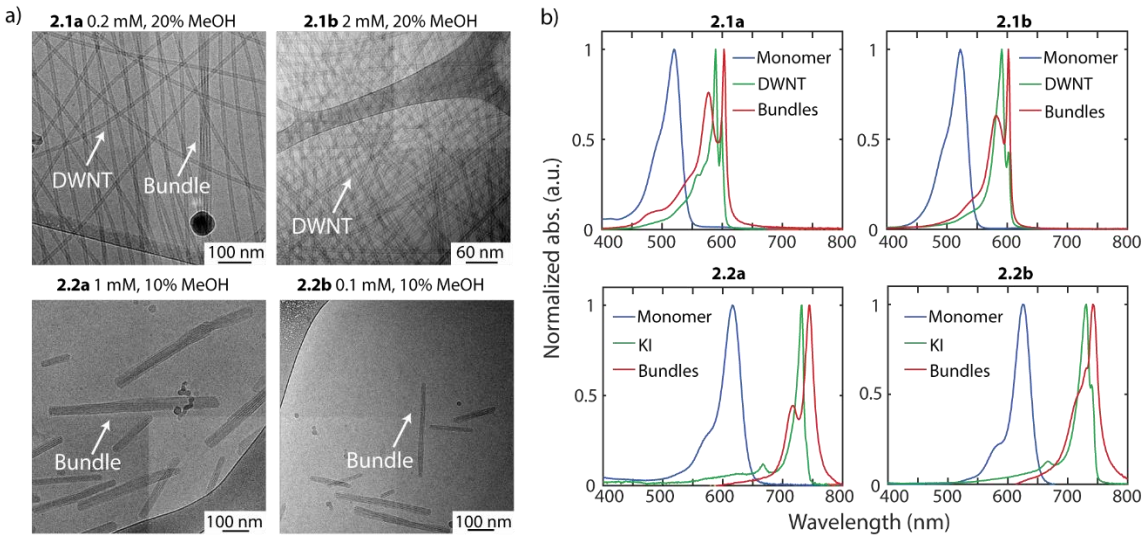

Figure 2.05. Cryo-EM and absorbance spectra for isolated aggregates of dyes **2.1a** and **2.2a**.

Thus, increasing the length of the polymethine bridge has a strong effect on the supramolecular packing of these chromophores. Trimethines **2.1a** and **2.1b** clearly have a propensity to form individual DWNTs, which slowly interconvert into bundles over many weeks, while pentamethines **2.2a** and **2.2b** rapidly form bundles within minutes.[49] We hypothesize that the pentamethine dyes aggregate into bundles more readily due to the increase in size, hydrophobicity, and polarizability. Additionally, bundles are the overall thermodynamic minimum of these aggregates, and therefore stronger non-covalent interactions in the assembly may imply a lower barrier to bundle formation. Overall, we observed only minor differences in the aggregates formed from **2.2a** and **2.2b**, most notably broader linewidths for the brominated dyes, suggesting a higher level of disorder in the **2.2b** nanostructures.

The recipe for each aggregate described in this section is provided in Table 2.1.

Table 2.1. Aggregate formation conditions.

Compound	Morphology	Dye concentration (mM)	%MeOH	%H_2O	Time
2.1a	DWNT	0.2	20	80	24 h.
2.1a	Bundles	0.2	20	80	10 weeks
2.1b	DWNT	0.2	20	80	24 h.
2.1b	Bundles	0.2	20	80	10 weeks
2.2a	KI	0.1	10	90	24 h.
2.2a	Bundles	1	10	90	24 h.
2.2b	KI	0.1	10	90	24 h.
2.2b	Bundles	1	10	90	24 h.

2.05. Photophysical characterization of Cy3 and Cy5 J-aggregates

Following the identification of the various aggregate morphologies, we probed the photophysical properties of **2.2a** and **2.2b** in comparison to **2.1a** and **2.1b** (Table 2.1). We obtained quantum yields (QY, Φ_F) and fluorescence lifetimes (τ) to obtain the transition dipole moment (TDM, μ) for each compound's electronic transitions, as well as each aggregate morphology's excitonic transitions. The emission spectra of **2.2a** are shown in Figure 2.06, as well as the lifetimes and fittings in Figure 2.07 and 2.08. The full suite of photophysical characterizations is provided in Table 1.

To begin, for the dye monomers **2.1a**, **2.1b** and **2.2a**, **2.2b** we performed relative quantum yields compared to known standards nile red and nile blue A perchlorate (Φ_F of 0.28 and 0.26 in MeOH, respectively).[50] The fluorescence quantum yield is defined as follows:

$$\Phi_F = \frac{P_E}{P_A} \tag{2.1}$$

Where P_E and P_A represent the number of photons emitted and absorbed, respectively. To determine the quantum yield, we used a relative method with either nile red (trimethine monomers) or nile blue A perchlorate (pentamethine monomers) as a known standard in the same region of

the electromagnetic spectrum. To compare an unknown to a reference with a known quantum yield, the following relationship was used:

$$\Phi_{F,x} = \Phi_{F,r}\,(m_x/m_r)(\eta_x{}^2/\eta_r{}^2) \quad (2.2)$$

Where m represents the slope of the line (y = mx + b) obtained from graphing integrated fluorescence intensity versus optical density across a series of samples, η is the refractive index of the solvent and the subscripts x and r represent values of the unknown and reference, respectively.

To obtain a plot of integrated fluorescence intensity versus absorbance for the reference and unknown, five solutions and a solvent blank were prepared with absorbance maxima between 0.01 and 0.1 au. Absorbance and emission spectra (with an excitation wavelength of 450 nm (trimethines) or 532 nm (pentamethines)) were acquired for all samples. Reference and unknown dyes were diluted in methanol to concentrations with optical densities less than 0.1 to minimize effects of reabsorption. The fluorescence traces were integrated, and the raw integrals were corrected by subtracting the integral over an identical range from fluorescence traces of the blank solvent. The integrated fluorescence intensities were then plotted against the baseline corrected absorbance values at the relevant wavelength and the slope and error in slope were obtained ($R^2 > 0.99$ for all traces).

However, quantum yields of J-aggregates are notoriously difficult to measure due to large reabsorption effects that result from near entirely overlapping absorption and emission. They are also not amenable to dilutions due to either disassembling the nanostructures or disordering them to the point where their original photophysics may not be retained. To minimize these problems, we employed the De Mello method for absolute quantum yield, which has been described in detail elsewhere.[35,51] In short, a short path length cuvette (0.1 or 0.01 mm depending on aggregate concentration) is inserted into a LabSphere 6" QE integrating sphere which uniformly illuminates

the sample on all sides from the input excitation beam. We used a variable wavelength superK laser as excitation for the trimethine (565 nm) and pentamethine (700 nm) aggregates and recorded the emission spectrum at three different concentrations for each aggregate.

Time-resolved photoluminescence (TRPL) were recorded at room temperature using a homebuilt, all-reflective epifluorescence setup.[52] The dye solutions were excited via a pulsed output from a 532 nm laser (LDH-P-FA-530B, PicoQuant). The emission was filtered (550 nm longpass dichroic, DMLP550R, Thorlabs; 550 nm longpass filter, FELH0550, Thorlabs, 532 nm notch, NF533-17, Thorlabs) and collected using time correlated single photon counting (TCPSC) histogramming with a Si-avalanche photodiode (PD-050-CTD, Micro Photon Devices) connected to a synchronized photon counter (Picoquant, Hydraharp 400).

We determined the monomer lifetimes by fitting the decay of the TCSPC trace to single exponentials for the **2.2a** and **2.2b** dyes and two exponentials for the **2.1a** and **2.1b** dyes. For aggregate lifetimes, we fit the TRPL traces to a numerical convolution of a biexponential function with the instrument response function (IRF) and extracted the corresponding rates. The IRF was measured as laser back-scatter from a cuvette with only solvent.

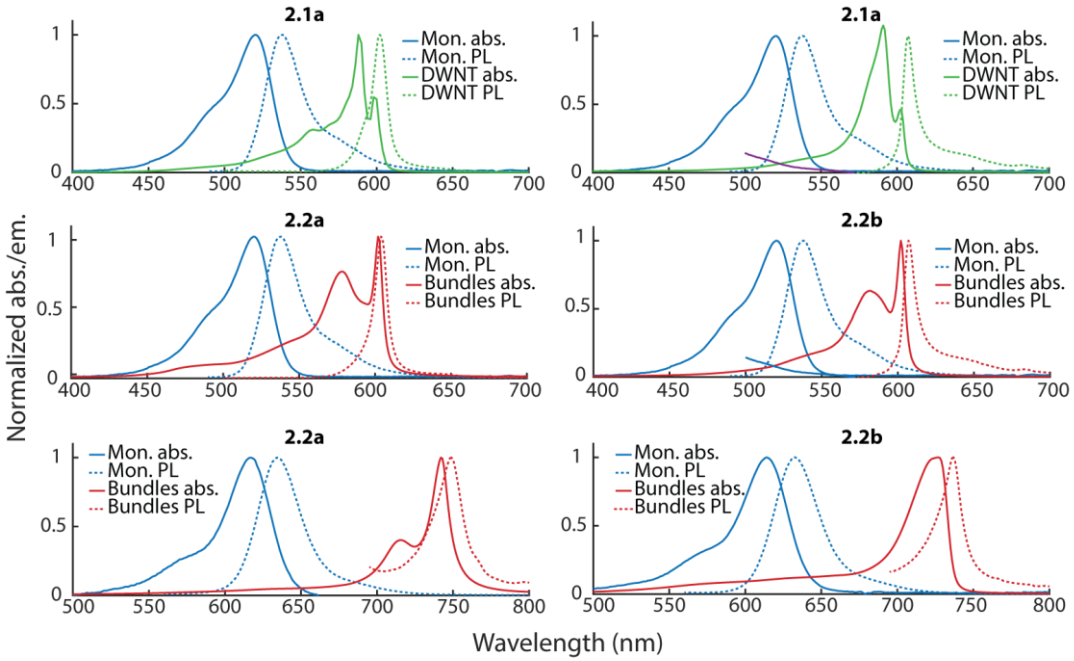

Figure 2.06. Absorption and emission spectra for all dyes and J-aggregates.

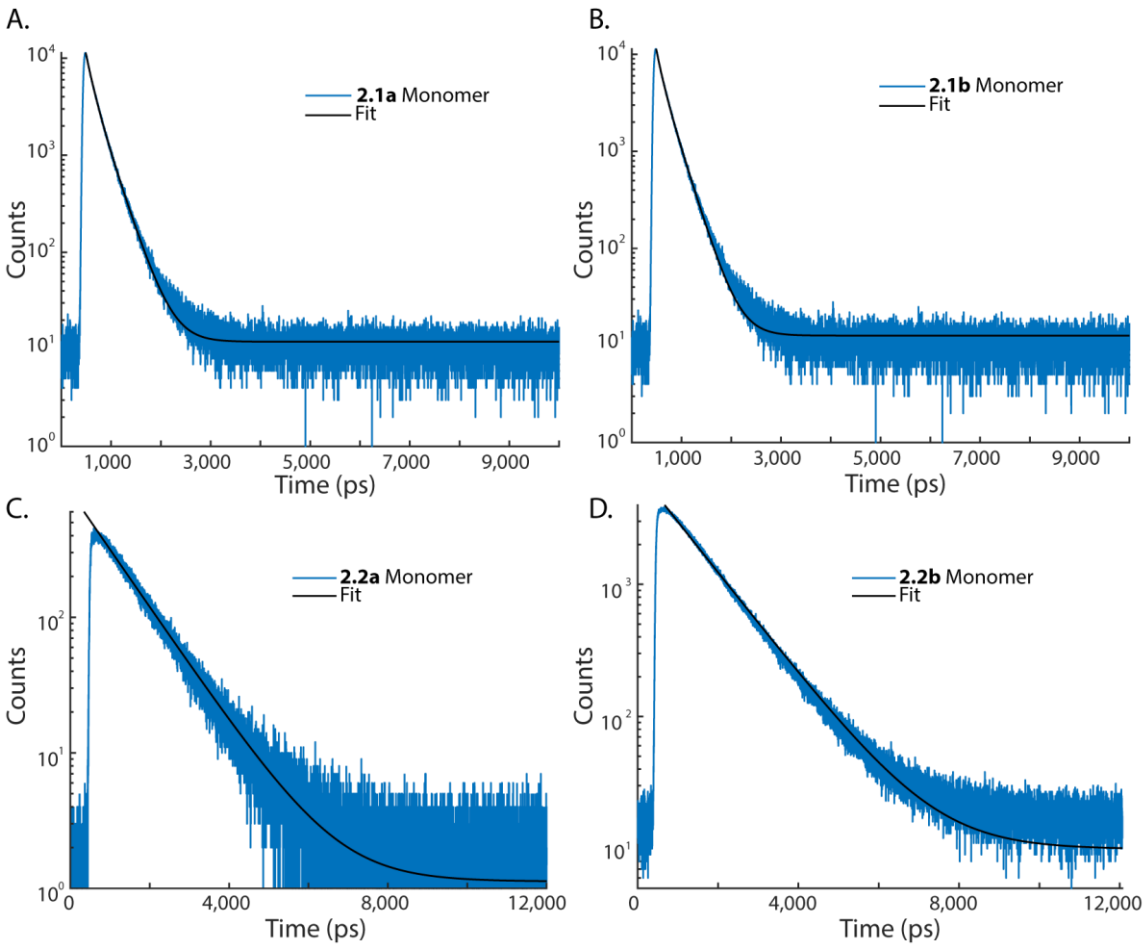

Figure 2.07. Fluorescence lifetimes for monomer dyes **2.1a-2.2b**.

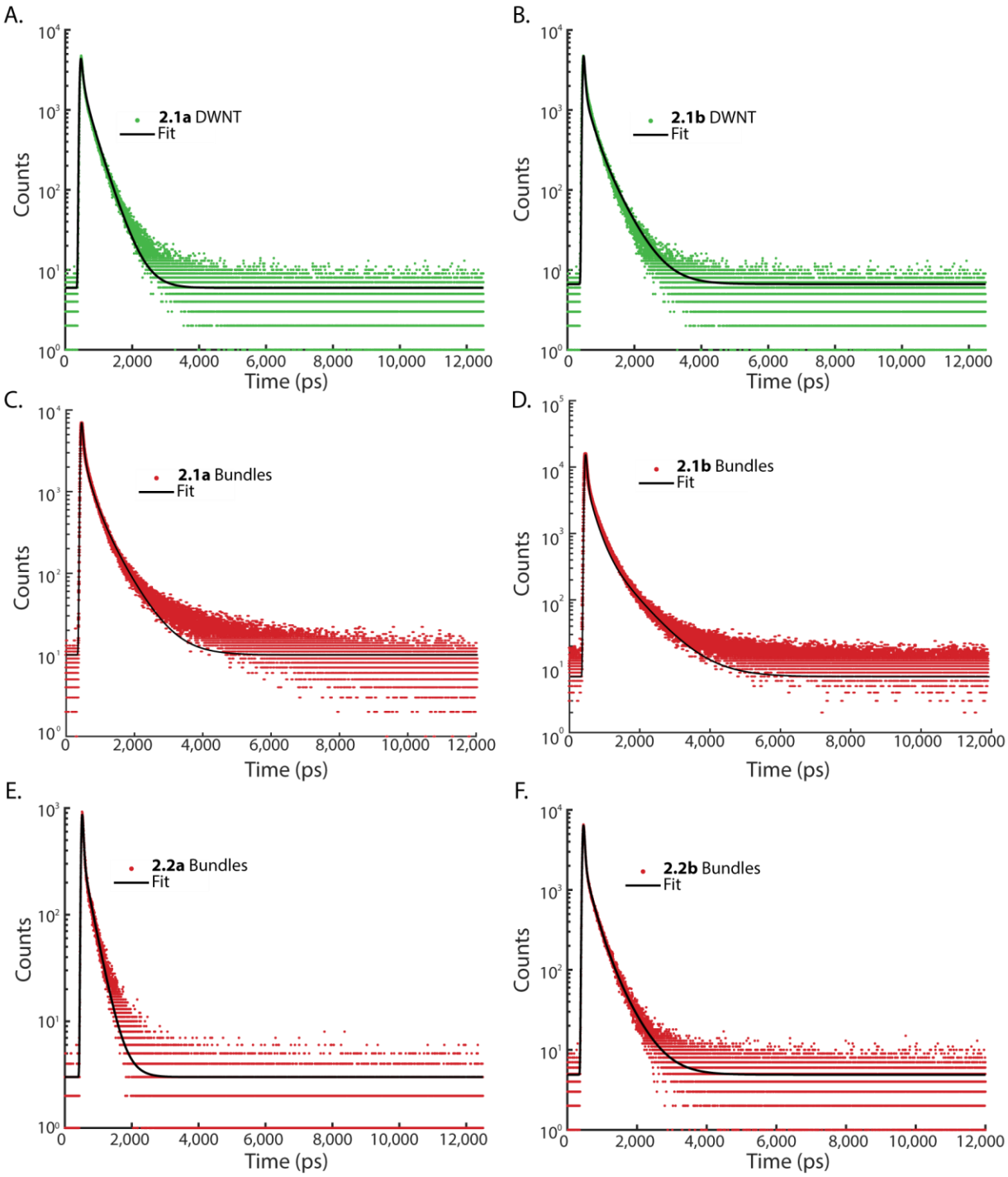

Figure 2.08. Fluorescence lifetimes for J-aggregates of **2.1a-2.2b**.

2.06. Assessing the superradiance of Cy3 and Cy5 J-aggregates

The ultimate goal of this work was to assess the improvement to the photophysical properties of these dye monomers as compared to their J-aggregates. This metric is referred to as superradiance, which is a phenomenon caused by the collective oscillation when many coupled emitters interfere constructively. In J-aggregates, this constructive interference manifests as an enhancement to the radiative rate of fluorescence compared to the monomer, where that enhancement scales linearly with the number of coupled emitters.

Following the identification of the quantum yields and lifetimes for all monomer and aggregate morphologies, we performed several intermediate calculations to obtain the transition dipole moment (TDM, μ). Within each aggregate lifetime, we recovered a short and long time components (τ_i) with an associated amplitude factor (A_i). To bring these values forward, we obtained the amplitude-weighted average lifetimes as done by Engelborghs and coworkers.[53] The amplitude-weighted total rate (k_{tot}) was obtained via the same process using the reciprocal of the lifetimes, demonstrated by equation 2.1.

$$\langle k \rangle_a = \frac{\sum A_i k_i}{\sum A_i} \tag{2.1}$$

We then obtain the radiative rate (k_r) by multiplying the averaged total rate and quantum yield (Φ_F) as in equation 2.2.

$$k_r = k_{tot} \Phi_F \tag{2.2}$$

We must also factor in the energy gap (E_g), taken as the average energy of absorption and emission for a particular monomer or aggregate. E_g is calculated via equation 2.3.[45]

$$E_g = \nu_{max} + \frac{\nu_{Stokes\ shift}}{2} \tag{2.3}$$

E_g can be converted into wavelength by performing E_g (nm) = 10^7/ E_g (cm-1). From k_r and E_g, we calculate TDM using equation 4, where ε_o is the dielectric of free space, ħ is the reduced Planck's constant, c is the speed of light, n is the index of refraction for the solvent in which quantum yield was measured. Note that E_g is used in Joules for equation 2.4.

$$\mu_{21} = \sqrt{\frac{k_r 3\pi\varepsilon_o \hbar^4 c^3}{n {E_g}^3}} \tag{2.4}$$

Building upon that derivation, the superradiance parameter ηSR is defined as the ratio of the square of transition dipole moments for the monomer and aggregate.

$$\eta_{SR} = \frac{{\mu_{agg}}^2}{{\mu_{mon}}^2} = \frac{k_{r,agg} {E_{g,mon}}^3}{k_{r,mon} {E_{g,agg}}^3} \tag{2.5}$$

Although other works have used different definitions for superradiance in J-aggregate systems[40,54,55], this method factors in the difference in energy gap, which by itself gives rise to an intrinsic change in radiative rates due to the redshift from monomer to aggregate.[45] We note that the ηSR parameter is also a measure of the coherence length for the fluorescent state, or the number of monomers over which the Frenkel excitons delocalize.[56] Therefore, after carefully characterizing the quantum yields and lifetimes, we were able to determine both the transition dipoles and superradiance parameters.

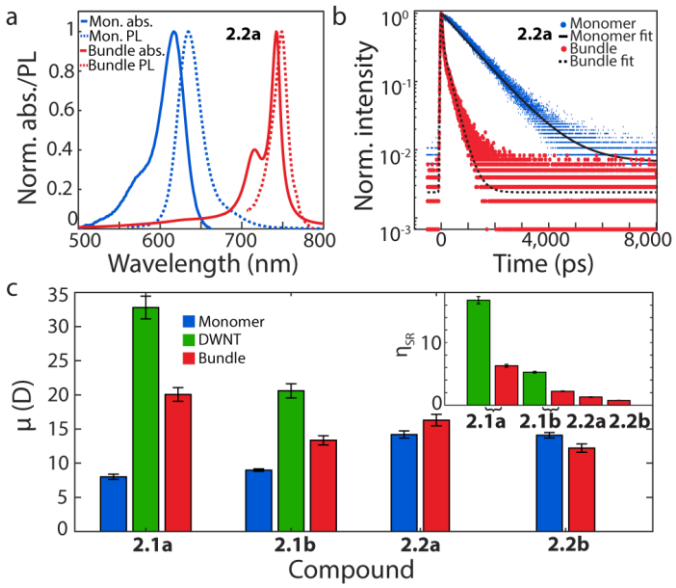

Figure 2.09. Summary of photophysical characterization of monomers and J-aggregates. a) Absorption and emission spectra of **2.2a.** b) Fluorescence lifetimes for monomer and J-aggregate of **2.2a**. c) Transition dipole moments and superradiance parameters for all dyes and J-aggregates.

Figure 2.09 demonstrates that the trimethine aggregates possess transition dipole moments up to 5 times larger than their monomer counterparts; this corresponds to high superradiance parameters (e.g. ~17 for **2.1a** DWNT). However, for the pentamethine dyes, the aggregate transition dipoles are comparable to those of the monomers. This accordingly leads to ηSR values that are closer to 1, meaning that they are less superradiant (or in the case of **2.2b**, subradiant). These data can be attributed to the higher disorder in aggregates of **2.2a** and **2.2b** which leads to decreased exciton delocalization despite retaining redshifted emission. We also observe that the brominated aggregates are less superradiant than their chlorinated counterparts; we hypothesize this is due to the additional energetic disorder, which is indicated by the broader absorption linewidths and also via qualitative estimates of structural disorder in the cryo-EM.

Table 2.2. Photophysical data for monomers and aggregates of dyes **2.1a**, **2.1b**, **2.2a**, and **2.2b**. Quantum yield (Φ_F) error was taken as the standard deviation of triplicate measurements. Lifetime (τ) error was taken from the 95% confidence interval in fitting. Error in radiative rate (k_r) and superradiance parameter (η_{SR}) were propagated from the original lifetime and quantum yield measurements.

Dye	Morphology	Φ_F	Avg. τ (ps)	k_r*10^8 (s^{-1})	E_g (nm)	μ (D)	η_{SR}
2.1a	Monomer	0.025 ± 0.002	138 ± 1	1.8 ± 0.1	528	8.0 ± 0.4	
2.1a	DWNT	0.15 ± 0.020[a]	140 ± 2	20 ± 2	597	33 ± 2	16.8 ± 0.6
2.1a	Bundle	0.036 ± 0.004	81 ± 1	7.3 ± 0.7	602	20 ± 1	6.3 ± 0.2
2.1b	Monomer	0.028 ± 0.002	110 ± 1	2.5 ± 0.1	530	8.99 ± 0.2	
2.1b	DWNT	0.040 ± 0.004[a]	68 ± 2	8.1 ± 0.7	593	21 ± 1	5.3 ± 0.1
2.1b	Bundle	0.013 ± 0.001	62 ± 1	3.2 ± 0.3	603	13.4 ± 0.7	2.2 ± 0.1
2.2a	Monomer	0.33 ± 0.025	1019 ± 3	3.3 ± 0.2	625	14.2 ± 0.5	
2.2a	Bundle	0.012 ± 0.001	72 ± 2	2.6 ± 0.3	740	16.3 ± 0.9	1.3 ± 0.1
2.2b	Monomer	0.36 ± 0.020	1126 ± 2	3.2 ± 0.2	623	14.1 ± 0.4	
2.2b	Bundle	0.006 ± 0.001	70 ± 1	1.6 ± 0.2	725	12.2 ± 0.6	0.8 ± 0.1

[a]Values taken from literature.[25,57]

2.07. Computational screening of redshift and disorder

We employed computational screening to gauge how tube radii, chiral angle, and slip between monomer units affect resultant spectral properties and in order to estimate a structure consistent with the excitonic result.[14,32,58] For simplicity, we focus on bundles derived from dyes **2.1a** and **2.2a**, though these results likely generalize to the brominated dyes as well. In Table 2.2, we report the experimentally determined tube radii and relative and absolute energies/heights of the parallel and perpendicular transition. In comparing values between aggregates, while similar overall shifts, we observe differences in peak ratios and parallel to perpendicular shifts.

Table 2.3. Experimental observables used for tube-wrapping computations.

Tube radii were taken from cryo-EM, absorption shifts were taken from spectra of **2.1a** and **2.2a** monomers and aggregates at 75K. Chiral angles were computed using the ratio of peaks and shift in the zero-disorder limit, see subchapter 2.07.

Dye Bundles	∥ to ⊥ **Height Ratio**	**Monomer to ∥ shift (cm^{-1})**	**∥ to ⊥ shift (cm^{-1})**	**Average tube radius (Å)**	**Chiral Angle (°)**
1a	0.71	-2573	658	44	±40
2a	0.44	-2793	506	23	±33

To construct model aggregates and determine their spectral properties we begin by asserting that the bundles are comprised of weakly coupled single-walled nanotubes.[49] Lattice brick dimensions were determined by adding 2 Å of slip to the Cl-Cl distance across the dye following prior work.[59] Potential tube structures (and thus Hamiltonians) were determined using a planar lattice with a variable slip between bricks. Furthermore, we considered only chiral angles that permit tubular radii within 1 Å of the measured value. Figure 4a shows examples of valid tube rolling parameters starting from a 2D planar lattice of aggregates of **2.2a**. Packing geometries that generate tubes of radii within the set tolerance are demarcated by red crosses. An exact procedure for generating the tubes is given below.

First, a 2D planar brick lattice is constructed for both the Cy3 and Cy5 dyes, estimating the brick lattice as 2 Å greater than the averaged Cl-Cl distance on the dyes. Then, for a given slip, a 2D planar lattice is generated. For the tube radius as measured by cryo-EM (see Table 2.2), all possible tube chiral vectors are constructed within a 1 Å tolerance, and then tube Hamiltonian parameters are constructed in the basis of 'stacked rings' of dipoles.[32,60] Examples of acceptable chiral vectors on a Cy5-like dye 2D lattice, and the corresponding tubes generated is shown in Figure 5c.

Parameters for a Cy3- and Cy5-like extended dipole Hamiltonian from a ZINDO calculation of a modified dye, exactly as presented in work from Deshmukh *et al*.[14,59] Given the predicted inter-ring angle of rotation, γ, a Farey rational approximation for $\gamma/2\pi$ is calculated such that the total number of dyes did not exceed 500,000.[61] Using this rational approximation for $\gamma/2\pi$ guarantees good periodic boundaries along the length of the tube, and with a total tube length > 1 μm for all simulations we are fully at the large system limit of the dipole model. Then for each acceptable chiral vector of a given radius, the extended dipole Frenkel Exciton Hamiltonian is constructed, setting the monomer energy equal to zero. At first, we do not treat disorder in the system and in this case, it can be diagonalized by Bloch-waves, which we execute by performing a 2D fast Fourier transform.

A best fit slip and chiral angle was selected for the **2.2a** dye and **2.2a** dye based off of matching the parallel ($E_0 \rightarrow E(k_z = 0, k_r = 0)$) and perpendicular ($E_{\pm 1} \rightarrow E(k_z = 0, k_r = \pm 1)$) absorption peak shifts from the monomer, as well as, to account for a potential aggregate solid state linear dielectric, the ratio of the peak shifts $E_{\pm 1}/E_0$. Additionally, we can estimate that the tube chiral angle is between 30 and 50˚ due to the relative oscillator strengths of the parallel and perpendicular peaks in the low temperature experimental spectra, $f_{\perp}/f_{/\!/} = \tan^2(\theta)$ for a disorder free absorption spectrum of a single tube.

Next, the best fit tube Hamiltonian is efficiently screened for disorder using a Chebyshev expansion of the Hamiltonian, until a condition for static disorder leads to a matching peak width compared to the experimental parallel peak.[58] We select the spectra with the best relative parallel to perpendicular shift, and allow for a linear solid-state dielectric scaling to match the total monomer-parallel shift of the tubular aggregate.

The polar plots in Figure 2.10 visualize the extended screening approach with the distance from the origin indicating slip and polar angle (θ) indicating chiral wrapping. To handle many realizations of slip, chiral angle, and diagonal disorder, we employed a stochastic method for estimating optical observables described in prior publications.[58] Within 2.10b, the left half of the polar plot shows the position of the tube parallel absorption peak shift relative to the monomer. The color of each state corresponds to the degree of spectral shift, i.e. redshifted parallel absorption in J- aggregates, and blueshifted parallel absorption in H-aggregates. On the right half of the polar plot, we use yellow to mark all simulations that give a valid match to the experimental 75 K absorption spectra for the ratio of absorption shifts between parallel and perpendicular peaks, $(E_{\perp} - E_{mon}) / (E - E_{mon})$. We further reduce the space by estimating the chiral angle based on the ratio of parallel and perpendicular peak heights, which yielded a value of ±40 and ±33 degrees (reported in Table 2.2). We then performed a close screening ±10 degrees from the predicted value denoted by the shaded blue region on the right side of Figures 2.10c and 2.10c. Similar to our previous work, we scanned all possible slips excluding the range of 0-2 Å, where H-aggregation predominates.[59]

Using the best fit solutions generated in Figure 2.10b/c, we generated spectra by implementing different amounts of diagonal disorder until we showed agreement with the FWHM of the experimental absorption spectra. The slip value and chiral angle between bundles of **2.1a** and **2.2a** dyes are consistent (24° vs. 30.4° and 6.15 Å vs. 5.5 Å, respectively). Interestingly, the differences in spectra seem to only arise due to differences in tube width. The apparent small differences in slip and chiral angle may only arise due to the increased length of the monomer unit, which subsequently influences packing.

Our results demonstrate how decreased tube widths and stronger dipolar coupling can mask higher disorder. As Figure 2.09c shows, bundles of **2.2a** have a larger space of allowed slips and chiral angles that produce ~3,000 cm^{-1} of redshift relative to **2.1a**. Both slip and the chiral angle also appears to have less influence on the redshift of the parallel peak in the simulations of **2.2a**. Our model shows that narrower tube widths result in a more quasi-one-dimensional system leading to chiral angle only weakly influencing the resultant spectral features. Additionally, modelling the absorption spectra of the **2.2a** bundles required that we include nearly twice the disorder (560 cm^{-1}), as opposed to 220 cm^{-1} for the bundles of **2.1a**. Despite similar ending linewidths for **2.1a** and **2.2a** bundles, this increased disorder likely matches the qualitative observation of increased structural disorder under cryo-EM and decreased superradiance observed for the **2.2a/2.2b** bundles.

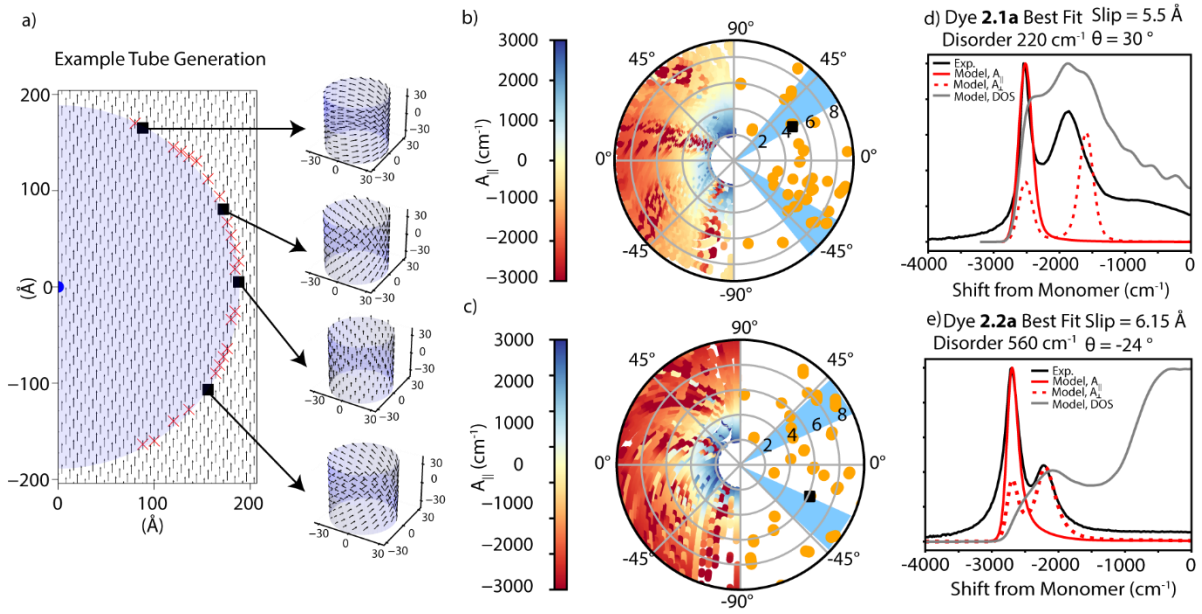

Figure 2.10. Computational screening of dyes **2.2a** and **2.1b**.

a) Examples of the tube-wrapping simulation used for bundles of **2.2a**. b,c) Polar plots of **2.1a** (b) and **2.2a** (c) visualizing the computational screening conditions of slip and chiral angle used to find matches between the monomer to aggregate shift and relative ratios of aggregate peaks. The

degree of blue/redshift for each slip/chiral angle is given on the left side of the plot. The space of possible solutions screened (right side) is shaded in blue, with yellow dots indicating possible solutions, and a black dot indicating the best match to experimental data. d,e) Experimental and modelled absorption spectra/DOS of **2.1a** (d) and **2.2a** (e) from screening fits shown in Figure 2.10.

We note that the energy difference between parallel and perpendicular peaks changes between the bundles of **2.1a** and **2.2a**. While our model accurately describes absorption spectra of the **2.2a** bundles, it somewhat fails to capture the peak separations for **2.1a**; we hypothesize this is the result of inter-tube coupling. Previous work has predicted that inter-tube coupling can only affect the perpendicular peak due to the coupling of parallel long-wavelength excitations only producing boundary charges on the aggregate.[62] Ultimately, we learn that the largest differences in excitonic aggregate properties seem to arise from the individual tube width; the **2.2a** and **2.2b** tubes are roughly twice as thin as the **2.1a** and **2.1b** tubes, implying that the bundles of **2.2a** and **2.2b** contain fewer dyes wrapping around the cylinder.

Overall, the modelling indicates that the changes in tube width lead to changes in the relative energies of the excitonic states, as well as the amount of disorder required to realize the experimental spectrum. Building upon our qualitative estimates of disorder from cryo-EM, it seems the thinner tubes yield less consistent packing and assemble into more disordered structures, potentially due to the more varied solutions of slip and chiral angle shown in Figure 2.10. These differences also demonstrate how radical changes in self-assembly can stem from only small modifications to the monomer building block.

2.08. Conclusion

We synthesized and aggregated two new pentamethine dyes based on the C8S3 scaffold to create two new emitters at ~750 nm. We maintain the lineshapes of the original aggregates while redshifting by 100 nm and found with cryo-EM imaging that the pentamethine dyes mainly self-assembled into large bundles of nanotubes, as opposed to long single or double-walled tubes. Photophysical characterization of these aggregates then allowed us to calculate transition dipole moments and superradiance parameters for each compound and aggregate morphology. Correlating the morphological and photophysical data, we were able conclude that the pentamethine dyes displayed different kinetics of self-assembly that resulted in generally more disordered aggregate bundles with lower superradiance relative to their trimethine comparators. We employed computational screening to examine how structural differences between the trimethine and pentamethine aggregates affect their excitonic properties, finding that the primary differences in spectral characteristics arise from differences in tube widths.

There are several key takeaways from our study. Initial screens showed highly redshifted aggregate structures in the pentamethine dye series that analogized easily to the prior observed trimethine bundles. However, despite similar spectral features (including nearly matching overall redshifts and peak positions) more detailed photophysical analysis revealed a significant decline in superradiance. Computational screening showed that we could reproduce the shifts and peak positions while invoking higher diagonal disorder and that the primary difference between the dyes arises from the smaller tube radii. Indeed, the smaller tube radii results in a quasi-1D density of excitonic states that serves to create increased dipolar coupling, while masking structural/diagonal disorder which leads to decreased superradiance. In short, while amphiphilic dyes can be coaxed

to form tubular aggregates, the properties that give rise to superradiant excitons are more sensitive to the conditions of assembly.

2.09. Experimental procedures

Chemical reagents were purchased from Fisher Scientific or Sigma-Aldrich and were used without purification unless specified. 5,6-Dichloro-2-methylbenzimidazole, 2-methylbenzimidazole and glutaconaldehydedianil hydrochloride were purchased from TCI America. Anhydrous DMSO was obtained from a Sure-Seal™ bottle from Sigma-Aldrich. Anhydrous DMF was obtained from a Grubb's-type Phoenix Solvent Drying System. Dry ethanol was prepared by drying over molecular sieves for 48 h. Thin layer chromatography was performed using Silica 60 F254 plates (Sigma-Aldrich). Flash chromatography was performed using Silica Gel 60 from Fisher Scientific (40-63 μm). Solvents were removed using a Buchi Rotavapor RE111 attached to a Cenco Pressovac pump. Bath sonication was performed using Branson 2510 model sonicator. Masses were measured on a Mettler Toledo AB204-S balance. Unless otherwise specified, all reactions were performed under Ar atmosphere on a ChemGlass CG-4441-02 Schlenk line.

Nuclear magnetic resonance (1H, 13C) spectra were taken on a Bruker Avance 400 spectrometer and processed using TopSpin 4.0.4. Absorbance spectra were measured on a Cary 60 UV-vis spectrophotometer with a 4800 nm/min. rate after blanking with the appropriate solvent.

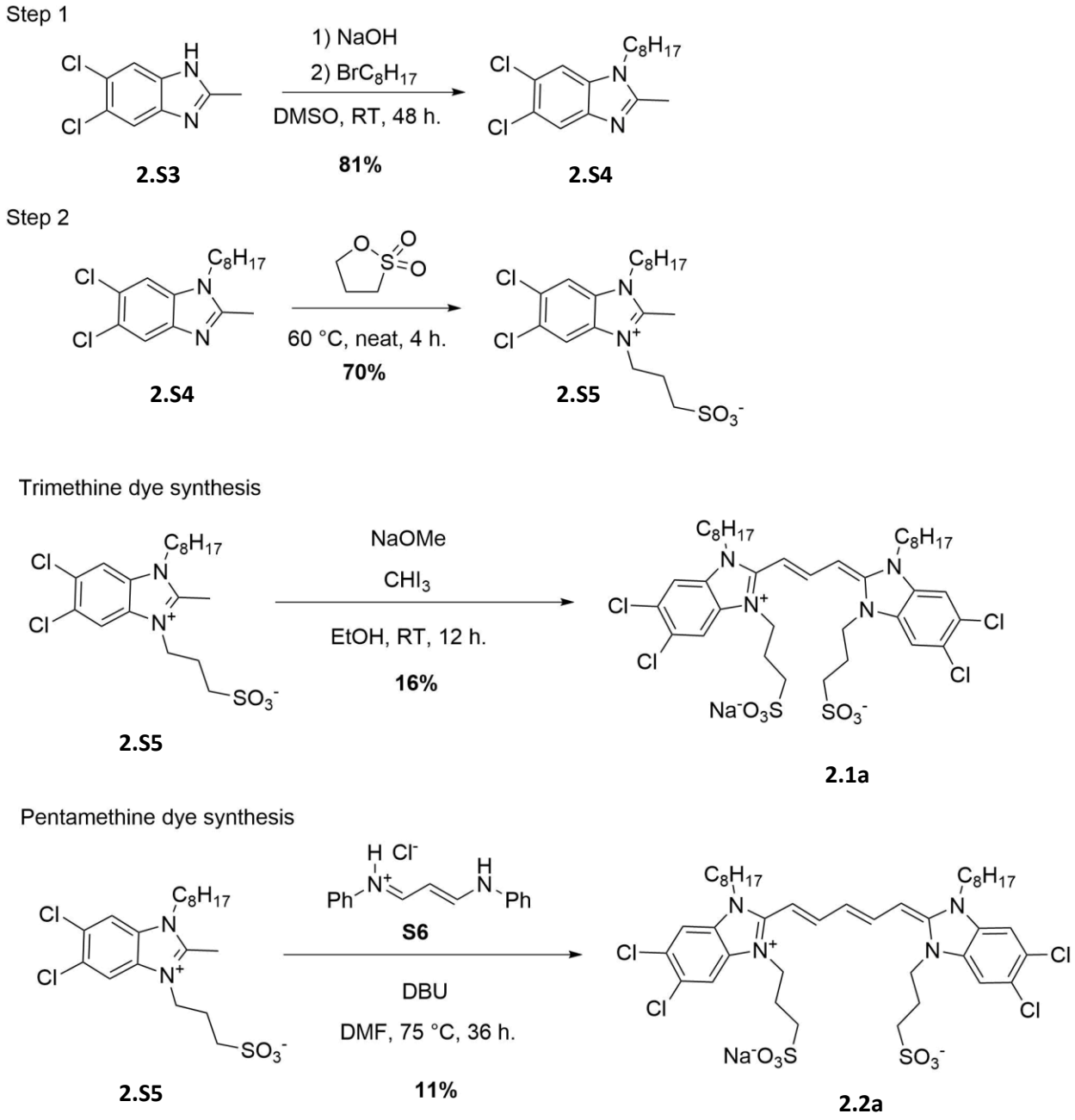

Figure 2.11. Synthesis of tetrachlorobenzimidazole heterocycles and dyes.

*Synthesis of **S4** (5,6-dichloro-2-methyl-1-octyl-1H-benzo[d]imidazole)*

5,6-dichloro-2-methylbenzimidazole (**S3**, 1.00 g, 5.0 mmol, 1 eq.) and ground NaOH (269 mg, 6.71 mmol, 1.35 eq) was evacuated and subsequently purged with argon for three cycles before adding anhydrous DMSO (9 mL). After stirring for 4 h. bromooctane (1.72 mL, 9.95 mmol, 2.0 equiv.). was added dropwise and allowed to stir for 48 h. The reaction was quenched with H_2O (20

mL) at which point a pink precipitate formed. The reaction mixture was suction filtered and washed with water and acetone to yield the product as a white, powdery solid (1.26 g, 4.02 mmol, 81%). ^{1}H NMR (400 MHz, CD_3OD): δ 7.61 (s, 2H), 4.13 (t, *J* = 15 Hz, 2H), 1.74 (t, *J* = 6.5 Hz, 2H), 1.25 (m, 10H), 0.852 (t, *J* = 6.95 Hz 3H). ^{1}H-NMR matches literature.[28]

*Synthesis of **S5** (2-(5,6-dichloro-2-methyl-1-octyl-1H-benzo[d]imidazol-3-ium-3-yl)ethane-1-sulfonate)*

5,6-dichloro-2-methyl-1-octyl-1H-benzo[d]imidazole (**S4**, 135 mg, 430 μmol, 1 eq.) and propane sultone (158 mg, 1.29 mmol, 3 eq.) were evacuated and subsequently purged with argon for three cycles before heating to 60^o C. After stirring for 4 h, the reaction was allowed to cool and acetone (25 mL) was added. The precipitate was suction filtered and washed using acetone to yield the product as a white, flaky solid (131 mg, 301 mmol, 70%) ^{1}H NMR (400 MHz, CD_3OD): δ 8.36 (s, 1H), 8.24 (s, 1H), 4.67 (t, *J* = 14.3 Hz, 2H), 4.45 (t, *J* = 7.5 Hz, 2H), 2.96 (s, 5H), 2.30 (q, 2H), 1.30 (m, 10 H), 0.89 (m, 3H). ^{1}H-NMR matches literature.[28]

*Synthesis of **1a** (sodium 3-(5,6-dichloro-2-((1E,3E)-3-(5,6-dichloro-1-octyl-3-(3-sulfonatopropyl)-1,3-dihydro-2H-benzo[d]imidazol-2-ylidene)prop-1-en-1-yl)-1-octyl-1H-benzo[d]imidazol-3-ium-3-yl)propane-1-sulfonate).*

3-(5,6-dichloro-2-methyl-1-octyl-1*H*-benzo[*d*]imidazol-3-ium-3-yl)propane-1-sulfonate (**S5**, 300 mg, 689 μmol, 1 eq), sodium methoxide (93 mg, 1.72 mmol, 2.5 eq.) and iodoform (163 mg, 413 μmol, 0.6 eq.) were added to a 25 mL Schlenk flask which was evacuated and subsequently purged with argon for three cycles. Anhydrous ethanol (8 mL) was added and the mixture was immediately frozen with liquid nitrogen and underwent three freeze, pump, thaw cycles. The mixture was allowed to warm to R.T. before heating to 60^o C in an oil bath and stirring for 10 min.

The mixture was returned to R.T. and allowed to stir for 15 h. The crude reaction mixture was then suction filtered and washed with cold acetone (10 mL) and cold H_2O (10 mL). The crude product was recrystallized in a 1:1 ratio of DMF:H_2O to give the product as a glittery red solid with an orange tinge (100 mg, 111 μmol, 16%). ^{1}H NMR (400 MHz, MeOD): δ 7.96 (t, 1H), 7.82 (s, 2H), 7.69 (s, 2H), 5.88 (d, 1H), 4.43 (t, 3H), 4.29 (t, 3H), 2.93 (t, 3H), 2.24 (m, 3H), 1.84 (m, 3H), 1.34-1.22 (m, 18H), 0.84 (s, 6H). ^{1}H-NMR matches literature.[28]

*Synthesis of **2a** (sodium 3-(5,6-dichloro-2-((1E,3E,5E)-5-(5,6-dichloro-1-octyl-3-(3-sulfonatopropyl)-1,3-dihydro-2H-benzo[d]imidazol-2-ylidene)penta-1,3-dien-1-yl)-1-octyl-1H-benzo[d]imidazol-3-ium-3-yl)propane-1-sulfonate).*

3-(5,6-dichloro-2-methyl-1-octyl-1*H*-benzo[*d*]imidazol-3-ium-3-yl)propane-1-sulfonate (**S5**, 120 mg, 0.28 mmol, 1 eq.), malonaldehyde bis(phenylimine) HCl (**S6** 34 mg, 0.13 mmol, 0.46 eq.) were added to a 25 mL Schlenk flask which was evacuated and subsequently purged with argon for three cycles then dissolved in dimethylformamide (anhydrous, 8 mL). To this solution, 1,8-diazabicycloundec-7-ene (DBU, 0.3 mL, 2 mmol, 7 equiv.) was added and the mixture was heated to 75^o C for 36 h. The mixture was cooled to rt and concentrated to give a green residue which was dissolved in DI water (150 mL) and washed with toluene (100 mL). The aqueous layer was basified with saturated $NaHCO_3$ and a fine blue/green precipitate was formed. The precipitate was collected by suction filtration and purified via silica gel chromatography twice using a dichloromethane/methanol solvent system with a gradient elution from 0 to 10% methanol. This procedure resulted in a pure blue powder (30 mg, 0.03 mmol, 11%). ^{1}H NMR (600 MHz, MeOD): δ 7.94 (t, *J* = 13.4 Hz, 2H), 7.78 (s, 2H), 7.64 (s, 2H), 6.29 (t, *J* = 11.2 Hz, 1H), 5.68 (d, *J* = 13.4 Hz, 2H), 4.48 (bs, 4H), 4.29 (bs, 4H), 3.02 (bs, 4H), 2.29 (bs, 4H), 1.84 (bs, 4H), 1.44–1.21 (m, 20H), 0.90 –0.84 (m, 6H). ^{13}C NMR (151 MHz, MeOD): δ 150.4, 149.8, 134.0, 133.8, 128.59,

128.58, 120.6, 112.32, 112.28, 88.4, 49.2, 46.1, 45.3, 33.1, 30.5, 30.4, 29.1, 27.7, 25.1, 23.9, 14.6.HRMS (ESI$^-$): Calculated for $C_{41}H_{55}Cl_4N_4O_6S_2$ $[M^-]^-$: 905.2311; found: 905.2307.

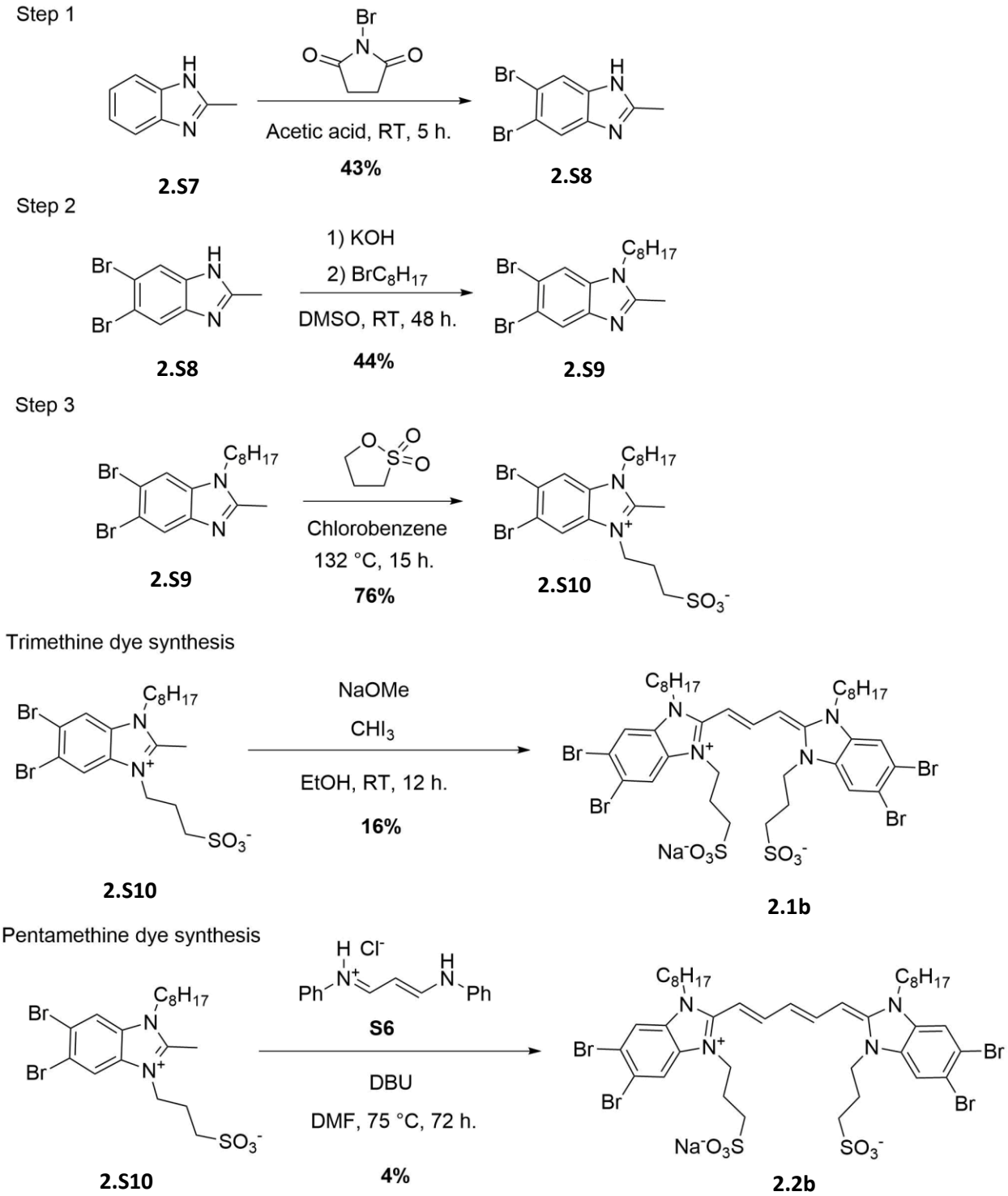

Figure 2.12. Synthesis of tetrachlorobenzimidazole heterocycles and dyes.

*Synthesis of **S8** (5,6-dibromo-2-methyl-benzimidazole).*

2-methyl-benzimidazole (**S7**, 1.500 g, 11.35 mmol, 1 eq.) and *N*-bromosuccinimide (4.240 g, 23.83 mmol, 2.1 eq.) were dissolved in glacial acetic acid (16 mL), heated to 60 ºC, and stirred for 5 h. The reaction mixture was suction filtered and washed several times with saturated aqueous $NaHCO_3$ and water to yield **2** as a white solid (1.43 g, 4.93 mmol, 43.3%). ^{1}H NMR (400 MHz, CD_3OD): δ7.78 (s, 2H), 2.54 (s, 3H). ^{1}H-NMR matches literature.[28]

*Synthesis of **S9** (5,6-dibromo-2-methyl-1-octyl-1H-benzo[d]imidazole).*

5,6-dibromo-2-methylbenzimidazole (**S8**, 5.32 g, 18.34 mmol, 1 eq.), KOH (2.06 g, 36.7 mmol, 2 eq.) were evacuated and subsequently purged with argon for three cycles. The flask was purged 3x using argon and vacuum before adding dry DMF (8 mL), cooling to 0 ºC, and allowing the mixture to stir for 4 h. After stirring, $C_8H_{17}Br$ (6.3 mL, 36.7 mmol, 2 eq.) was added and the reaction was left to stir for 48 h. The mixture was then suction filtered and washed using cold acetone yield **3** as a white, powdery solid (3.23 g, 8.03 mmol, 44%) ^{1}H NMR (400 MHz, CD_3OD): δ 7.85 (d, *J* = 9.81, 2H), 4.17 (t, *J* = 14.69, 2H), 2.57 (s, 2H), 1.76 (m, 3H), 1.32-1.24 (m, 10H), 0.86 (t, *J* = 6.94, 3H). ^{1}H-NMR matches literature.[28]

*Synthesis of **10** (3-(5,6-dibromo-2-methyl-1-octyl-1H-benzo[d]imidazol-3-ium-3-yl)propane-1-sulfonate.)*

5,6-dibromo-2-methyl-1-octyl-1H-benzo[d]imidazole (**S9**, 312 mg, 775 μmol, 1 eq.), 1,3-propanesultone (95 mg, 775 μmol, 1 eq.) dissolved in chlorobenzene (15 mL). The mixture was heated to 132 ºC and allowed to reflux for 15 h. After refluxing the reaction was cooled to R.T. and a white precipitate formed. The solid was suction filtered and washed 3x with diethyl ether (10 mL) to yield a white, powdery solid (309 mg, 0.59 mmol, 76%) ^{1}H NMR (400 MHz, CD_3OD):

δ 8.49 (s, 1H), 8.37 (s, 1H), 4.64 (t, *J* = 15.6 Hz, 2H), 4.41 (t, *J* = 15.3, 2H), 2.91 (t, *J* = 13.3, 2H), 2.27 (q, *J* = 14.2 Hz, 2H), 1.847 (q, *J* = 14.9, 2H), 1.37 (m, 10H), 0.87 (t, 13.7, 3H). ^{1}H-NMR matches literature.[28]

*Synthesis of **1b** (sodium 3-(5,6-dibromo-2-((1E,3E)-3-(5,6-dibromo-1-octyl-3-(3-sulfonatopropyl)-1,3-dihydro-2H-benzo[d]imidazol-2-ylidene)prop-1-en-1-yl)-1-octyl-1H-benzo[d]imidazol-3-ium-3-yl)propane-1-sulfonate).*

3-(5,6-dibromo-2-methyl-1-octyl-1*H*-benzo[*d*]imidazol-3-ium-3-yl)propane-1-sulfonate (**S10**, 313 mg, 597 μmol, 1 eq.), sodium methoxide (80 mg, 1.49 mmol, 2.5 eq.) and iodoform (141 mg, 358 μmol, 0.6 eq.) were added to a 25 mL Schlenk flask which was evacuated and subsequently purged with argon for three cycles. Dry ethanol (8 mL) was then added and the mixture was immediately frozen with liquid nitrogen and underwent three freeze, pump, thaw cycles to ensure an O_2 free environment. The mixture was allowed to warm to R.T. before heating to 60 ^{o}C in an oil bath and stirring for 10 min. After heating, the mixture was returned to R.T. and allowed to stir for 15 h. The reaction mixture was then suction filtered and washed with 10 mL cold acetone and 10 mL cold H_2O. The crude product was recrystallized in a 1:1 ratio of DMF:H_2O to give the product as a glittery red solid with an orange tinge (168 mg, 155 μmol, 26%). ^{1}H NMR (400 MHz, DMSO-d6): δ 8.12 (s, 2H), 8.04 (s, 2H), 7.86 (t, *J* = 13.9 Hz, 1H) 5.87 (d, *J* = 13.5 Hz, 2H), 4.36 (t, *J* = 6.80, 4H), 4.2611 (t, *J* = 6.78, 4H), 1.99 (m, 4H), 1.69 (m, 4H), 1.21 (m, 20H), 0.76 (t, *J* = 13.7, 6H). ^{1}H-NMR matches literature.[28]

*Synthesis of **2b** (sodium 3-(5,6-dibromo-2-((1E,3E,5E)-5-(5,6-dibromo-1-octyl-3-(3-sulfonatopropyl)-1,3-dihydro-2H-benzo[d]imidazol-2-ylidene)penta-1,3-dien-1-yl)-1-octyl-1H-benzo[d]imidazol-3-ium-3-yl)propane-1-sulfonate).*

3-(5,6-dibromo-2-methyl-1-octyl-1*H*-benzo[*d*]imidazol-3-ium-3-yl)propane-1-sulfonate (**S10**, 120 mg, 0.28 mmol, 1 eq.) and malonaldehyde bis(phenylimine) HCl (**S6**, 34 mg, 0.13 mmol, 0.46 eq.) were added to a 25 mL Schlenk flask which was evacuated and subsequently purged with argon for three cycles. These reagents were dissolved in dimethylformamide (DMF, anhydrous, 8 mL). To this solution, 1,8-diazabicycloundec-7-ene (DBU, 0.3 mL, 2 mmol, 7 equiv.) was added and the mixture was degassed via 3 cycles of freeze, pump, thaw. The reaction was then heated to 75 °C for 72 h at which point the mixture was cooled to R.T. and evaporated to dryness. The green residue was dissolved in DI water (150 mL) and washed with toluene (1 x 100 mL). The aqueous layer was basified with saturated $NaHCO_3$ and a fine blue/green precipitate was formed. The precipitate was collected by suction filtration and twice chromatographed on silica gel using a dichloromethane/methanol solvent system with a gradient elution from 0 to 10% methanol. This procedure yielded the product as a blue powder. (30 mg, 0.03 mmol, 11%). ^{1}H NMR (400 MHz, MeOD): δ 7.95 (t, *J* = 12.9 Hz, 1H), 7.91 (s, 2H), 7.77 (s, 2H), 6.29 (t, *J* = 11.7 Hz, 1H), 5.70 (d, *J* = 14.2 Hz, 1H), 4.47 (t, *J* = 15.9 Hz, 3H), 4.28 (t, *J* = 6.94 Hz, 2H), 3.02 (t, *J* = 6.48 Hz, 3H), 2.28 (m, 4H), 1.83 (t, *J* = 7.92 Hz, 4H), 1.47-1.18 (m, 20 H), 0.9-0.82 (m, 6H). ^{13}C NMR (500 MHz, DMSO-d6) 133.1, 118.2, 113.7, 54.4, 44.5, 43.6, 31.5, 31.5, 29.0, 28.9, 27.5, 26.1, 23.5, 22.3, 22.2, 13.1 HRMS (ESI): calcd for $C_{41}H_{57}Br_4N_4O_6S_2^+$: 1081.0453 found: 1081.0470.

2.10. NMR spectra relevant to Chapter 2

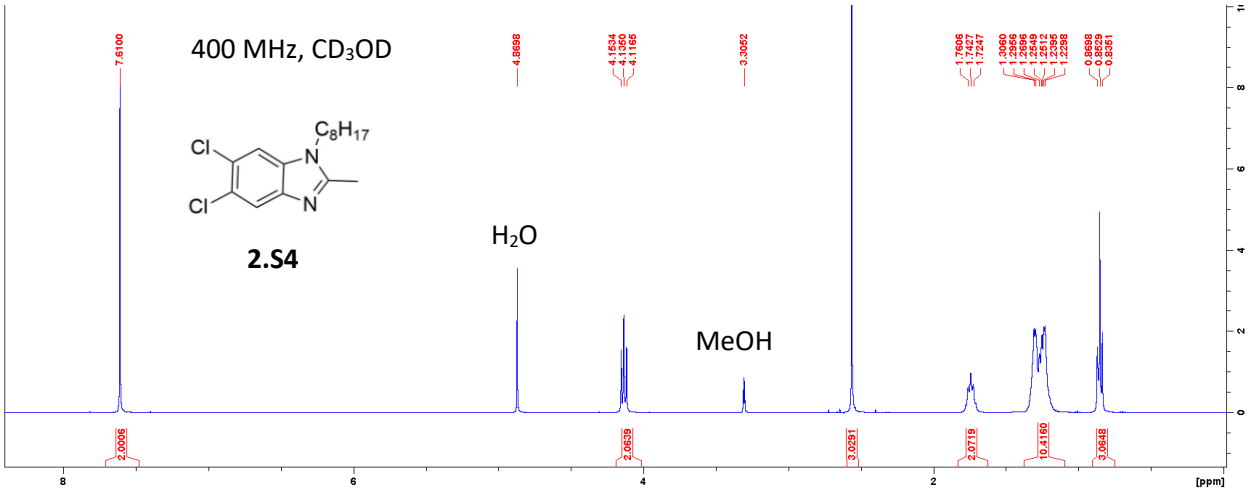
400 MHz, CD3OD
2.S4
H2O
MeOH
[ppm]

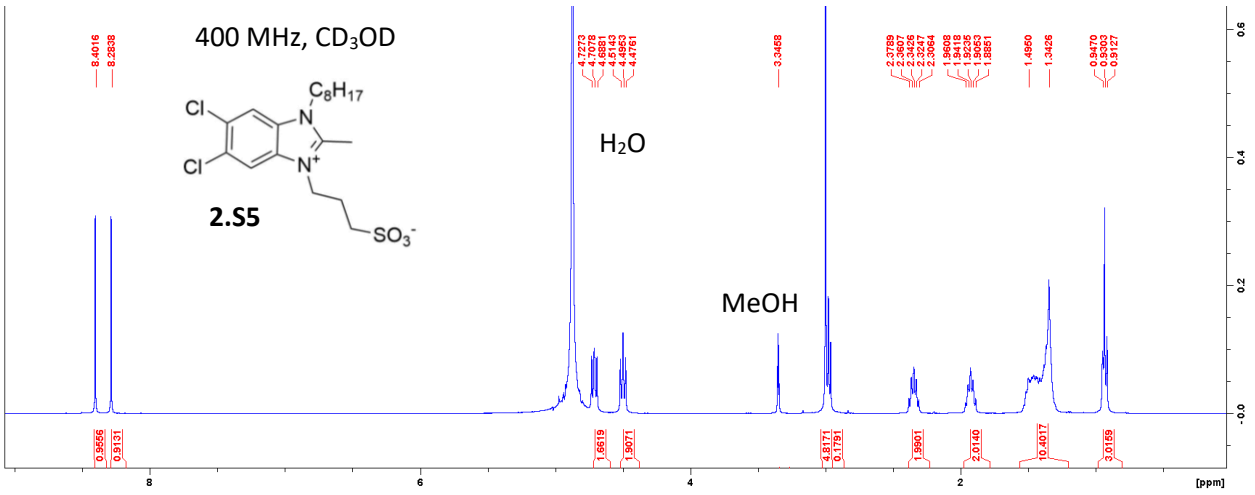
400 MHz, CD3OD
2.S5
H2O
MeOH
[ppm]

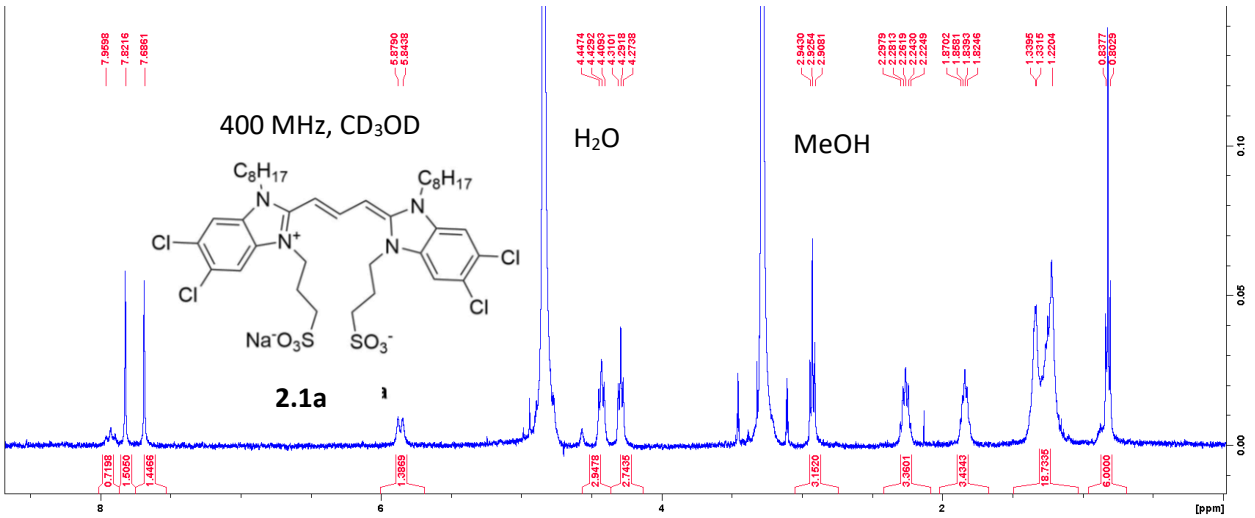
400 MHz, CD3OD
2.1a
H2O
MeOH
[ppm]

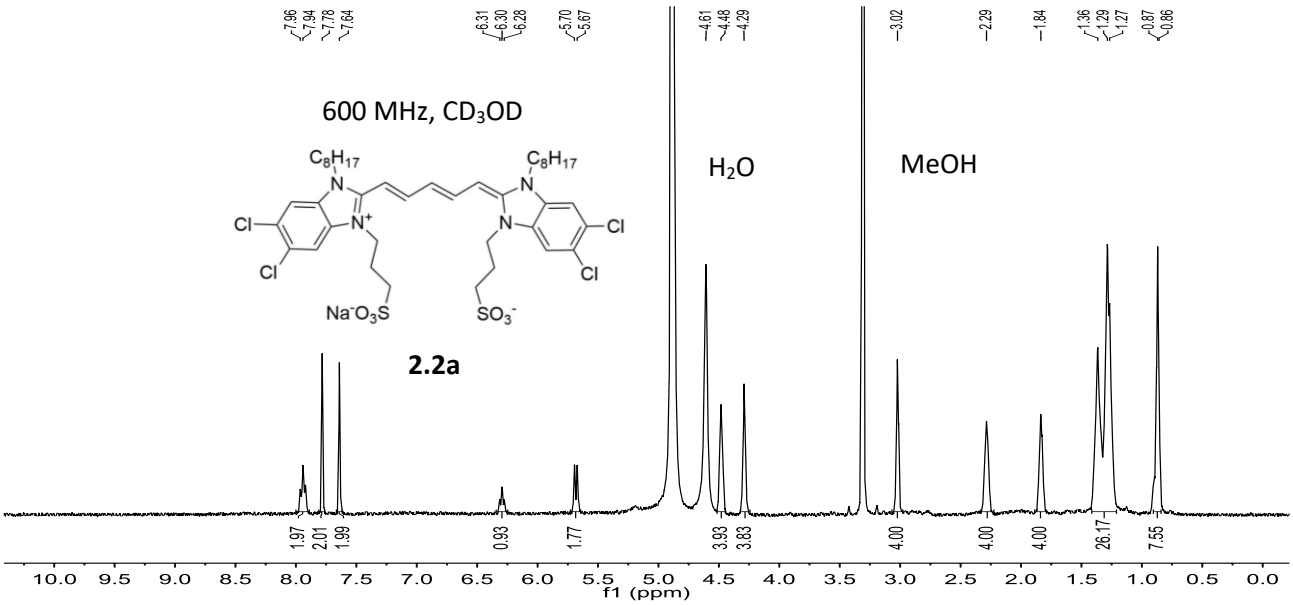
600 MHz, CD3OD
H2O
MeOH
2.2a
f1 (ppm)

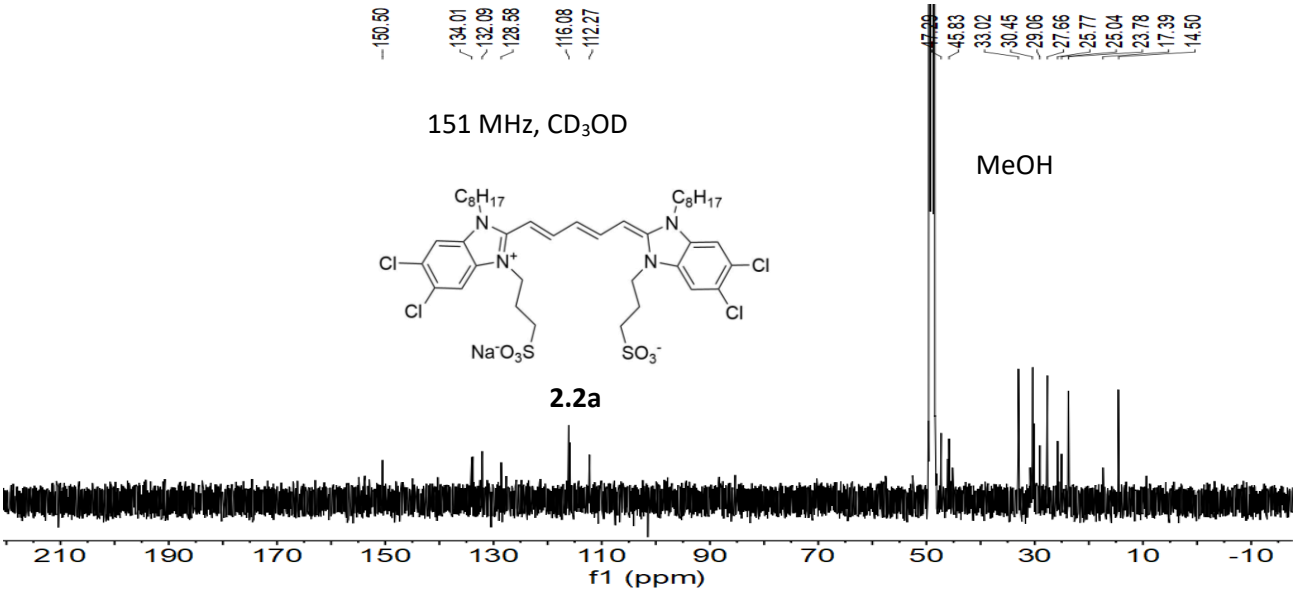
151 MHz, CD3OD
MeOH
2.2a
f1 (ppm)

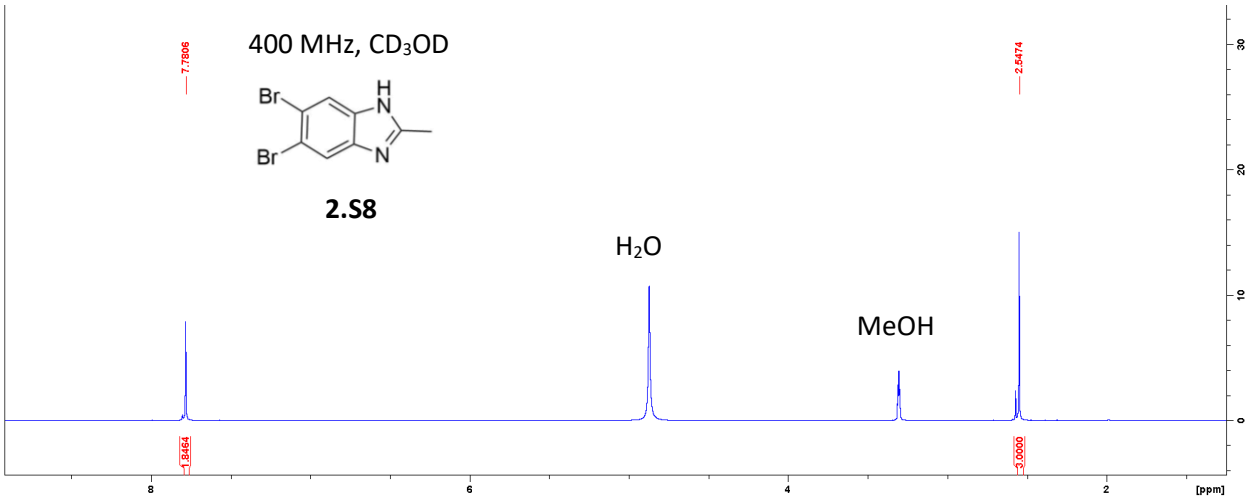
400 MHz, CD3OD
Br
Br
H
N
N
2.S8
H2O
MeOH
7.7806
2.5474
1.8464
3.0000
[ppm]

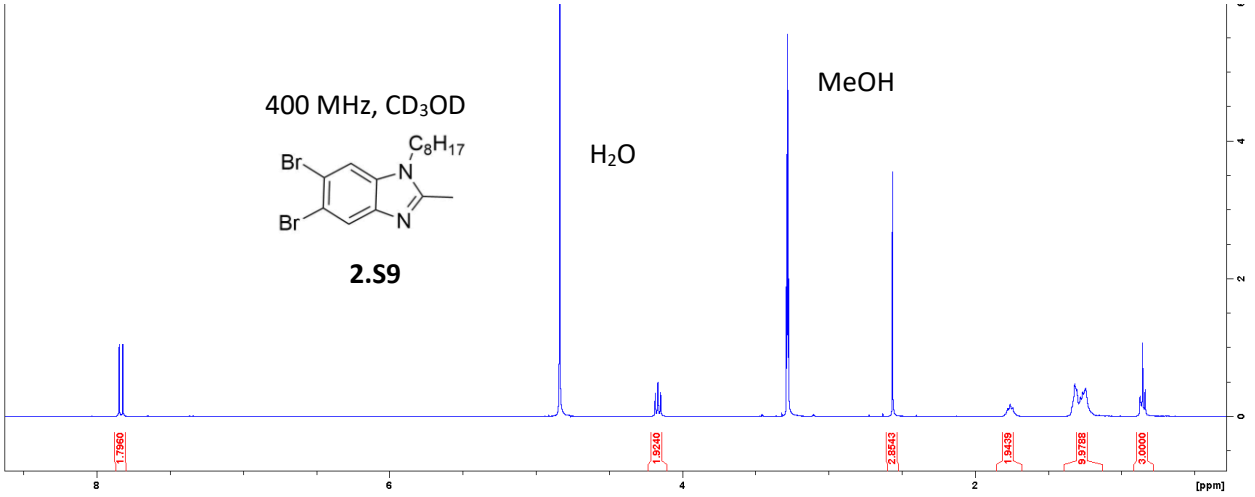
400 MHz, CD3OD
Br
Br
C8H17
N
N
2.S9
H2O
MeOH
1.7960
1.9240
2.8543
1.9439
9.9788
3.0000
[ppm]

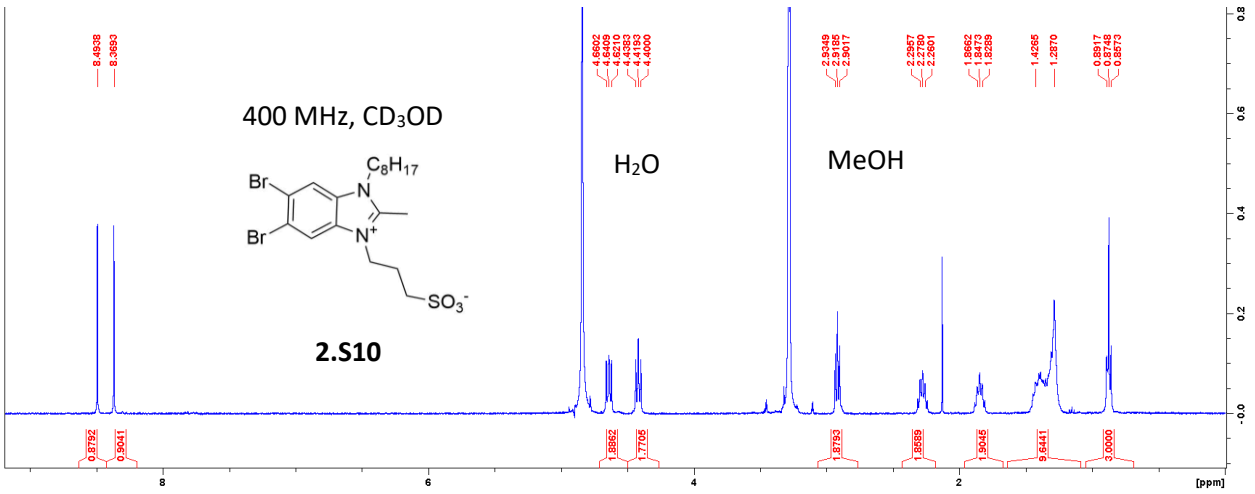
400 MHz, CD3OD
Br
Br
C8H17
N
N+
SO3-
2.S10
H2O
MeOH
8.4938
8.3693
0.8792
0.9041
1.8882
1.7709
1.8793
1.8659
1.9046
9.6441
3.0000
[ppm]

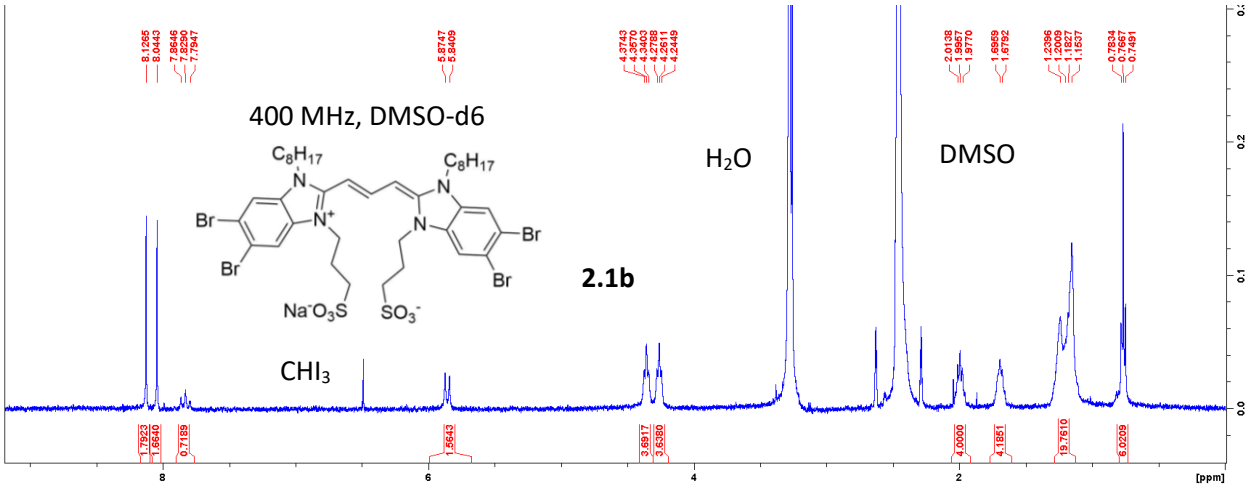
400 MHz, DMSO-d6
H2O
DMSO
CHI3
2.1b
[ppm]

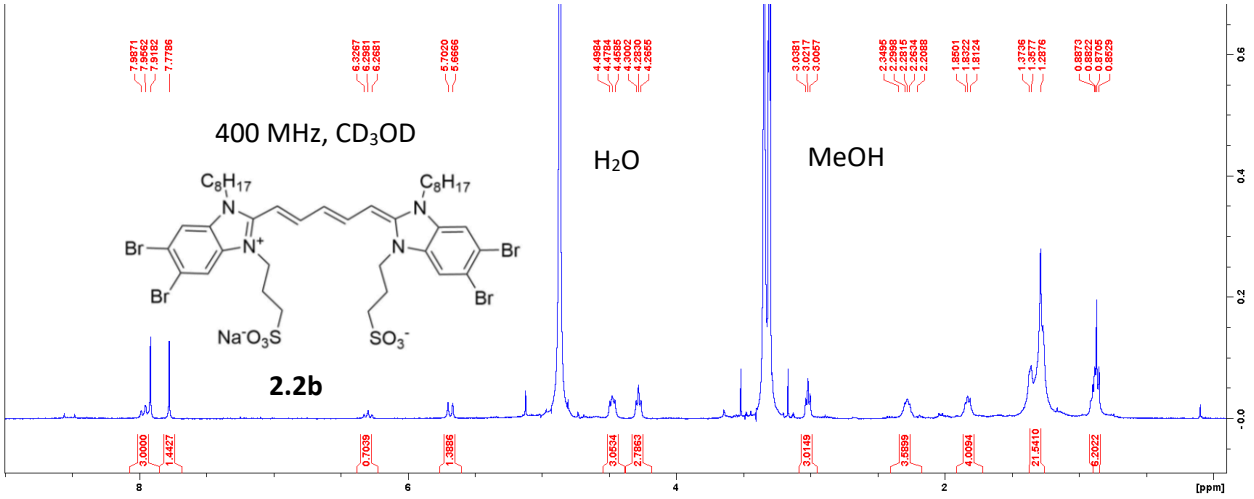
400 MHz, CD3OD
H2O
MeOH
2.2b
[ppm]

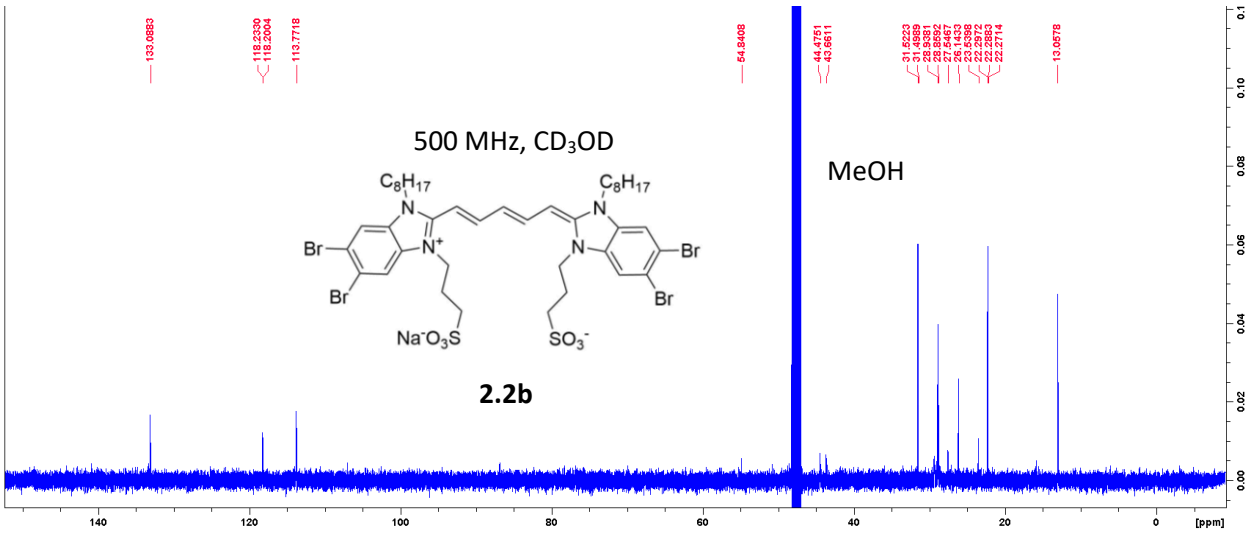
500 MHz, CD3OD
MeOH
2.2b
[ppm]

2.11 pH sensitivity of C8S3 derivatives and J-aggregates

As mentioned in subchapter 2.2, the use of an acid-mediated HPLC method caused us to realize that these dyes have pH-sensitive absorption. We tested this for both the **2.2a** Cy5-C8S3-Cl and **2.1a** Cy3-C8S3-Cl, observing that both compounds undergo full reversible bleaching upon the addition of acid. Figure 2.13 shows the absorbance of the dyes in methanol at various stages of the acid/base addition.

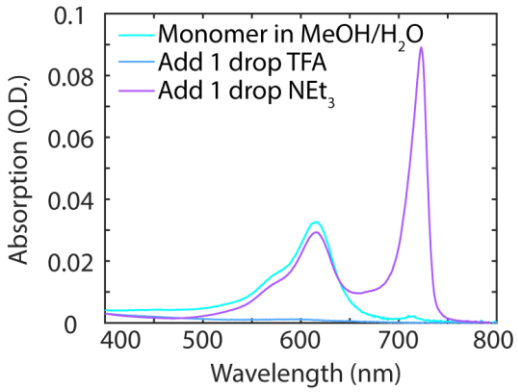

Figure 2.13. Absorbance showing acid-promoted bleaching of C8S3 derivatives.

It is also apparent that the addition of acid and base causes formation of a J-aggregated species, likely due to the solution's increased ionic strength. The cause for the reversible bleaching is likely a protonation equilibrium within the molecule that disrupts conjugation. Prior works on cyanines with pH sensitivity indicate that the protonation may occur on the tertiary nitrogen.[63] While this phenomenon considerably complicates the treatment of these compounds, it is also a valuable feature that increases the versatility of these materials. In addition to classifying these molecules as indicators, this property could allow researchers to turn on/off J-aggregate fluorescence using a simple chemical modification. It's clear that C8S3 derivatives have a complete and reversible dissipation of color, though other dye scaffolds show different pH behavior, which warrants further investigation into the mechanism of this transformation.[64–66]

Chapter 3

Elucidating Molecular Packing of C8S3 J-aggregates with Near-Atomic Resolution Using Cryo-EM Reconstruction

Sections and figures adapted with permission from "A.P. Deshmukh.; W. Zheng; C. Chuang; **A.D. Bailey**; J.A. Williams; E.M. Sletten; E.H. Egelman; J.R. Caram "Near-Atomic Resolution Structure of J-Aggregated Helical Light Harvesting Nanotubes" *ChemRxiv* (2022). *Submitted*."

In the previous chapter, we described how the addition of two methine units to C8S3 successfully redshifted the monomer and aggregate absorption, yet thoroughly changed the kinetics of self-assembly and excitonic superradiance. This chapter details work our lab did in conjunction with Professor Ed Egelman at University of Virginia, which ultimately produced a near-angstrom resolution structure of the C8S3 DWNT inner wall. By understanding this structure, we gained intuition on why C8S3 rises above nearly every other dye as an ideal J-aggregator. My contributions to this work include polarized absorbance spectra (i.e. CD/LD) of C8S3 and synthesis/aggregate screening of two C8S3 derivatives which demonstrated different self-assembly. Ultimately, this collaboration led to a follow-up work which I describe in chapter four.

3.1. Prior research on the structure of C8S3 LHNs

Since Didraga *et al*. presented their initial cryo-EM micrographs and models of the C8S3 double-walled nanotubes in 2004, researchers have been debating the molecular packing of C8S3 J-aggregates.[60] While electron micrographs of the LHN structures are readily obtained, an atomic-level understanding of how the constituent chromophores arrange themselves in tubular structure

is much more difficult to achieve for many reasons. First, because these soft materials are native to the solution state and, moreover, deeply sensitive to their specific solvation conditions, they cannot be studied as solids or in pure solvents (e.g. only methanol or only water). Second, they lack the extensive periodic order and higher symmetry elements required to obtain crystalline samples. For those reasons, the traditional techniques for solving mesoscale structures such as x-ray scattering are not applicable.

Despite these limitations, many groups have attempted to use spectroscopic observables as a way to understand the molecular packing of C8S3 J-aggregates. In their seminal work, Didraga *et al*. modeled the packing as a brick layer lattice wrapped on a cylindrical surface, where each unit cell is occupied by one molecule.[60] They developed a Frenkel exciton model and showed how such an arrangement leads to two dominant excitons for each the inner and outer tubes, parallel and perpendicular. In 2012, Eisele *et al*. utilized a redox chemistry approach to selectively degrade the outer wall of the C8S3 tube.[67] This technique allowed them to probe spectroscopic transitions relating to only the inner structure, which exhibited four distinct features. Based on that observation, they hypothesized that the C8S3 J-aggregate's unit cell must contain two molecules, arranged in a herringbone pattern. This hypothesis accounted for the four transitions by having two separate excitonic subsystems which were weakly electronically coupled. Many others have since performed similar work on analogous systems or conducted further measurements on C8S3 to deduce either a brick layer or herringbone structures.[68] However, until this work, it was unknown which model was correct.

3.2. Near-atomic resolution structure of C8S3 LHNs.

In the past forty years, cryo-EM has emerged as a transformative technique for structural biologists to determine the atomic structure of proteins and other nanoscale objects.[69–72] Because the freeze plunging method ensures the preservation of a native solvated structure, this technique allowed us an unprecedented opportunity to investigate the pristine structure of proteins and lipid/viral assemblies. As knowledge increases surrounding atomic-level resolution cryo-EM, this strategy is expanding beyond structural biology and into other disciplines; however, at this time there are few examples of non-biological systems on the protein data bank (PDB) and no data banks for atomic-resolution information of other molecular structures.[27,73]

One such methodology for this approach is referred to as iterative helical real space reconstruction (IHRSR), and was designed for single-particle analysis of weakly diffracting helical polymers.[74–76] In short, this method relies on many thousands of reference images, which are processed by cross-correlating up to tens of thousands of segments of the helical object. From that point, the analysis undergoes many cycles of optimization to determine the rotation and displacement parameters that best fit a symmetrized volume to the actual volume from the micrographs. And although this technique is extraordinarily powerful, one drawback lies in the assessment of handedness; because helical objects can possess a chirality (even when assembled from achiral units) and the objects imaged by EM do not present an obvious top/bottom, there exists an ambiguity for an exact handedness of the reconstructed model.

Using this method, we were able to achieve a near-atomic resolution reconstruction of the C8S3 light harvesting nanotubes. Unfortunately, because the outer layer of the DWNT was more heterogeneous due to solvation effects, only the inner wall was able to be determined with a high

level of confidence. Nevertheless, we determined the inner wall's cryo-EM map with 3.3 Å resolution, showing a helical rise of 9.9 Å and twist of 33.6 Å, both of which match existing work.[67] Due to the aforementioned discrepancy of helicity, the exact handedness of the inner wall is unfortunately not known. We then used an optimized geometry for two C8S3 molecules (organized in a dimer) and overlaid the reconstructed electron density, seeing excellent agreement between the two models. The reconstructed electron density is shown in Figure 3.01A-F.

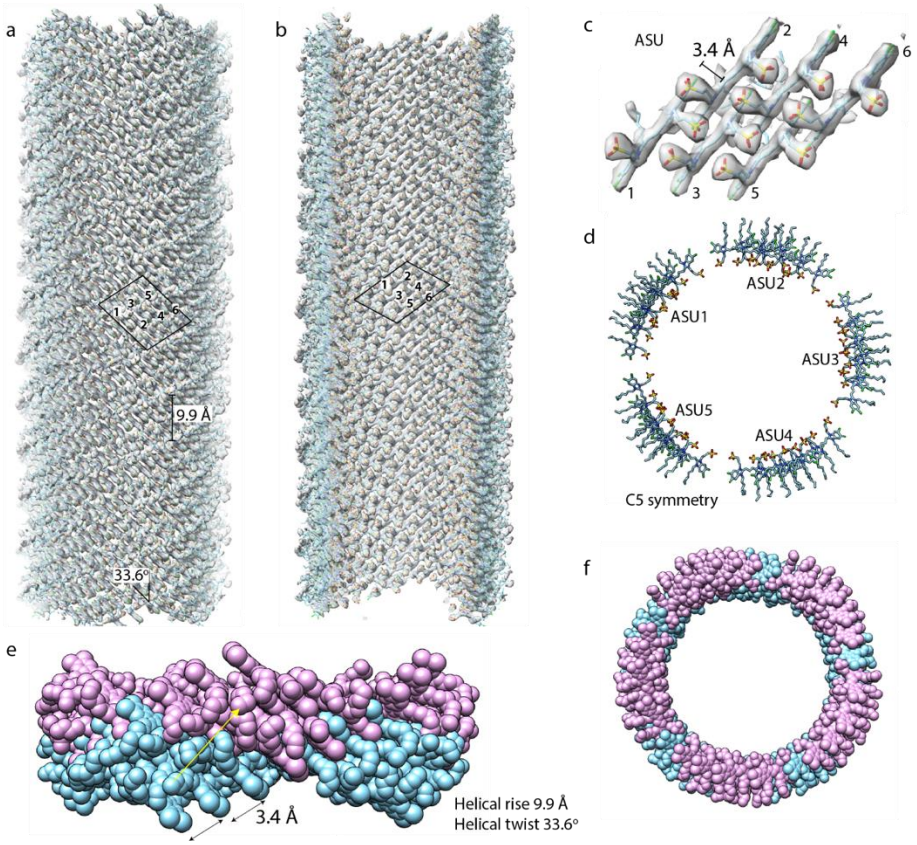

Figure 3.01. Molecular structure of inner wall obtained using IHRSR density maps. a, b) Inner wall density overlaid with the structure showing excellent agreement with the reconstructed density, a) Side view, and b) Cut away view showing regularity of interlocked sulfonates, c) Structure of asymmetric unit (ASU) with 6 non-identical monomers, d) Top down view of the 5 repeats of the ASUs around the circumference, e) Side view and f) Top down view of two translated repeats of the ring in part d.

The model from Figure 3.01C represents an enormous advance to our knowledge about J-aggregates and contains many exciting results. First, that the inner wall's entire supramolecular assembly reduces to an asymmetric unit (ASU) composed of six dye monomers (eight for the outer wall). We also find that tube's circumference is templated by five ASUs and that 14 unique environments exist for the individual C8S3 molecule which lead to its excitonic features. Additionally, this model confirms that individual dye molecules adopt a brick layer (slip stacked) arrangement, as opposed to the herringbone model mentioned in subchapter 3.1.

We also confirm several key parameters concerning the geometry of J-aggregation. The canonical π,π-stacking distance is known to between 3.35 and 3.78 Å, which perfectly agrees with the vertical distance of 3.4 Å measured between chromophores.[77] The slip value was found to be 5.3 Å (or 12.7 Å, due to absence of boundary effects), which yields J-aggregation with a band edge bright state.[54] This is also in agreement with previous knowledge that the ideal slip values are approximately 1/3 the length of the dye monomer.

Yet, perhaps the most insightful discovery, is our observation of interlocking patterns between adjacent dyes in the inner wall electron density. Figure 5.1c shows the unique patterning of dyes in the ASU, which upon closer inspection, appears that the negatively charged sulfonate groups coordinate to the positively charged cyanine backbone of each dye. It seems these molecules are programmed to arrange themselves in this way, with a unique, non-biological motif for self-assembly built into their structure. Previously, it was thought that the hydrophobic and hydrophilic heads of the molecule caused the DWNT structure, yet this information suggests that the organization of these molecules may also be significantly influenced by electrostatics.

3.3. Chemical oxidation and linear dichroism of C8S3 LHNs

Linear dichroism (LD) is a powerful spectroscopic tool that uses polarized absorption to extract information about molecular orientation and transition moments of both small and large molecules.[78,79] It is defined as a sample's difference in light absorption between fully x- and y-polarized light perpendicular to the axis of the anisotropic sample.

$$LD = A_{\parallel} - A_{\perp} \tag{3.1}$$

Another useful version of this quantity is the reduced linear dichroism (LD^r), which is normalized by the isotropic absorbance (A_{iso}).

$$A_{iso} = \frac{A_{\parallel} - 2A_{\perp}}{3} \tag{3.2}$$

$$LD^r = \frac{LD}{A_{iso}} \tag{3.3}$$

The reduced linear dichroism can also be useful in extracting information about the orientation factor of samples with large aspect ratios (e.g. long cylinders). A simplified instrumental diagram of how researchers measure linear dichroism is given in Figure 3.02

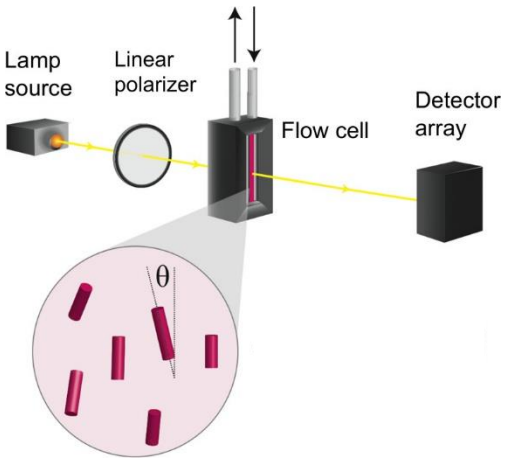

Figure 3.02. Schematic for linear dichroism measurement. Adapted from Clark *et al*.[48]

In C8S3 J-aggregates, LD has been used in conjunction with circular dichroism (CD) to verify Frenkel exciton models of the nanotube structure. Because the double-walled nanotubes are known to exhibit excitonic features caused by excitons in the parallel and perpendicular axes of the tube, LD in particular serves as a valuable tool to interrogate those individual transitions.[48] Using both the herringbone and brick layer arrangement, researchers have developed Frenkel exciton models that allow them to calculate the exact energies and oscillator strengths for given transitions of these excitonic nanostructures.

To obtain the linear dichroism of only the C8S3 inner wall, we performed chemical oxidation of the outer wall with silver nitrate. This was done as described by Clark *et al*. using a 1:1.45 ratio of AgNO3 to dye.[48] In short, 30 μL of 11 mM AgNO3 solution in water was added to 1 mL of 0.48 mM aggregate solution (20% methanol). A white light source was used to trigger the oxidation, which occurred over approximately 40 minutes. Upon full disappearance of the outer wall peak (589 nm), we injected the oxidized J-aggregates into a flow cell (Starna Cells Type 48 Flow Cuvette with 0.2 mm window) within the UV-vis and measured absorbance with a ThorLabs LPVIS050 polarizer fully aligned to the x- and y- directions. We also obtained circular dichroism spectra for the oxidized LHNs using a Chirascan V100. The chemical oxidation and subsequent LD are shown in Figure 3.03.

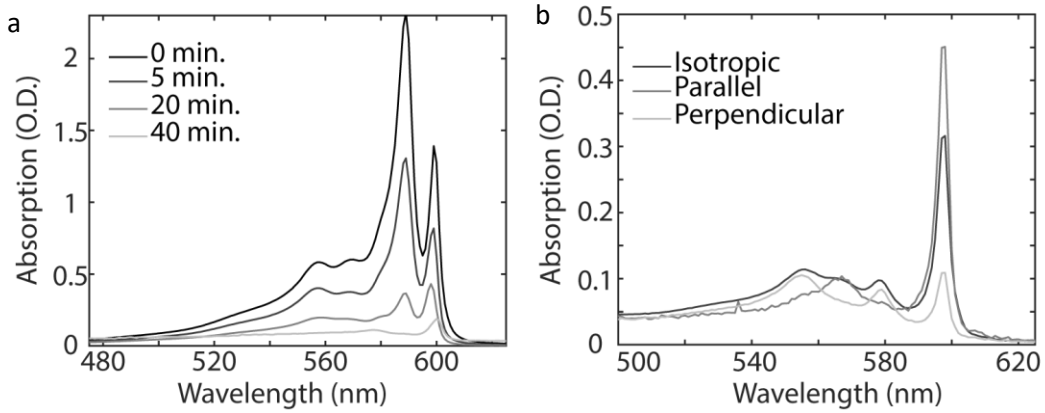

Figure 3.03. Spectroscopic characterization of oxidized C8S3 LHNs. a) Absorbance spectra showing the decrease in absorbance (chemical oxidation) of the outer wall (589 nm) feature. b) Linear dichroism showing the change in absorbance based on polarization of light.

After measuring CD/LD spectra of the oxidized DWNTs, we were able to confirm the physicality of our aforementioned structural parameters (slip and chiral angle) with a Frenkel exciton model. The construction of the matrix, as well as the experimental spectra and fitted spectra are depicted in Figure 3.04.

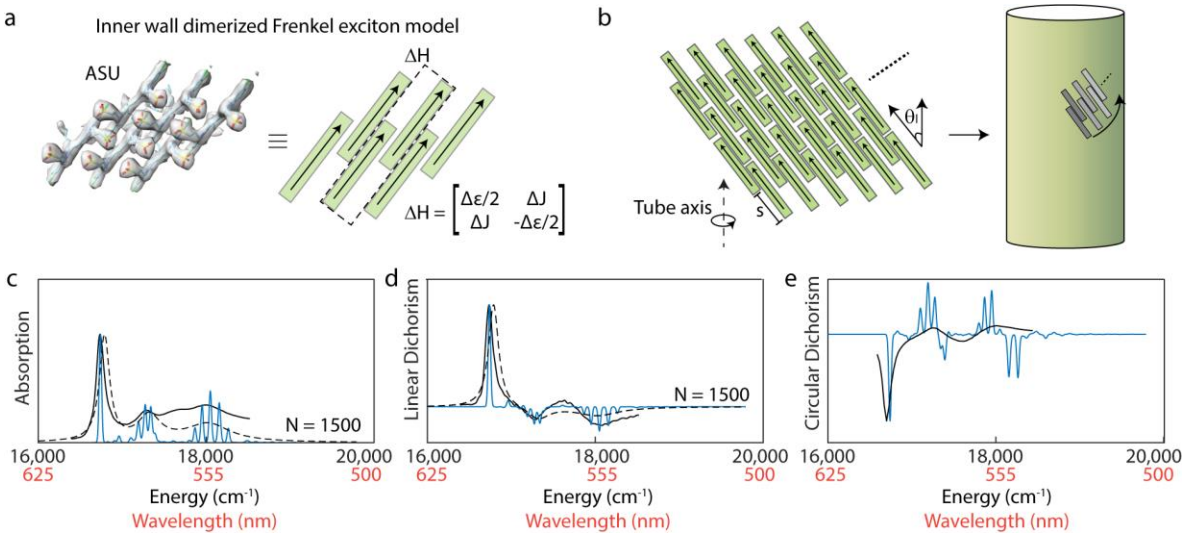

Figure 3.04. Frenkel model for Modeling the optical spectra of isolated inner walls (IW) of LHNs using the cryo-EM structure and dimerized Frenkel exciton model. a) Asymmetric unit with intra-

dimer coupling matrix. b) Schematic showing the relevant geometric parameters and construction of the nanotube from the ASU. c) Experimental and modelled absorption of C8S3 inner wall. d) Experimental and modelled linear dichroism for C8S3 inner wall. e) Experimental and modelled circular dichroism for C8S3 inner wall.

Within subfigures c, d, and e, the blue lines represent spectra calculated from the Frenkel exciton Hamiltonian with inner wall sizes of 1500 monomers. The dashed black lines are calculated spectra (assuming periodic boundary conditions) with Lorentzian broadening obtained from the experimental spectra. Overall, we observe excellent agreement between the Frenkel exciton model and isotropic absorbance/linear dichroism/circular dichroism, which highlights the highly precise structural characterizations we achieved from the reconstructed model.

3.4. Impact of chemical modifications on the self-assembly: C8S3-Br

After seeing the successful reconstruction of the C8S3 LHNs, we originally wanted to showcase the versatility of the IHRSR method by solving several other similar structures. To do this, we wanted a small but meaningful modification to the monomer dye's structure that would yield a modified supramolecular structure. Based on work by Kriete *et al.*, we knew that changing the C8S3 monomer's halogen substitution changed the diameter of the tube.[25] Therefore, we chose to investigate a brominated analog of C8S3, which we refer to as C8S3-Br (the original molecule being C8S3-Cl). The syntheses of C8S3-Cl and C8S3-Br are described in Chapter 2.

Upon the synthesis of C8S3-Br monomer, we characterized its J-aggregation using methanol/water screening at the previously used concentrations for C8S3 DWNTs (i.e. 0.2 to 0.5

mM and 10-30% MeOH). Figure 3.05 shows differences in J-aggregation between C8S3-Cl and C8S3-Br.

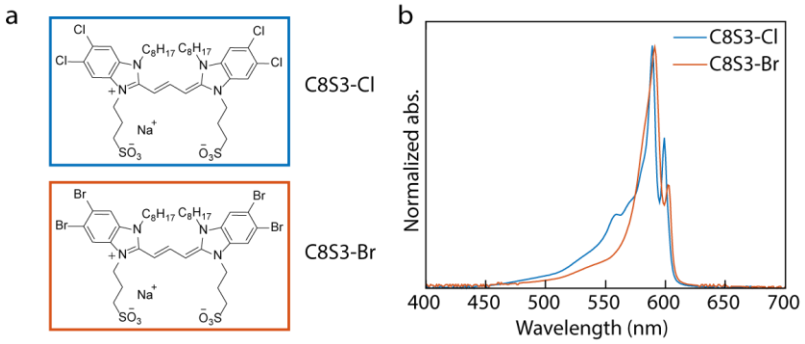

Figure 3.05. Absorption spectrum of C8S3-Cl and C8S3-Br J-aggregates. a) Chemical structure of C8S3-Cl vs. C8S4-Br. b) J-aggregates of C8S3-Cl and C8S3-Br.

We noticed in the absorption spectra that J-aggregates of C8S3-Br lack the fine structure that is associated with C8S3's LHNs. While the overall lineshape is similar, it is broadened and less refined, indicating the presence of greater structural disorder. Because the individual molecular environments are different from tube to tube, the energies of the various transitions become less homogeneous.

We also conducted cryo-electron microscopy and found not only that the tubes were much wider, but that they varied hugely in their width from tube to tube. Figure 3.06 shows an electron micrograph with several tubes of different diameters, as well as a histogram containing a distribution of tube widths for C8S3-Cl vs. C8S3-Br taken from over 10^4 measurements.

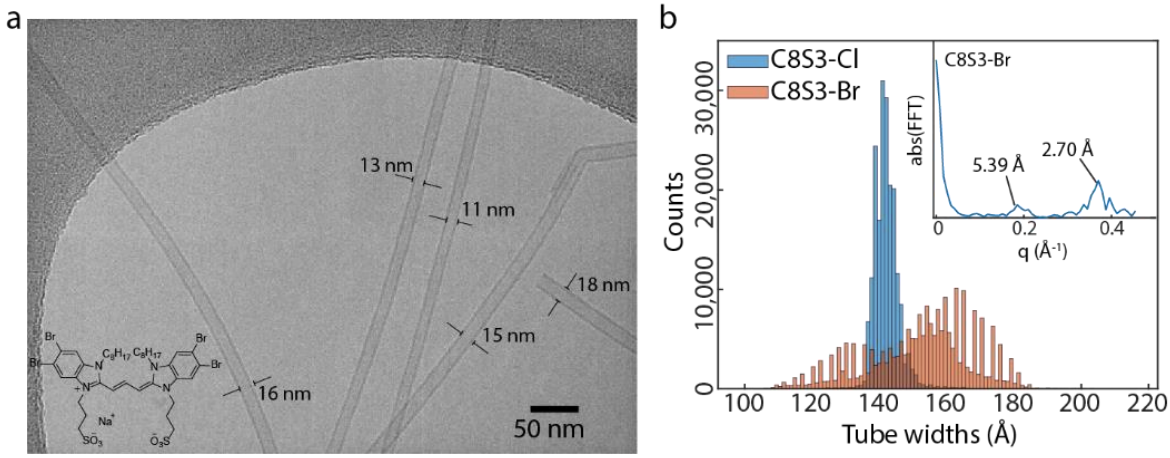

Figure 3.06. Cryo-EM of C8S3-Br DWNTs and width comparison to C8S3.

a) Cryo-EM micrograph of C8S3-Br nanotubes showing variable tube diameters (labelled on the image inset), structure of C8S3-Br. b) Histograms of C8S3-Cl and C8S3-Br tube widths over ~104 segments, inset: Fourier spectrum of C8S3-Br histogram showing the step size of the discretized tube widths.

Figure 3.06 demonstrates the striking difference in width between DWNTs of the chlorinated vs. brominated dyes. C8S3-Cl has an extremely narrow distribution of tube widths, centered around 140 Å, while C8S3-Br has a large distribution from 110-180 Å. This result agrees with our observations of structural heterogeneity from the absorbance spectrum. However, due to the variable diameters, we were not able to reconstruct the C8S3-Br nanotubes and obtain a 3D map.

Despite these heterogeneous widths, our analysis of the C8S3-Br DWNTs still led to several findings. Interestingly, the widths of the C8S3-Br tubes also show discrete step sizes, as opposed to a continuous distribution. The inset of Figure 3.6B shows a Fourier transform of said distribution, with clear peaks at 5.39 and 2.70 Å. We hypothesize that these increases correspond to the addition of a single chromophore adding into the tube's circumference. To explore this

further, we developed a simplistic geometric model for the brominated tubes to estimate the chiral angle.

Starting from the brick layer arrangement shown in Figure 3.07, we assumed that each width increment corresponded to the inclusion of an additional brick in the circumferential direction.

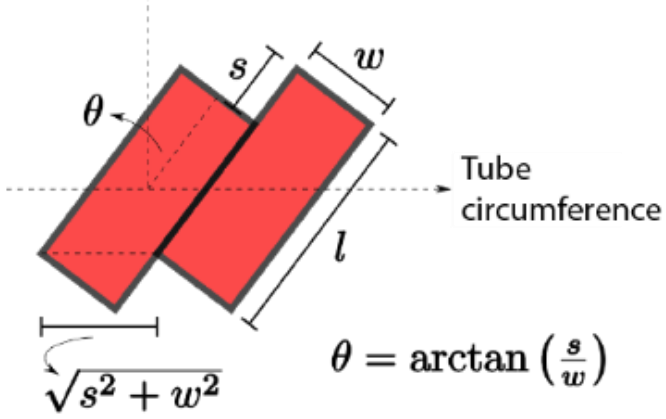

Figure 3.07. Brick layer model for the C8S3-Br DWNT structure.

From there, the projection of a single monomer brick along the circumference of the tube was given by $\sqrt{s^2 + w^2}$, where s and w are the slip between adjacent molecules and the perpendicular distance between stacked faces, respectively. The slip and stacking distance are related by $s = w \cdot \tan(\theta)$. We then assume that the smallest discrete jump in width results from a single monomer joining the tube's circumference. Therefore, $\sqrt{s^2 + w^2} = \pi d'$, where d' is the step size of the tube widths. Substituting for s from the above equation and solving for theta allows us to obtain $\theta = \cos^{-1}\left(\frac{w}{\pi d'}\right)$. We then extrapolate using $w = 3.4$ Å and $d' = 2.7$ Å, to yield a possible chiral angle of $\theta = 66.4°$. Based on the chiral angle of C8S3-Cl (57°), this value suggests a significantly modified structure for the brominated tubes.

Additionally, we completed a thorough set of characterizations of the C8S3-Br to watch its self-assembly over time. We performed dynamic light scattering (DLS), absorption screening, and cryo-EM at timepoints ranging from 1 day to 5 weeks, shown in Figure 3.08.

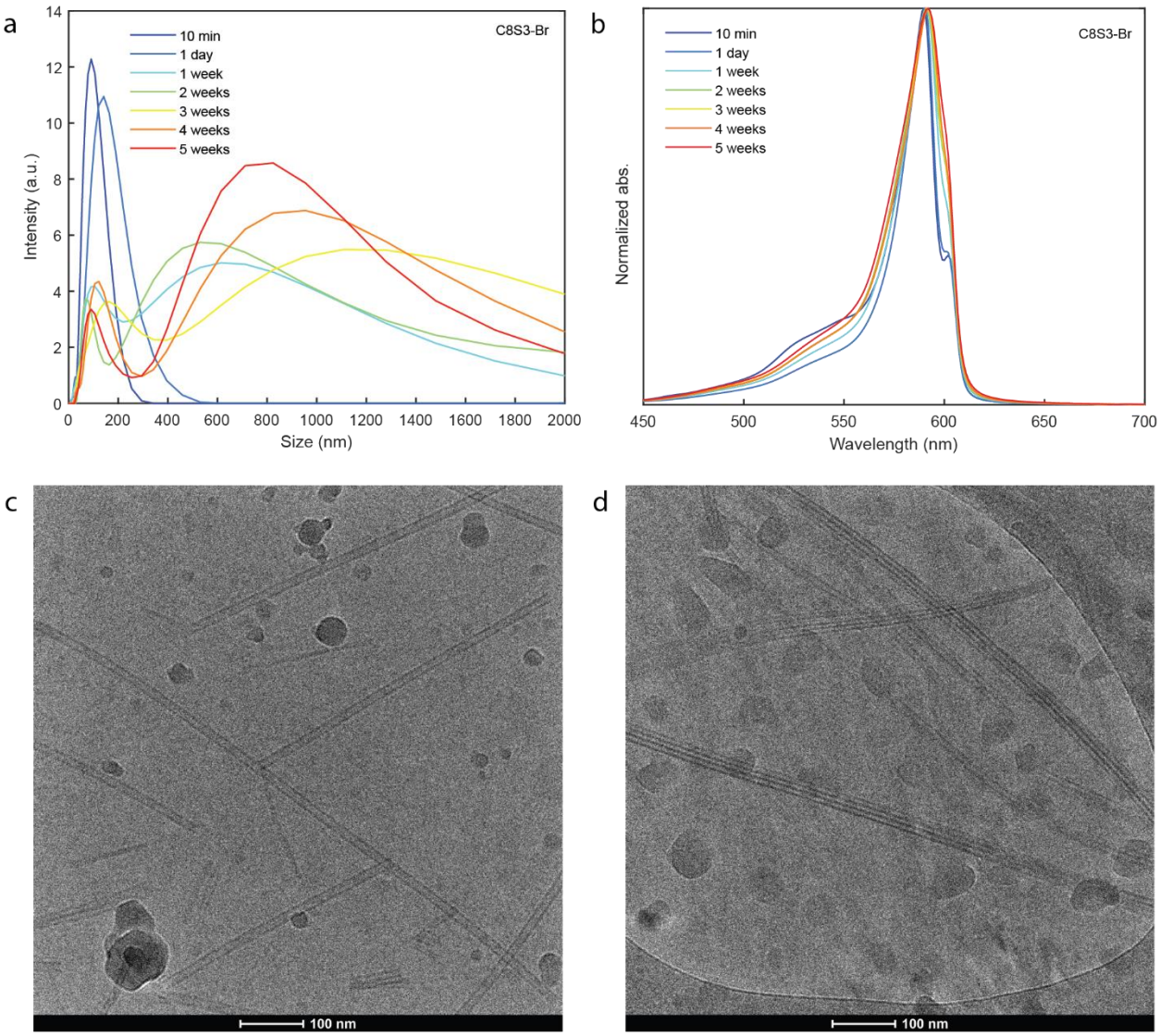

Figure 3.08. Characterizations of C8S3-Br from 1 day to 5 weeks. a) Dynamic light scattering (DLS) showing intensity profile (average size distribution). b) Absorbance spectrum c) Cryo-EM of C8S3-Br aggregates after 1 day. D) Cryo-EM of C8S3-Br aggregates after 5 weeks. Data taken by Jill Williams.

Figure 3.08A shows that the dynamic light scattering traces generally increase in size distribution over time. DLS assumes freely diffusing spherical particles and therefore is not a perfect method for measuring size of molecular aggregates. However, it can still relate a diffusion coefficient to a mean hydrodynamic diameter for samples with different dimensions, which has been explored more thoroughly in previous works.[80,81] We view DLS as a qualitative method for surveying a bulk ensemble and do not report actual radii; for our use case it can be seen as a complementary measurement to cryo-EM that offers higher throughput and classifies general trends in size. That being said, Figure 3.08A shows a clear increase and broadening in size profile from 10 min. to 5 weeks that is consistent with growth and eventual bundling of nanotubes.

The absorbance traces in Figure 3.08B demonstrate broadening over time, typically associated with bundling of the individual nanotubes. However, because the original DWNT spectrum of C8S3-Br already lacks fine structure compared to the C8S3-Cl the overall change to the lineshape is less drastic. Additionally, our cryo-EM images (Figure 3.06C) show that the nanotubes of C8S3-Br start with a wide distribution of lengths and widths at the one day timepoint. Over time, they become more uniform and eventually (~3 weeks) show bundling, similar to the nanotubes of C8S3-Cl (Figure 3.06D), which is consistent with the DLS and absorption spectra.

3.5. Impact of chemical modifications on the self-assembly: C8S4-Cl

After finding that the LHN's asymmetric unit contains six dye molecules organized with an interlocking arrangement of sulfonate groups, we decided to test the sensitivity of the self-assembly by synthesizing a similar dye with a modified alkylsulfonate chain. As evidenced by the name, C8S3 contains a propylsulfonate chain meaning that there are three methylene groups

between the nitrogen and sulfur atoms. The S3 chain is typically installed using 1,3-propane sultone, though a similar reagent (1,4-butane sultone) exists and is commonly used for installing an S4, or butylsulfonate, group. Therefore, the easiest modification to make from a synthetic perspective was adding a single methylene unit to that sulfoalkyl group, i.e. making C8S4 as opposed to C8S3.

The synthesis of C8S4-Cl began from the alkylated 5,6-dichloro-2-methyl-1-octyl-1H-benzo[d]imidazole (described in Chapter 2). This molecule was reacted with butane sultone at 135° C to yield the C8S4 heterocycle, which was then subjected to identical dye formation conditions as mentioned previously to yield C8S4-Cl. Figure 3.09 shows the synthesis of C8S4-Cl.

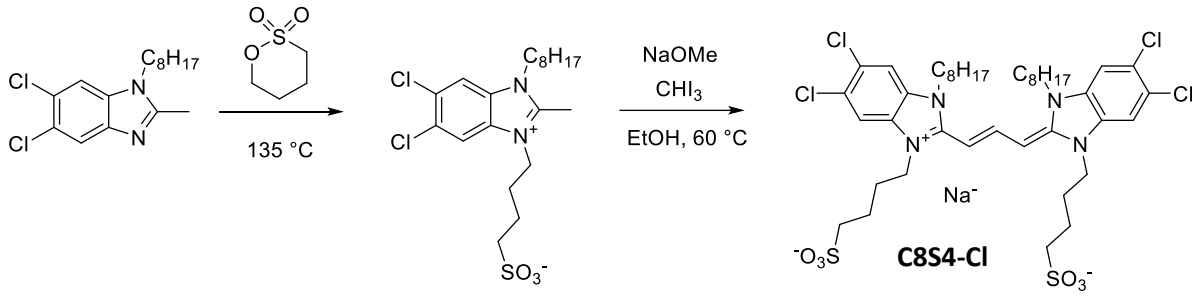

Figure 3.09. Synthesis of C8S4-Cl.

Upon successful purification of the dye, we screened its J-aggregation by absorption at several concentrations, methanol:water ratios, and time points. Figure 3.10 shows methanol screening of C8S4-Cl at 0.1 mM and the distinct spectral signatures we observed.

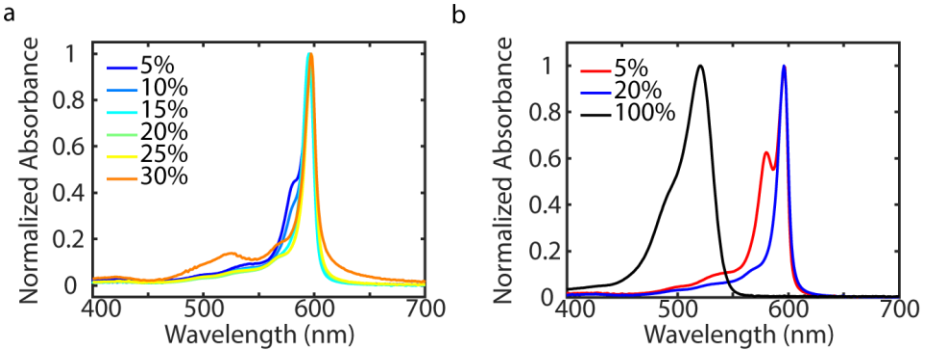

Figure 3.10. Absorption spectra of C8S4-Cl J-aggregates.
a) Absorbance as a function of methanol screening of 0.1 mM C8S4-Cl after 3 days. b) Isolated morphologies of J-aggregates. Data taken by Jill Williams.

Interestingly, our screening showed that the addition of the only one CH_2 unit allowed this dye to exhibit two unique absorption lineshapes, indicating the presence of two distinct aggregate morphologies. Figure 3.11 shows cryo-EM of these aggregates.

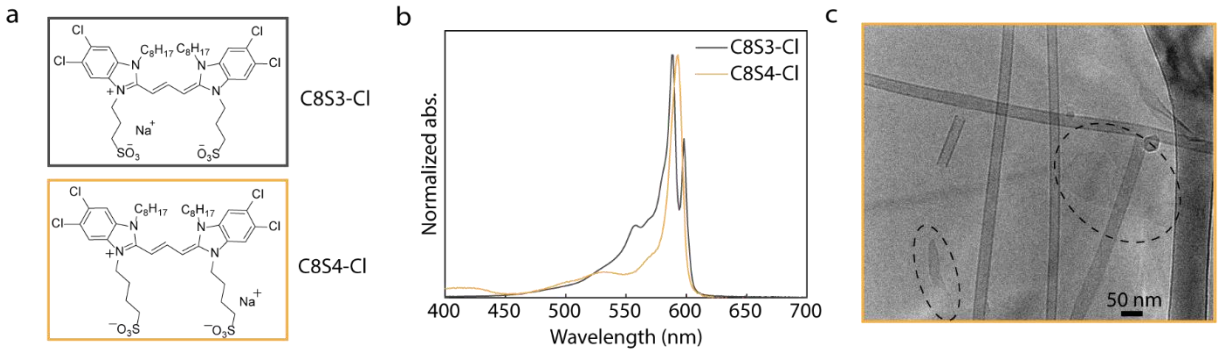

Figure 3.11. Comparison of J-aggregates formed from C8S3 and C8S4.
a) Chemical structures of C8S3-Cl and C8S4-Cl. b) Absorption spectra of J-aggregates formed from C8S3-Cl vs. C8S4-Cl. c) Cryo-EM of C8S4 J-aggregates showing coexistence of both double-walled nanotube and sheetlike (circled) aggregates.

While the 5% MeOH spectrum (Figure 3.10B) is typically associated with bundled nanotubes, we observed that the 20% MeOH sample has a sheetlike nanostructure. The existence of a second morphology indicates that the self-assembly is sensitive to the addition of only a single methylene unit. We also noted that the tubular aggregates of C8S4-Cl were highly unstable, meaning that their self-assembly was somehow weakened; DWNTs of C8S3-Cl are stable over many weeks to months (though bundling can occur).

Overall, this behavior demonstrates the highly delicate noncovalent forces that control supramolecular aggregation. Both the nanoscale morphology and excitonic properties of the C8S3-Cl DWNTs were drastically changed by a simple halogen substitution or addition of a single methylene group. These observations inspired further work which is thoroughly documented in Chapter 4.

3.6. Conclusion

We used 3D reconstruction from many thousands of cryo-EM images to obtain a high-resolution structure of the C8S3 DWNT. Up to this point, it was impossible to know the molecular arrangement of chromophores within this type of supramolecular assembly. Remarkably, we were able to settle the long-standing debate regarding a herringbone or brick layer structure that is crucial to modeling the excitonic/photophysical properties of these materials. In particular, we found that the brick layer structure possesses an axial rise of 9.9 Å and rotation of 33.6° for both walls.

Beyond this, we also discovered that the supramolecular arrangement templates from a six-monomer asymmetric unit. Additionally, there is good evidence from the structure of the ASU and other experiments that the self-assembly of C8S3 DWNTs relies on highly precise noncovalent

interactions between the cationic cyanine core and anionic sulfonate groups. We explored the structure of two C8S3 derivates (termed C8S3-Br and C8S4-Cl), which both show highly varied self-assembly compared to their parent chromophore (C8S3-Cl). These experiments inspired a follow-up paper studying the effects of methylene count on self-assembly.

However, even outside of supramolecular chromophores, this work carries weight as an early example of cryo-EM reconstruction providing enormous insights outside of structural biology. This technique is expected to revolutionize many other areas as more molecular level details are brought to light in higher resolution than ever seen before.

3.7. Experimental procedures

*Synthesis of **C8S4 heterocycle:** (4-(5,6-dichloro-2-methyl-1-octyl-1H-benzo[d]imidazol-3-ium-3-yl)butane-1-sulfonate)*

5,6-dichloro-2-methyl-1-octyl-1H-benzo[d]imidazole (781 mg, 2.49 mmol, 1 eq.) and butane sultone (1.15 mL, 11.2 mmol, 4.5 eq.) were heated 135^{o} C in an oil bath. After stirring for 1 h, the reaction was allowed to cool, and acetone (25 mL) was added. The precipitate was suction filtered and washed using acetone to yield the product **1** as a white, flaky solid (972 mg, 2.16 mmol, 87%). ^{1}H NMR (400 MHz, CD_3OD): δ 8.36 (s, 1H), 8.26 (s, 1H), 4.47 (m, 4H), 2.87 (t, *J* = 7.12, 2H), 2.11 (sextet, *J* = 6.14, 2H), 1.86 (p, *J* = 7.37, 4H), 1.39 (m, 10H), 0.91 (t, *J* = 6.86, 3H).

*Synthesis of **C8S4-Cl:** (4-(5,6-dichloro-2-((1E,3E)-3-(5,6-dichloro-1-octyl-3-(4-sulfonatobutyl)-1,3-dihydro-2H-benzo[d]imidazol-2-ylidene)prop-1-en-1-yl)-1-octyl-1H-benzo[d]imidazol-3-ium-3-yl)butane-1-sulfonate)*

3-(5,6-dibromo-2-methyl-1-octyl-1*H*-benzo[*d*]imidazol-3-ium-3-yl)propane-1-sulfonate (**1**, 300 mg, 668 µmol, 1 eq.), sodium methoxide (108 mg, 1.49 mmol, 3 eq.) and iodoform (158 mg, 358 µmol, 0.6 eq.) were added to a 25 mL Schlenk flask which was evacuated and subsequently purged with argon for three cycles. Dry ethanol (8 mL) was then added and the mixture was immediately frozen with liquid nitrogen and underwent three freeze, pump, thaw cycles to ensure an O_2 free environment. The mixture was allowed to warm to R.T. before heating to 60° C in an oil bath and stirring for 10 min. After heating, the mixture was returned to R.T. and allowed to stir for 15 h. The reaction mixture was then suction filtered and washed with 10 mL cold acetone and 10 mL cold H_2O. The crude product was recrystallized in a 1:1 ratio of DMF:H_2O to give the product, **C8S4-Cl**, as a glittery red solid with an orange tinge (70 mg, 77 µmol, 12%). ^{1}H NMR (400 MHz, CD_3OD): δ 7.91 (t, *J* = 13.6 Hz, 1H), 7.81 (s, 2H), 7.72 (s, 2H), 5.89 (d, *J* = 13.0 Hz, 2H), 4.31 (t, *J* = 6.4 Hz, 6H), 2.90-2.86 (m, 5H) 2.09-2.01 (q, *J* = 7.66 Hz, 4H), 1.94-1.86 (sextet, J= 7.04 Hz, 8H), 1.37-1.27 (m, 20H), 0.88-0.85 (t, *J* = 6.922 Hz, 6H).

3.8. NMR spectra relevant to Chapter 3

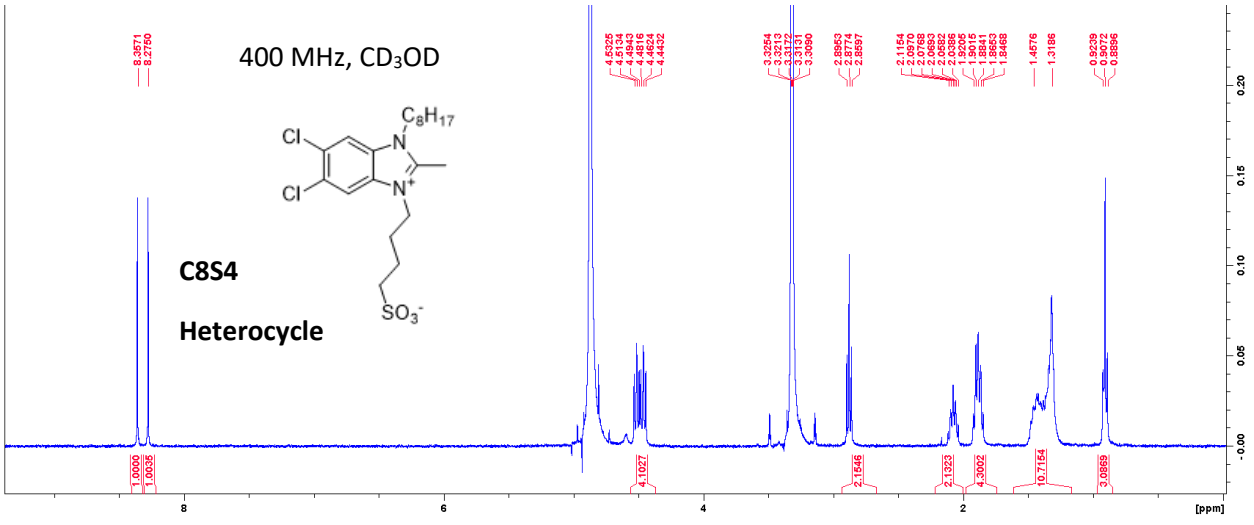

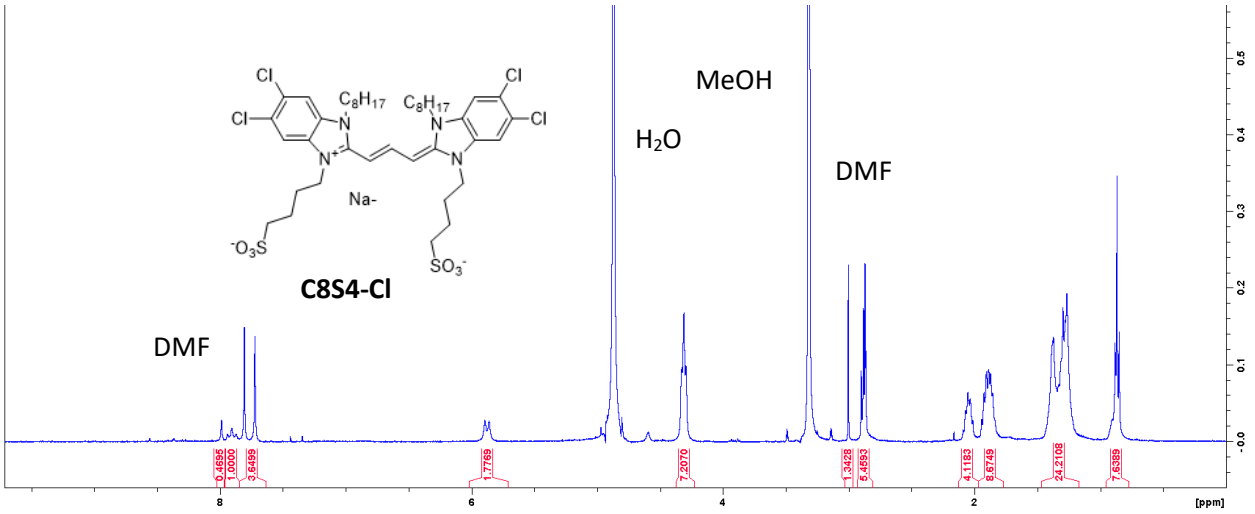
Cl
Cl
C_8H_{17}
C_8H_{17}
Cl
Cl
N
N
N
N
Na-
^-O_3S
SO_3^-
C8S4-Cl
DMF
H_2O
MeOH
DMF
0.4895
1.0000
3.6499
1.7769
7.2070
1.3428
5.4593
4.1183
8.6749
24.2108
7.6389
8
6
4
2
[ppm]
0.5
0.4
0.3
0.2
0.1
-0.0

Chapter 4

Determining the Role of Electrostatics in C8S3 J-aggregate Self-Assembly

Modified from "Bailey, A. D.; Williams, J.A.; Deshmukh, A.P.; Sletten, E. M.; Caram, J. R. Electrostatic Interactions Drive Self-Assembly of Light-Harvesting Nanotubes. *In preparation.*"

After seeing the near-angstrom resolution structure of C8S3 and interlocking sulfonate motif of the asymmetric unit, we possessed a strong hypothesis for how individual dye molecules built upon each other to create a nanoscale object. Specifically, we knew that changing the length of the sulfoalkyl chain (i.e. the number of methylene or -CH_2 units), impacted the different morphologies of nanostructures we observed. In this work, we took a deep dive into how the sulfoalkyl chain length affects J-aggregation by first synthesizing a family of dyes ranging from C8S2 to C8S8. We screened their self-assembly through absorption, then determined the morphologies of those aggregates using cryo-EM. After discovering an even-odd effect between the self-assembly and methylene number, we synthesized dyes with differently charged functional groups, finding them to exhibit far less J-aggregation.

4.01. Abstract

J-aggregates derived from cyanine dyes are known for their extraordinary photophysics, yet our knowledge of how to connect dye structure to self-organization and ultimately extended excitonic properties (superradiance, exchange narrowing) remains murky. Recently, we published a near-atomic resolution structure of a well-studied cyanine dye J-aggregate (colloquially known

as C8S3 light harvesting nanotubes, LHNs), revealing its molecular packing. Interestingly, the structure showed interlocking alkylsulfonate anions that appear to coordinate to the delocalized positive charge of the cyanine backbone on adjacent dyes. Here, we test this unique motif for self-assembly by synthesizing a family of new C8S3 derivatives while varying the number of methylene units between the cationic cyanine core and anionic sulfonate groups. We screen their J-aggregation using absorption, finding that even and odd number of methylene units produce J-aggregates with different absorption lineshapes. We confirm this trend with cryo-electron microscopy, seeing that odd-methylene aggregates have tubular or rod-like morphology, while even-methylene aggregates tend to form sheet/ribbonlike aggregates that can sometimes interconvert to tubular morphologies. Additionally, we explore the self-assembly of these materials by exchanging the sulfonate for differently charged substituents, finding that J-aggregation occurs only for a negatively charged substituent. These findings address longstanding discrepancies in the literature between cyanine dye structure and self-assembly, as well as provide guidance for the design of excitonic J-aggregate materials.

4.02. Motivation for modifying the C8S3 sulfoalkyl chain

As optical materials, cyanine dye J-aggregates offer water-solubility, redshifted absorption/emission, and superradiant emission relative to the constituent monomers. However, we currently lack intuitive knowledge that relates the design of individual dye monomers to the size, shape, and ultimately excitonic properties of self-assembled J-aggregate structures. Much of our knowledge on these artificial photosynthetic systems comes from research that uses C8S3 as a model system.[54,82] Upon addition of water to a methanolic dye solution, the chromophores self-assemble into double-walled nanotubes (DWNTs, sometimes referred to as light-harvesting

nanotubes or LHNs) that can grow up to tens of microns in length, with a consistent 14 nm diameter.[49,83] Many experimental and theoretical studies have sought a deep understanding of the exciton dynamics in these DWNT systems, stemming from an interest in biomimetic analogs of nature's most efficient light harvesters.[48,49,84–86] Others have shown how modifications to the C8S3 scaffold can modulate specific aspects of its J-aggregation; however, at this time there are no clear guidelines for structural parameters of a cyanine dye that will induce its self-assembly into superradiant J-aggregates nor tubular J-aggregates.[25,33,34,36,87]

For nearly twenty years, the structure of C8S3 nanotubes was posited from spectroscopic evidence and cryo-electron micrographs, stemming from earlier work on the Fenna-Mathews-Olson (FMO) complex.[88–91] However, in 2023, Deshmukh *et al*. published a near-angstrom resolution reconstruction of these J-aggregates from cryo-electron micrographs, providing new insights into the supramolecular structure and molecular packing.[27] Notably, they found that the micron-scale nanotubes are templated by an asymmetric unit (ASU, smallest repeating unit), comprised of six dye monomers organized in a brick layer arrangement. This ASU also revealed a new motif for self-assembly, featuring interlocking sulfonate groups that appear to screen the cyanine's delocalized positive charge. An overview of C8S3, its J-aggregates (including cryo-EM and spectra), as well as the structural model is given in Figure 4.01.

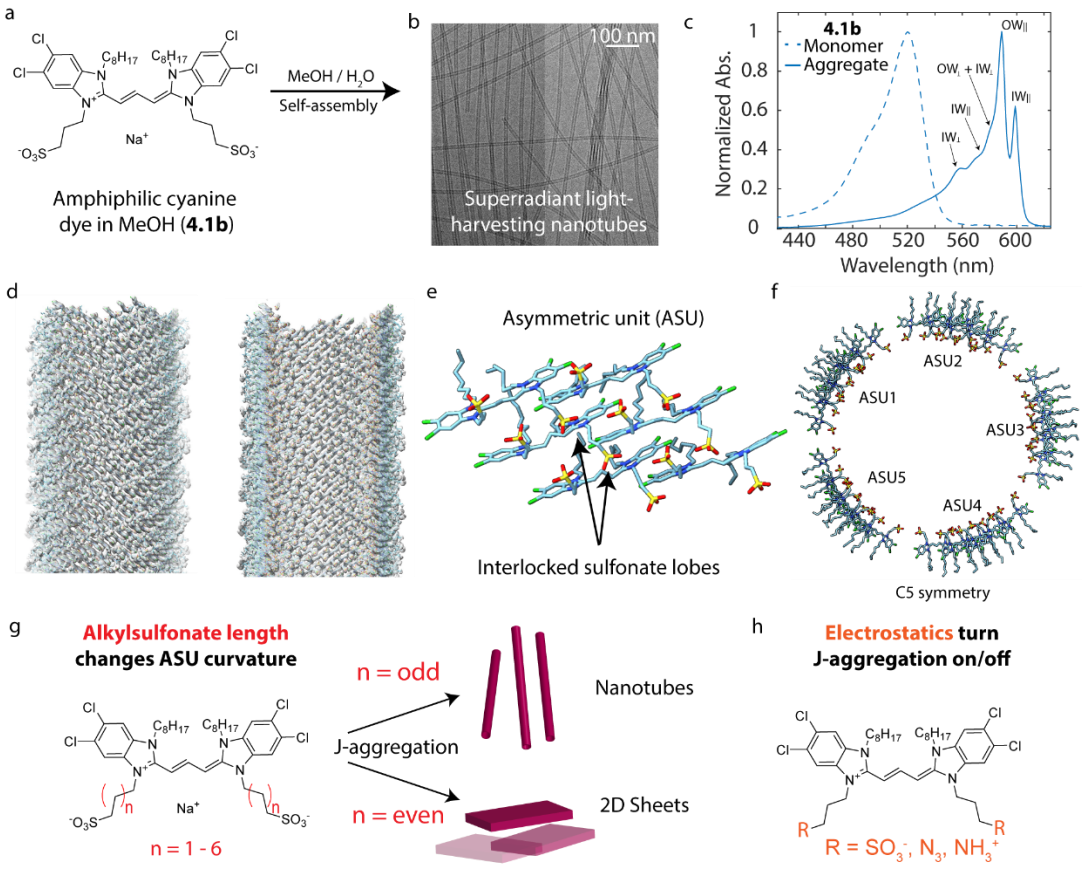

Figure 4.01. Summary of past work on C8S3 structure and new work on modifications to C8S3.a) Structure of C8S3. b) Cryo-EM of C8S3 LHNs. c) Absorption spectra of C8S3 monomer and LHN. d) Inner and outer wall density overlaid with structure. e) Model of C8S3 ASU. f) Top-down view of 5 repeated ASUs templating the tube's circumference. g) Cartoon showing how alkylsulfonate length influences J-aggregation. h) Structure of differently charged C8S3 derivatives.

Previously, it was noted that the exceptional superradiance of C8S3 J-aggregates may be attributed to their high degree of mesoscale order; these aggregates have also been previously shown to migrate their excitations over several microns at room temperature, likely indicating uniform packing with few defects.[20,36] Because of these observations in conjunction with the interlocking sulfonate motif revealed from cryo-EM reconstruction, we hypothesized that the

reason for this highly-ordered packing could be due to the electrostatic interaction which drives long range order throughout the self-assembly process.

Additionally, there are several instances within the J-aggregate literature where authors remark on the extreme differences in J-aggregate morphology and photophysics that result from adding one methylene unit to a dye's sulfoalkyl chain. Sorokin *et al*. noticed that two tetrachlorobenzimidazole cyanine dyes (colloquially known as BIC and TDBC, or C2S3 and C2S4) differ greatly in their optical and morphological properties based on the modification of one methylene unit in the sulfoalkyl (propyl vs. butyl) chain.[92] A similar observation was made by von Berlepsch *et al*. who found that C8O3 and C8O4 (carboxylalkyl chain) dyes have different responses to their supramolecular morphology based on the addition of surfactants to their solution; separately von Berlepsch. *et al*. have remarked on differences between C8S2 and C8S3.[90,93] We have also observed comparable effects across different cyanine dye J-aggregate systems, namely from C8S3 and C8S4.[27] Thus, we sought to explore the effects of the sulfoalkyl chain length of J-aggregate formation using C8S3 as the model system.

In order to test this, we first synthesized C8S3 derivatives with variable length methylene spacers between the cyanine cation and sulfonate anion. Figure 1G and 1H illustrate how C8S3's J-aggregation can be changed based on modification to the alkylsulfonate substituent. Because of our preliminary finding with C8S4, we continued this investigation by synthesizing C8S2-C8S8 (**4.1a-1g**) derivatives. By carefully screening the self-assembly, we discovered that even and odd numbers of methylenes produce aggregates with different absorption lineshapes. We then employed cryo-electron microscopy (cryo-EM) to confirm that the changes in lineshape correlate to changes in nanoscale morphology, oscillating between tubular/rodlike and sheet/ribbonlike structures.

Additionally, we explore the role of charge in self-assembly. Traditionally, J-aggregates of cyanine dyes come from cationic cyanines bearing negatively charged substituents, such as sulfonate or carboxylate (in basic solutions), though other examples have been shown.[33,94] We synthesize derivatives of C8S3 (**4.1b**) with azide and trimethylammonium functional groups, to demonstrate how self-assembly changes with neutral and positively charged substituents, respectively.

Ultimately, these findings show that the electrostatic interactions have a remarkable effect on J-aggregate self-assembly. Through tuning the direction and presence of these forces, we have shown the ability to guide the morphological component of molecular aggregation, thereby paving new avenues to generate highly ordered nanostructures with exceptional photophysical properties and drive energy or charge transfer at the nanoscale.

4.03. Synthesis of C8SX dyes

The synthesis of dyes **4.1a-g** began from commercial precursor, 5,6-dichloro-2-methylbenzimidazole (TCI), which was reacted with potassium hydroxide and bromooctane to yield, 5,6-dichloro-2-methyl-1-octyl-1H-benzo[d]imidazole (**4.2**), as described previously.[25] This heterocycle was heated in a large excess of dihaloalkane (neat), either -bromo or -iodo, and ranging from 1,2-dibromoethane (**4.3a**) to 1,8-diiodooctane (**4.3g**) to yield substituted heterocycles **4.4a-g**. The sulfonate group was installed by refluxing with sodium sulfite to obtain sulfonated heterocycles **4.5a-g**. The dyes were prepared according to a literature precedent, using sodium methoxide and iodoform, yielding cyanines substituted with 2 (**4.1a**) to 8 (**4.1g**) methylene units between the quaternary nitrogen and anionic sulfonate.[25] Following existing nomenclature, we also refer to these dyes as C8S2 (**4.1a**) to C8S8 (**4.1g**). Reaction conditions and compound numbers are shown in Figure 4.02.

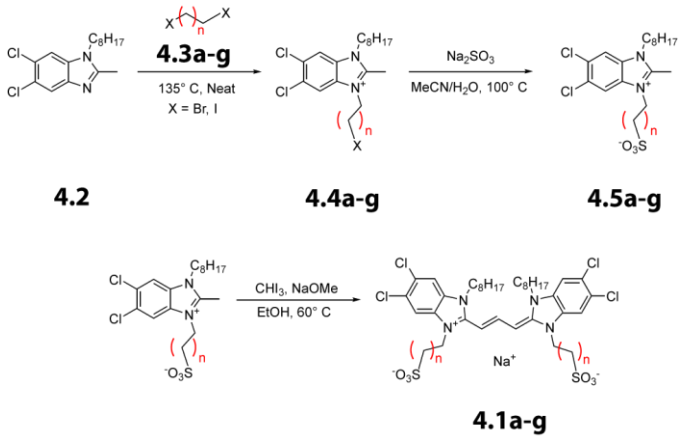

Figure 4.02. Synthetic route for trimethine cyanines with variable methylene spacer between heterocycle and sulfonate **4.1a-g**. a) complete list of synthetic procedures, characterizations, and more are provided in subchapter 4.10.

4.04. Photophysical and morphological characterization of C8SX J-aggregates

Upon the synthesis of dye monomers **4.1a-g**, we screened their aggregation by preparing and measuring absorbance of dye solutions (0.1 to 1 mM) with methanol/water composition that varied from 5 to 35% by volume. We also monitored the absorbance over several timepoints (0 min., 60 min., 24 h., and 1 w.) to watch the process of self-assembly. Additionally, we noticed that the **4.1a** monomer possessed noticeably lower methanol solubility than **4.1b-1g**; in methanol/water solutions, it coexisted as a mixture of H- and J-aggregates before precipitating (see subchapter 4.08), which is consistent with reports of **4.1a** found elsewhere.[90] For this reason, we focus our attention on fully J-aggregating dyes **4.1b-g**.

After careful absorption screening over many sets of conditions, we observed several trends in the self-assembly of J-aggregating dyes **4.1b-g**. Namely, that the dyes with an even or odd number of methylene units showed a clear difference in the absorption lineshape of their J-

aggregates. Isolated aggregate absorption for each dye is given in Figure 4.03. The preparation conditions and maximum absorption wavelengths for each aggregate are provided in Table 1.

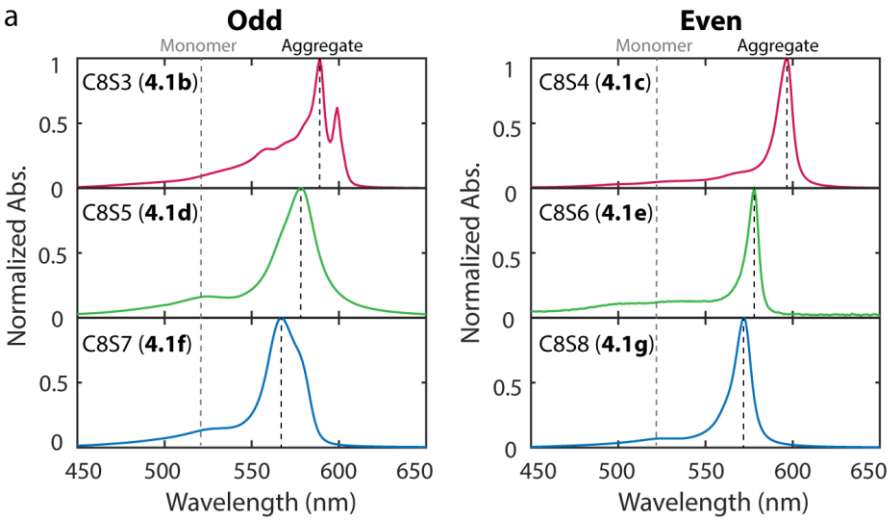

Figure 4.03. J-aggregate absorption for C8S2-C8S8 (**4.1a-g**). Absorption separated by even and odd number of methylenes. Monomer absorption wavelengths are marked by the grey dashed line.

Table 4.1. C8SX J-aggregate preparation conditions.
Preparation conditions and absorption maxima for isolated J-aggregates shown in Figure 4.

Dye (Sulfoalkyl Methylenes)	Concentration (mM)	% MeOH	Time	λ_{abs} (nm)
4.1b (C8S3)	0.2	20	24 h.	599
4.1c (C8S4)	0.1	10	24 h.	597
4.1d (C8S5)	0.25	35	2 w.	587
4.1e (C8S6)	0.5	5	24 h.	578
4.1f (C8S7)	0.25	35	24 h.	574
4.1g (C8S8)	0.5	35	2 w.	572

Figure 4 shows a trend in the absorption lineshape of odd methylene dyes (i.e. **4.b**, **4.1d**, and **4.1f**) vs. even methylene dyes (i.e. **4.1c**, **4.1e**, and **4.1g**). The odd methylene dyes are broader and contain more than one absorption feature, while the even methylene dyes tend to be narrower and have one primary absorption. Even-odd effects are common in chemistry, appearing in trends that range from the boiling points of n-alkylcarboxylic acids to charge transport in n-alkylthiolate

monolayers.[95,96] However, this finding represents an exciting confirmation that the even or odd number of sulfoalkyl methylenes on a dye monomer can influence the excitonic properties of J-aggregate materials.

We performed cryo-electron microscopy (cryo-EM) on each aggregate to determine its nanoscale morphology. Figure 4.04 shows cryo-EM micrographs for aggregates of **4.1b-g**.

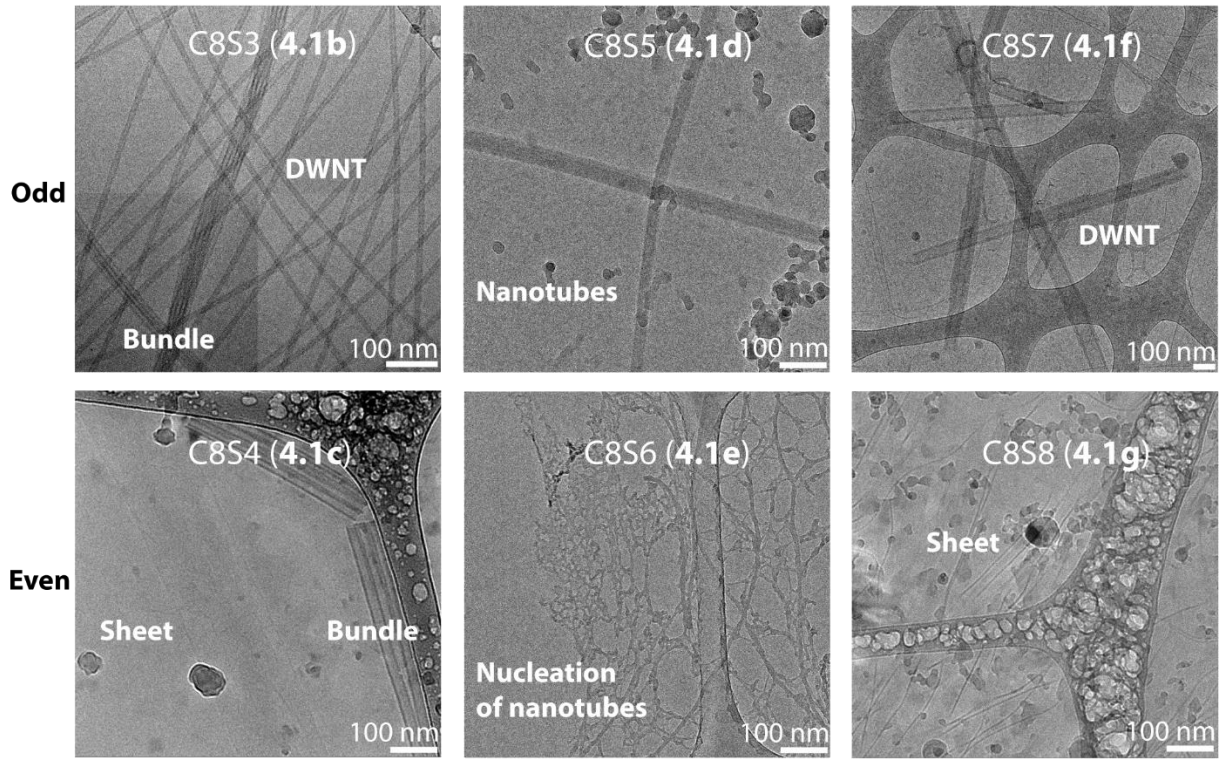

Figure 4.04. Cryo-EM of C8SX J-aggregates. Cryo-EM micrographs of **4.1b-g** showing tubular/rodlike and sheetlike lineshapes. Aggregate samples were prepared according to recipes in Table 4.1.

There is a trend that the odd methylene dyes form DWNT, bundled, and more disordered tubular aggregates. However, we also saw that the even methylene dyes tend to form ribbon/sheetlike aggregates, some of which show interconversion with a tubular (bundled or DWNT) morphology that degrades, as in the case of **4.1c** and **4.1e**.

Interestingly, we were not able to capture clear images of a sheetlike aggregate for C8S6 (**4.1e**). Despite the lineshape observed in absorbance screening, cryo-EM images taken with the same conditions showed a highly heterogeneous sample that appears to be networked aggregates growing into a tubular morphology. We conducted additional cryo-EM experiments of **4.1e** at lower concentrations (0.1 mM vs 0.5 mM) and shorter times (1 vs. 24 h.), but were not able to visualize any nanostructures. It's possible the sheetlike aggregates of C8S6 may be small and/or difficult to observe by electron microscopy, while the contrast of tubular aggregates is much higher, leading to an observation of the tubular aggregates during their formation. Additionally, we found that at higher %MeOH content (~35%), **4.1e** forms DWNTs (see additional cryo-EM in subchapter 4.09) which have curved, heterogeneous structure, and quickly degrade.

4.05. Discussion of changes to morphology based on even/odd trend

We hypothesize that the even-odd effect and changes in morphology are due to a change in the dipole direction of the sulfonate group. The anion's dipole then modulates the curvature of the asymmetric unit, leading to large-scale changes in morphology based on the addition of a single -CH_2 unit. If the curvature of the asymmetric unit no longer has the requisite helicity for tube formation, sheetlike aggregates will occur instead. We do observe DWNT formation from C8S4 (**4.1c**) and C8S6 (**4.1e**) that partially contradicts this observation; however, we noticed that the DWNTs formed from these dyes have irregular curvature, depicted in subchapter 4.09. It was also noted that these DWNTs formed from **4.1c** and **4.1e** degrade quickly. Therefore, it may be the case that although some even methylene dyes can pack into a DWNT arrangement, they quickly fall apart due to the unfavorable curvature of ASU. In a similar vein, the tubular aggregates of C8S3, C8S5, and C8S7 were found to be stable over several weeks.

Additionally, as the methylene number increases (i.e. going from **4.1b** to **4.1g**) we found that the aggregates become more disordered and present a greater degree of heterogeneity in their nanoscale morphology. Because there are instances in the literature of similar morphological structures bearing different names, we outline clear definitions for every type of structure we observed. Double-walled nanotubes contain a clear inner and outer ring, while bundles occur when DWNTs conglomerate which has been described in prior publications.[49] Multi-walled nanotubes are structures that contain more than two walls, evidenced by increased widths across the tube. We use the general term nanotube/rodlike to indicate a tubular aggregate, but make no assumptions about its formal packing; based on observations of **4.1d**, nanotubes can be highly disordered and vary widths even across a single tube. Sheetlike aggregates are also common from cyanine dyes, though there is not a clear differentiator in the literature between sheet and ribbonlike morphologies. We define sheetlike aggregates as extended 2D structures having uniform width and an aspect ratio ~5. However, ribbonlike morphologies are unique in having non-uniform width, many folds or creases that change their direction, and much larger aspect ratios on the order of ~50.

To this point, C8S2 (**4.1a**) has been shown in prior work to form both double-walled nanotubes and bilayer ribbons.[90] It is also well-established that C8S3 (**4.1b**) forms only uniform double-walled nanotubes that over time interconvert to bundles. We found that C8S4 (**4.1c**) forms sheetlike, double-walled nanotube, and bundled tube aggregates. However, C8S5 (**4.1d**) forms only tubular aggregates that sometimes vary in width across segments of the tube. As mentioned above, C8S6 (**4.1e**) seems to form sheet/ribbonlike aggregates (based on absorption lineshape), that convert to a tubular morphology before degrading. C8S7 (**4.1f**) was found to form DWNTs, MWNTs, as well as some extended ribbonlike structures (see additional cryo-EM images in

subchapter 4.09). Lastly, C8S8 (**4.1g**) formed sheet and ribbonlike aggregates. We list the various morphologies each dye forms in Table 2.

Table 4.2. Different morphological structures observed in cryo-EM for dyes **4.1a-g**.
[a] Data taken from von Berlepsch *et al*.[90]

Dye (Sulfoalkyl Methylenes)	Even/Odd	Observed Morphologies
4.1a (C8S2)	Even	DWNT, Bilayer ribbon[a]
4.1b (C8S3)	Odd	DWNT, Bundle
4.1c (C8S4)	Even	Sheet, DWNT, Bundle
4.1d (C8S5)	Odd	Nanotubes
4.1e (C8S6)	Even	Ribbon, Nanotube, DWNT
4.1f (C8S7)	Odd	DWNT, MWNT, Sheet, Ribbon
4.1g (C8S8)	Even	Sheet, Ribbon

Table 4.2 demonstrates that both the even and odd methylene dyes produce many different morphologies of aggregates. Expanding upon the ASU curvature hypothesis from earlier, we believe that the increasing alkylsulfonate length introduces a larger degree of flexibility into the monomers, which allows them to sample larger conformation spaces. Due to this expanded self-assembly, we observe larger numbers of morphologies, as well as more heterogeneous morphologies. For example, C8S5 (**4.d**) aggregates are still tubular, but lack the fine structure and order of the C8S3 DWNTs. Similarly, C8S7 (**4.f**) forms two different types of tubes, as well as sheet/ribbonlike structures.

Interestingly, we also observed that the lowest energy aggregate absorption feature blueshifts with the number of sulfoalkyl methylenes. Figure 4.05A shows the monomer absorption of **4.1a-g** in methanol and Figure 4.05B shows the J-coupling (i.e. energy difference between λ_{max} absorption of the monomer and J-aggregate) as a function of sulfoalkyl methylenes.

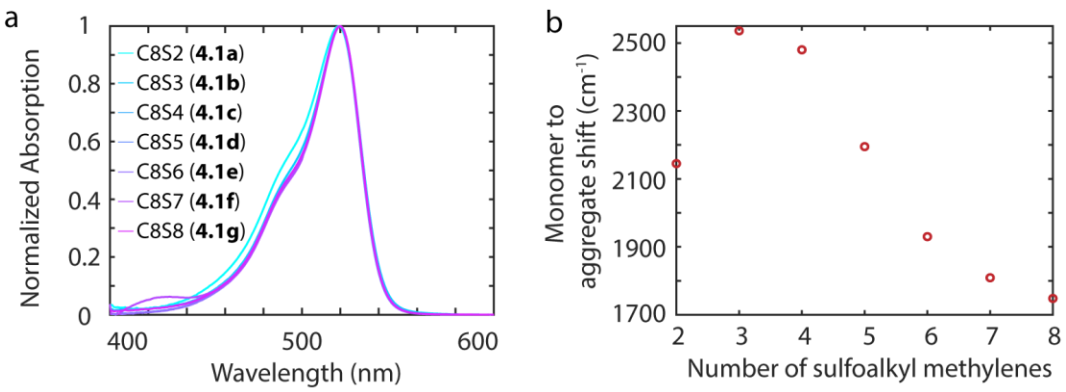

Figure 4.05. Monomer absorption spectra of **4.1a-g** and monomer to aggregate shift.
a) Absorbance spectra of **4.1a-g** in methanol showing identical monomer photophysics b) Monomer to aggregate shift in wavenumbers, showing blueshifting of the aggregate peak as the number of sulfoalkyl methylenes increase.

We hypothesize that the apparent decrease in J-coupling shown in Figure 4.05B could be due to the individual dimer units within the ASU being pushed further apart by the longer sulfoalkyl chains. Because the dyes are separated further from each other spatially, the extent of their dipole-dipole interactions may be diminished.

We observed a similar trend in the emission wavelengths of each aggregate (see fluorescence data, subchapter 4.9). We also qualitatively estimated the emissivity of the different J-aggregates based on preparing normalized concentration solutions of each aggregate and integrating the signal intensity. Unsurprisingly, the DWNTs of **4.1b** were most emissive, likely due to their high degree of internal order as shown previously. We attempted to measure fluorescence lifetimes for each aggregate, but found that the decay was highly variable and could not be fit cleanly to a biexponential (or stretched exponential) model for dyes **4.1d-g**.

4.06. Synthesis and J-aggregation of differently charged C8S3 derivatives

Lastly, we wanted to investigate the role of charge in self-assembly. Because of the apparent electrostatic interaction from the cryo-EM reconstruction, we hypothesized that by retaining the three methylene groups and changing the substituent's charge, we could determine to what extent electrostatics influence the DWNT self-assembly. To begin, literature precedent has demonstrated that both sulfonate and carboxylate-substituted (in basic solution) dyes form tubular J-aggregates with similar spectral properties, indicating two prior examples of negatively charged substituents forming superradiant DWNTs.[97,98] Therefore, our initial goal was to synthesize C8S3 derivatives with uncharged and positively charged substituents, shown in Figure 4.7A. We selected an azide as the primary candidate for an uncharged substituent, since the azide functional group carries a large electron density but lacks a net formal charge. For a positively charged substituent, we chose an amine group because it confers similar water solubility, yet ensures a positive charge (in neutral water) due to the amine's pKa.

Due to the versatile nature of halogenated starting material **4.3c**, the synthesis of azide dye **4.6a** requires only two steps. To achieve the azide heterocycle, we simply displaced bromide using sodium azide. This heterocycle was then subjected to identical dye formation conditions mentioned in Figure 4.3. To prepare the amine-substituted dye, we performed a Staudinger reduction to the azide heterocycle, then Boc-protected the amine group, formed the dye, and cleaved the Boc group. Complete details for the synthesis of the uncharged and positively charged dyes are given in subchapter 4.09. Upon successful characterization of **4.6a** and **4.6b**, we performed aggregate screening, with the most J-aggregated species shown in Figure 4.06B.

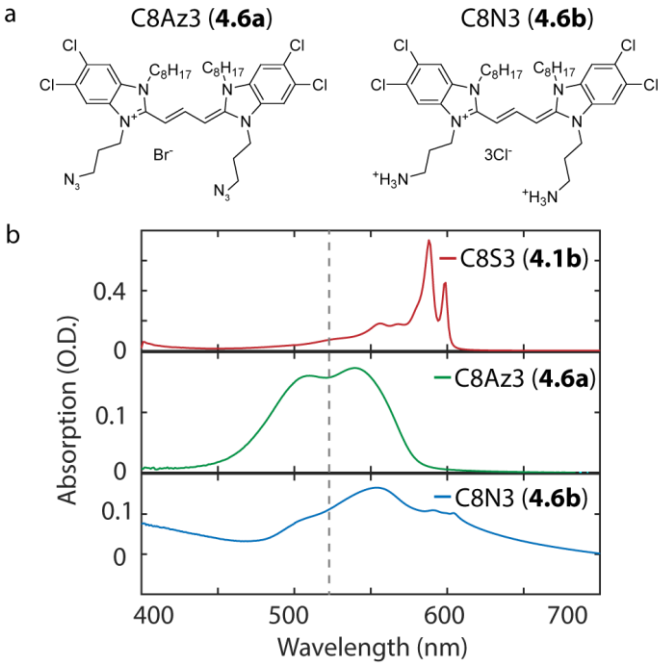

Figure 4.06. Differently charged C8S3 derivatives and absorption spectra showing their J-aggregation a) **4.1b** derivatives **4.6a** (C8Az3) and **4.6b** (C8N3) with neutral and positively-charged substituents. b) Absorption stack plot showing aggregation of dyes **4.6a** (0.5 mM in 35% MeOH/H_2O after 24 h.) and **4.6b** (0.1 mM in 35% MeOH/H2O after 1 min.) compared to **4.1b**. Monomer absorption wavelength of all dyes is highlighted by the dashed grey line.

Figure 4.06B shows that the neutral and positively charged dyes lack significant J-aggregation compared to **4.1b**. We note that both dyes retain excellent solubility in methanol and poor solubility directly into water (similar to **4.1b**). In the case of azide dye **4.6a**, we observe H-aggregate and monomer absorption, meaning that the extended slip-stacked structures do not form in solution. For the amine dye **4.6b**, we observe broad, weak absorption, with two small J-peaks appearing near 600 nm. The existence of these redshifted features implies the formation of J-aggregates, and potentially a DWNT structure; however, all aggregates precipitate from solution

within minutes. Therefore, our data suggest that negatively charged groups are critical to the self-assembly of J-aggregated nanostructures.

Combined, these results clearly indicate that the cation-anion interaction greatly affects J-aggregate self-assembly of **4.1b**. Synthesizing our knowledge from the reconstructed model of the ASU, the even-odd effect caused by alkylsulfonate chain length, and the lack of J-aggregation for dyes **4.6a** and **4.6b**, we believe that the self-assembly of these light-harvesting nanotubes is driven by the electrostatic interaction built into the dye's structure. This exciting discovery has great significance for the design of J-aggregated optical materials. In prior characterizations of the C8S3 DWNTs, we show that a high degree of internal order is a prerequisite for superradiance, but now we have shown the molecular motif that directs highly-ordered self-assembly. While tuning the exact dimensions of a dye to achieve uniform packing across different methine lengths and heterocyclic scaffolds still represents a challenge, we believe this result will aid in the development of next-generation J-aggregated optical materials.

4.07. Conclusion

Together, these results speak to the incredibly precise noncovalent interactions that control the self-assembly of superradiant J-aggregates from **4.1b** monomers. By making alterations to the sulfoalkyl chain length of this well-studied cyanine dye, we have shown that the excitonic properties of their aggregates can be modulated. Specifically, we demonstrated an even-odd effect in J-aggregate morphology and absorption lineshape, with odd dyes preferring tubular/rodlike aggregates and even dyes preferring a sheet/ribbonlike morphology. Moreover, we found that increasing the number of sulfoalkyl methylenes can blueshift the aggregate absorption and emission, allowing further tunability. We also synthesized **4.1b** derivatives with differently

charged substituents, showing that only for negatively charged substituents does DWNT formation occur. Broadly, these results open the chemical space for cyanine dye J-aggregates and show that systematic explorations of these dye structures can inform general principles towards the construction of next-generation optical materials with exceptionally fast energy and charge transfer.

4.08. Additional information on C8S2 (4.1a)

The synthesis of compound **4.1a** was unusual in that the sulfonation reaction only proceeded using the -iodo alkylated heterocycle. However, this was complicated by the fact that the -iodo product was not directly accessible from heterocycle **4.2** (1,2-diiodoethane was too reactive and degraded during heating, so 1,2-dibromoethane was used instead). In order to convert the -bromo heterocycle to -iodo, we utilized a Finkelstein reaction, as shown below.

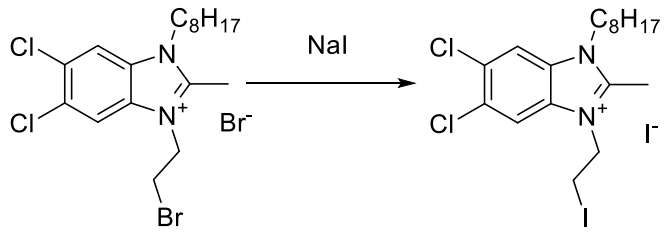

Figure 4.07 Synthesis of **4.4ab**.

3-(2-bromoethyl)-5,6-dichloro-2-methyl-1-octyl-1H-benzo[d]imidazol-3-ium bromide (1.1 g, 2.61 mmol, 1 eq.) was combined with sodium iodide (0.867 g, 5.22 mmol, 2 eq.) and heated to 55 °C in acetone for 6 h. This mixture was filtered, washed with acetone and water, and dried to yield 5,6-dichloro-3-(2-iodoethyl)-2-methyl-1-octyl-1H-benzo[d]imidazol-3-ium iodide as a white solid. (1.18 g, 2.52 mmol, 96%).

The dye formation conditions from this heterocycle were identical to the others. Upon isolation of the C8S2 dye, we performed the standard J-aggregate screening based on methanol/water ratio. The absorption spectra for C8S2 (**4.1a**) J-aggregates prepared at 0.5 mM are shown in Figure 4.08.

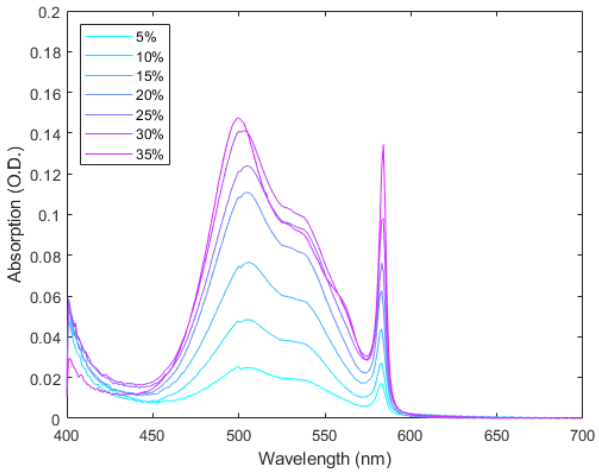

Figure 4.08. Methanol screening of 0.5 mM **4.1a** after 24 h.

Unfortunately, samples of **4.1a** were found to significantly H-aggregate across different concentrations and methanol compositions. We attempted to drive J-aggregation by adding a small amount (0.05 mM) of NaCl to the solution, which resulted in the precipitation of all dye from the solution. However, prior work with this dye, shows the existence of both tubular and bilayer ribbonlike aggregates.[90]

4.09. Additional characterizations of C8SX J-aggregates

Fluorescence spectra (Figure 4.09) were taken of J-aggregates of dyes **4.1b-g** at 0.5 mM using the preparations from Table 4.1.

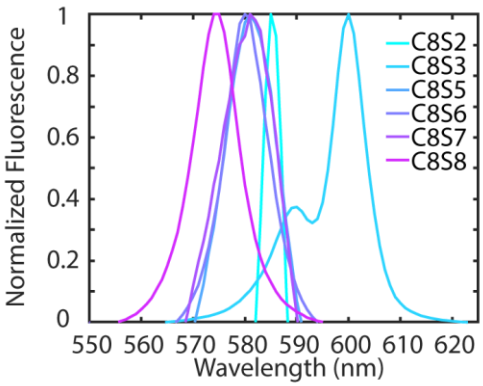

Figure 4.09. Normalized emission spectra of 0.5 mM J-aggregates formed from **4.1b-g**.

Interestingly, the most fluorescent aggregate was C8S3 based on the emission of a set of solutions where dye concentrations were normalized to 0.5 mM. The %MeOH of each solution was dictated by the ratio that produced the largest absorption optical density. Qualitatively, these data agree with our previous work that highly ordered J-aggregates are more emissive. Therefore, less ordered J-aggregates (such as those seen in **4.1f** or **4.1e**) are likely to be less emissive.

Additionally, we recorded cryo-EM images of **4.1e** that appear to show highly disordered double-walled nanotubes (Figure 4.10).

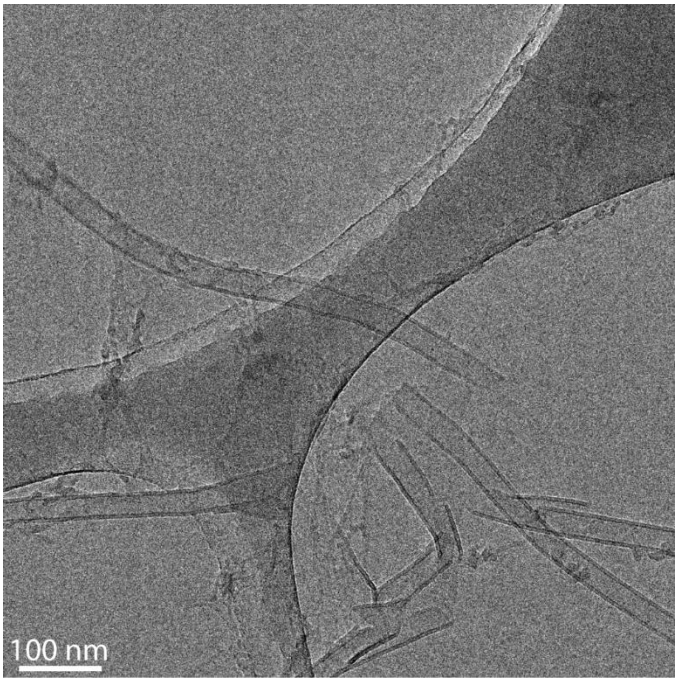

Figure 4.10. Cryo-EM of C8S6 (**4.1e**) DWNTs. Aggregates prepared at 0.5 mM **4.1e** dye and 35% MeOH.

The images contain several nanotubes with a curved backbone, likely indicating a mismatched curvature of the ASU compared to the odd-numbered methylene dyes. The occurrence of these structures lends credence to the theory the ASU curvature controls the morphological properties of the aggregates.

Additionally, we found images of **4.1f** aggregates that appear to contain multi-walled nanotubes. These strange-looking structures have a highly variable inner and outer diameter that appears to have discretized changes in width, corresponding to the number of tube layers.

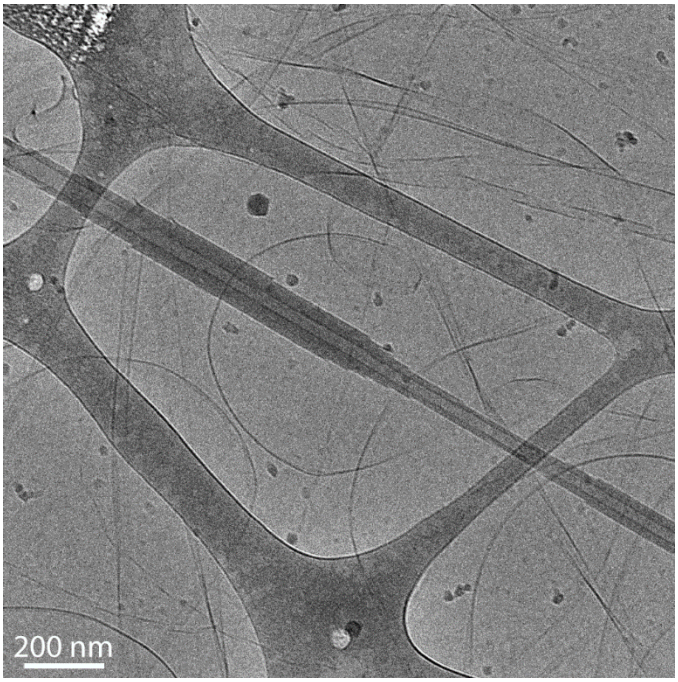

Figure 4.11. Cryo-EM of C8S7 (**4.1f**) MWNTs. Aggregates prepared at 0.5 mM **4.1f** dye and 35% MeOH.

The existence and confluence of these new nanostructures at higher sulfoalkyl methylene numbers appears to indicate that the key intermolecular forces responsible for templating ordered nanotubes can be broken by introducing longer chain sulfonates.

4.10. Experimental procedures for C8SX dyes

Chemical reagents were purchased from Fisher Scientific or Sigma-Aldrich and were used without purification unless otherwise specified. 5,6-Dichloro-2-methylbenzimidazole was purchased from TCI America. Anhydrous methanol was obtained from a Grubb's-type Phoenix Solvent Drying System. Dry ethanol was prepared by drying over molecular sieves for 48 h. Thin layer chromatography was performed using Silica 60 F_{254} plates (Sigma-Aldrich). Flash chromatography was performed using Silica Gel 60 from Fisher Scientific (40-63 μm).

Nuclear magnetic resonance (^{1}H, ^{13}C) spectra were taken on a Bruker Avance 400 spectrometer and processed using TopSpin 4.0.4. ^{13}C spectra of all dye molecules were taken on a Bruker AV500 spectrometer and processed using TopSpin 4.0.4. HRMS was performed on an LCT-Premier system using the positive ionization mode. Absorbance spectra were measured on a Jasco V-730 UV-vis spectrophotometer with a 2000 nm/min. rate after blanking with the appropriate solvent. Absorbance measurements were taken in Starna Cells cuvettes, ranging in path length from 1 cm to 0.1 mm, depending on sample and concentration. Fluorescence spectra were taken on a Horiba Instruments PTI QM-400.

General experimental for dihaloalkane reaction of dialkylated heterocycles:

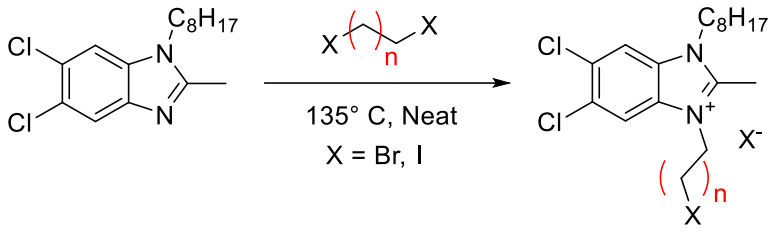

5,6-dichloro-2-methyl-1-octyl-1H-benzo[d]imidazole **4.2** (1 eq.) and the appropriate dihaloalkane **4.3a-g** (10 equiv.) were heated to 135 °C overnight before being cooled to room temperature. To this sludgy brown mixture was added diethyl ether (~5 mL) and ethyl acetate (~10 mL) before sonicating for several minutes to dissolve unreacted dihaloalkane. The sonicated mixture was then suction filtered and washed with excess ethyl acetate to yield the dialkylated heterocycles, then dried under vacuum. This procedure provided the dialkylated heterocycles **4.4a-g** as an off-white solid in yields of 68-94%.

3-(2-bromoethyl)-5,6-dichloro-2-methyl-1-octyl-1H-benzo[d]imidazol-3-ium bromide (**4.4a)**

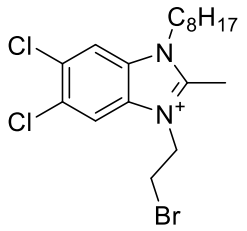

^{1}H NMR (400 MHz, MeOD) δ 8.37 (d, *J* = 8.7 Hz, 2H), 5.00 (t, *J* = 6.0 Hz, 2H), 4.62 – 4.50 (m, 2H), 3.97 (t, *J* = 5.9 Hz, 2H), 1.91 (q, *J* = 7.5 Hz, 2H), 1.37 (d, *J* = 43.0 Hz, 10H), 0.95 – 0.87 (m, 3H).

^{13}C NMR (101 MHz, MeOD) δ 154.01, 131.02, 130.98, 130.52, 130.36, 115.38, 114.87, 114.66, 114.24, 31.46, 28.82, 28.60, 28.57, 28.53, 26.19, 26.07, 22.26, 13.00, 10.82, 10.52.

HRMS (ESI+): Calculated for $C_{18}H_{26}BrCl_2N_2$ [M+]: 465.0656; found: 419.0661.

*5,6-dichloro-3-(5-iodopentyl)-2-methyl-1-octyl-1H-benzo[d]imidazol-3-ium (***4.4d**)

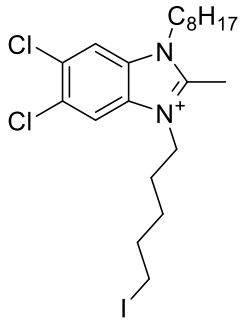

^{1}H NMR (400 MHz, MeOD) δ 8.32 (d, *J* = 5.7 Hz, 2H), 4.49 (q, *J* = 7.2 Hz, 4H), 1.90 (dp, *J* = 21.6, 7.3 Hz, 6H), 1.55 (p, *J* = 7.6 Hz, 2H), 1.37 (d, *J* = 41.0 Hz, 11H), 0.95 – 0.87 (m, 3H).

^{13}C NMR (101 MHz, MeOD) δ 153.13, 130.74, 130.72, 130.63, 114.61, 114.55, 46.07, 45.80, 32.49, 31.51, 28.87, 28.84, 28.72, 27.48, 27.09, 26.22, 22.28, 13.03, 10.32, 5.14.

HRMS (ESI+): Calculated for $C_{21}H_{35}ICl_2N_2$ [M+]: 509.0987; found: 509.1010.

5,6-dichloro-3-(6-iodohexyl)-2-methyl-1-octyl-1H-benzo[d]imidazol-3-ium (**4.4e**)

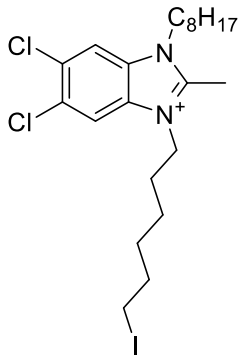

1H NMR (400 MHz, MeOD) δ 8.32 (d, *J* = 5.2 Hz, 2H), 4.49 (td, *J* = 7.6, 2.4 Hz, 4H), 3.26 (t, *J* = 6.8 Hz, 2H), 1.89 (ddt, *J* = 28.0, 13.9, 7.3 Hz, 6H), 1.54 – 1.48 (m, 4H), 1.48 – 1.36 (m, 5H), 1.35 (s, 2H), 1.33 (s, 3H), 0.96 – 0.88 (m, 3H).

^{13}C NMR (101 MHz, MeOD) δ 153.05, 130.73, 130.61, 114.54, 48.24, 48.03, 47.82, 47.61, 47.39, 47.18, 46.97, 46.01, 45.89, 33.02, 31.49, 29.64, 28.85, 28.83, 28.68, 28.47, 26.19, 25.06, 22.27, 13.01, 5.33.

HRMS (ESI+): Calculated for $C_{22}H_{34}ICl_2N_2$ [M+]-: 523.1144; found: 523.1161.

5,6-dichloro-3-(7-iodoheptyl)-2-methyl-1-octyl-1H-benzo[d]imidazol-3-ium iodide (**4.4f**)

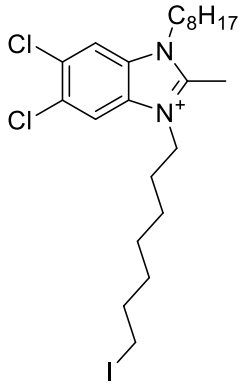

^{1}H NMR (400 MHz, MeOD) δ 8.27 (d, *J* = 4.0 Hz, 2H), 4.46 (td, *J* = 7.7, 2.5 Hz, 4H), 3.42 (t, *J* = 6.7 Hz, 2H), 2.93 (s, 3H), 1.84 (tdd, *J* = 13.2, 10.3, 6.0 Hz, 6H), 1.43 (m, *J* = 18.0, 12.2, 6.1, 2.9 Hz, 10H), 1.35 – 1.24 (m, 7H), 0.91 – 0.83 (m, 3H).

^{13}C NMR (101 MHz, MeOD) δ 153.08, 130.75, 130.58, 114.50, 48.23, 48.02, 47.81, 47.59, 47.38, 47.17, 46.95, 45.87, 45.80, 32.95, 32.34, 31.49, 28.85, 28.83, 28.64, 28.50, 27.89, 27.47, 26.15, 25.92, 22.26, 12.98.

HRMS (ESI+): Calculated for $C_{23}H_{36}BrCl_2N_2$ [M+]: 489.1439; found: 489.1462.

5,6-dichloro-3-(8-iodooctyl)-2-methyl-1-octyl-1H-benzo[d]imidazol-3-ium (**4.4g**)

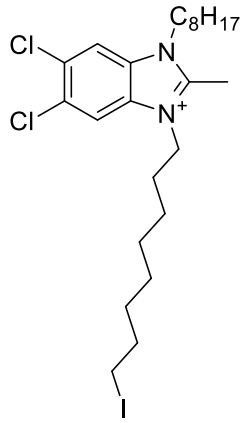

^{1}H NMR (400 MHz, MeOD) δ 8.31 (d, *J* = 1.8 Hz, 2H), 4.49 (td, *J* = 7.6, 2.1 Hz, 4H), 3.24 (t, *J* = 6.9 Hz, 2H), 2.99 – 2.90 (m, 2H), 1.97 – 1.80 (m, 5H), 1.78 (d, *J* = 6.9 Hz, 1H), 1.52 – 1.43 (m, 7H), 1.43 – 1.27 (m, 12H), 0.96 – 0.88 (m, 3H).

^{13}C NMR (101 MHz, MeOD) δ 153.08, 130.69, 130.63, 114.59, 114.57, 48.27, 48.13, 48.06, 47.84, 47.63, 47.42, 47.20, 46.99, 46.07, 33.16, 31.51, 29.84, 28.87, 28.85, 28.70, 28.64, 28.62, 27.88, 26.22, 26.05, 22.29, 13.05, 10.35, 5.88.

HRMS (ESI+): Calculated for $C_{24}H_{38}ICl_2N_2$ [M+]: 551.1457; found: 551.1447.

General experimental for sulfonation of alkyl halide heterocycles:

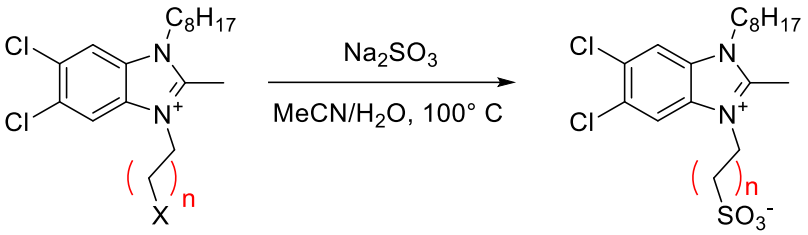

Dialkylated benzimidazole **4.4** (1 eq.) and sodium sulfite (5 eq.) were dissolved in acetonitrile (5 mL) and water (5 mL). The reaction was heated to 100 °C and stirred for 2 h., or until the starting material was consumed by TLC (10% DCM/methanol). The crude mixture was then cooled to room temperature and the organic solvent removed by rotary evaporation, resulting in formation of a white precipitate. The resulting solid was suction filtered and washed with water to obtain the sulfonated heterocycle **4.5a-g** as a white powder, with yields of 67-99%.

*2-(5,6-dichloro-2-methyl-1-octyl-1H-benzo[d]imidazol-3-ium-3-yl)ethane-1-sulfonate (***4.5a)**

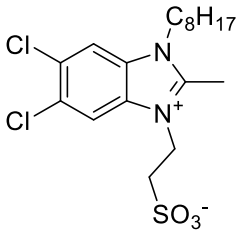

^{1}H NMR (400 MHz, MeOD) δ 8.34 (s, 1H), 8.28 (s, 1H), 4.87 – 4.80 (m, 2H), 4.48 (t, *J* = 7.6 Hz, 2H), 3.32 – 3.27 (m, 2H), 3.04 (s, 3H), 1.87 (h, *J* = 7.4 Hz, 2H), 1.54 – 1.28 (m, 10H), 0.96 – 0.88 (m, 3H).

^{13}C NMR (101 MHz, MeOD) δ 154.57, 130.65, 130.61, 130.58, 130.18, 114.69, 114.44, 54.65, 47.30, 45.74, 41.98, 31.51, 28.85, 28.80, 28.66, 28.13, 26.03, 22.26, 12.99, 10.14.

HRMS (ESI+): Calculated for $C_{18}H_{26}Cl_2N_2O_3SH$ [M+]: 421.1119; found: 421.1125.

5-(5,6-dichloro-2-methyl-1-octyl-1H-benzo[d]imidazol-3-ium-3-yl)pentane-1-sulfonate (**4.5d**)

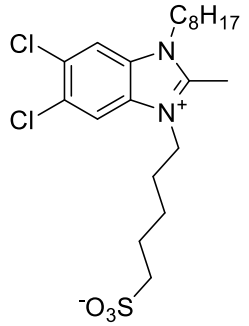

^{1}H NMR (500 MHz, MeOD) δ 8.32 (s, 1H), 8.28 (s, 1H), 4.47 (q, *J* = 8.0 Hz, 4H), 2.80 (dd, *J* = 8.2, 6.7 Hz, 2H), 1.97 – 1.78 (m, 6H), 1.63 – 1.53 (m, 2H), 1.44 (ddtd, *J* = 22.1, 17.7, 8.7, 4.0 Hz, 4H), 1.37 – 1.27 (m, 6H), 0.94 – 0.87 (m, 3H).

^{13}C NMR (75 MHz, MeOD) δ 130.66, 114.56, 114.44, 50.45, 47.33, 47.04, 46.76, 45.83, 45.65, 31.51, 28.85, 28.62, 28.05, 26.17, 24.84, 24.13, 22.27, 13.01.

HRMS (ESI+): Calculated for $C_{21}H_{32}Cl_2N_2O_3SH$ [M+]: 463.1589; found: 463.1619.

6-(5,6-dichloro-2-methyl-1-octyl-1H-benzo[d]imidazol-3-ium-3-yl)hexane-1-sulfonate (**4.5e**)

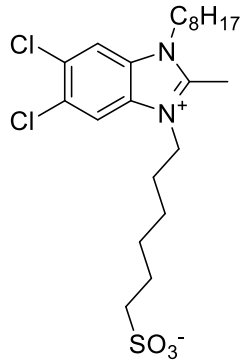

^{1}H NMR (400 MHz, MeOD) δ 8.35 (d, *J* = 9.5 Hz, 2H), 4.58 – 4.47 (m, 4H), 3.00 (dq, *J* = 4.7, 3.1 Hz, 1H), 2.87 – 2.79 (m, 2H), 2.02 – 1.89 (m, 5H), 1.89 – 1.78 (m, 2H), 1.64 – 1.49 (m, 2H), 1.52 – 1.30 (m, 6H), 0.99 – 0.90 (m, 3H).

^{13}C NMR (101 MHz, MeOD) δ 153.12, 130.64, 130.61, 114.57, 114.52, 50.92, 48.26, 48.05, 47.84, 47.62, 47.41, 47.20, 46.99, 46.03, 45.93, 31.50, 28.85, 28.83, 28.67, 28.36, 27.70, 26.20, 25.96, 25.69, 24.30, 22.27, 13.02.

HRMS (ESI+): Calculated for $C_{22}H_{34}Cl_2N_2O_3SH$ [M+]: 477.1746; found: 477.1748.

7-(5,6-dichloro-2-methyl-1-octyl-1H-benzo[d]imidazol-3-ium-3-yl)heptane-1-sulfonate (**4.5f**)

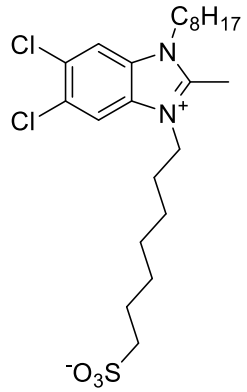

^{1}H NMR (400 MHz, MeOD) δ 8.33 (d, *J* = 7.0 Hz, 2H), 4.51 (t, *J* = 7.6 Hz, 4H), 2.84 – 2.76 (m, 2H), 2.00 – 1.86 (m, 5H), 1.80 (dq, *J* = 10.1, 7.3 Hz, 2H), 1.56 – 1.43 (m, 9H), 1.43 – 1.28 (m, 8H), 0.97 – 0.89 (m, 3H).

^{13}C NMR (101 MHz, MeOD) δ 153.12, 130.66, 130.60, 114.53, 114.49, 51.04, 48.24, 48.03, 47.82, 47.60, 47.39, 47.18, 46.96, 45.89, 45.85, 31.49, 28.83, 28.63, 28.47, 28.28, 27.88, 26.16, 25.75, 24.33, 22.26, 12.99.

HRMS (ESI+): Calculated for $C_{23}H_{36}Cl_2N_2O_3SH$ [M+]: 491.1902; found: 491.1886.

8-(5,6-dichloro-2-methyl-1-octyl-1H-benzo[d]imidazol-3-ium-3-yl)octane-1-sulfonate (**4.5g**)

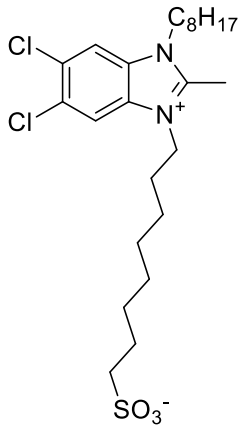

^{1}H NMR (400 MHz, MeOD) δ 8.33 (d, *J* = 4.0 Hz, 2H), 4.52 (t, *J* = 7.6 Hz, 4H), 2.84 – 2.76 (m, 2H), 2.01 – 1.88 (m, 4H), 1.80 (ddd, *J* = 12.3, 10.0, 6.4 Hz, 2H), 1.54 – 1.36 (m, 14H), 1.36 – 1.29 (m, 5H), 0.98 – 0.90 (m, 3H).

^{13}C NMR (101 MHz, MeOD) δ 153.09, 130.63, 114.55, 51.18, 48.26, 48.05, 47.83, 47.62, 47.41, 47.19, 46.98, 46.02, 46.00, 31.49, 28.84, 28.66, 28.61, 28.58, 28.50, 28.09, 26.19, 25.99, 24.45, 22.27, 13.02.

HRMS (ESI+): Calculated for $C_{24}H_{38}Cl_2N_2O_3SH$ [M+]: 505.2058; found: 505.2070.

General experimental for trimethine dye synthesis:

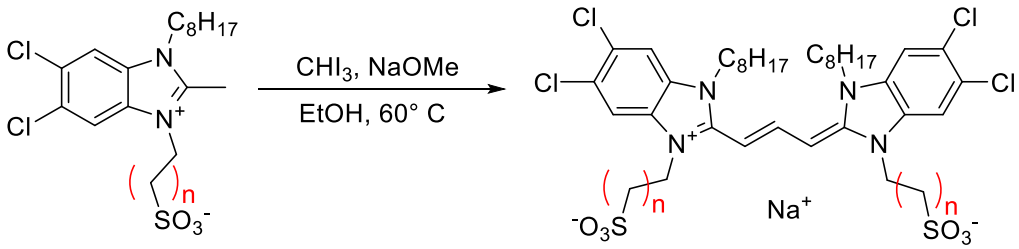

Sulfonated heterocycle **4.5a-g** (1 eq.), iodoform (0.6 eq.), and sodium methoxide (3 eq.) were combined in a 10 mL Schlenk tube, which was evacuated and purged 3x with argon. Immediately upon adding anhydrous ethanol (7 mL), the reaction was subjected to 3 cycles of freeze, pump, thaw to ensure an oxygen-free environment. The reaction was then heated to 65 °C for 1 h., before

stirring overnight. The solvent was then removed by rotary evaporation and purified via silica column chromatography using gradient elution from 0 to 10% methanol in DCM. This procedure provided trimethine dyes **4.5a-g** as a red solid in yields from 2-15%.

Sodium 2-(5,6-dichloro-2-((1E,3E)-3-(5,6-dichloro-1-octyl-3-(2-sulfonatoethyl)-1,3-dihydro-2H-benzo[d]imidazol-2-ylidene)prop-1-en-1-yl)-1-octyl-1H-benzo[d]imidazol-3-ium-3-yl)ethane-1-sulfonate (**4.1a**)

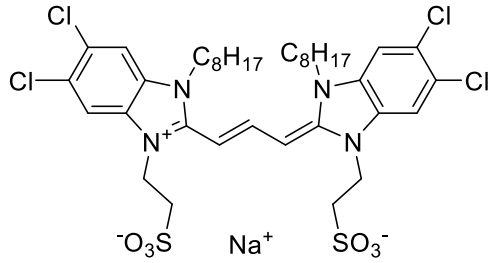

1H NMR (400 MHz, DMSO) δ 7.93 (s, 1H), 7.76 (s, 1H), 5.80 (d, *J* = 13.2 Hz, 1H), 4.47 (t, *J* = 7.0 Hz, 2H), 4.24 (t, *J* = 7.2 Hz, 2H), 2.91 (t, *J* = 7.0 Hz, 2H), 1.66 (qd, *J* = 8.0, 5.3 Hz, 3H), 1.29 (d, *J* = 7.4 Hz, 2H), 1.25 (s, 3H), 1.19 (s, 4H), 1.15 (d, *J* = 3.9 Hz, 7H), 1.06 (s, 1H), 0.79 (dt, *J* = 18.9, 6.2 Hz, 5H), 0.71 (s, 1H).

13C NMR (126 MHz, DMSO) δ 149.52, 132.81, 132.60, 126.16, 125.94, 112.45, 111.70, 48.25, 44.73, 42.61, 31.68, 29.16, 29.06, 27.91, 26.23, 22.56, 22.51, 14.42, 14.38.

HRMS (ESI-): Calculated for $C_{37}H_{49}Cl_4N_4O_6S_2^-$ [M-]: 849.1848; found: 849.1801

Sodium 5-(5,6-dichloro-2-((1E,3E)-3-(5,6-dichloro-1-octyl-3-(5-sulfonatopentyl)-1,3-dihydro-2H-benzo[d]imidazol-2-ylidene)prop-1-en-1-yl)-1-octyl-1H-benzo[d]imidazol-3-ium-3-yl)pentane-1-sulfonate (**4.1d**)

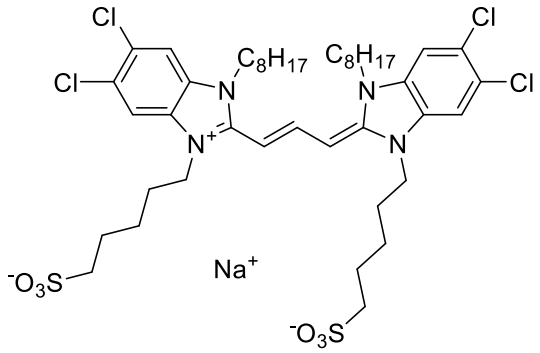

^{1}H NMR (400 MHz, MeOD) δ 7.91 (t, *J* = 13.4 Hz, 1H), 7.75 (d, *J* = 12.3 Hz, 4H), 5.86 (d, *J* = 13.3 Hz, 2H), 4.30 (dt, *J* = 11.7, 7.4 Hz, 8H), 2.85 – 2.77 (m, 4H), 1.86 (h, *J* = 7.8 Hz, 12H), 1.58 (p, *J* = 7.9 Hz, 4H), 1.43 – 1.18 (m, 20H), 0.89 – 0.79 (m, 6H).

^{13}C NMR (126 MHz, MeOD) δ 149.84, 142.30, 132.41, 132.18, 127.23, 127.18, 111.21, 111.15, 85.10, 50.70, 48.11, 48.06, 47.94, 47.89, 47.72, 47.60, 44.93, 44.68, 31.50, 28.97, 28.88, 27.64, 27.41, 26.21, 25.11, 24.31, 22.28.

HRMS (ESI+): Calculated for $C_{43}H_{61}Cl_4N_4NaO_6S_2$ [M+]: 957.2762; found: 957.2773.

Sodium 6-(5,6-dichloro-2-((1E,3E)-3-(5,6-dichloro-1-octyl-3-(6-sulfonatohexyl)-1,3-dihydro-2H-benzo[d]imidazol-2-ylidene)prop-1-en-1-yl)-1-octyl-1H-benzo[d]imidazol-3-ium-3-yl)hexane-1-sulfonate (**4.1e**)

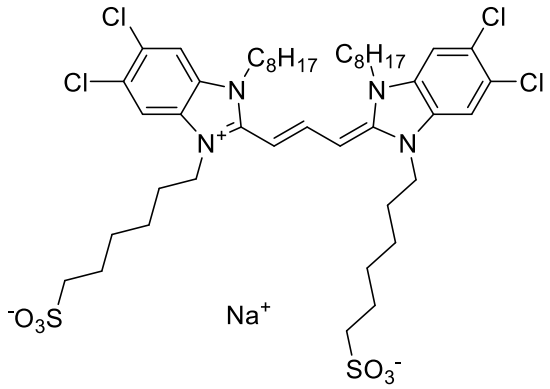

^{1}H NMR (400 MHz, MeOD) δ 7.74 (d, *J* = 9.7 Hz, 4H), 5.85 (d, *J* = 13.2 Hz, 2H), 4.29 (q, *J* = 8.0 Hz, 8H), 2.81 – 2.72 (m, 4H), 1.91 – 1.84 (m, 6H), 1.56 – 1.14 (m, 28H), 0.87 – 0.79 (m, 6H).

^{13}C NMR (126 MHz, MeOD) δ 132.38, 132.26, 111.19, 50.94, 44.87, 44.73, 31.50, 28.95, 28.88, 27.85, 27.64, 27.53, 26.19, 25.79, 24.40, 22.34, 22.28.

HRMS (ESI+): Calculated for $C_{45}H_{65}Cl_4N_4NaO_6S_2$ [M+]: 985.3076; found: 985.3104.

Sodium 7-(5,6-dichloro-2-((1E,3E)-3-(5,6-dichloro-1-octyl-3-(7-sulfonatoheptyl)-1,3-dihydro-2H-benzo[d]imidazol-2-ylidene)prop-1-en-1-yl)-1-octyl-1H-benzo[d]imidazol-3-ium-3-yl)heptane-1-sulfonate (**4.1f**)

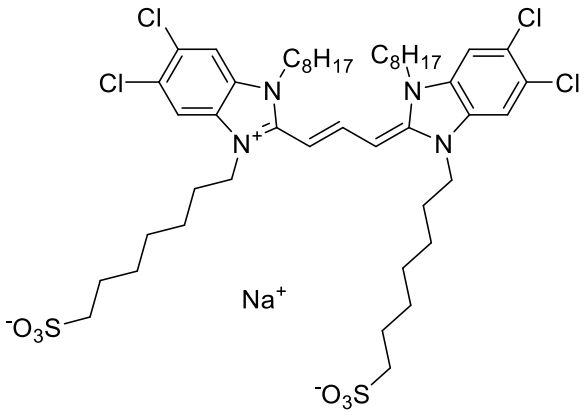

^{1}H NMR (400 MHz, MeOD) δ 7.72 (d, *J* = 5.6 Hz, 4H), 4.28 (q, *J* = 6.8 Hz, 8H), 2.78 – 2.70 (m, 5H), 1.85 (p, *J* = 7.2 Hz, 9H), 1.79 – 1.70 (m, 5H), 1.47 – 1.18 (m, 32H), 0.91 – 0.79 (m, 6H).

^{13}C NMR (126 MHz, MeOD) δ 132.35, 132.26, 127.25, 111.22, 51.09, 48.23, 48.11, 48.06, 48.05, 47.94, 47.88, 47.86, 47.85, 47.77, 47.60, 47.43, 47.26, 47.09, 44.82, 31.50, 28.97, 28.89, 28.83, 28.52, 28.03, 27.69, 27.66, 26.20, 25.88, 25.50, 24.40, 22.29, 13.04.

HRMS (ESI+): Calculated for $C_{47}H_{69}Cl_4N_4NaO_6S_2$ [M+]: 1013.3389; found: 1013.3365.

Sodium 8-(5,6-dichloro-2-((1E,3E)-3-(5,6-dichloro-1-octyl-3-(8-sulfonatooctyl)-1,3-dihydro-2H-benzo[d]imidazol-2-ylidene)prop-1-en-1-yl)-1-octyl-1H-benzo[d]imidazol-3-ium-3-yl)octane-1-sulfonate (**4.1g**)

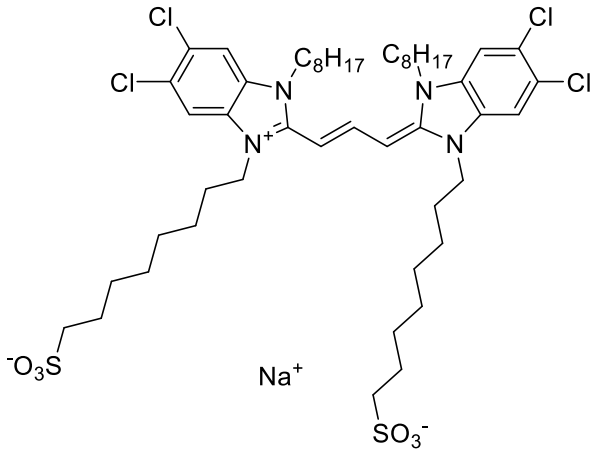

^{1}H NMR (400 MHz, MeOD) δ 7.75 (d, *J* = 3.6 Hz, 4H), 4.32 (q, *J* = 6.8 Hz, 8H), 2.82 – 2.71 (m, 5H), 1.88 (p, *J* = 7.1 Hz, 9H), 1.82 – 1.70 (m, 6H), 1.40 – 1.20 (m, 36H), 0.94 – 0.82 (m, 6H).

^{13}C NMR (126 MHz, MeOD) δ 208.67, 132.34, 51.19, 48.44, 48.22, 47.76, 47.67, 47.49, 47.42, 47.36, 47.30, 47.25, 47.08, 31.50, 29.26, 28.96, 28.89, 28.63, 28.60, 28.10, 27.67, 26.19, 26.02, 24.44, 22.28, 13.03.

HRMS (ESI+): Calculated for $C_{49}H_{73}Cl_4N_4NaO_6S_2$ [M+]: 1041.3701; found: 1041.3655.

4.11. Experimental procedures for differently charged C8S3 derivatives

*Synthesis of 3-(3-azidopropyl)-5,6-dichloro-2-methyl-1-octyl-1H-benzo[d]imidazol-3-ium bromide (**4.S1**)*

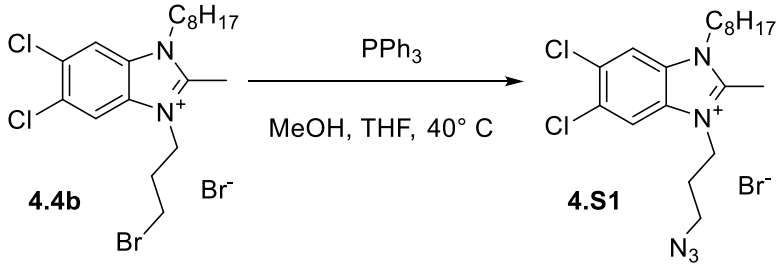

3-(3-bromopropyl)-5,6-dichloro-2-methyl-1-octyl-1H-benzo[d]imidazol-3-ium **4b** (1.99 g, 4.57 mmol, 1 eq.) and sodium azide (892 mg, 13.7 mmol, 3 eq.) were added to a flask with H_2O

(10 mL) and acetone (10 mL). The mixture was stirred for 72 h. at room temperature at which point the solvent was removed by rotary evaporation. The resulting white solid was suction filtered with water to yield **4.S1** as a clumpy white solid. (1.66 g, 4.18 mmol, 91%).

*Synthesis of 3-(3-azidopropyl)-2-((1E,3E)-3-(1-(3-azidopropyl)-5,6-dichloro-3-octyl-1,3-dihydro-2H-benzo[d]imidazol-2-ylidene)prop-1-en-1-yl)-5,6-dichloro-1-octyl-1H-benzo[d]imidazol-3-ium bromide (***4.6a***)*

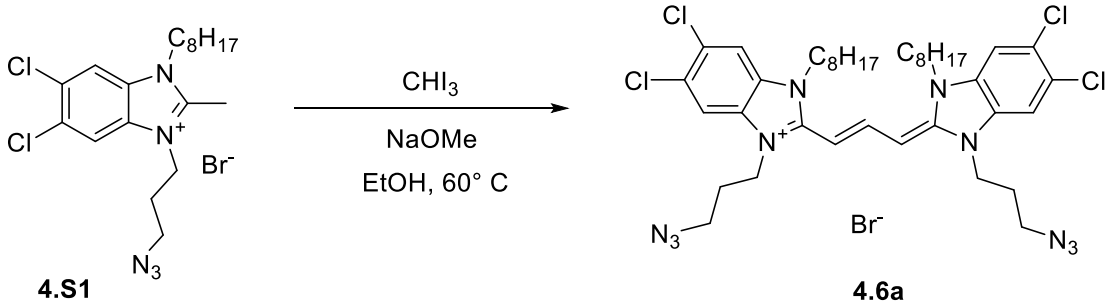

4.S1 **4.6a**

Azide heterocycle **4.S1** (1 eq.), iodoform (0.6 eq.), and sodium methoxide (3 eq.) were combined in a 10 mL Schlenk tube, which was evacuated and purged 3x with argon. Immediately upon adding anhydrous ethanol (7 mL), the reaction was subjected to 3 cycles of freeze, pump, thaw to ensure an oxygen-free environment. The reaction was then heated to 65° C for 1 h., before stirring overnight. The solvent was then removed by rotary evaporation and purified via silica column chromatography using gradient elution from 0 to 10% methanol in DCM. This procedure provided trimethine dye **4.6a** as a red solid. (92 mg, 0.11 mmol, 9.3%).

^{1}H NMR (400 MHz, MeOD) δ 7.74 (d, *J* = 8.5 Hz, 2H), 5.86 (d, *J* = 13.0 Hz, 1H), 4.37 (t, *J* = 7.1 Hz, 2H), 4.30 (t, *J* = 7.3 Hz, 2H), 3.48 (t, *J* = 6.1 Hz, 2H), 2.07 (p, *J* = 6.4 Hz, 2H), 1.84 (q, *J* = 7.3 Hz, 2H), 1.36 (s, 3H), 1.30 – 1.20 (m, 11H), 0.84 (q, *J* = 8.3 Hz, 5H).

^{13}C NMR (126 MHz, MeOD) δ 149.95, 132.43, 132.10, 115.25, 115.13, 111.27, 56.64, 48.11, 47.93, 47.09, 45.11, 45.00, 42.28, 31.52, 31.49, 29.00, 28.88, 28.82, 28.80, 28.74, 28.73, 27.78, 27.71, 26.81, 26.24, 26.07, 22.28, 13.02, 12.99.

HRMS (ESI+): Calculated for $C_{39}H_{52}Cl_4N_{10}^+$ [M+]: 801.3209; found: 801.3189.

*Synthesis of 3-(3-aminopropyl)-5,6-dichloro-2-methyl-1-octyl-1H-benzo[d]imidazol-3-ium bromide (***4.S2***)*

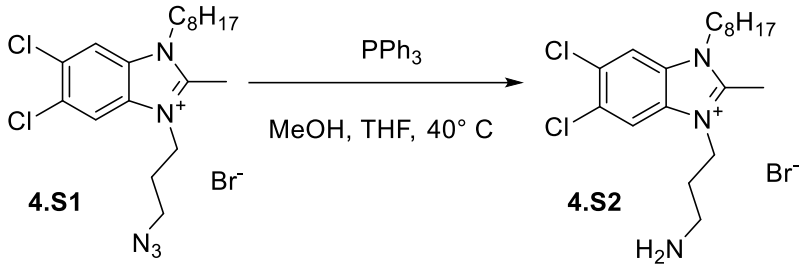

3-(3-bromopropyl)-5,6-dichloro-2-methyl-1-octyl-1H-benzo[d]imidazol-3-ium **4.S1** (3.40 g, 8.56 mmol, 1 eq.) and triphenylphosphine (5.58 g, 21.3 mmol, 10 eq.) were added to a flask with MeOH (30 mL) and acetone (30 mL). The mixture was stirred and heated to 40 C for 18 h. at which point any undissolved triphenylphosphine was suction filtered. The filtrate was concentrated by rotary evaporation and purified using flash column chromatography with 10% DCM/MeOH. This procedure resulted in **4.S2** as a gummy, off-white solid. (850 mg, 2.29 mmol, 27%).

^{1}H NMR (400 MHz, MeOD) δ 8.38 (s, 1H), 8.31 (s, 1H), 4.64 – 4.54 (m, 2H), 4.52 – 4.43 (m, 2H), 3.20 – 3.12 (m, 2H), 2.32 – 2.20 (m, 2H), 1.90 (p, *J* = 7.6 Hz, 2H), 1.51 – 1.37 (m, 4H), 1.32 (td, *J* = 7.7, 3.4 Hz, 7H), 0.94 – 0.86 (m, 3H).

^{13}C NMR (126 MHz, MeOD) δ 130.89, 130.70, 114.68, 114.31, 48.05, 47.87, 47.71, 47.70, 47.68, 47.67, 47.51, 47.50, 47.49, 47.33, 47.32, 47.32, 47.31, 47.16, 47.15, 47.14, 46.03, 42.93, 36.46, 31.52, 28.88, 28.86, 28.66, 26.78, 26.20, 22.28, 12.99.

HRMS (ESI+): Calculated for $C_{19}H_{30}Cl_2N_3^+$ [M+]: 370.1808; found: 370.1817.

*Synthesis of 3-(3-((tert-butoxycarbonyl)amino)propyl)-5,6-dichloro-2-methyl-1-octyl-1H-benzo[d]imidazol-3-ium bromide (**4.S3**)*

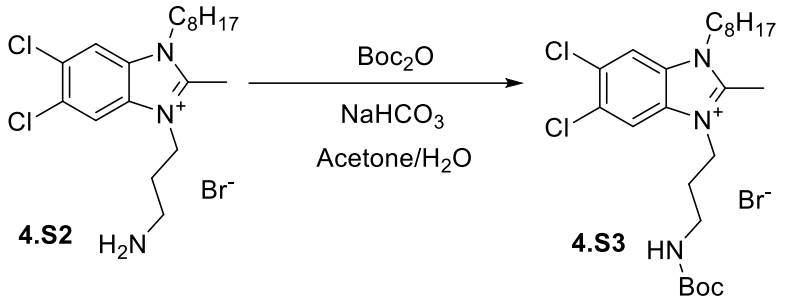

3-(3-aminopropyl)-5,6-dichloro-2-methyl-1-octyl-1H-benzo[d]imidazol-3-ium **4.S2** (350 mg, 0.94 mmol, 1 eq.), boc anhydride (507 mg, 2.3 mmol, 3 eq.), and sodium bicarbonate (107 mg, 1.27 mmol, 1.5 eq.) were combined with H_2O (3 mL) and acetone (3 mL). The reaction was stirred at room temperature overnight before the acetone was removed by rotary evaporation. The resulting solid was washed with hexane and filtered to provide **4.S3** as an off-white solid. (440 mg, 0.93 mmol, 99%).

^{1}H NMR (400 MHz, MeOD) δ 8.30 (dd, *J* = 11.8, 2.4 Hz, 2H), 4.50 (qd, *J* = 7.4, 2.8 Hz, 4H), 3.19 (t, *J* = 6.6 Hz, 2H), 2.16 – 2.04 (m, 2H), 1.89 (q, *J* = 7.0 Hz, 2H), 1.53 (d, *J* = 2.3 Hz, 29H), 1.45 (d, *J* = 2.4 Hz, 14H), 1.39 – 1.29 (m, 8H), 0.96 – 0.88 (m, 3H).

^{13}C NMR (101 MHz, MeOD) δ 130.78, 130.63, 114.51, 114.42, 45.89, 43.53, 31.50, 28.86, 28.82, 28.68, 28.44, 27.32, 26.14, 22.26, 12.98.

HRMS (ESI+): Calculated for $C_{24}H_{37}Cl_2N_3O_2^+$ [M+]: 470.2354; found: 470.2341.

*Synthesis of 3-(3-((tert-butoxycarbonyl)amino)propyl)-2-((1E,3E)-3-(1-(3-((tert-butoxycarbonyl)amino)propyl)-5,6-dichloro-3-octyl-1,3-dihydro-2H-benzo[d]imidazol-2-ylidene)prop-1-en-1-yl)-5,6-dichloro-1-octyl-1H-benzo[d]imidazol-3-ium bromide (**4.S4**)*

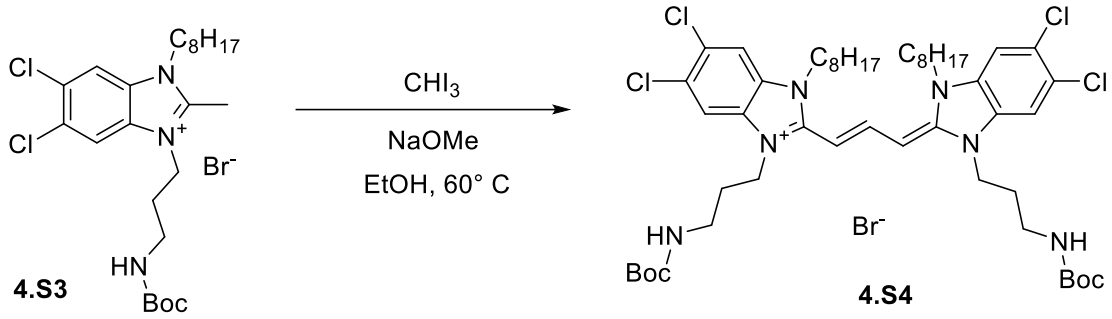

Boc-protected amine **4.S3** (150 mg, 0.272 mmol, 1 eq.), iodoform (64 mg, 0.163 mmol, 0.6 eq.), and sodium methoxide (44 mg, 0.816 mmol, 3 eq.) were combined in a 10 mL Schlenk tube, which was evacuated and purged 3x with argon. Immediately upon adding anhydrous ethanol (7 mL), the reaction was subjected to 3 cycles of freeze, pump, thaw to ensure an oxygen-free environment. The reaction was then heated to 65° C for 1 h., before stirring overnight. The solvent was then removed by rotary evaporation and purified via silica column chromatography using gradient elution from 0 to 10% methanol in DCM. This procedure provided trimethine dye **4.S4** as a red solid. (27 mg, 0.026 mmol, 9.6%.)

^{1}H NMR (400 MHz, MeOD) δ 7.93 (s, 1H), 7.76 (dd, *J* = 7.8, 3.9 Hz, 3H), 5.89 (d, *J* = 13.1 Hz, 1H), 4.33 (q, *J* = 6.7 Hz, 6H), 3.19 (t, *J* = 6.8 Hz, 3H), 2.07 (t, *J* = 7.4 Hz, 3H), 1.90 (s, 2H), 1.45 (s, 3H), 1.41 (s, 9H), 1.41 – 1.37 (m, 9H), 1.37 – 1.23 (m, 16H), 1.22 – 1.16 (m, 1H), 0.93 – 0.84 (m, 6H).

^{13}C NMR (126 MHz, MeOD) δ 157.07, 132.40, 132.07, 127.36, 115.21, 111.25, 111.07, 78.85, 48.23, 42.77, 37.23, 33.64, 31.53, 31.50, 29.02, 28.90, 28.81, 27.92, 27.74, 27.37, 27.33, 27.30, 26.27, 26.09, 22.29, 13.04, 13.02.

HRMS (ESI+): Calculated for $C_{49}H_{72}Cl_4N_6O_4^+$ [M+]: 949.4448; found: 949.4427.

*Synthesis of 3-(3-aminopropyl)-2-((1E,3E)-3-(1-(3-aminopropyl)-5,6-dichloro-3-octyl-1,3-dihydro-2H-benzo[d]imidazol-2-ylidene)prop-1-en-1-yl)-5,6-dichloro-1-octyl-1H-benzo[d]imidazol-3-ium bromide (**4.6b**)*

4.S4 **4.6b**

Boc-protected dye **4.S4** (11.4 mg, 0.012 mmol, 1 eq.) was dissolved in 1.5 mL dichloromethane, to which 0.5 mL of concentrated HCl was added. The reaction was stirred for 90 min. at room temperature. The authors note that the addition of acid causes a change to the dye's color, which has been documented for similar compounds elsewhere.[65] To return the dye's color to its original state, a saturated solution of NaOH in methanol was added dropwise until the red color no longer dissipated upon shaking. This mixture was syringe filtered to remove any NaCl precipitate, concentrated by rotary evaporation, and dried over high vacuum overnight to yield the amine-substituted dye **6b** as a red solid. (8.7 mg, 0.010 mmol, 95%.)

^{1}H NMR (500 MHz, MeOD) δ 7.95 (s, 0H), 7.72 (s, 1H), 5.89 (d, *J* = 13.9 Hz, 1H), 4.31 (s, 3H), 2.75 (td, *J* = 6.7, 3.5 Hz, 1H), 1.99 (q, *J* = 6.4 Hz, 1H), 1.90 – 1.82 (m, 2H), 1.26 (s, 15H), 1.26 (s, 1H), 1.22 (s, 2H), 0.89 – 0.80 (m, 2H), 0.84 (s, 3H).

^{13}C NMR (126 MHz, MeOD) δ 169.31, 159.93, 132.20, 128.52, 127.11, 110.90, 51.941, 48.46, 38.26, 31.50, 30.81, 28.97, 26.22, 22.27, 13.06.

HRMS (ESI+): Calculated for $C_{39}H_{57}Cl_4N_6^+$ [M+]: 749.3399; found: 749.3392.

4.12. NMR spectra relevant to Chapter 4

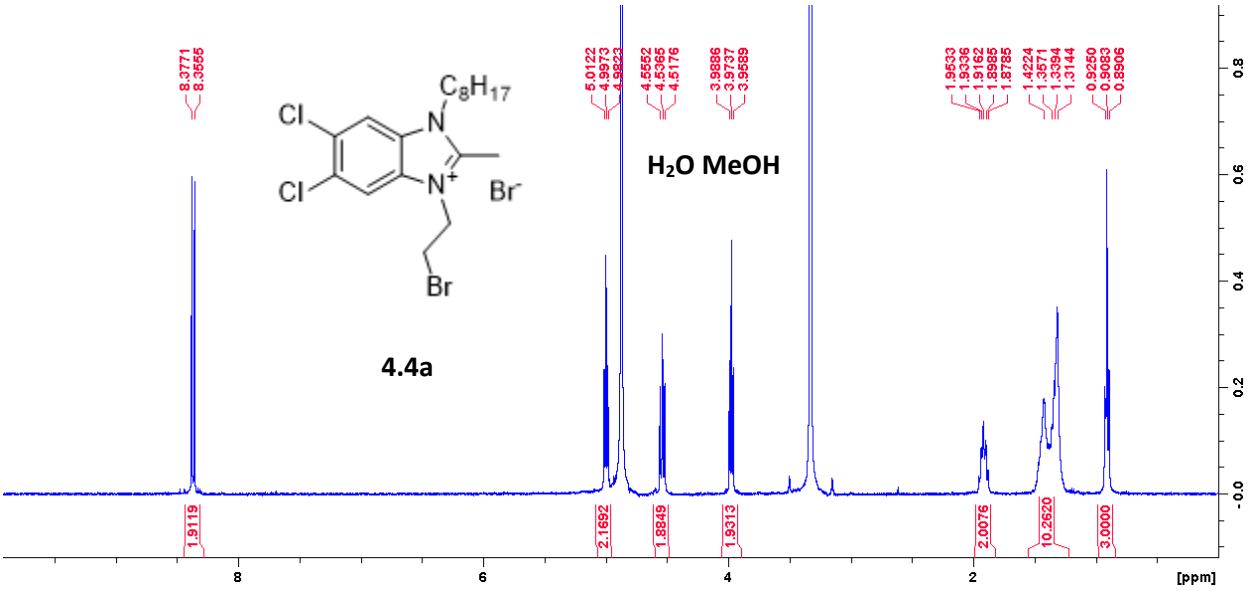

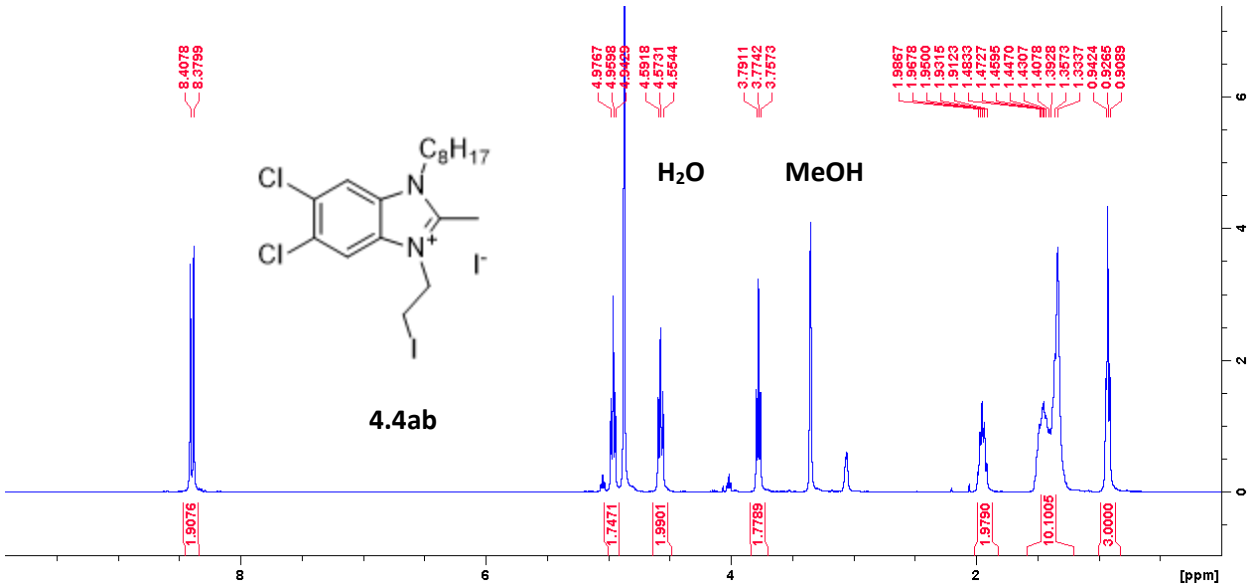
8.4078
8.3799
4.9767
4.9588
4.9429
4.5918
4.5731
4.5544
3.7911
3.7742
3.7573
1.9867
1.9678
1.9500
1.9315
1.9123
1.4833
1.4727
1.4595
1.4470
1.4307
1.4078
1.3928
1.3573
1.3337
0.9424
0.9265
0.9089
H2O
MeOH
4.4ab
1.9076
1.7471
1.9901
1.7789
1.9790
10.1005
3.0000
[ppm]

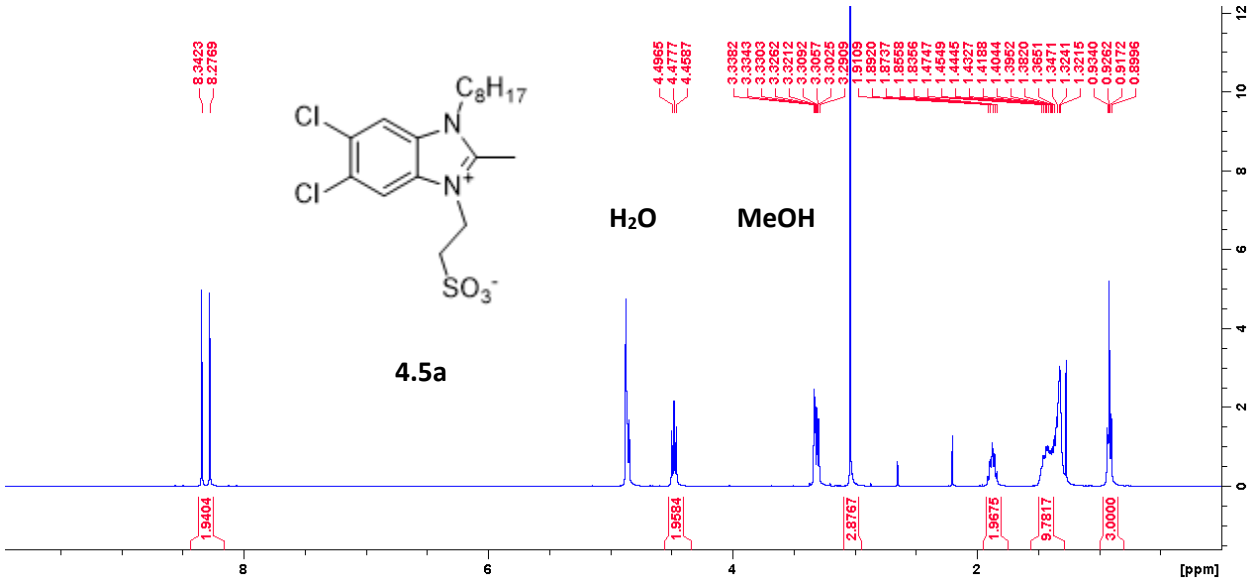
8.3423
8.2769
4.4965
4.4777
4.4587
3.3382
3.3343
3.3303
3.3262
3.3212
3.3092
3.3057
3.3025
3.2909
1.9109
1.8920
1.8737
1.8558
1.8356
1.4747
1.4549
1.4445
1.4327
1.4188
1.4044
1.3952
1.3820
1.3651
1.3471
1.3241
1.3215
0.9340
0.9262
0.9172
0.8996
H2O
MeOH
4.5a
1.9404
1.9684
2.8767
1.9675
9.7817
3.0000
[ppm]

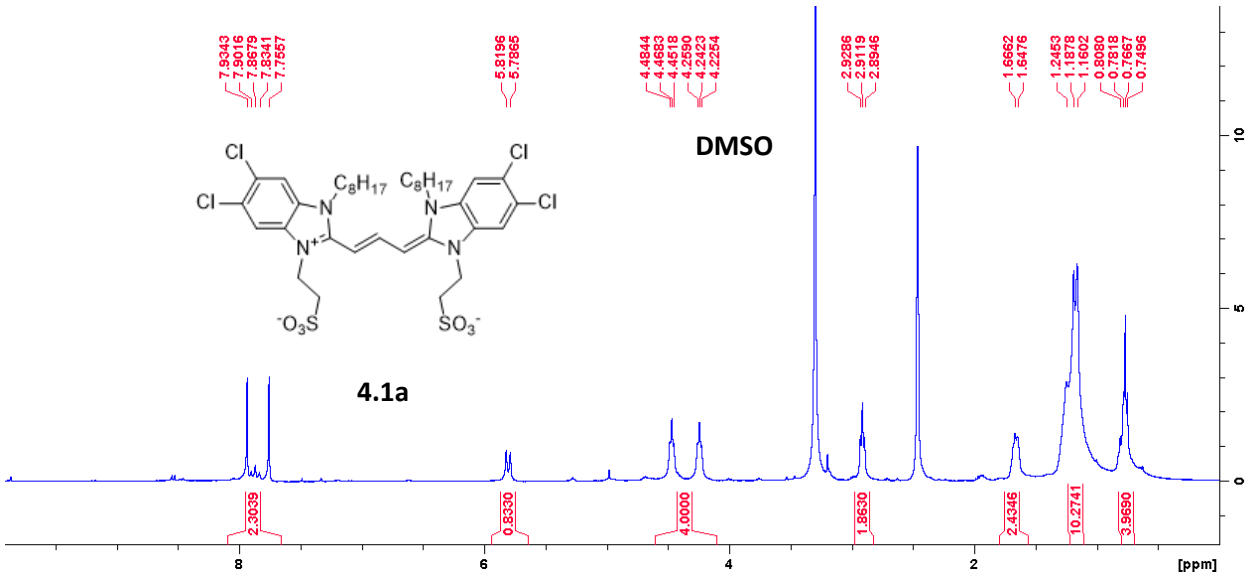
7.9343
7.9016
7.8679
7.8341
7.7557
5.8196
5.7865
4.4844
4.4683
4.4518
4.2590
4.2423
4.2254
2.9286
2.9119
2.8946
1.6662
1.6476
1.2453
1.1878
1.1602
0.8080
0.7818
0.7567
0.7496
DMSO
4.1a
2.3039
0.8330
4.0000
1.8630
2.4346
10.2741
3.9690
[ppm]

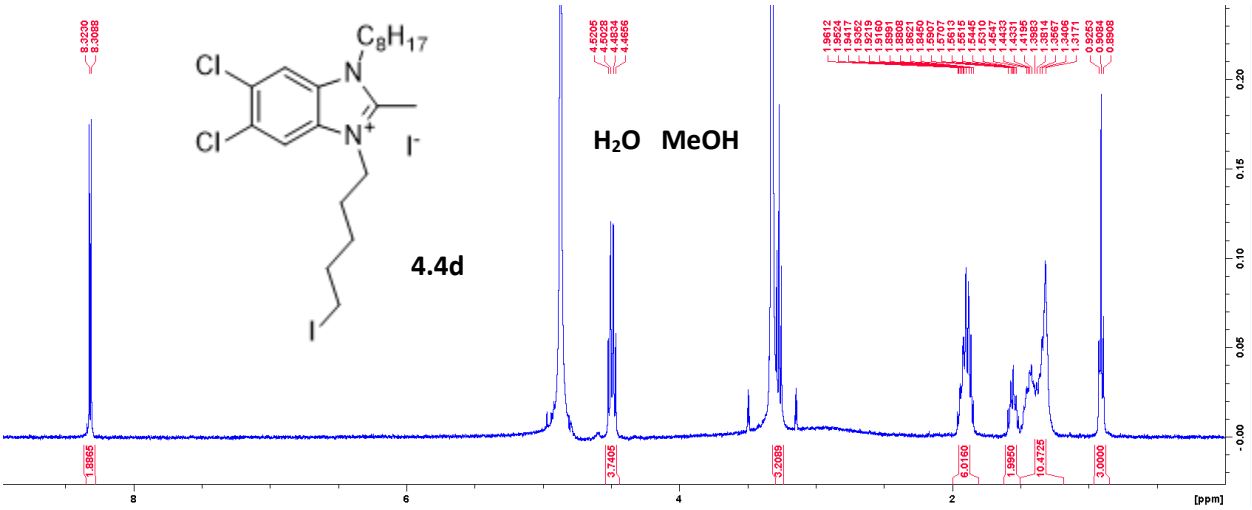
Cl
Cl
C_8H_{17}
N
N+
I-
I
4.4d
H_2O MeOH
[ppm]

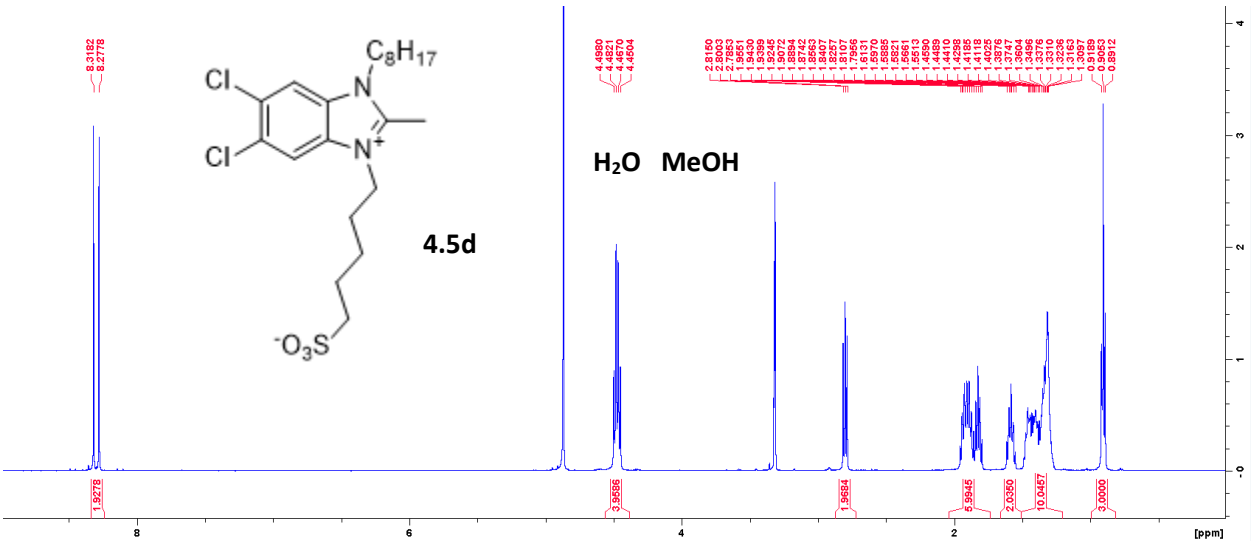
Cl
Cl
C_8H_{17}
N
N+
^-O_3S
4.5d
H_2O MeOH
[ppm]

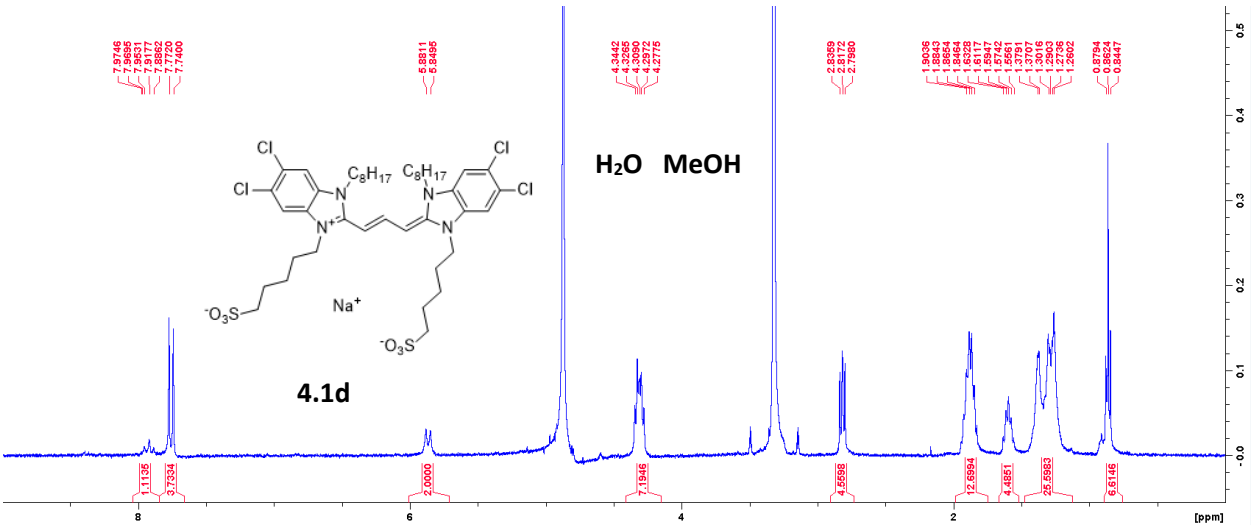
Cl
Cl
C_8H_{17}
C_8H_{17}
Cl
Cl
^-O_3S
Na+
^-O_3S
4.1d
H_2O MeOH
[ppm]

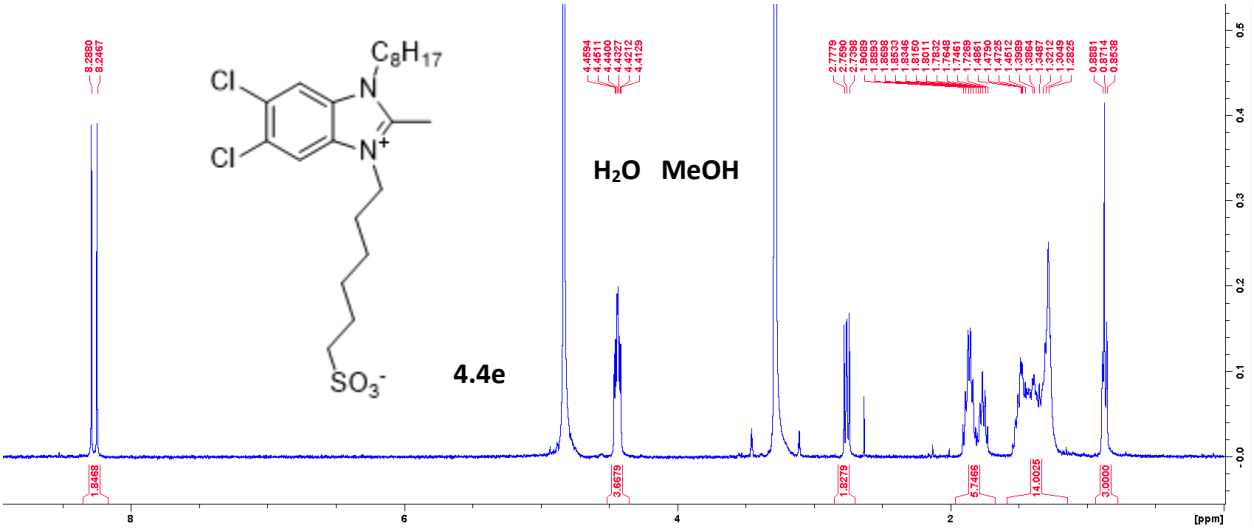
Cl
Cl
C_8H_{17}
N
N+
SO_3^-
4.4e
H_2O MeOH
[ppm]

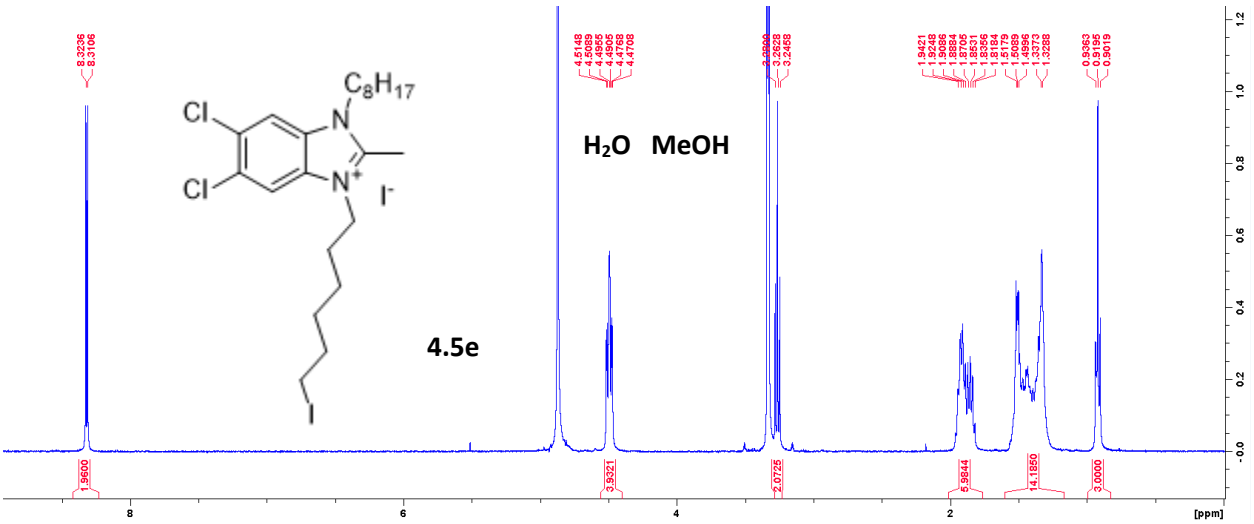
Cl
Cl
C_8H_{17}
N
N+
I^-
4.5e
H_2O MeOH
[ppm]

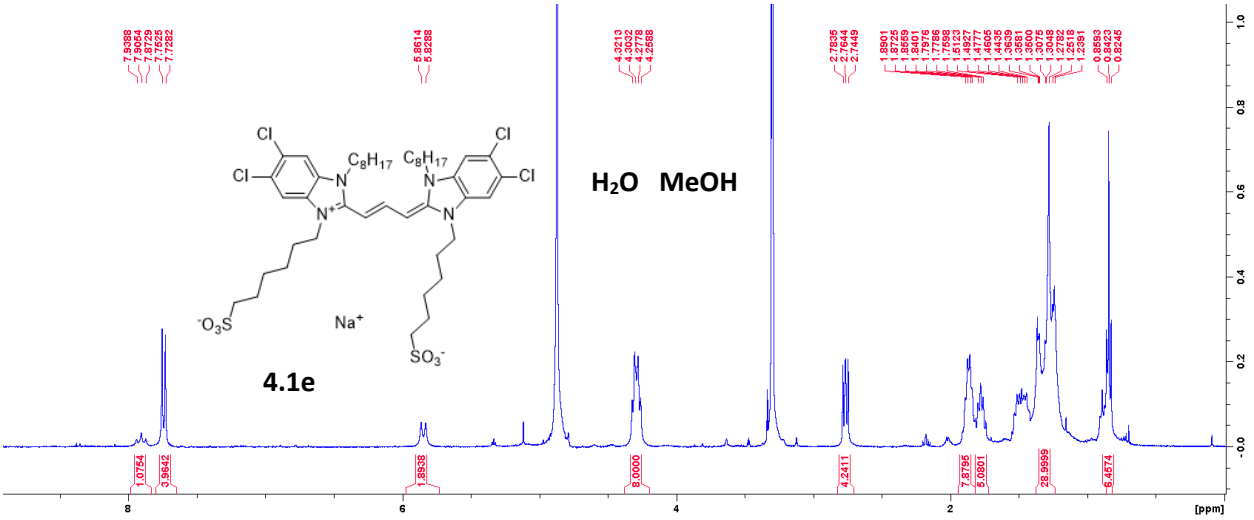
Cl
Cl
C_8H_{17}
C_8H_{17}
Cl
Cl
^-O_3S
Na^+
SO_3^-
4.1e
H_2O MeOH
[ppm]

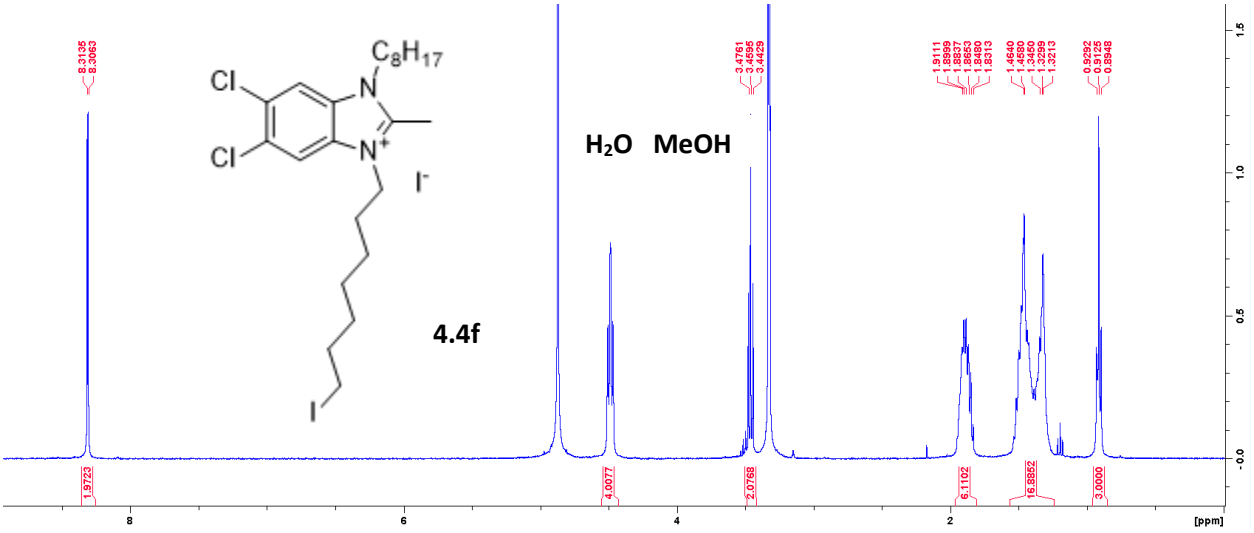
H2O MeOH
4.4f
[ppm]

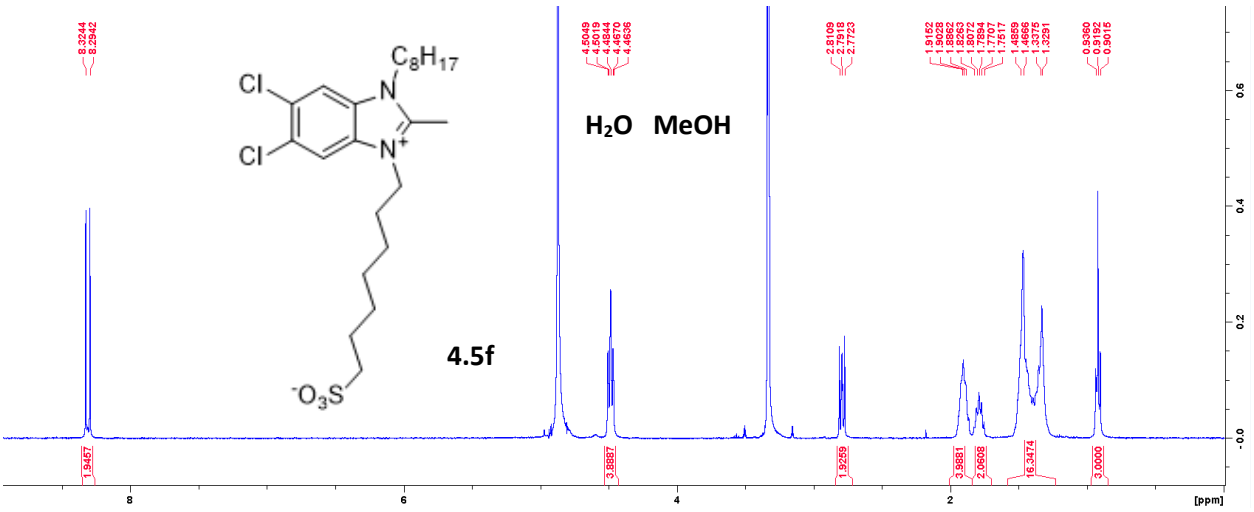
H2O MeOH
4.5f
[ppm]

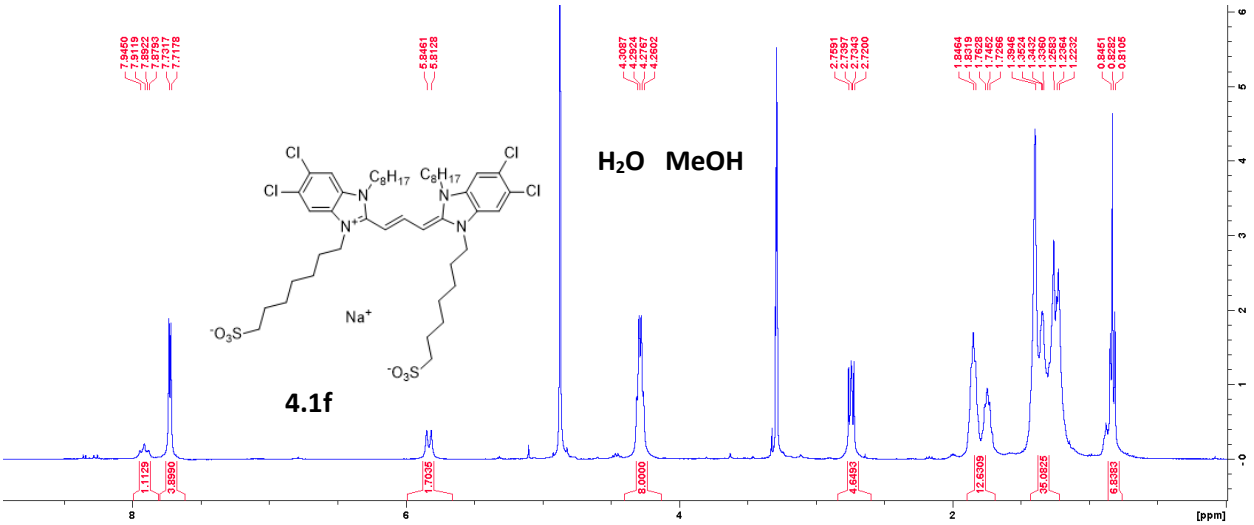
H2O MeOH
4.1f
[ppm]

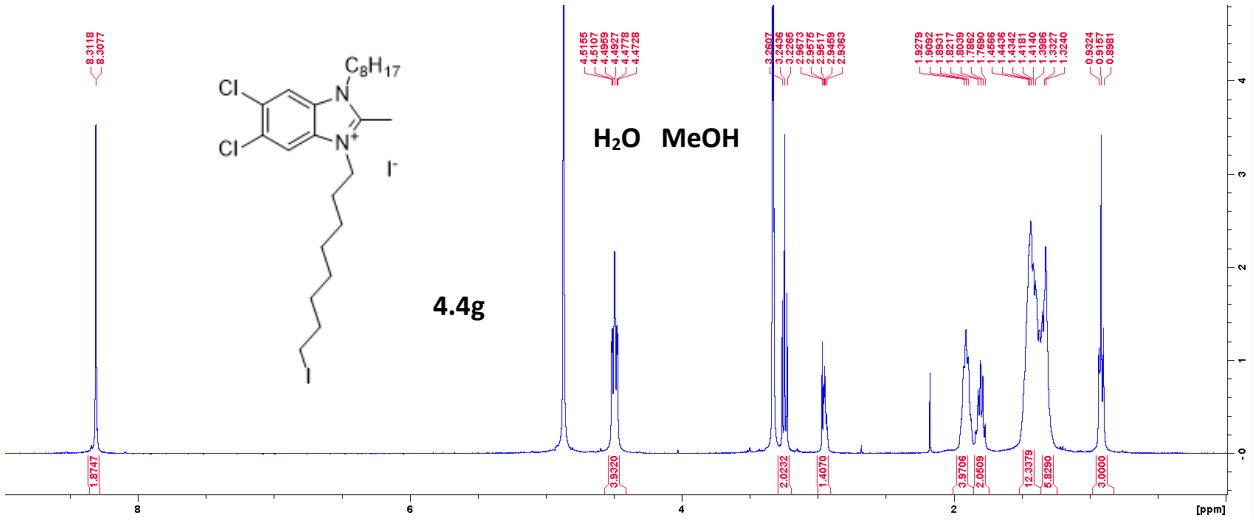
Cl
Cl
C_8H_{17}
N
N+
I-
I
4.4g
H2O MeOH
[ppm]

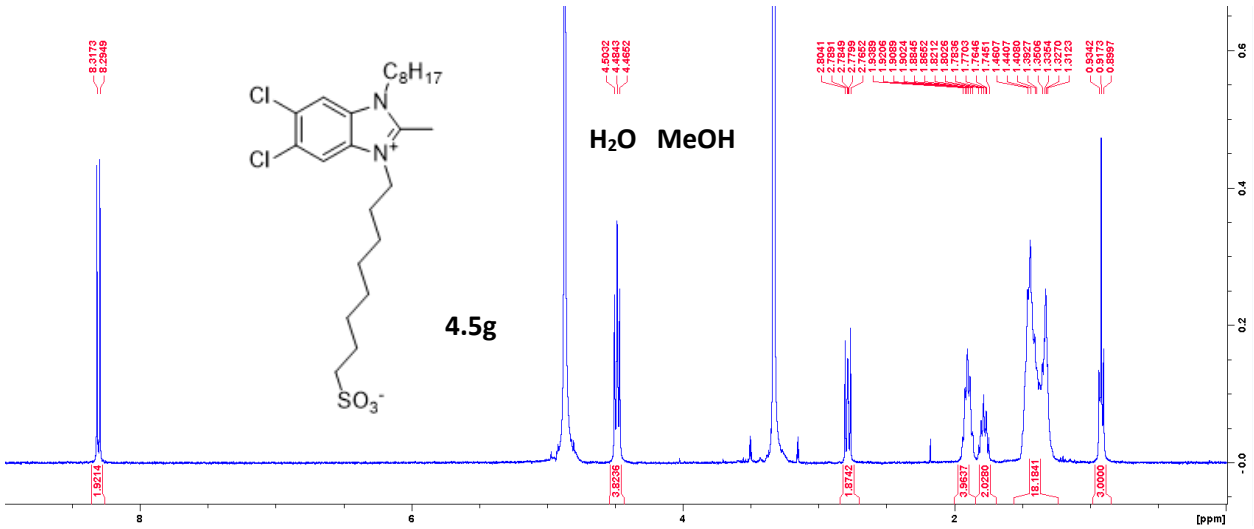
Cl
Cl
C_8H_{17}
N
N+
SO_3^-
4.5g
H2O MeOH
[ppm]

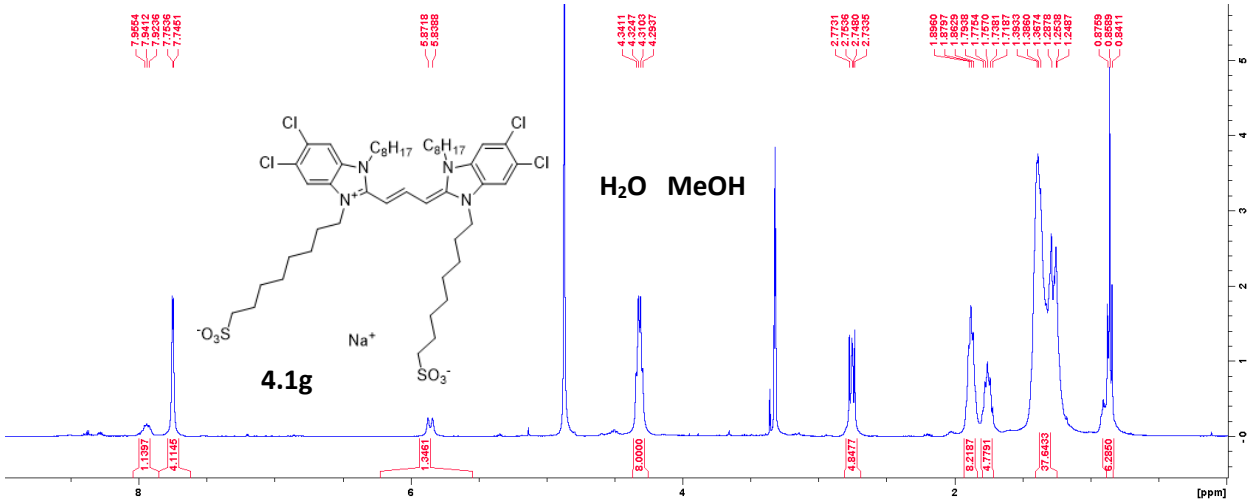
Cl
Cl
C_8H_{17}
C_8H_{17}
Cl
Cl
N
N+
^-O_3S
Na^+
SO_3^-
4.1g
H2O MeOH
[ppm]

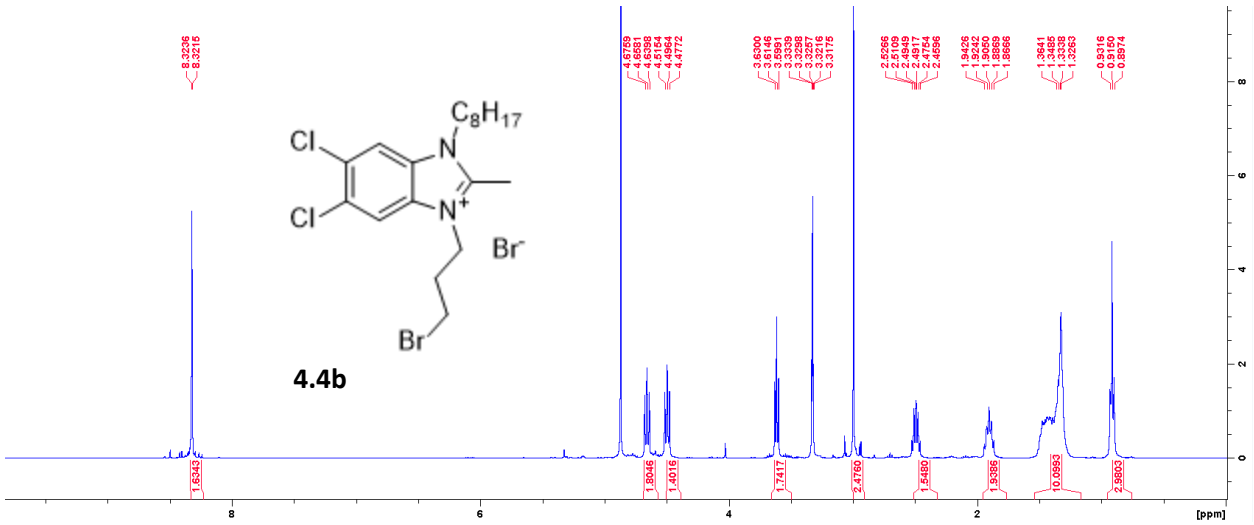
Cl
Cl
N
N+
C8H17
Br-
Br
4.4b

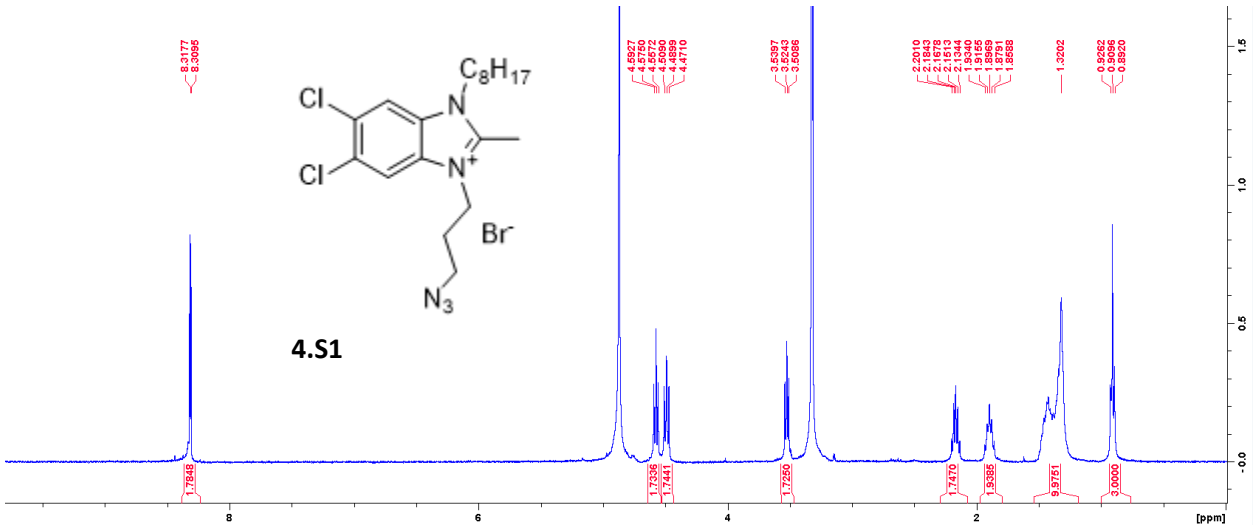
Cl
Cl
N
N+
C8H17
Br-
N3
4.S1

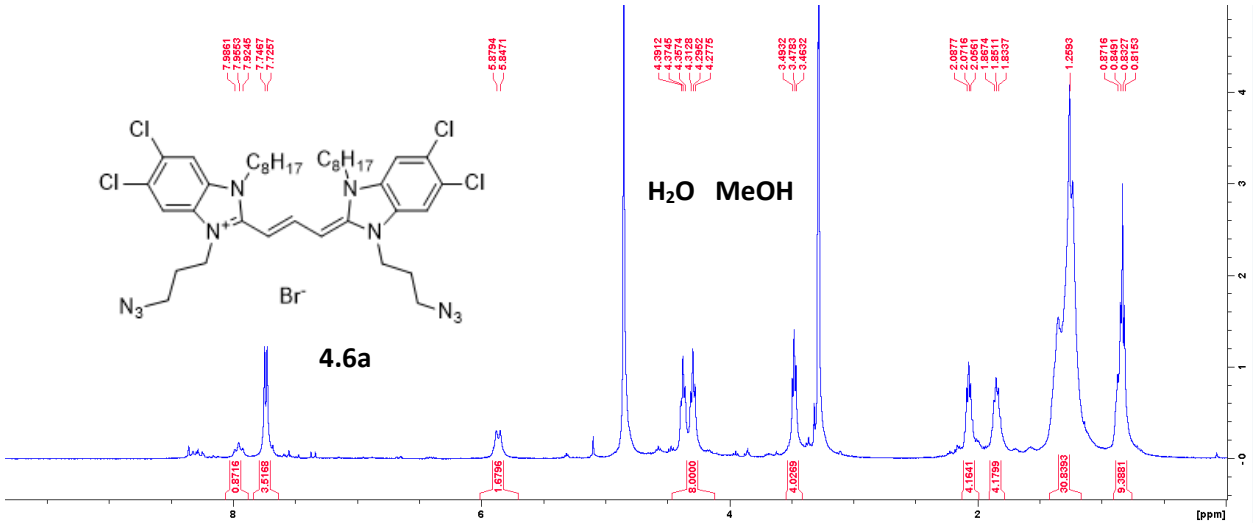
Cl
Cl
C8H17
C8H17
Cl
Cl
N
N+
N3
Br-
N3
4.6a
H2O
MeOH

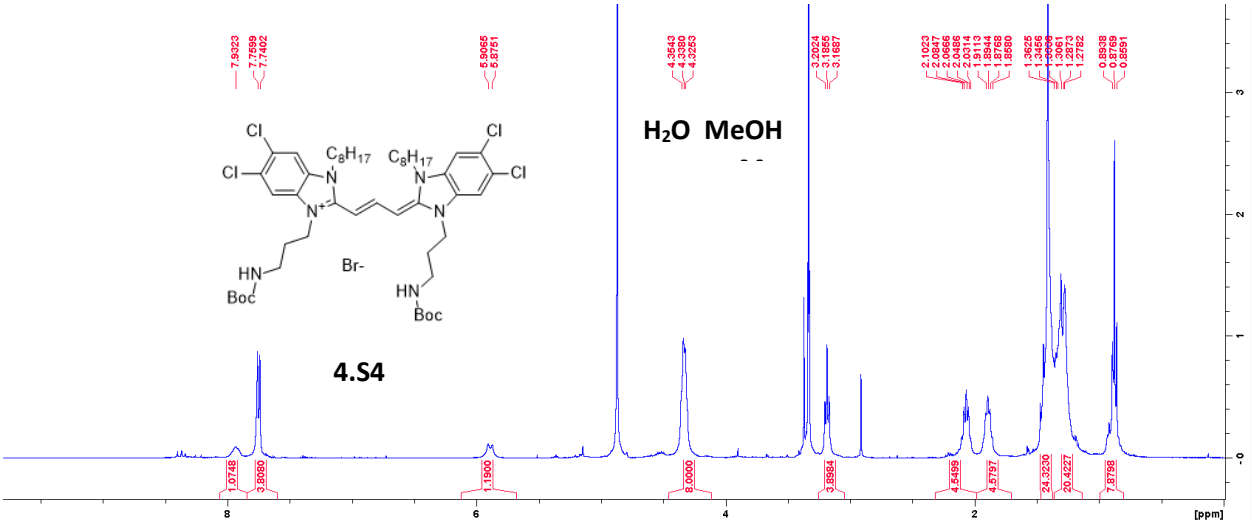
H2O MeOH
4.S4

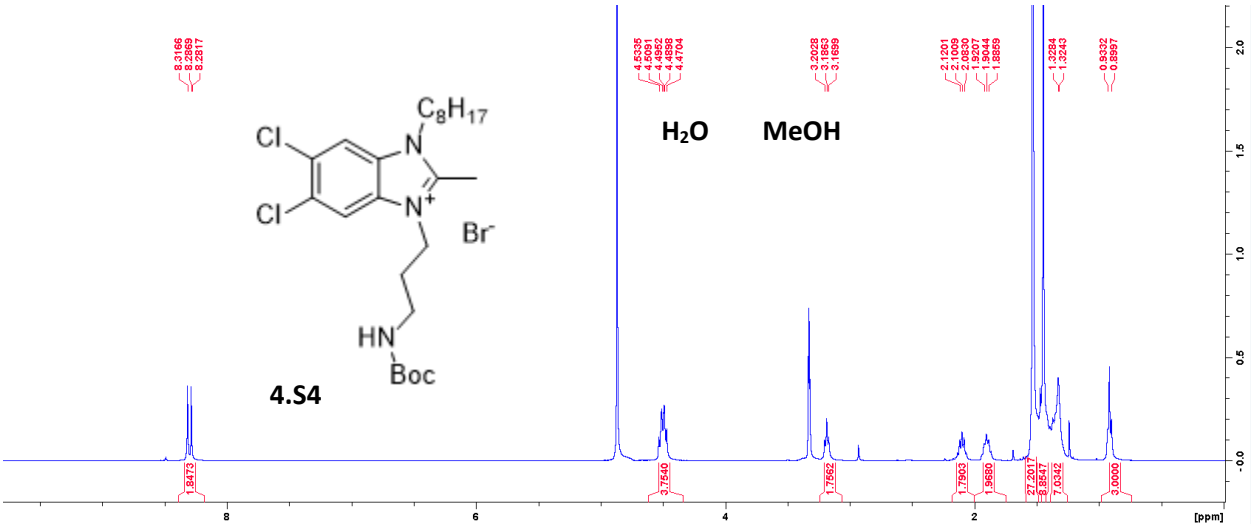
H2O MeOH
4.S4

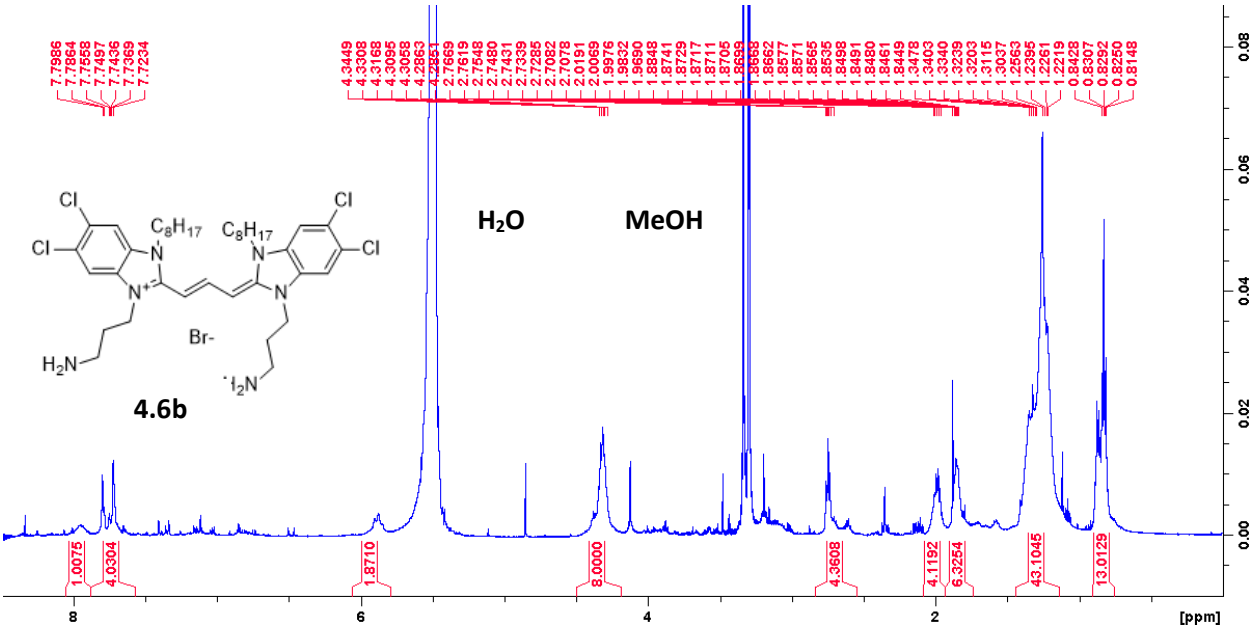
H2O
MeOH
4.6b
[ppm]

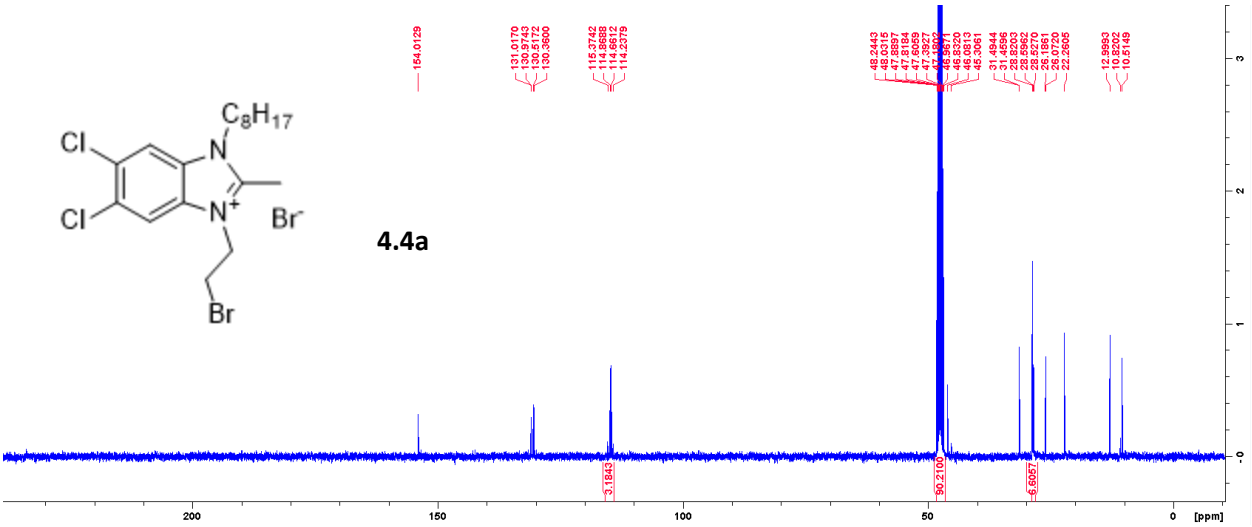
Cl
Cl
N
N+
C8H17
Br-
Br
4.4a
154.0129
131.0170
130.6172
130.3600
115.3742
114.8688
114.6612
114.2379
49.2443
49.0315
47.8897
47.6184
47.3927
45.3061
31.4844
31.4496
28.8203
28.5962
28.5270
26.1951
26.0730
22.2605
12.9993
10.8202
10.5148
3.1843
90.2100
6.6087
200
150
100
50
0
[ppm]

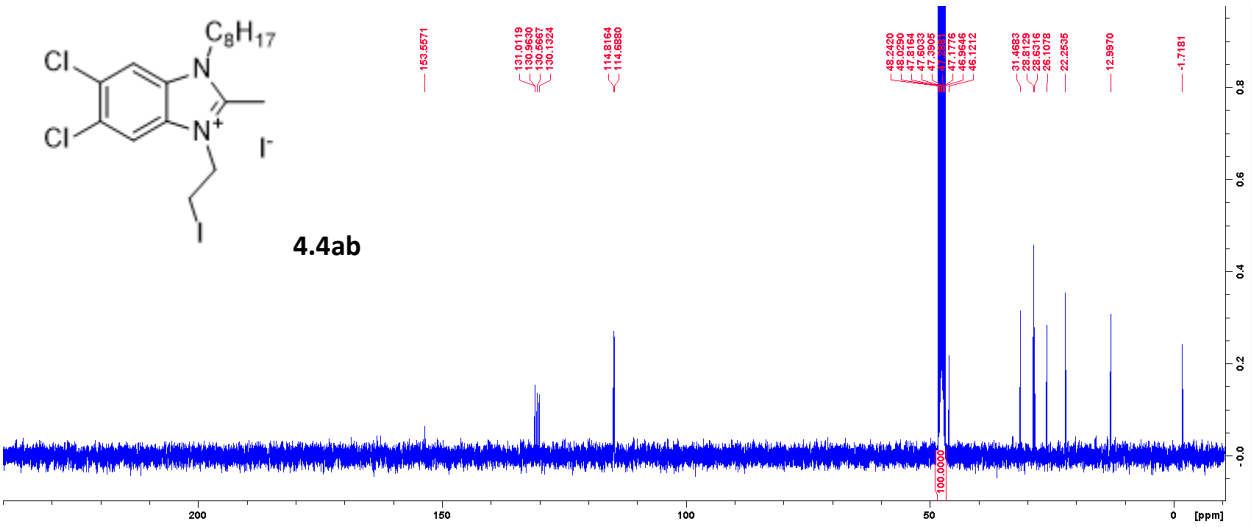
Cl
Cl
N
N+
C8H17
I-
I
4.4ab
153.5571
131.0119
130.9630
130.6577
130.1324
114.8164
114.6880
49.0420
48.8250
47.8164
47.6003
47.3905
47.1776
46.9646
46.7212
31.4693
28.8129
28.6316
26.1078
22.2535
12.9970
-1.7181
100.0000
200
150
100
50
0
[ppm]

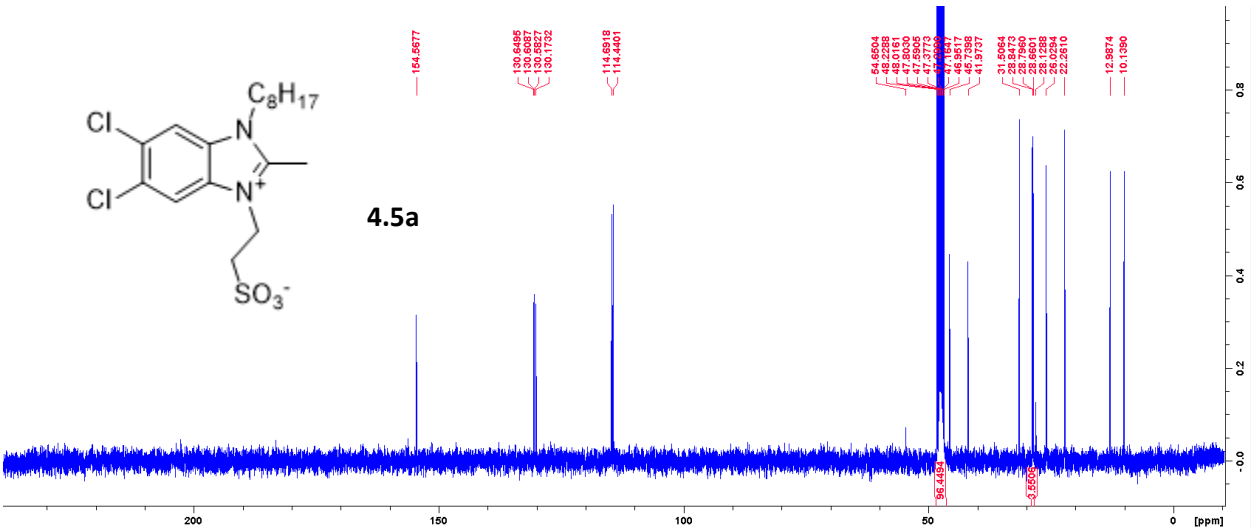
Cl
Cl
N
N+
C8H17
SO3-
4.5a
154.5577
130.6495
130.6087
130.3527
130.1732
114.6918
114.4401
54.6504
48.2288
48.0161
47.8030
47.5895
47.3773
47.1647
46.9517
45.7388
41.9737
31.5064
28.8473
28.7960
28.6601
28.0288
26.0294
22.2610
12.9874
10.1390
96.4494
3.5505
200
150
100
50
0
[ppm]

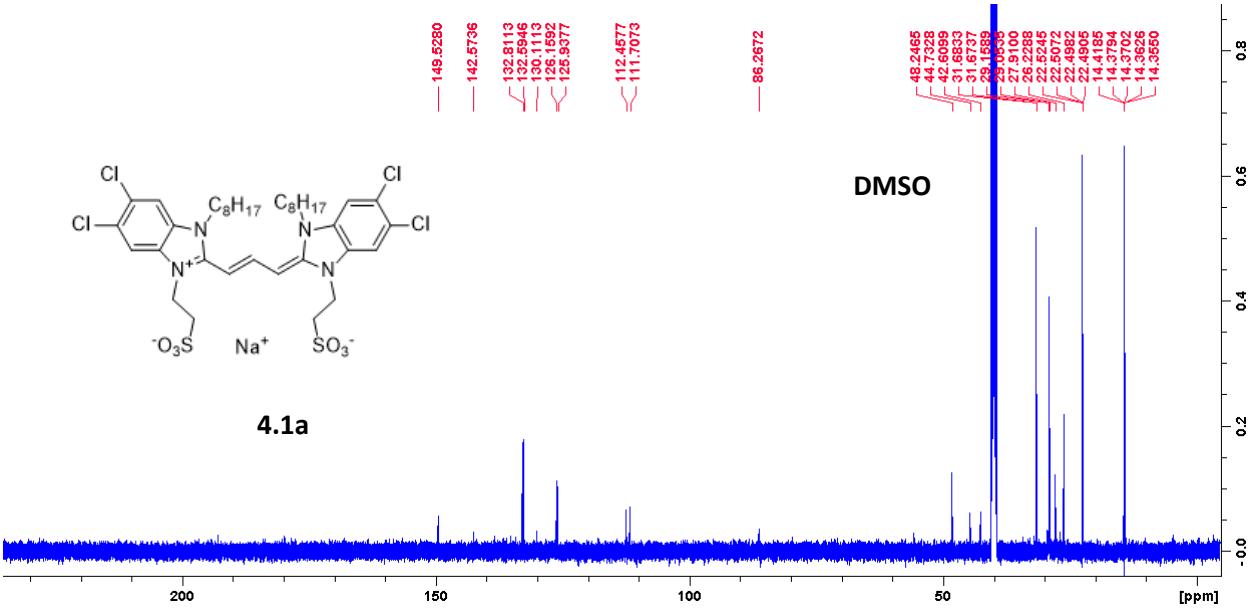
149.5280
142.5736
132.8113
132.5946
130.1113
126.1592
125.5377
112.4577
111.7073
86.2672
48.2465
44.7328
42.6099
31.6833
31.6737
29.1589
27.9100
26.2289
22.5245
22.5072
22.4982
22.4906
14.4185
14.3794
14.3704
14.3626
14.3550
DMSO
4.1a
200
150
100
50
[ppm]

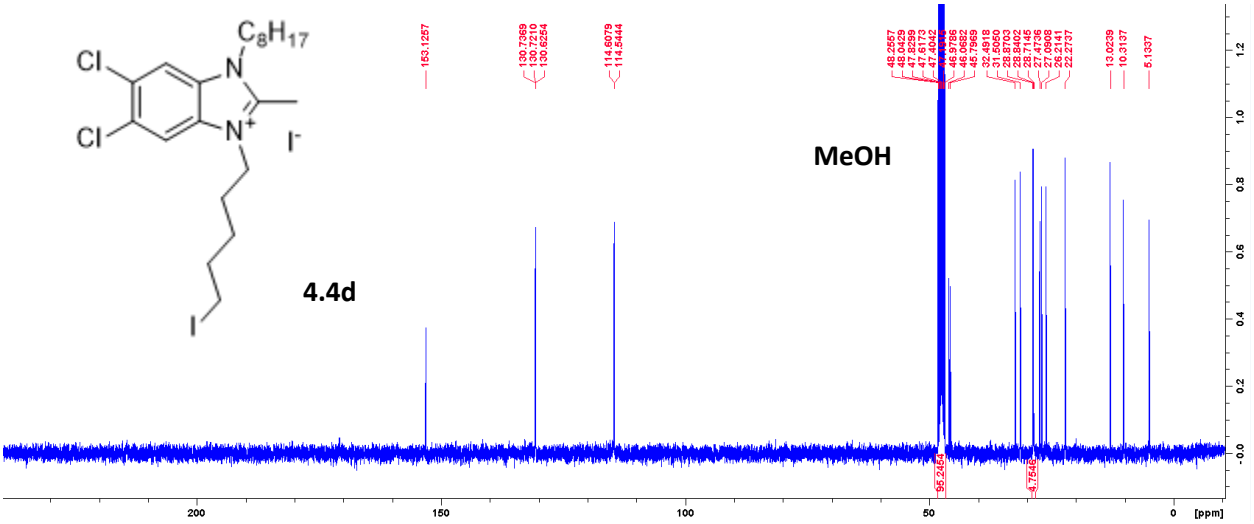
153.1257
130.7369
130.7210
130.6254
114.6079
114.5444
48.2457
48.2429
47.8299
47.6173
47.4042
46.9786
46.0682
45.7968
45.6493
31.5060
28.8703
28.8442
28.7746
27.4736
27.0908
26.2141
22.2737
13.0239
10.3137
5.1337
95.2454
5.7545
MeOH
4.4d
200
150
100
50
0
[ppm]

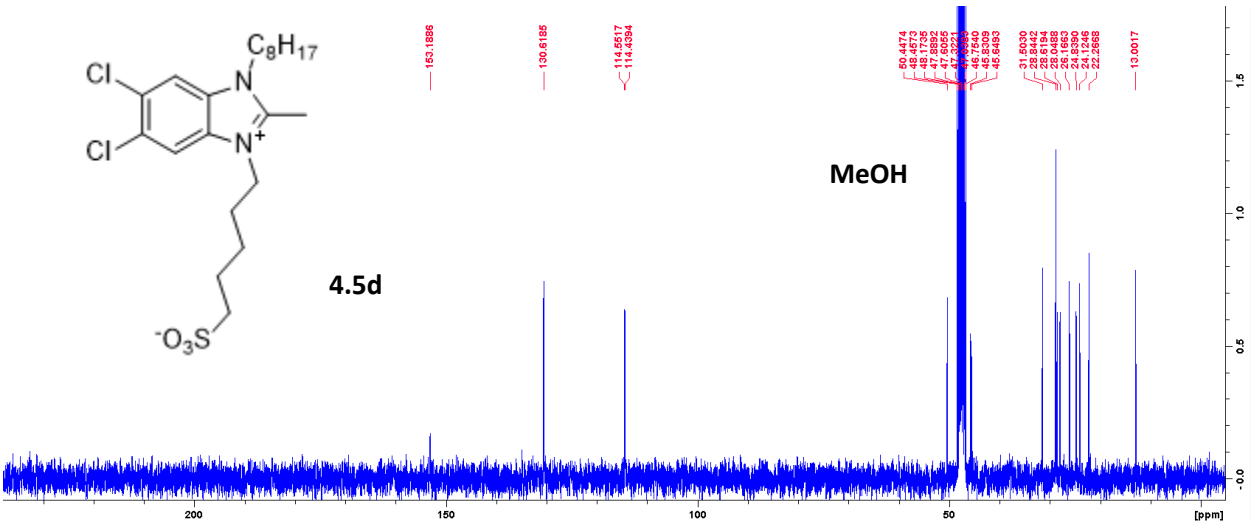
153.1886
130.6188
114.5517
114.4394
50.4474
48.4573
48.1735
47.8892
47.6051
47.3221
46.7540
46.4699
45.6493
31.5030
28.8442
28.8414
28.6484
26.1663
24.8390
22.7446
22.2668
13.0017
MeOH
4.5d
200
150
100
50
[ppm]

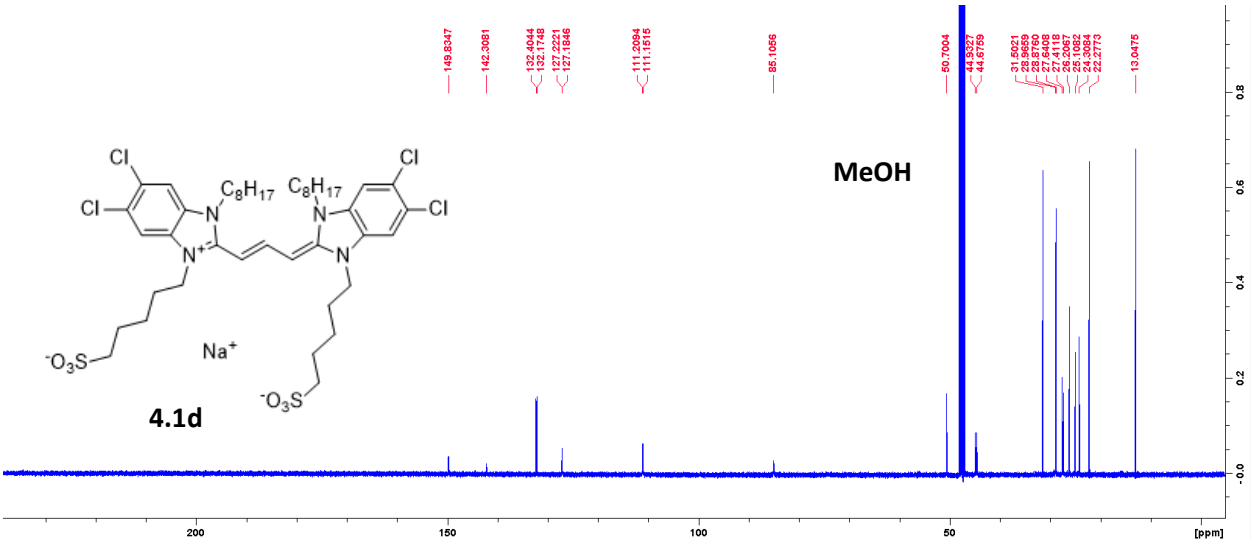
MeOH
4.1d
Cl
Cl
C_8H_{17}
N
N^+
^-O_3S
Na^+
149.8347
142.3081
132.4044
132.1748
127.2221
127.1946
111.2094
111.1515
85.1056
50.7004
44.9227
44.6769
31.6021
29.9659
28.8760
27.6408
27.4115
26.2067
25.1082
24.3094
22.2713
13.0475
200
150
100
50
[ppm]

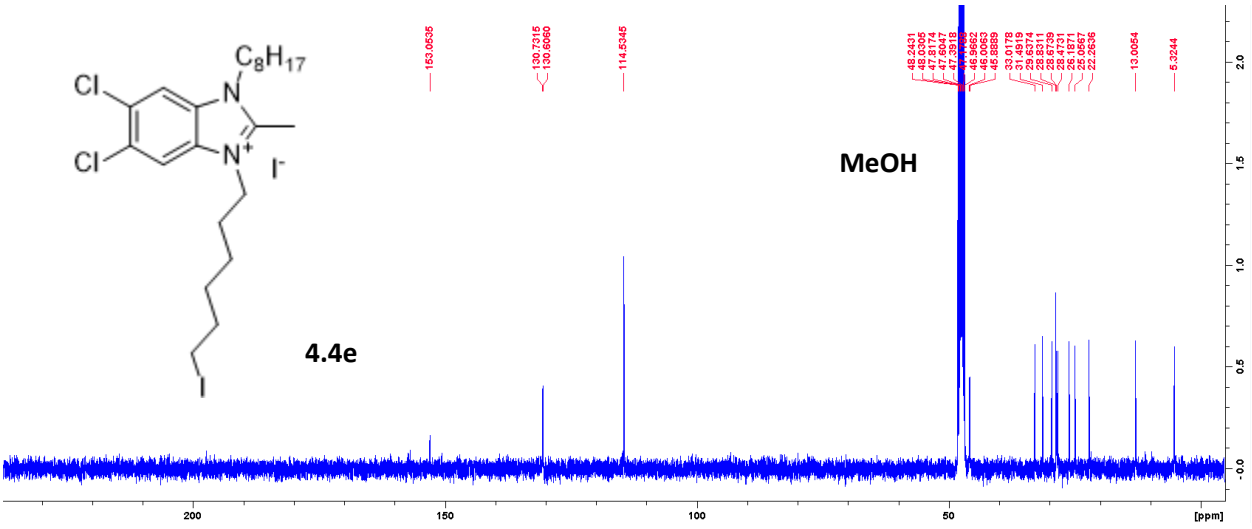
MeOH
4.4e
Cl
Cl
C_8H_{17}
N
N^+
I^-
153.0536
130.7315
130.6060
114.5345
48.2431
48.0305
47.8174
47.6043
47.3918
46.0952
45.8889
33.0178
31.4819
29.6774
28.8331
28.6739
28.4731
28.2727
25.0567
22.2636
13.0054
5.3244
200
150
100
50
[ppm]

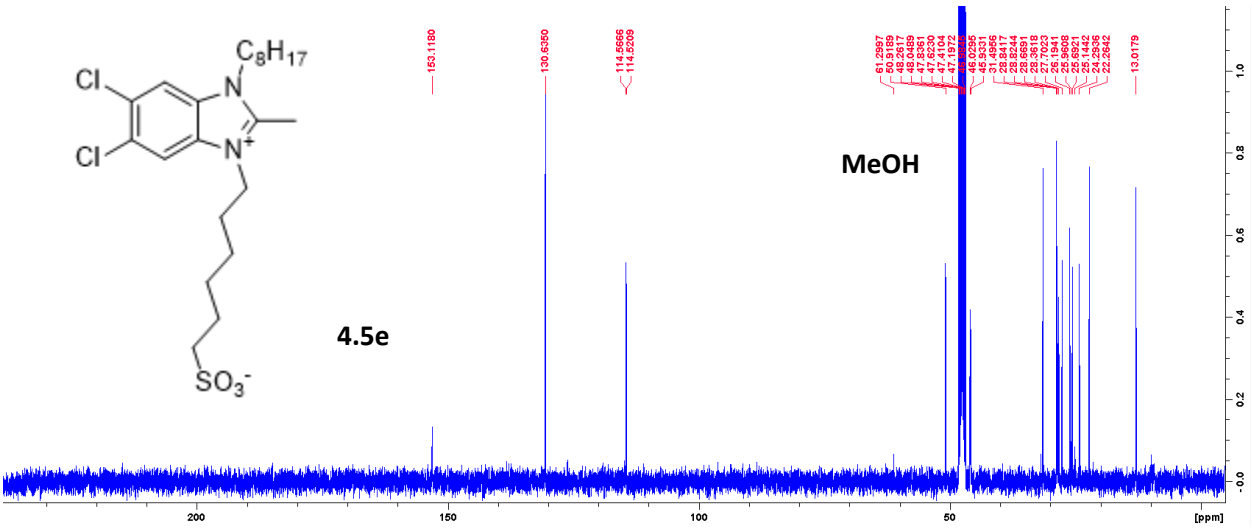
MeOH
4.5e
Cl
Cl
C_8H_{17}
N
N^+
SO_3^-
153.1180
130.6350
114.5666
114.5209
61.2997
49.2179
48.2417
48.0489
47.8361
47.6230
47.4104
47.1972
45.5331
31.4956
28.8441
28.6691
28.3618
27.1923
25.9608
25.6921
25.4240
24.2936
22.2642
13.0179
200
150
100
50
[ppm]

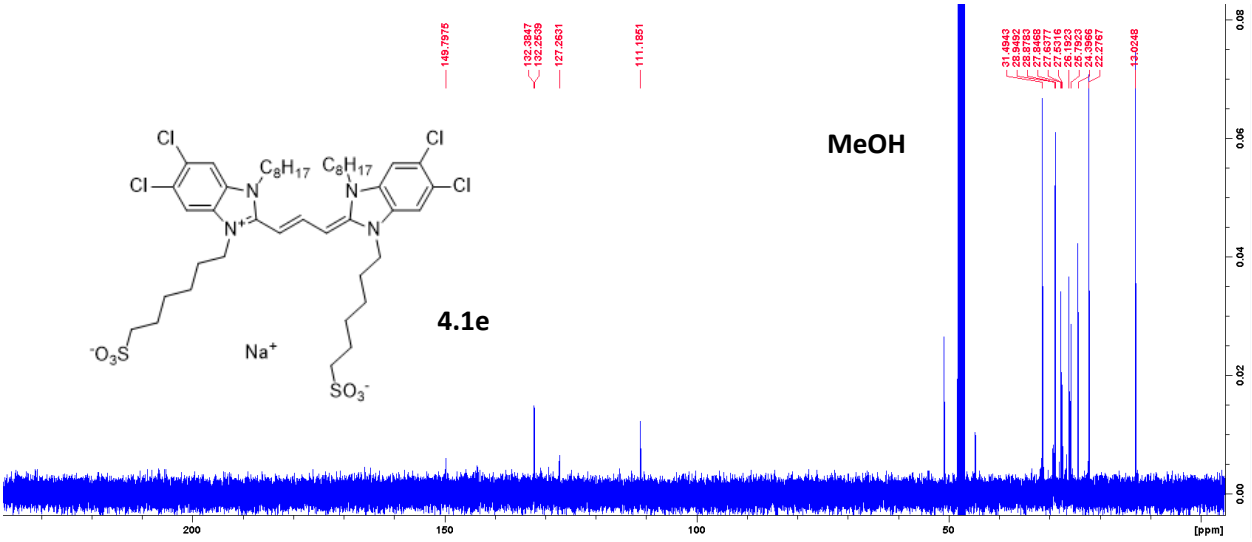
MeOH
4.1e
149.7975
132.3847
132.2539
127.2631
111.1851
31.4943
28.8452
28.8152
27.8468
27.6377
27.5116
25.1913
25.7923
24.3966
22.2767
13.0248
200
150
100
50
[ppm]

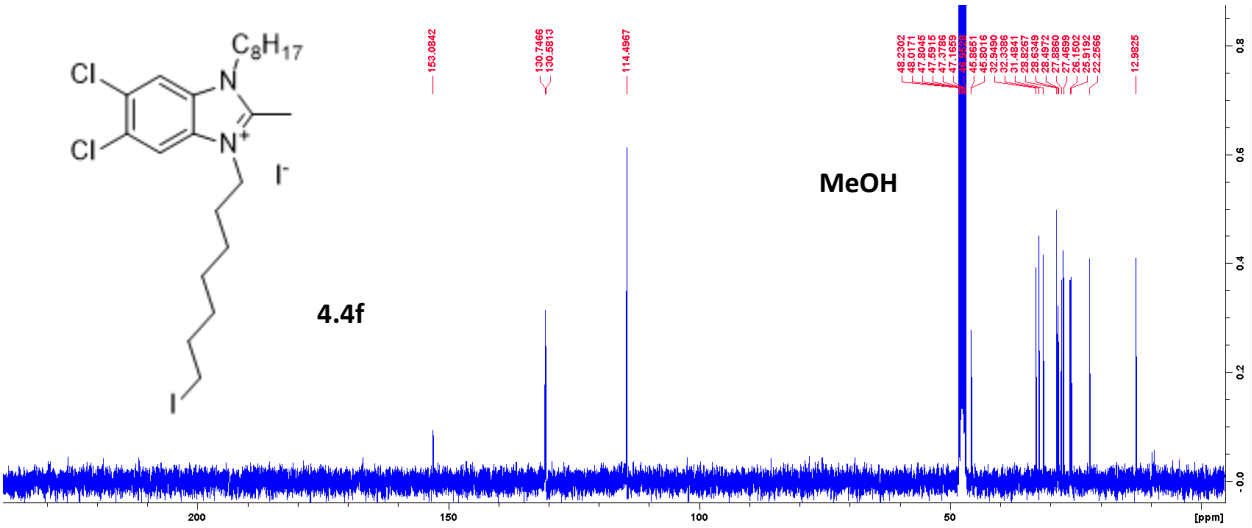
MeOH
4.4f
153.0842
130.7466
130.5813
114.4967
48.2302
48.0171
47.8045
47.5919
47.3793
47.1659
45.8016
32.9490
32.3386
31.4841
28.8267
28.6349
28.4972
28.3650
27.4699
25.1602
25.9182
22.2956
12.9825
200
150
100
50
[ppm]

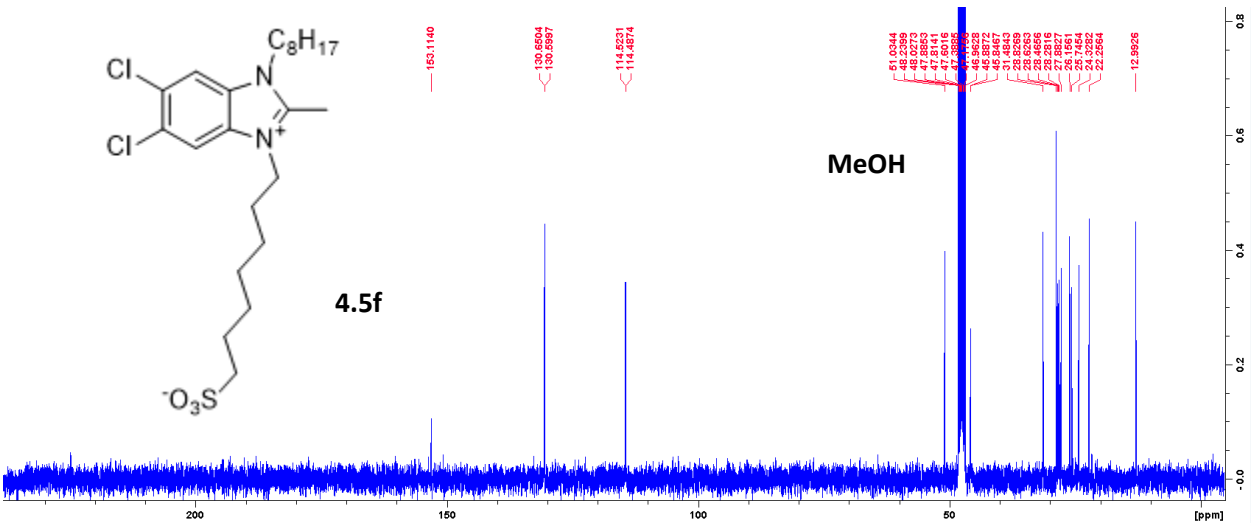
MeOH
4.5f
153.1140
130.6504
130.5997
114.5231
114.4874
51.0344
48.2302
48.0279
47.8853
47.8141
47.6015
47.3888
46.9628
45.8672
45.8467
31.4843
28.8259
28.6350
28.4656
28.2816
27.4521
25.1561
25.7454
24.3282
22.2564
12.9926
200
150
100
50
[ppm]

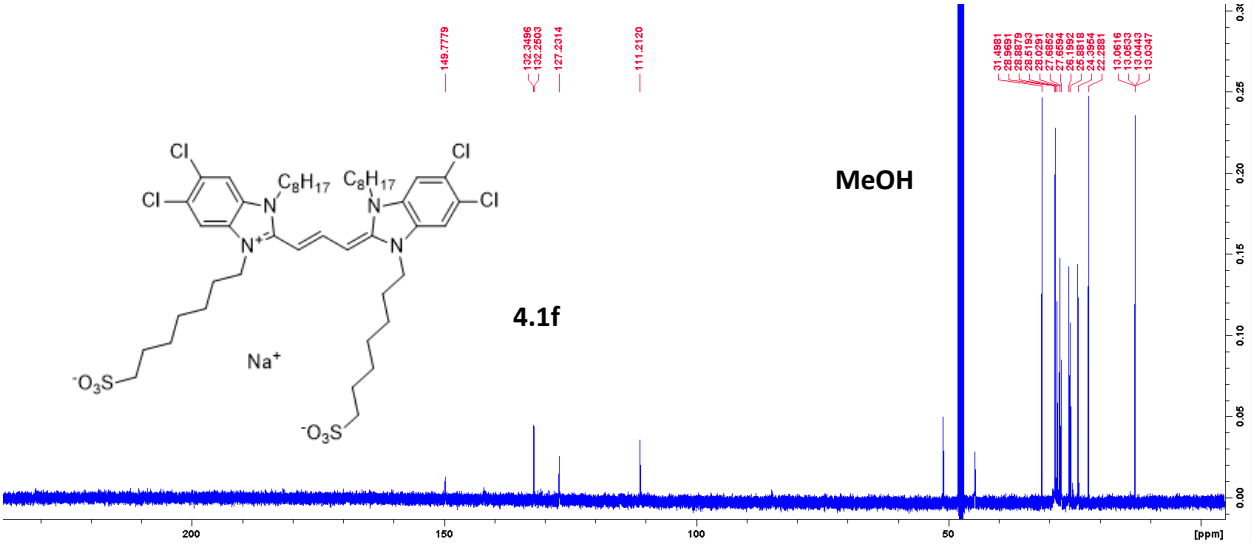
MeOH
4.1f
Cl
Cl
C_8H_{17}
C_8H_{17}
Cl
Cl
N
N
N^+
N
^-O_3S
Na^+
^-O_3S
149.7779
132.2486
122.2930
127.2314
111.2120
31.4981
29.9691
28.8879
28.6153
28.0291
27.6852
27.6594
25.8818
24.3954
22.2881
13.0616
13.0533
13.0443
13.0347
200
150
100
50
[ppm]

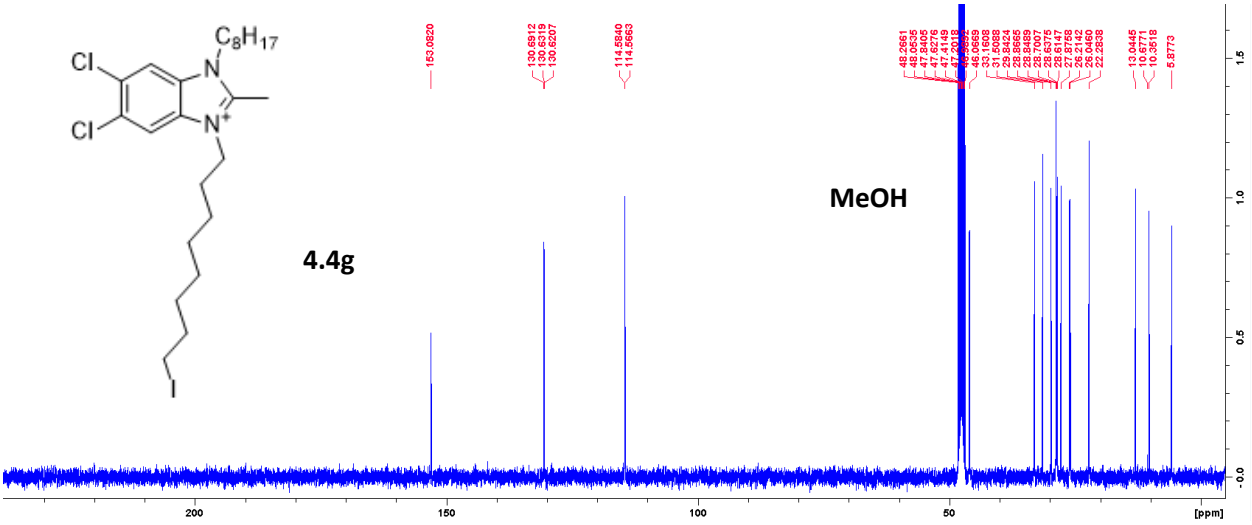
MeOH
4.4g
Cl
Cl
C_8H_{17}
N
N^+
I
153.0820
130.6912
130.6319
130.5207
114.5840
114.5663
48.2661
48.0535
47.8405
47.6276
47.4146
47.2018
45.9689
45.7560
31.5088
29.8424
28.8865
28.8669
28.7007
28.6375
28.6157
28.5749
26.2142
26.0460
22.2808
13.0445
10.8271
10.7518
5.8773
200
150
100
50
[ppm]

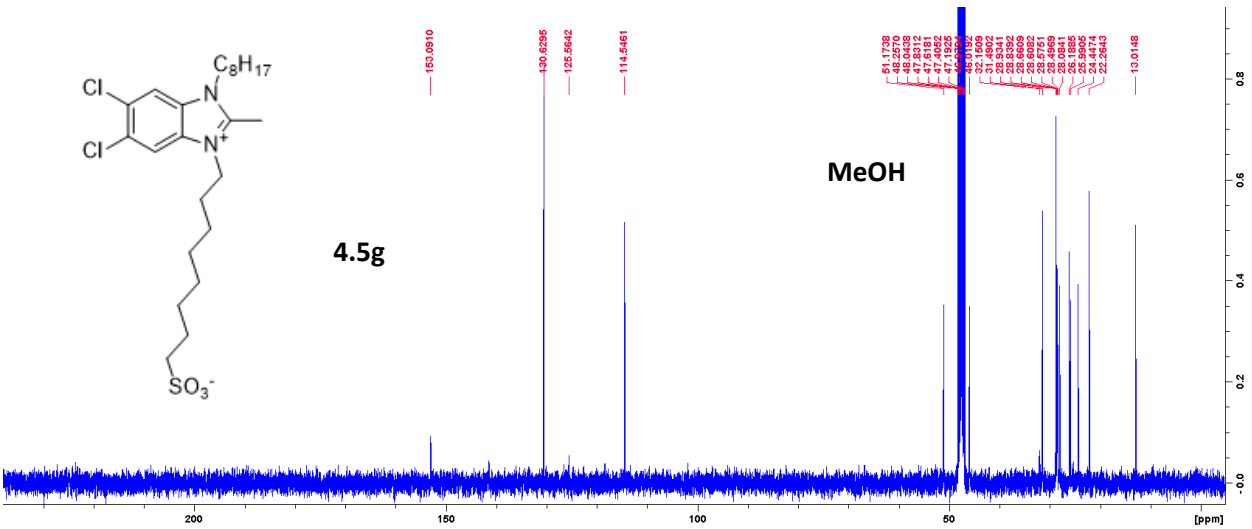
MeOH
4.5g
Cl
Cl
C_8H_{17}
N
N^+
SO_3^-
150.0910
130.6298
125.5642
114.5461
51.1738
48.2570
48.0438
47.8307
47.6191
47.4052
47.1925
46.9792
32.1509
31.4902
29.8341
28.8392
28.6609
28.6392
28.5757
28.4969
28.0841
26.3985
26.1805
24.4474
22.2643
13.0148
200
150
100
50
[ppm]

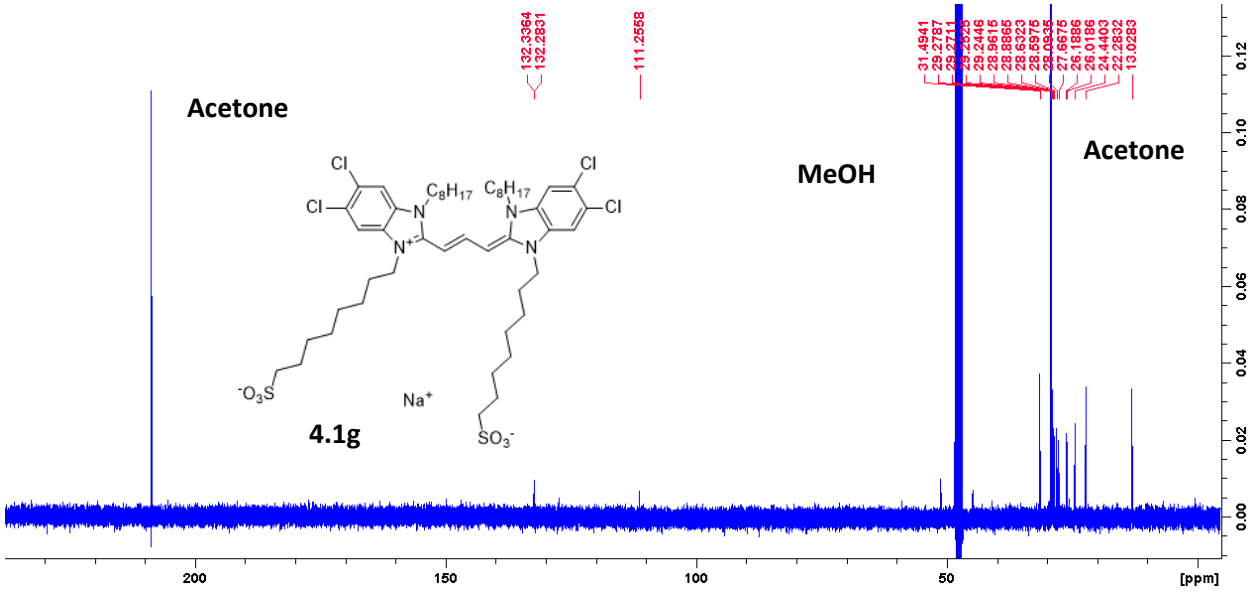
Acetone
MeOH
Acetone
4.1g
132.3364
132.2831
111.2558
31.4941
29.2787
29.2711
29.2526
29.2446
28.9615
28.8865
28.6323
28.5975
28.0535
27.6675
26.1886
26.0186
24.4403
22.2832
13.0283
200
150
100
50
[ppm]

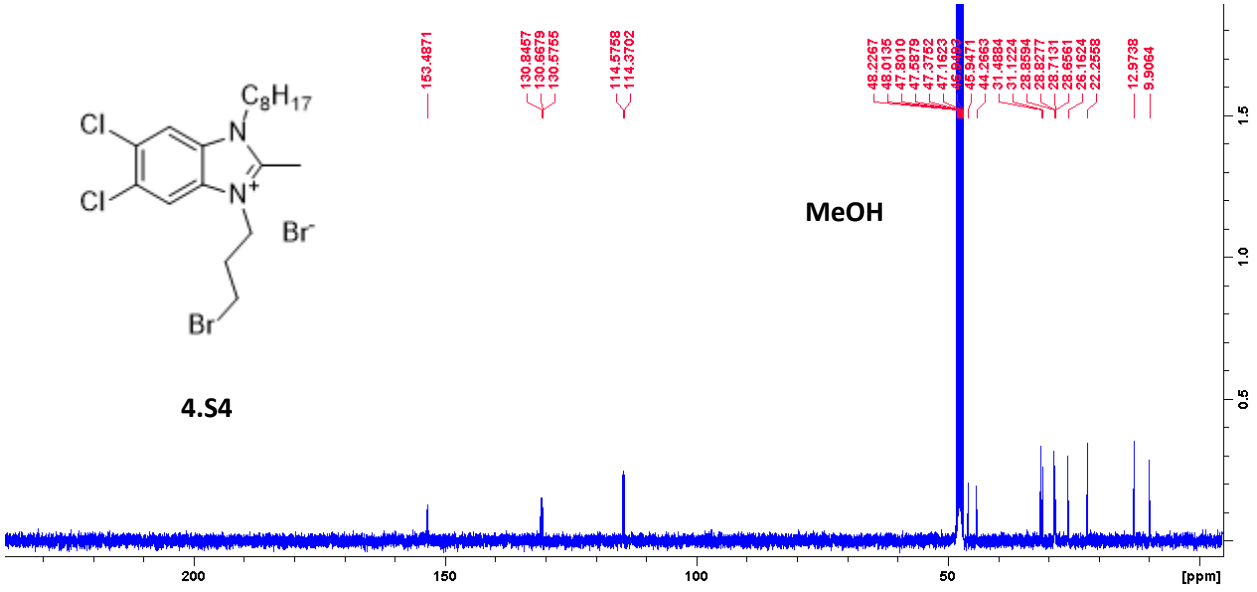
4.S4
MeOH
153.4871
130.8457
130.6679
130.5755
114.5768
114.3702
48.2267
48.0135
47.8010
47.5879
47.3752
47.1623
45.9471
44.2663
31.4884
31.1224
28.8594
28.8277
28.7131
28.6561
26.1624
22.2558
12.9738
9.9064
200
150
100
50
[ppm]

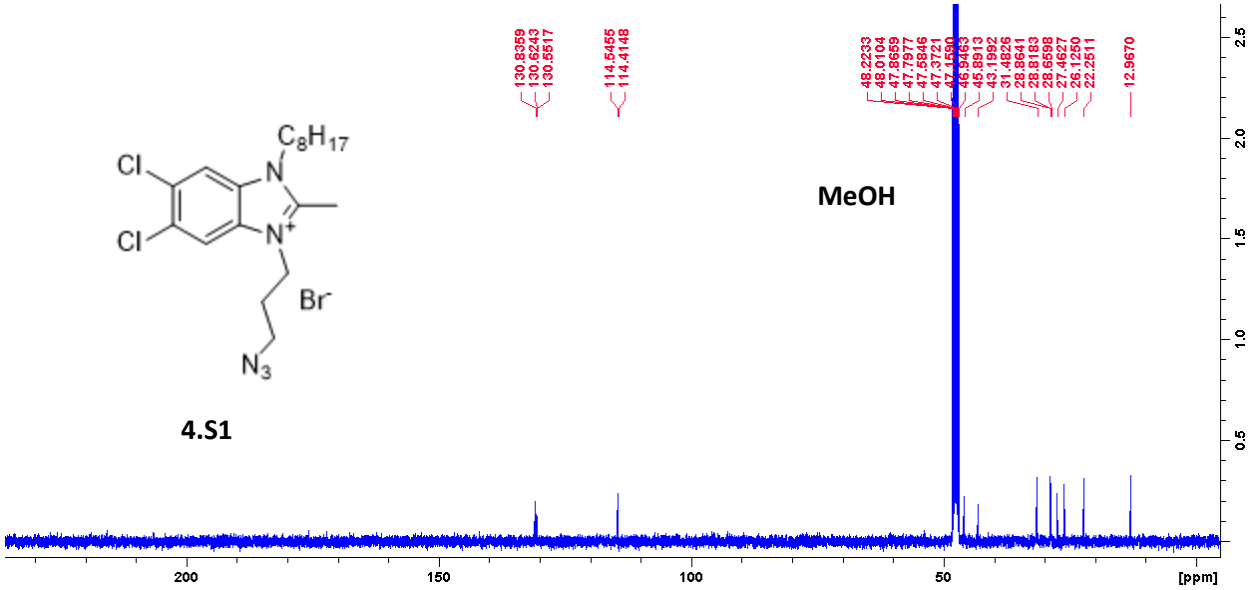
130.8359
130.6243
130.5517
114.5455
114.4148
48.2233
48.0104
47.8659
47.7977
47.5846
47.3721
47.1590
46.9463
45.8913
43.1992
31.4826
28.8641
28.8183
28.6598
27.4627
26.1250
22.2611
12.9670
MeOH
Cl
Cl
C_8H_{17}
N
N+
Br-
N_3
200
150
100
50
[ppm]
0.5
1.0
1.5
2.0
2.5

4.S1

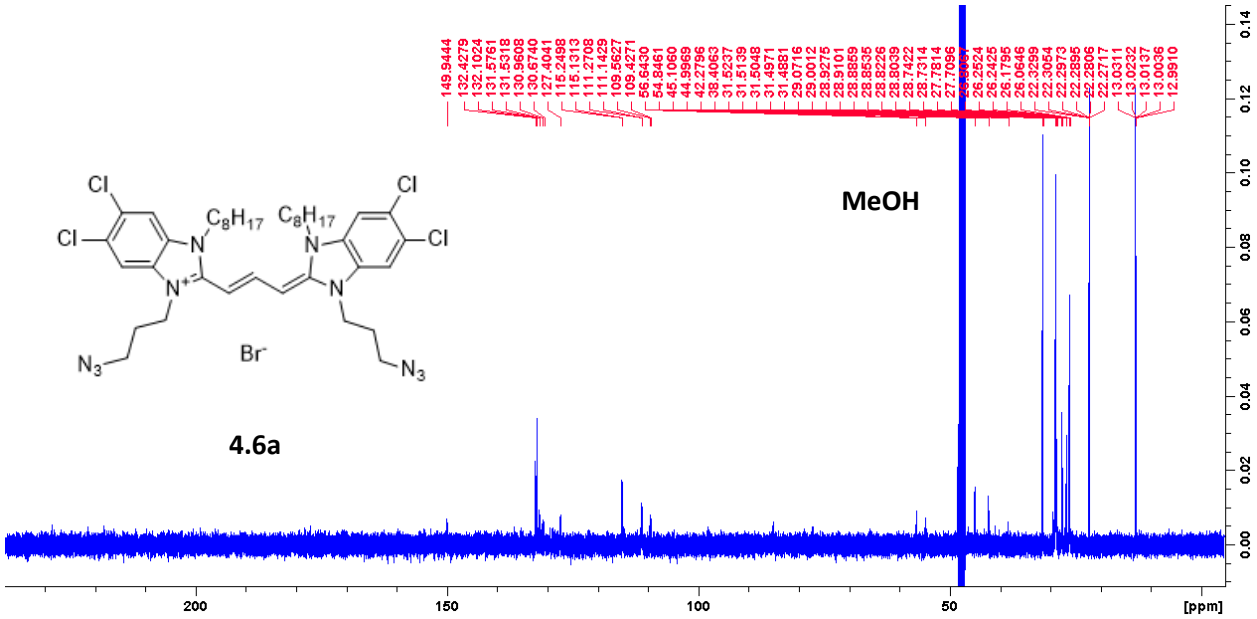
149.9444
132.4279
132.1024
131.5761
131.5318
130.9608
130.6740
127.4041
115.2498
115.1313
111.2708
111.1429
109.5627
109.4271
56.6430
54.8461
45.1060
44.9969
42.2796
38.4063
31.5237
31.5139
31.5048
31.4971
31.4881
29.0716
29.0012
28.9275
28.9101
28.8859
28.8536
28.8226
28.8039
28.7422
28.7314
27.7814
27.7096
26.2524
26.2425
26.1796
26.0646
22.3299
22.3054
22.2973
22.2896
22.2806
22.2717
13.0311
13.0232
13.0137
13.0036
12.9910
MeOH
Cl
Cl
C_8H_{17}
C_8H_{17}
N
N+
Br-
N_3
200
150
100
50
[ppm]
0.00
0.02
0.04
0.06
0.08
0.10
0.12
0.14

4.6a

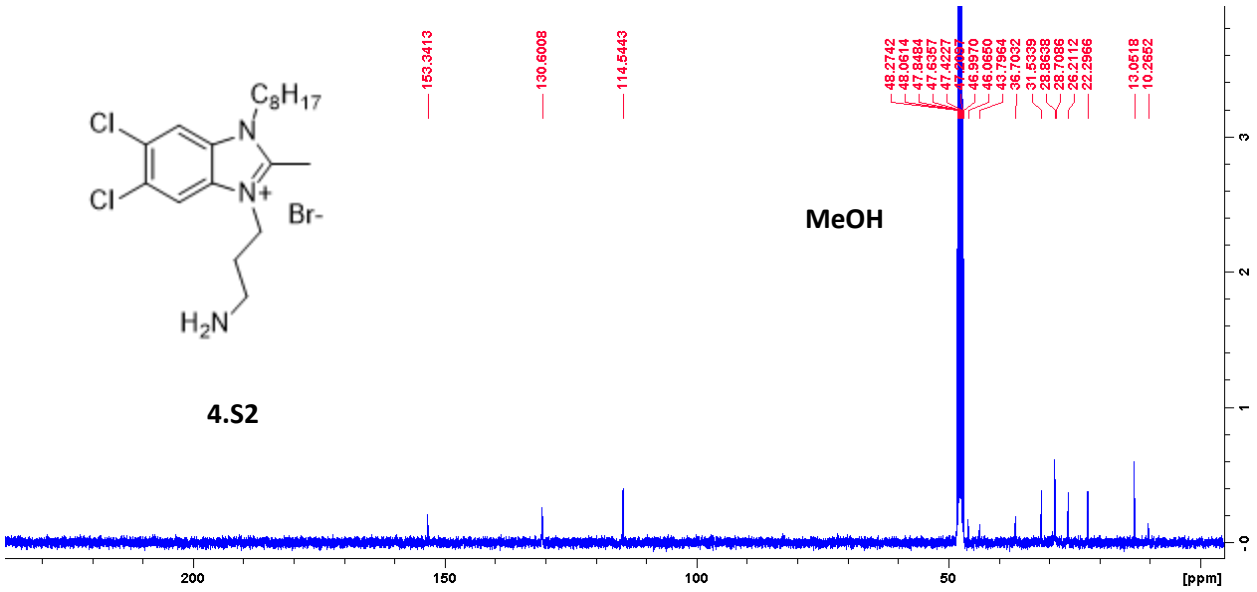
153.3413
130.6008
114.5443
48.2742
48.0614
47.8484
47.6357
47.4227
46.9970
46.0650
43.7964
36.7032
31.5339
28.8638
28.7066
26.2112
22.2966
13.0518
10.2662
MeOH
Cl
Cl
C_8H_{17}
N
N+
Br-
H_2N
200
150
100
50
[ppm]

4.S2

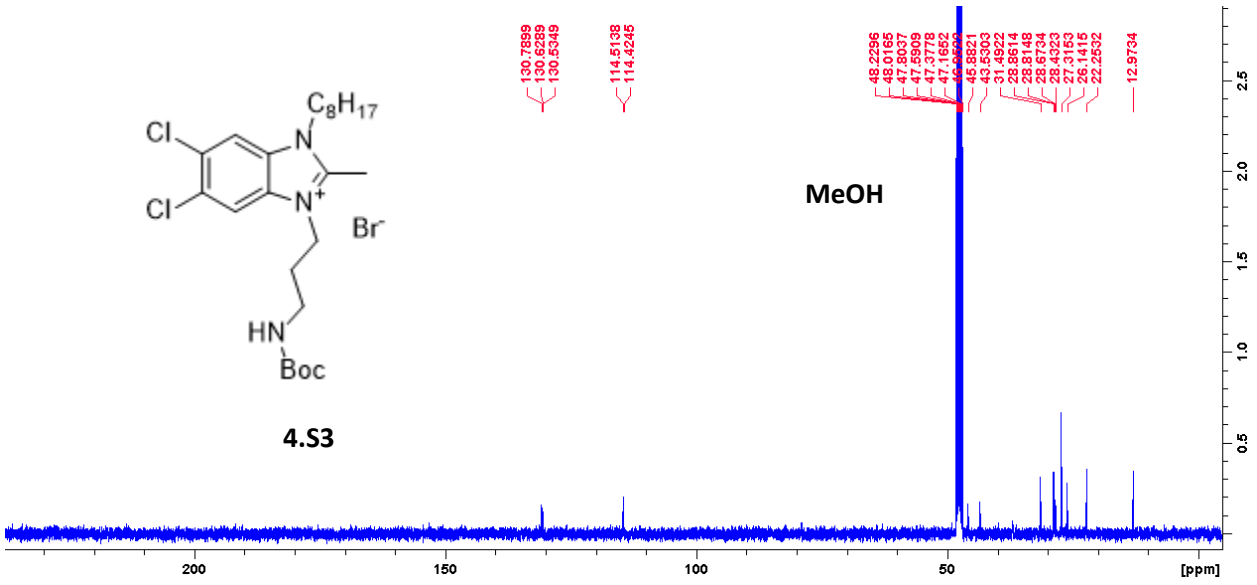
130.7899
130.6289
130.5349
114.5138
114.4245
48.2296
48.0165
47.8037
47.5909
47.3778
47.1652
45.8821
43.5303
31.4922
28.8614
28.8148
28.6734
28.4323
27.3153
26.1415
22.2532
12.9734
MeOH
Cl
Cl
C_8H_{17}
N
N+
Br-
HN
Boc
200
150
100
50
[ppm]

4.S3

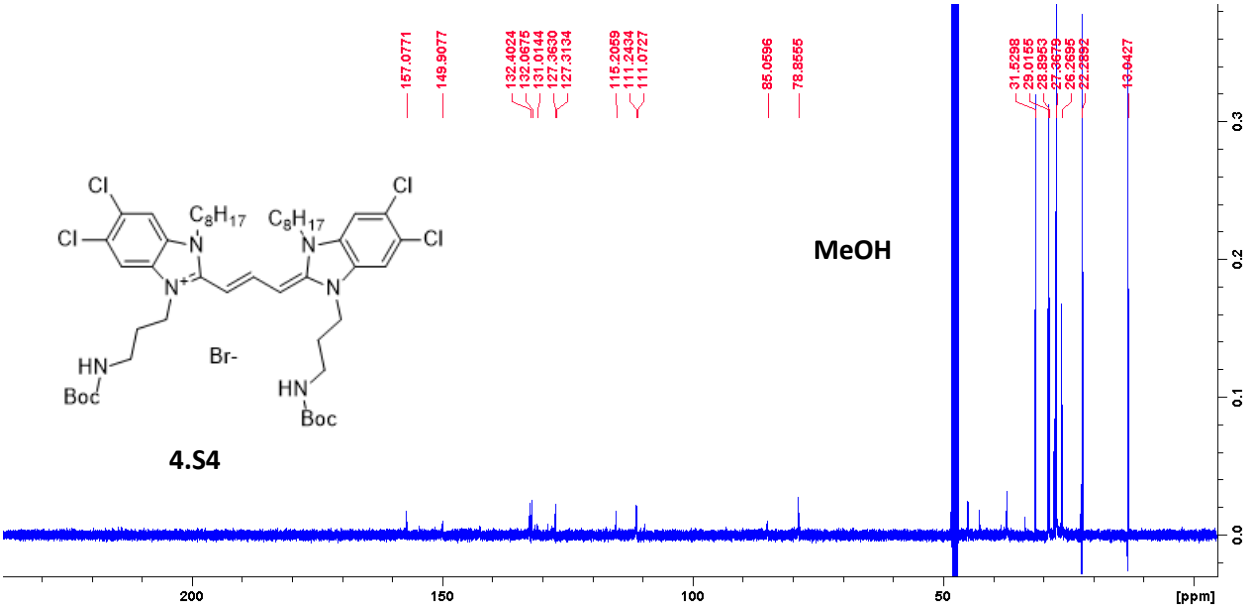
157.0771
149.9077
132.4024
132.0675
131.0144
127.3630
127.3134
115.2059
111.2434
111.0727
85.0596
78.8555
31.5298
29.0155
28.8953
27.3679
26.2656
22.2892
13.0427
MeOH
Cl
Cl
C_8H_{17}
C_8H_{17}
Cl
Cl
N
N
N+
N
HN
Boc
Br-
HN
Boc
4.S4
0.3
0.2
0.1
0.0
200
150
100
50
[ppm]

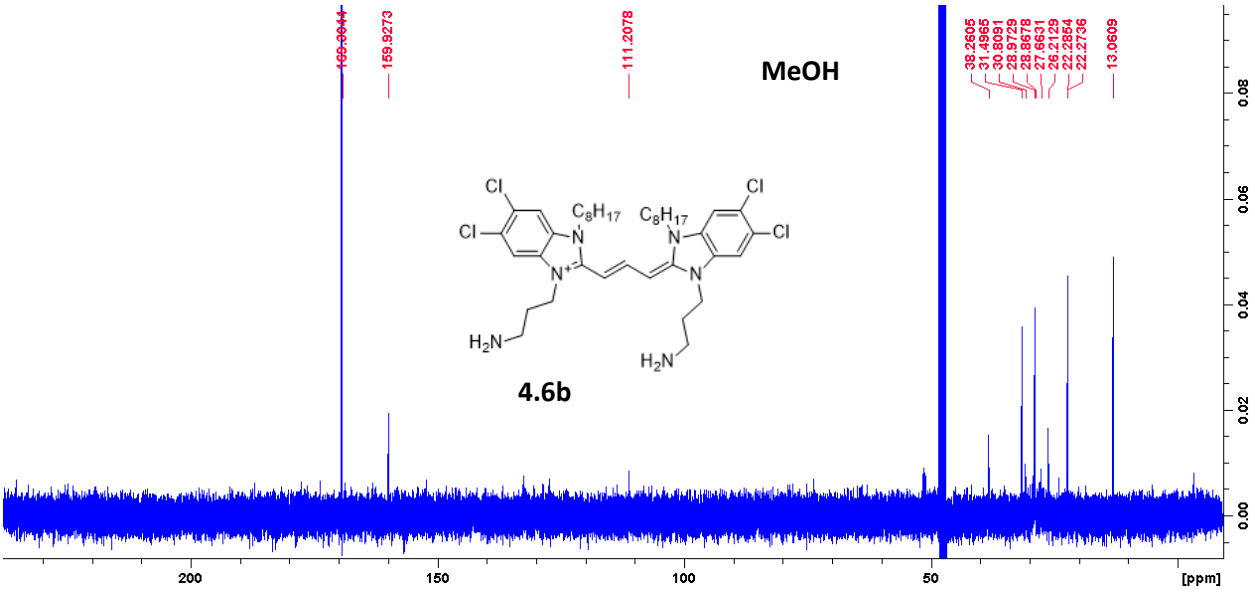
159.9273
111.2078
MeOH
38.2605
31.4965
30.8091
28.9729
28.8678
27.6631
26.2129
22.2854
22.2736
13.0609
Cl
Cl
C_8H_{17}
C_8H_{17}
Cl
Cl
N
N
N+
N
H_2N
H_2N
4.6b
0.08
0.06
0.04
0.02
0.00
200
150
100
50
[ppm]

Chapter 5

Understanding the Effects of Steric Bulk on Molecular Aggregate Self-Assembly and Photophysics

Adapted from "Bailey, A. D.[†]; Williams, J.A.[†]; Pengshung, M.; Garcia, C.A.; Deshmukh, A.P.; Cao, J.; Li, B.Y.; Bradbury, N.C.; Neuhauser, D.; Chuang, C.; Sletten, E. M.; Caram, J. R. Structural Engineering of Cyanine Dyes to Access Highly Redshifted J-Aggregates. *In preparation*." [†]Co-first authors.

One of the standing issues with chromophore molecular aggregates is the lack of knowledge surrounding structure-property relationships between a monomer dye's structure and its resulting J-aggregates. Here, we address this void by asking how the steric bulk of a dye can change the way it self-assembles. To do this, we synthesized four new heptamethine dyes that were substituted at the 4' position, meaning that there would be minimal changes to solubility or electronics with the addition of sterically bulky groups. Our pendant groups (4' substituents) ranged from a phenyl ring to 3,5-ditertbutylphenyl group. We ultimately found that these dyes form a minimum of three unique J-aggregates each, all of which have 2D sheetlike morphology (with the exception of one tubular aggregate). In studying these materials, we found that steric bulk is successful in redshifting the aggregate absorption, but stabilizes different morphological phases of aggregates. We also propose several experiments, such as AFM and dynamic light scattering for differentiating the unique morphologies.

5.01. Abstract

Molecular design of 2D/tubular excitonic aggregates would enable access to extraordinary photophysical properties via control over supramolecular structure. Here, we synthesize four heptamethine cyanines that enable a rational investigation of the role of steric bulk on aggregate self-assembly, morphology and photophysics. Despite near identical monomer photophysical properties, minute changes to structure and solvation lead to extreme differences in resultant J-aggregate morphology and photophysics. We find that additional steric bulk not only redshifts aggregate absorption, it alters the kinetics/thermodynamics of self-assembly, yielding a variety of connected morphological supramolecular phases. We employ cryo-electron and atomic force microscopy, dynamic light scattering, temperature dependent photophysics and computational screening to reveal 3-4 2D/tubular J-aggregates all derived from highly similar benzothiazole heptamethine cyanine chromophores. Differentiating and tuning each unique morphology demonstrates approaches to structurally engineer highly redshifted 2D molecular aggregates through synthetic design and achieve supramolecular control over photophysical properties.

5.02. Motivation for investigating the effect of steric bulk on J-aggregation

Cyanine dye J-aggregates were discovered in the early 20th century and have since become an emergent class of optical materials known for their extraordinary absorption cross-section, increased radiative rates, and redshifted photophysical properties.[99,100] Although J-aggregates of many different conjugated macrocycles (e.g. perylene bisimides, BODIPYs, or anthracene derivatives) are known, cyanine dyes display unique J-aggregate properties due to their near/shortwave infrared wavelength tunability, high transition dipole moment, water solubility, and modular/well characterized synthesis enabling facile customization.[10–12] Recent advances have

employed J-aggregates in applications of solar energy harvesting, bioimaging and as platforms for polaritonics.[39,101] Therefore, elucidating supramolecular cyanine architectures represents a foundational goal of realizing control over photonic properties through molecular design.

Cyanine chromophores tend to assemble in water to form extended 2D and tubular structures. These morphologies result in more complex excitonic properties, tuned via short- and long-range order and coupling.[14,59,62,102] 2D aggregates are unique as they often display large redshifts (~2000-3000 cm^{-1}), increased exciton delocalization, bigger changes in radiative rates, narrower absorption linewidths and longer-range energy transfer compared to their one dimensional counterparts. These enhanced properties arise from the high transition dipole moments and denser packing availed by 2D and tubular chromophore arrangements. Cyanine dyes also allow for aggregate design in the near- and shortwave infrared (700-1000 and 1000-2000 nm, respectively), where enhanced tissue penetration and decreased Rayleigh scattering adds to their potential application space. General design principles to achieve emissive infrared J-aggregates would enable researchers with a new strategy for generating optically active matter.

Despite the many advantages of water-soluble chromophore aggregates, there have been few examples of systematic structure-property relationships between dye structure and their resulting supramolecular aggregate.[25,28,103,104] This lack of control has hindered the development of cyanine dye aggregates for specific spectral windows and applications. Previous work has shown that the length of hydrophilic and hydrophobic substituents plays a major role in the self-assembly of J-aggregates derived from benzimidazole dyes.[27,92,93] These alterations to the monomer structure dictate the delicate balance of intermolecular forces which lead to molecular packing in different geometries; namely, sheetlike aggregates, double and single-walled nanotubes, bundles of tubes, and ribbonlike aggregates.[36,49,90,105] Additionally, it has been shown preliminarily that the optical

properties of these materials can be fine-tuned based on a bottom-up approach of engineering the dye monomer; by forcing a larger dye-to-dye slip, one can tune the relative energy of the excitonic bright state.[14] However, this prior study utilized somewhat different chromophore scaffolds, limiting the comparability between structures. Ultimately, both the dye-to-dye packing and overall aggregate disorder play an important role in determining the optical properties of the resulting materials.

Here, we investigate how J-aggregate photophysics of benzothiazole cyanine dyes are affected by adding steric bulk at the central position (4' substituent) of the dye, shown in Figure 5.01A. The 4' position was specifically chosen to minimize any changes in solubility or perturbations to the electronic states of the dye monomer. We hypothesize that adding steric bulk results in changes to the shift between dyes, which in turn alters the coupling among chromophores. To accomplish this, we first synthesize a series of dyes that vary in the steric bulk of their pendant group (4' substitution, Figure 5.01B). We selected four pendant groups for this study: phenyl (**5.1a**), 3,5-dimethylphenyl (**5.1b**), 3,5-diethylphenyl (**5.1c**), and 3,5-ditertbutylphenyl (**5.1d**). We next screened the aggregate formation of each dye and observed a trend between steric bulk and aggregate redshift (Figure 5.01C).

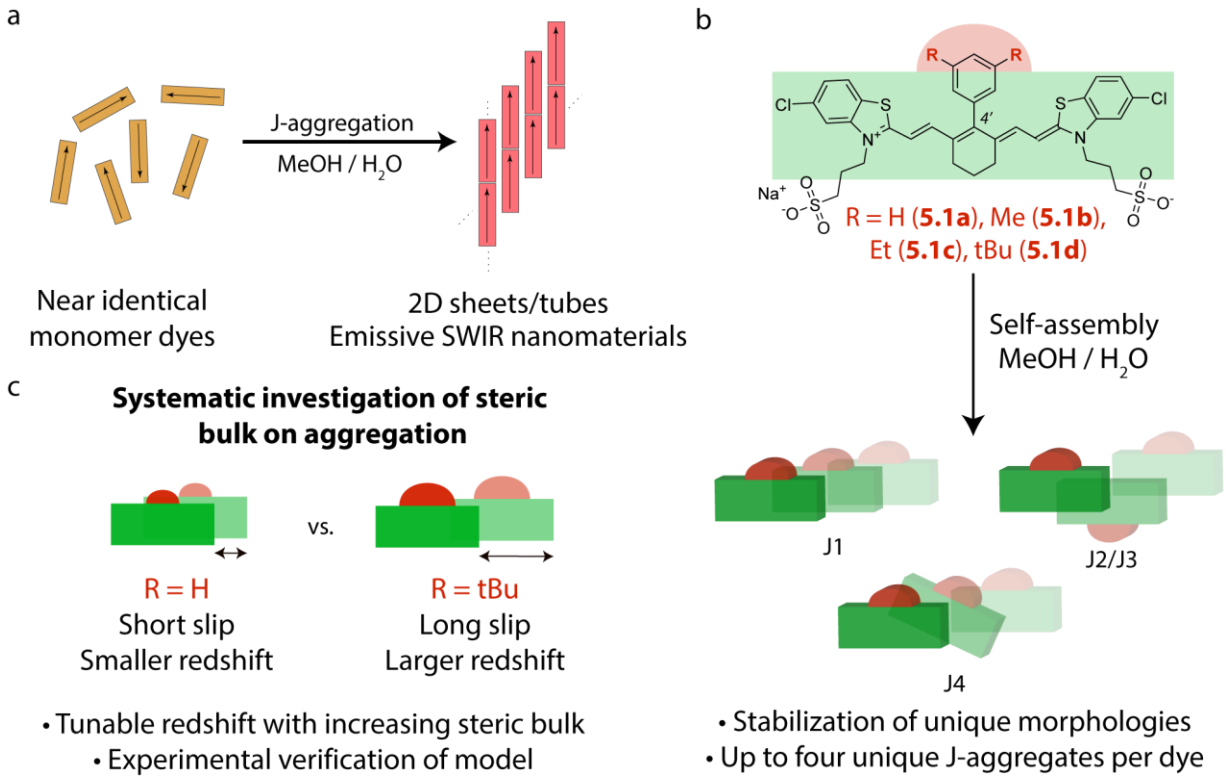

Figure 5.01. Cartoon showing J-aggregation and the effects of steric bulk on J-aggregation.

We found that the 4'-substituted dye monomers have extremely rich aggregation behavior, with each dye forming a minimum of three unique J-aggregate morphologies. This abundance of morphological phases is highly unusual among cyanine dyes, for which only 1-2 unique J-aggregates are identified.

Upon isolating the unique aggregates, we conducted cryo-electron microscopy to determine the nanoscale mesostructures and found our aggregates to show predominantly sheetlike appearance, with the exception of one tubular species. Additional studies such as dynamic light scattering (DLS), atomic force microscopy (AFM), linear dichroism (LD), kinetics experiments and computation allowed us to further elucidate the complex aggregation behavior of these compounds, and hypothesize on their underlying aggregation structure, and the kinetics and

thermodynamics that underlie extended tubular/sheet aggregation. Combining all of these data furthers our understanding of how distinct morphological phases can occur during supramolecular organization and how chromophore structure informs the self-assembly that ultimately dictates J-aggregate photophysics. Ultimately, fully understanding the bridge between a dye monomer's structure and its resulting J-aggregate's optical properties will enable the broad development of dynamic optical materials.

5.03. Synthesis of sterically bulky heptamethine cyanines

Modular synthesis of dye monomers **5.1a-d** began by functionalizing a traditional heptamethine electrophile **5.2** (Sigma Aldrich) with a boronic acid bearing the various steric substituents (**5.3a-d**). This key Suzuki reaction yielded electrophilic linkers with varying steric bulk **5.4a-d**, which we were reacted with heterocycle **5** in the presence of base to yield **5.1a-d**. The benzothiazole heterocycle **5.5** was prepared by adaptation from a literature precedent.[25] Our procedure provided dyes **5.1a-d** in varying yields of 9-54% as shiny, green solids. Unsurprisingly, we found that the monomers all share near identical absorption and emission wavelengths, as well as molar absorptivity (ε) and fluorescence quantum yield (Φ_F). The synthesis and monomer photophysical characterization are detailed in Figure 5.02. Full synthetic procedures are provided in subchapter 5.10.

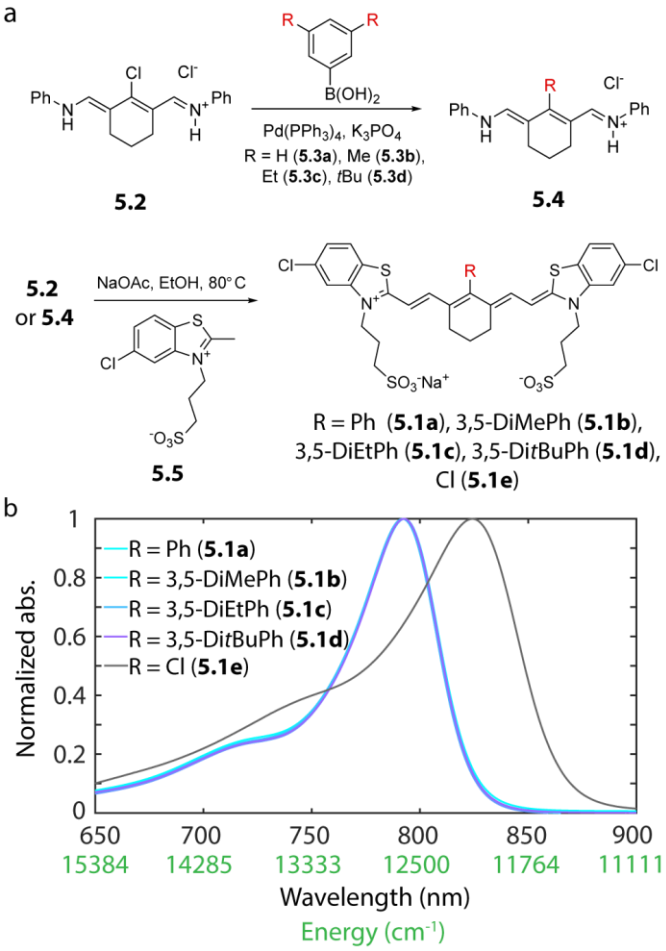

c

Dye	λ_{abs} (nm)	λ_{em} (nm)	ε (x 10^5 $M^{-1}cm^{-1}$)	Φ_F (%)
5.1a	798	813	1.1 ± 0.1	5.2 ± 0.2
5.1b	798	814	2.0 ± 0.1	6.6 ± 0.4
5.1c	798	812	2.5 ± 0.02	5.1 ± 0.2
5.1d	798	813	0.63 ± 0.06	6.7 ± 0.6
5.1e	828	834	0.15 ± 0.01	0.57 ± 0.1

Figure 5.02. Synthesis and monomer photophysics of dyes **5.1a-d**. a) Synthesis of monomer dyes. b) Absorption spectra of dyes **5.1a-d** in methanol. c) Photophysical data including absorption coefficient and quantum yield of dyes **5.1a-d**. Dye synthesis performed by Monica Pengshung and Cesar Garcia.

5.04. Absorption screening of J-aggregates

After synthesizing the dye monomers, we surveyed the aggregation landscape of each dye by preparing 0.1 mM dye solutions with methanol/water composition that varied from 0 to 40% (v/v) in 5% increments. We noted that the aggregation of dyes **5.1a-d** also contains kinetically accessed intermediates, meaning that these methanol/water solutions needed to be screened at different timepoints to determine the full breadth of J-aggregate formation.

Through this screening, we found that the dyes form a minimum of three unique aggregates which can be isolated with some combination of methanol/water ratio, time, and temperature. Because of this, we enumerate the J-aggregates as J1, J2, J3, and J4 based on their physical characterizations and self-assembly conditions (*vide infra*). In short, J1 represents the aggregates formed at low (~5%) methanol and short times, J2 is a special case only forming from **5.1b** at 20% methanol, J3 is stable at higher (~30%) methanol, and J4 is the slower-forming product from J1 aggregates (~5% methanol) over extended times. Figure 5.3A shows an example of MeOH/H_2O screens for **5.1b** after 24 hours and Figure 5.3B shows different kinetic timepoints for a 5% MeOH/H_2O sample of **5.1b**. Figure 5.5C displays the normalized absorption of each isolated aggregate from dyes **5.1a-d.** Table 5.1 describes the assignment of J1-J4 aggregates based on spectroscopic and characterization conditions.

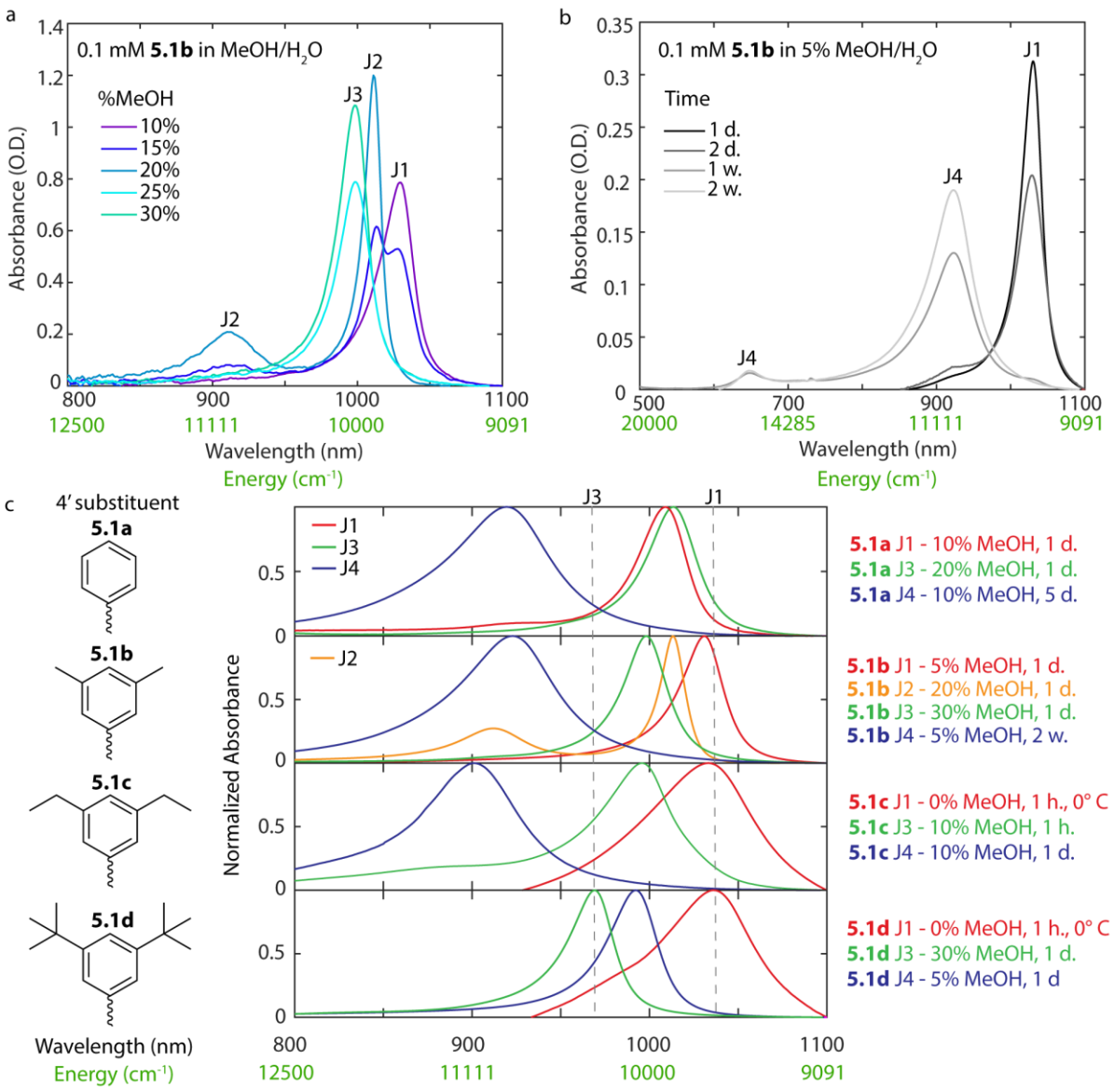

Figure 5.03. Absorption screening of **5.1a-d** J-aggregates. a) Absorption screening of 0.1 mM **5.1b** in different MeOH/H_2O composition solutions after 24 h. b) Kinetic absorption screening of 0.1 mM **5.1b** in 5% MeOH/H_2O. after different timepoints. c) Isolated aggregate absorption for J1, J2, J3, and J4 of **5.1a-d.**

Table 5.1. Structural information regarding J1-J4 aggregates of dyes **5.1a-d**.

Aggregate	Information
J1	Generally most redshifted, kinetically trapped, formed at low MeOH
J2	Formed only from **5.1b** at 20% MeOH, stable, tubular
J3	Formed at higher MeOH, stable, less redshifted than J1
J4	Generally most blueshifted, forms over extended times (weeks) from J1

Upon analyzing the optimized conditions for J1–J4 for all dyes (Figure 5.3A), we observed some intriguing relationships between structure and aggregate absorbance. For J1 aggregates, there is a clear trend in redshifting with steric bulk, while J3 shows blueshifting spectral features. There is no discernible trend between the J4 aggregates. J2 aggregate is only observed in the **5.1b** dye at 20% MeOH. Quantum yields (QY) of J1-J4 aggregates of **5.1b** varied from 0.02-0.05%, estimated via comparison to a well characterized heptamethine chromenylium dye.[106]

5.05. Computational screening and slip/redshift correlation

To quantify the effects of steric bulk on J-aggregate redshift, we employed a computational approach that allowed us to estimate the relative slip for a given 4' substitution. We employ density functional theory (DFT) method to optimize the ground state geometries of each dye (**5.1a-d**) in a dimer arrangement, then calculate energies of those dimers as they are slipped across each other from a distance of 1 to 7 Å. We found a trend that as steric bulk increased (i.e. from **5.1a** to **5.1d**), the slip that produces the lowest energy for the dimers increased, visualized in Figure 5.4A. Because previous reports have shown that the dye-to-dye slip increases with number of monomer units, we added 2 Å of slip to each estimate to compensate for the dimeric limit.[107] This allowed us to plot the redshift for J1 aggregates of **5.1a-d** as a function of their slip (steric bulk) in Figure 5.4B.

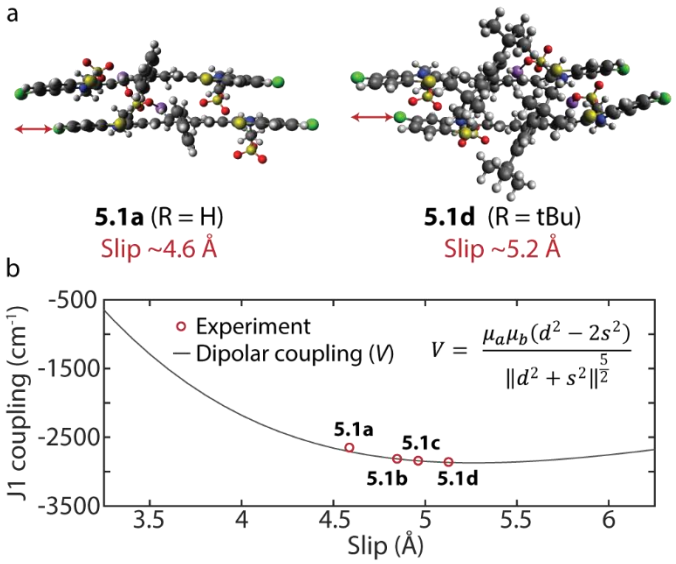

Figure 5.04. Effect of dye steric bulk (slip) on J-aggregate coupling. a) Optimized geometry of cyanine monomers **5.1a** and **5.1d**. b) Redshift vs. slip with dipolar coupling equation. Computations done by Barry Li.

5.06. Investigation of differences between morphological phases of J1-J3

Upon isolation of the distinct aggregate spectra for each dye, we performed cryo-electron microscopy to view the native morphologies of each aggregate, shown in Figure 5.05. The J1, J3, and J4 aggregates were all found to have sheetlike appearance. However, the J2 aggregate of **5.1b** was anomalous, consisting of micron-scale single-walled nanotubes. Figure 5.4 shows the electron microscopy for all aggregates of **5.1b** (J1, J2, J3, and J4). Additional characterizations of the tubes (such as linear dichroism, modeling, sample preparation, and cryo-EM of other dyes) are provided in subchapters 5.6-5.9.

Observing that the J1, J3, and J4 aggregates share a similar sheetlike morphology, implies that sheetlike aggregates can adopt distinct structures that vary in absorption energy by nearly 100 nm (~1,100 cm^{-1}). Traditional techniques for solving mesoscale structures, such as x-ray scattering,

are not useful here due to low periodic order and the lack of long-range symmetry elements preventing crystallization. Instead, we employ several experimental techniques (DLS, AFM, CD, and kinetic experiments) to gain additional information on the morphological phases J1, J3, and J4. AFM is shown in Figure 5.4e-l, demonstrating that each aggregate shows widths consistent with single monolayers, though differing widths are observed for each morphology. Additional structural data, including cryo-EM morphology and AFM monolayer thicknesses, are collected in Table 5.2.

We used cryo-EM imaging to elucidate the structures of the different aggregates formed. Figure 5.4A, 5.4C, and 5.4D show that J1, J3 and J4 aggregate of **5.1b** form 2D sheet-like aggregates, while Figure 5.4B shows the J2 aggregate has a tubular structure that measures ~ 5 nm in diameter. Imaging done on the aggregates of the remaining dyes (**5.1a**, **5.1c**, **5.1d**) also show a 2D structure. The J1 aggregate of the **5.1c** and **5.1d** dyes and the J3 aggregate of the **5.1c** dyes were unable to be isolated for imaging, but based on the single-peak lineshapes observed in the absorption spectra, it is most likely that these dyes also produce 2D sheet-like structures. These results indicate that **5.1b** dye is the only dye which allows formation of the J2 aggregate.

In order to determine the heights of the structure, AFM images were also obtained for all aggregates that could be isolated. Figure 5.4e-h shows the AFM images of the **5.1b** dye aggregates J1-4, respectively, while Figure 5.4i-l shows the respective height analysis for these images (see subchapter 5.11 for analysis details). The heights of all the aggregates measured via AFM are presented in Table 5.2. The tubular J-aggregate was measured with height of 5.04 nm, which is confirmed by the diameter measured in the cryo-EM images. The heights of the sheet-like aggregates appear to increase with wavelength of absorption (J1 < J3 < J4). These heights are consistent with a single monomer height for each dye, and we hypothesize that the changes in the

aggregate dye heights are caused by out-of-plane or alternating orientations of the monomer within the aggregate structure.

In addition to those characterizations, we employed dynamic light scattering (DLS) to get a relative estimate of the aggregate size in solution. Our DLS analysis revealed general patterns, namely that the J1 aggregates appeared smaller than their J3 and J4 counterparts across dyes **5.1a** and **5.1b**. The aggregates of **5.1c**, which were too small to see by cryo-EM, also appeared smaller than others by DLS. Unfortunately, because the J1 aggregates of **5.1c** and **5.1d** were not fully isolated, we were not able to get a consistent size estimate for their structures from DLS. Additionally, because DLS is not intended for extended sheet structures, we cautiously report one significant digit for each aggregate's size, intending its use to be generally classifying large size differences, in contrast to the more precise sizing from AFM. Table 5.2 shows that systematic trends exist between the J1, J3, and J4 aggregates of dyes **5.1a-d** and that our structural characterizations are consistent between each other.

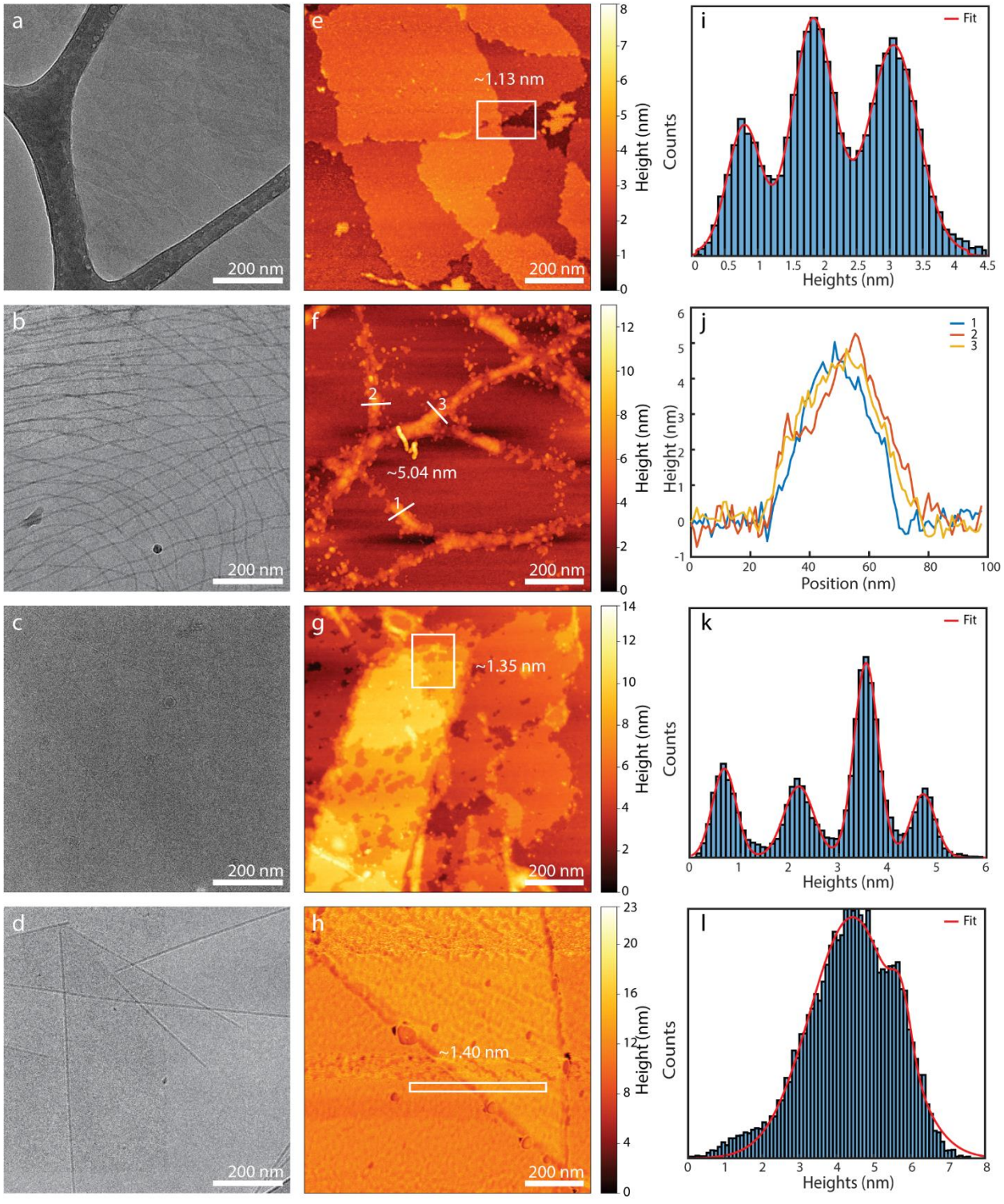

Figure 5.05. Cryo-EM and AFM characterization of J1-J4 aggregates of **5.1b**. a-d) CryoEM images **5.1b** aggregates (a) J1 (5% MeOH, 0.1 mM dye, 1 day) (b) J2 (20% MeOH, 0.1 mM dye, 1 day) (c) J3 (30% MeOH, 0.1 mM, 1 day) (d) J4 (5% MeOH, 0.1 mM dye, 2 weeks). e-h) AFM

images of J1 (e), J2 (f), J3 (g), and J4 (h). i-l) Height analysis of the regions indicated in the AFM images of J1 (i), J2 (j), J3 (k), and J4 (l). Cryo-EM and AFM were performed by Jill Williams.

Table 5.2. Structural information (AFM, DLS) of all aggregates.
Aggregates that were not able to be isolated fully are marked with an asterisk. Aggregates that were not visible/inconsistent on cryo-EM, AFM, or DLS over multiple attempts are marked with a hyphen.

Dye	Aggregate	Morphology	AFM thickness (nm)	DLS Size (nm)
5.1a	J1	--	1.79	300
5.1b	J1	Sheets	1.13	200
5.1c	J1	*	*	*
5.1d	J1	*	*	*
5.1b	J2	Tubes	5.04	200
5.1a	J3	Sheets	1.36	300
5.1b	J3	Sheets	1.35	600
5.1c	J3	*	--	--
5.1d	J3	--	1.60	600
5.1a	J4	--	1.66	500
5.1b	J4	--	1.40	600
5.1c	J4	Sheets	1.37	270
5.1d	J4	Sheets	2.55	600

5.07. Investigation of self-assembly pathways between J1-4 aggregates

Lastly, we performed a thorough investigation of the kinetics aggregated derived from **5.1b** to rationalize the conversion among J1, J2, J3, and J4 aggregates. We rapidly took absorbance spectra (every ~30 s.) immediately upon mixing the dye stock solution with water for a period of at least 10 minutes. We then continued collecting spectra at shorter timepoints (every 10 min. to every 2 h.) to carefully watch the self-assembly unfold. The absorption spectra from initial and extended timepoints are presented in Figure 5.5.

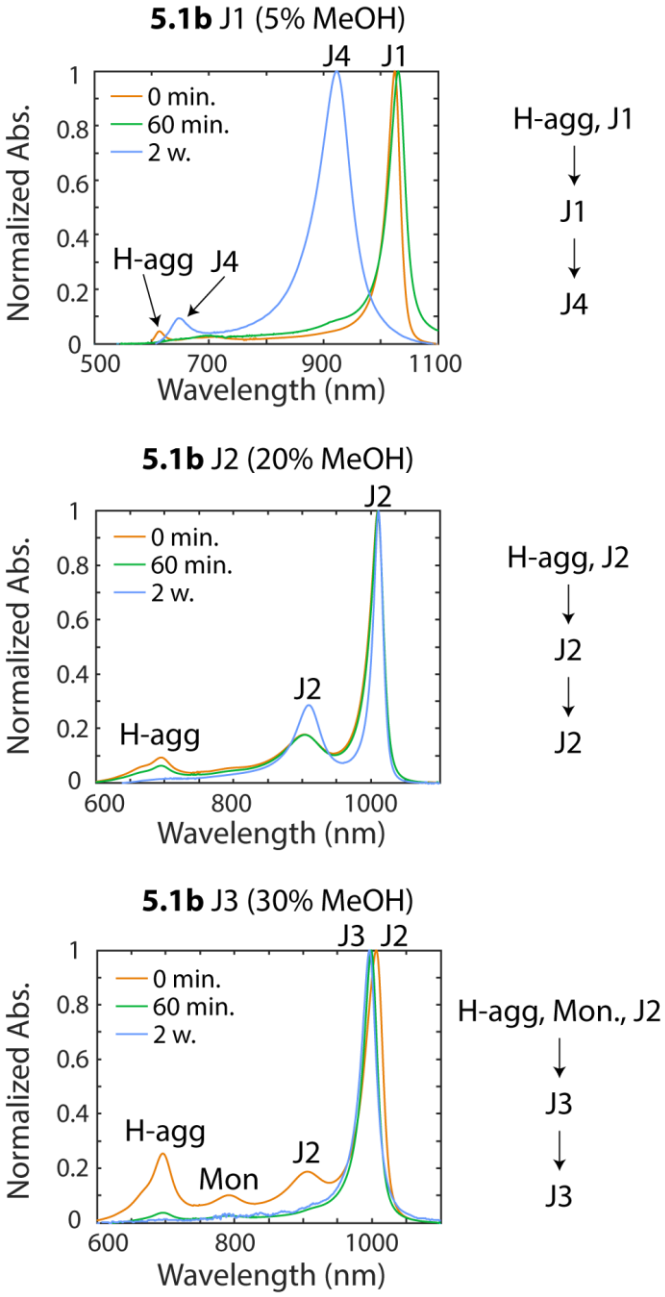

Figure 5.06. Absorbance spectra showing initialization of J1, J2, and J3 aggregates of **5.1b**. Initialization experiments performed by John Cao.

Figure 5.5 shows that the **5.1b** J1 (0-15% MeOH) initializes with a small amount of H-aggregate (~600 nm) present, which becomes much less prominent after 1 hour. Depending on the

%MeOH content of the solution, the J1 will interconvert to J4 over time, with higher percentages converting faster. At 5% MeOH, the full J1 to J4 conversion of **5.1b** occurs over approximately 14 days (Figure 5.3b). The **5.1b** J2 aggregate (20% MeOH) also initializes with a small amount of H-aggregate, indicating that the J1 and J2 aggregates are formed directly from an H-aggregate at very early (before 1 s) timepoints. Interestingly, the **5.1b** J3 (30% MeOH) aggregate initializes in the J2 aggregate, and quickly converts to the fully J3 species over roughly 1 h.

Beyond initialization experiments, we conducted methanol and water dilutions to see how the aggregates of **5.1b** respond to changing methanol:water ratio. Interestingly, the J1-J3 aggregates display a high degree of interconversion. By diluting the J1 with methanol up to 20 or 30%, we see conversion to the J2 and J3 aggregates, respectively. By diluting the J2 aggregate up to 30% methanol, we observe conversion from J2 to J3. Additionally, dilution of the J3 aggregate (30% MeOH) with water down to 20 and 10% methanol allows for interconversion back to the J2 and J1 aggregates, respectively.

We also observed trends in the self-assembly and stability of these aggregates. Particularly, we found that the J1 aggregates were increasingly unstable as steric bulk increased. For example, the J1 aggregates of **5.1a** and **5.2b** are readily isolated at room temperature and convert over weeks (**5.1a**) to days (**5.1b**) to the J4 species depending on methanol composition; however, J1 aggregates of **5.1c** and **5.1d** were only able to be isolated at low (0° C) temperatures, meaning they convert immediately to a different species (J4) upon preparation at room temperature. Additionally, the J1 formed from **5.1a** and **5.1b** does not convert, even in small amounts, to J4 at low temperatures (4-8° C) over several weeks. These data imply that the J1 species is a kinetic trap which, if given sufficient activation energy, interconverts to more stable aggregate morphology. The opposite trend was not found for J3 aggregates, which were stable at room temperature across **5.1a-d.**

Combining these observations and others, we compiled the energetics of the self-assembly equilibria between J1-J4 of **5.1b** with hypothesized structures into a flowchart, shown in Figure 5.07.

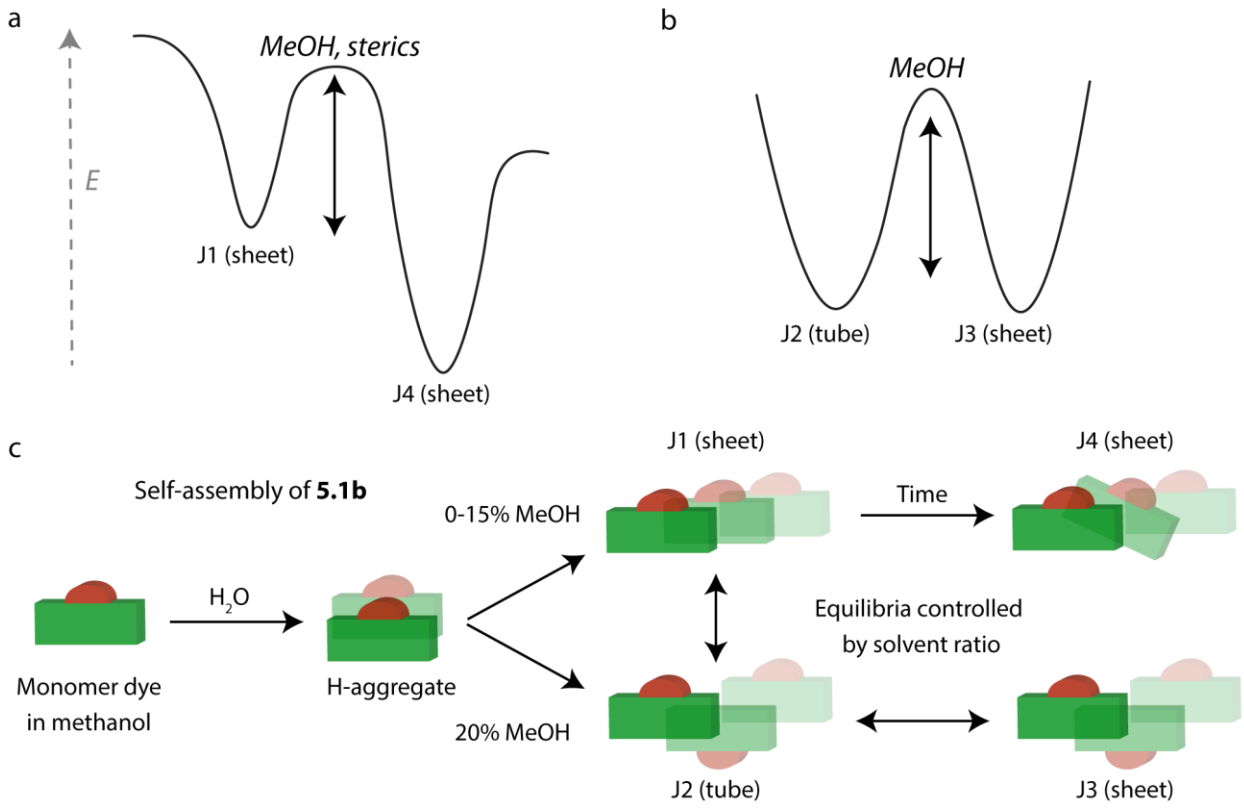

Figure 5.07. Cartoon depicting energetics of J-aggregate phases and self-assembly pathways. a) Potential energy diagrams depicting the transition of J1 to J4 b) Energy diagram of J2 to J3 c) Cartoon depicting self-assembly for aggregates of **5.1b.**

By combining observations from the initialization experiments (i.e. that J1 converts to J4 and J2 interconverts with J3) and dilution experiments, we believe that the J1 is a kinetic trap. Its interconversion with J4 over time also suggests that J4 is the thermodynamic product for low methanol aggregates (Figure 5.07A). Both the steric bulk of the monomer dye and methanol composition seem to affect the energy barrier between J1 and J4. Because dyes **5.1c** and **5.1d** do

not form J1 aggregates at room temperature, we know their barrier between J1 and J4 is much lower. Additionally, because the J1 to J4 interconversion occurs more quickly at high MeOH percentages, we know that the barrier must also be lower. In Figure 5.07B, we propose that the relative energies of the J2 and J3 aggregates are quite similar, with the barrier for interconversion changing at different methanol ratios. When methanol is lower (20%), the J2 aggregate is favored, but at higher ratios (30%) the J3 aggregate is favored. And due to the reversible nature of this transition, it is clear that neither aggregate is much more stable than the other.

5.08. Discussion of structural assignments

These observations can be connected to potential structural morphology changes. To summarize, the cryo-EM showed us that J1, J3, and J4 share 2D sheetlike morphologies, and that J2 is a single-walled nanotube. Because there are only a small number of ways to pattern the dye monomer such that a single molecule thick 2D sheet organizes from its constituent unit, we began by considering the simplest possible cases of supramolecular organization where each dye has the same orientation and monomers are slipped from their nearest neighbors.

Based on stability, we attribute that structure to the J1 species, which becomes increasingly unstable with steric bulk, meaning the pendant groups begin to approach each other and therefore push the dyes further apart (leading to redshift). This simple organization allows the dyes to rapidly assemble, though it also explains why the J1 is kinetically disfavored in dyes **5.1c** and **5.1d**—the energy penalty of steric clash from their pendant groups becomes large enough that other morphologies (J3 and J4) form immediately, as opposed to slow conversion over time. In the case of **5.1a** and **5.1b**, the J1 is a kinetic trap that, while relatively unstable, can organize quickly and slowly find a lower energy conformation over time. Additionally, the AFM reveals that J1

aggregates show the smallest monolayer thickness, which agrees with the proposed structure. DLS also consistently suggests a smaller size than the J3 and J4 morphologies. We note that this is consistent with increased redshift as a function of steric bulk, as the slip among monomers results in stronger J-coupling.

We assign the J4 structure to a frustrated, slightly larger, and more disordered morphology that forms from the J1. The J4 structure must be similar to J1, due to their interconversion over time. However, we know from AFM that J4 is a thicker monolayer (1.47 vs. 1.01 nm), meaning that some change must occur which widens the monolayer's thickness. For **5.1b** and **5.1d**, we see that the J4 aggregate has a secondary, blueshifted peak that photobleaches concurrently with the main peak; we attribute this side feature to an out of plane transition within the 2D sheet; that secondary transition suggests a slightly angled orientation of dye monomers within the extended sheet, depicted in Figure 5.5.

J2 and J3 structures likely feature dyes in a configuration such that nearest neighbors are rotated 180 degrees (i.e. antiparallel) from one another. We primarily suspect this because the J3 aggregates blueshift with increasing steric bulk; this means that as the pendant group grows larger, the dyes become less slipped from one another, thereby decreasing the J-coupling (blueshifting). Additionally, we know that the J3 dyes are thicker than J1 based on AFM (1.56 vs. 1.01 nm) and DLS (200 vs 600 nm) characterizations that show slightly larger monolayers. The formation of single-walled nanotubes in the J2 of **5.1b** indicates that there are hydrophilic groups (i.e. sulfonates) present on the inner and outer walls of the tube, which would intuitively require the antiparallel packing. Lastly, the fact that J3 aggregates initialize in the J2 phase and convert quickly over ~1 h. at room temperature also indicates that these structures share similarity.

5.09. Conclusion

We synthesized four new cyanine dyes with varying steric bulk in their pendant (4') position and demonstrated that increasing the steric bulk leads to an increased redshift of the dye's J-aggregates. The dyes display rich aggregation behavior, leading to 3-4 J-aggregates with unique spectral signatures that come from different 2D-sheet (one tubular) morphologies despite near identical monomer photophysical properties. We correlate the cryo-electron microscopy to several other structural measurements (AFM, DLS, CD, and kinetic observations) to gain intuition on the structures and hypothesize how different packing arrangements of the monomers yields three unique sheetlike morphologies and one tubular morphology with varying degrees of redshift. In particular, we find the J1 aggregates to be a kinetic trap that slowly interconvert to a blueshifted J4 species. The J2 aggregate is a single-walled nanotube morphology that shares an anti-parallel arrangement with the J3 sheets. J4 we tentatively assign to be a larger, more disordered sheet, with some out of plane component.

This work provides several key insights. First, that the addition of substituents to the 4' position of a cyanine dye is an effective way to induce systematic changes in the chromophore's scaffold without significantly altering solubility or electronic structure. Second, we show generally how minute modifications to a dye monomer structure can lead to extreme changes in the resulting J-aggregate's morphology and photophysics. In particular, we maintain that the addition of steric bulk is effective in slipping dyes further apart within a J-aggregate, and therefore modulating the photophysics. Second, we demonstrate distinct morphological phases can form within 2D sheetlike J-aggregates, based on subtle changes in solubility and co-solvent concentrations. These differences are not obvious from overall mesoscale structure, but are clear form changes in J-aggregate photophysics. Finally, we demonstrate that combining photophysical characterization

with detailed structural analysis could enable new studies of self-assembly and complexity in supramolecular aggregates.

5.10. Experimental information

Materials

Reagents were purchased from Acros Organic, Alfa Aesar, Fisher Scientific, or Sigma-Aldrich and used without further purification unless otherwise noted. Anhydrous solvents were obtained from a Grubb's-type Phoenix Solvent system. Column chromatography was performed using technical grade Silica Gel (60 A pores, 40-64 um mesh particle size, Sorbtech Technologies). Thin layer chromatography was performed using Silica Gel F_{254} (EMD Millipore).

Instrumentation

Rotary evaporation was done using a Buchi Rotovapor with a Welch self-cleaning dry vacuum pump and compounds were further dried over high vacuum using a Welch DuoSeal pump. NMR spectra were taken on a Bruker Avance AV-400 and AV-500 then processed with TopSpin or MestReNova. All signals are reported relative to their respective solvent signals. High resolution mass spectra (electrospray ionization (ESI)) were obtained on a Thermo Scientific Q ExactiveTM Plus Hybrid Quadrupole-OrbitrapTM M with Dionex UltiMate 3000 RSLCnano System.

Synthetic Procedures

The design of all reactions towards the synthesis of **5.1a-d**, as well as the compound synthesis/characterization, and writing of the procedure was performed by Monica Pengshung. The experimental procedures are reproduced here for completeness.

Synthesis of 3-(5-chloro-2-methylbenzo[d]thiazol-3-ium-3-yl)propane-1-sulfonate (**5.5**)

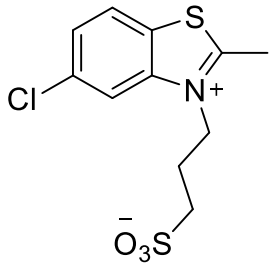

5-chloro-2-methylbenzothiazole (500 mg, 2.7 mmol, 1 eq) and 1,3-propane sultone (403 mg, 3.3 mmol, 1.2 eq) are heated at 120 °C for 3 h. The precipitate formed during the reaction is refluxed shortly in MeOH in order to dissolve solid, then excess Et_2O is added to precipitate solid. The product was collected via vacuum filtration and washed with excess Et_2O to afford pure **3-(5-chloro-2-methylbenzo[d]thiazol-3-ium-3-yl)propane-1-sulfonate (5.5)** as a fluffy white solid (300 mg, 1.0 mmol, 36%).

^{1}H NMR (400 MHz, Deuterium Oxide) δ 8.15 (d, *J* = 1.9 Hz, 1H), 8.00 (d, *J* = 8.8 Hz, 1H), 7.63 (dd, *J* = 8.8, 1.8 Hz, 1H), 4.72 (dd, *J* = 6.6, 4.1 Hz, 1H), 3.06 (s, 2H), 2.99 (t, *J* = 7.1 Hz, 2H), 2.30 – 2.15 (m, 2H).

^{13}C NMR (101 MHz, Deuterium Oxide) δ 178.2, 141.7, 135.9, 129.10, 127.6, 124.9, 116.4, 47.9, 47.3, 23.0, 16.4.

Synthesis of N-((E)-((E)-6-((phenylamino)methylene)-3,4,5,6-tetrahydro-[1,1'-biphenyl]-2-yl)methylene)benzenaminium chloride (**5.4a**)

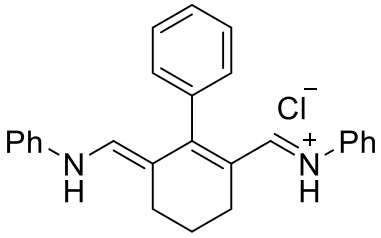

N-((E)-((E)-2-chloro-3-((phenylamino)methylene)cyclohex-1-en-1-yl)methylene)benzenaminium chloride **2** (500 mg, 1.40 mmol, 1.0 eq, Sigma Aldrich), phenyl boronic acid **3a** (340 mg, 2.8 mmol, 2.0 eq), tetrakis(triphenylphosphine)palladium(0) (160 mg, 0.1 mmol, 0.1 eq) and tripotassium phosphate K_3PO_4 (890 mg, 4.1 mmol, 3.0 eq) was dissolved in a 13:2 mixture of 1,4-dioxane: water (12.4 mL: 2.6 mL). The solution was freeze-pump-thawed x3 then heated at 75 °C for 5h. Upon cooling to room temperature, the reaction was quenched via addition of $NaHCO_3$ solution then extracted into DCM (3 x 20 mL), dried over Na_2SO_4, filtered and evaporated to give a dark red oil. The crude product was purified via silica gel chromatography with hexanes: ethyl acetate (9:1) to afford ***N*-((E)-((E)-6-((phenylamino)methylene)-3,4,5,6-tetrahydro-[1,1'-biphenyl]-2-yl)methylene)benzenaminium chloride (5.4a)** as a dark red oil. Acidification with 2M HCl (2 mL) gave the salt version as a dark red solid (304 mg, 0.76 mmol, 54 %) and was utilized crude in the next reaction.

Synthesis of N-((E)-((E)-3',5'-dimethyl-6-((phenylamino)methylene)-3,4,5,6-tetrahydro-[1,1'-biphenyl]-2-yl)methylene)benzenaminium chloride (**5.4b**)

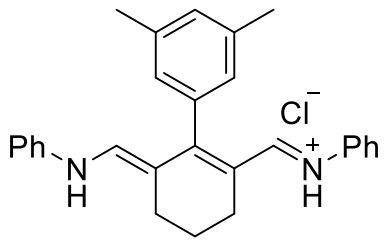

N-((E)-((E)-2-chloro-3-((phenylamino)methylene)cyclohex-1-en-1-yl)methylene)benzenaminium chloride **2** (500 mg, 1.4 mmol, 1.0 eq), 3,5-dimethylphenyl boronic acid **3b** (420 mg, 2.8 mmol, 2.0 eq), tetrakis(triphenylphosphine)palladium(0) (160 mg, 0.14 mmol, 0.1 eq) and tripotassium phosphate K_3PO_4 (890 mg, 4.2 mmol, 3.0 eq) was dissolved in a 13:2 mixture of 1,4-dioxane: water (12.5 mL: 2.5 mL). The solution was freeze-pump-thawed x3

then heated at 75 °C for 5 h. Upon cooling to room temperature, the reaction was quenched via addition of $NaHCO_3$ solution then extracted into DCM (3 x 20 mL), dried over Na_2SO_4, filtered and evaporated to give a dark red oil. The crude product was purified via silica gel chromatography with hexanes: ethyl acetate (9:1) to afford ***N*-((E)-((E)-3',5'-dimethyl-6-((phenylamino)methylene)-3,4,5,6-tetrahydro-[1,1'-biphenyl]-2-yl)methylene)benzenaminium chloride (5.4b)** as a dark red oil. Acidification with 2M HCl (2 mL) gave the salt version as a dark red solid (300 mg, 0.70 mol, 50 %) and was utilized crude in the next reaction.

Synthesis of (3,5-diethylphenyl)boronic acid (**5.3c**)

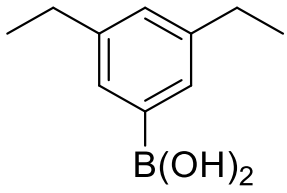

Bromo-3,5-diethyl benzene (0.200 mL, 1.0 mmol, 1 eq) was dissolved in THF (3.0 mL, anhydrous) and cooled to -78 °C. A solution of *n*-BuLi (1.2M in hexanes, 1.5 mL, 2.0 mmol, 1.7 eq) was added dropwise slowly turning solution yellow then left to stir for 30 min. To a second flask was combined triisopropyl borate (0.530 mL, 2.3 mmol, 2 eq) in THF (17.25 mL, anhydrous) then added slowly to first flask at -78 °C. After 2h of stirring at -78 °C, reaction was quenched with H_2O and acidified with 3M H_2SO_4 (2 mL) until pH = 2. This created a biphasic solution and the top phase was removed and extracted into EtOAc (3 x 10 mL), dried over Na_2SO_4, filtered and evaporated to give pure **(3,5-diethylphenyl)boronic acid (5.3c)** as a white solid (160 mg, 0.8 mmol, 78%) ^{1}H-NMR matched literature.[108,109]

^{1}H NMR (400 MHz, DMSO-d_6) δ 7.86 (s, 2H), 7.40 (d, J = 1.8 Hz, 2H), 7.02 (t, J = 1.8 Hz, 1H), 2.52 (q, J = 7.6 Hz, 4H), 1.21 – 1.06 (m, 6H).

Synthesis of N-((E)-((E)-3',5'-diethyl-6-((phenylamino)methylene)-3,4,5,6-tetrahydro-[1,1'-biphenyl]-2-yl)methylene)benzenaminium chloride (**5.4c**)

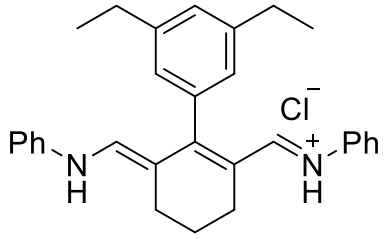

N-((E)-((E)-2-chloro-3-((phenylamino)methylene)cyclohex-1-en-1-yl)methylene)benzenaminium chloride **2** (250 mg, 0.7 mmol, 1.0 eq), 3,5-diethyllphenyl boronic acid **2c** (250 mg, 1.4 mmol, 2.0 eq), tetrakis(triphenylphosphine)palladium(0) (80 mg, 0.10 mmol, 0.1 eq) and tripotassium phosphate K_3PO_4 (460 mg, 2.1 mmol, 3.0 eq) was dissolved in a 13:2 mixture of 1,4-dioxane: water (6.3 mL: 1.2 mL). The solution was freeze-pump-thawed x3 then heated at 75 °C for 5 h. Upon cooling to room temperature, the reaction was quenched via addition of $NaHCO_3$ solution then extracted into DCM (3 x 10 mL), dried over Na_2SO_4, filtered and evaporated to give a dark red oil. The crude product was purified via silica gel chromatography with hexanes: ethyl acetate (9:1) to afford ***N*-((E)-((E)-3',5'-diethyl-6-((phenylamino)methylene)-3,4,5,6-tetrahydro-[1,1'-biphenyl]-2-yl)methylene)benzenaminium chloride (4c)** as a dark red oil. Acidification with 2M HCl (2 mL) gave the salt version as a dark red solid (90 mg, 0.20 mmol, 27 %) and was utilized crude in the next reaction.

Synthesis of N-((E)-((E)-3',5'-di-tert-butyl-6-((phenylamino)methylene)-3,4,5,6-tetrahydro-[1,1'-biphenyl]-2-yl)methylene)benzenaminium chloride (**5.4d**)

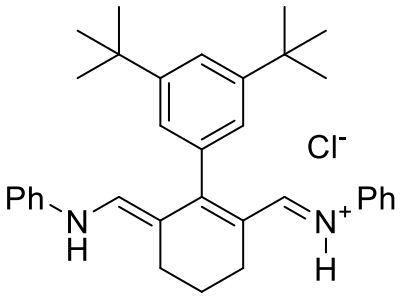

N-((E)-((E)-2-chloro-3-((phenylamino)methylene)cyclohex-1-en-1-yl)methylene)benzenaminium chloride **2** (150 mg, 0.4 mmol, 1.0 eq), 3,5-ditertbutyllphenyl boronic acid **3d** (200 mg, 0.8 mmol, 2.0 eq), tetrakis(triphenylphosphine)palladium(0) (50 mg, 0.04 mmol, 0.1 eq) and tripotassium phosphate K_3PO_4 (270 mg, 1.3 mmol, 3.0 eq) was dissolved in a 13:2 mixture of 1,4-dioxane: water (3.75 mL: 0.75 mL). The solution was freeze-pump-thawed x3 then heated at 100 °C for 5 h. Upon cooling to room temperature, the reaction was quenched via addition of $NaHCO_3$ solution then extracted into DCM (3 x 20 mL), dried over Na_2SO_4, filtered and evaporated to give a dark red oil. The crude product was purified via silica gel chromatography with hexanes: ethyl acetate (9:1) to afford pure ***N*-((E)-((E)-3',5'-di-tert-butyl-6-((phenylamino)methylene)-3,4,5,6-tetrahydro-[1,1'-biphenyl]-2-yl)methylene)benzenaminium chloride (4d)** as a dark red oil. Acidification with 2M HCl (2 mL) gave the salt version as a dark red solid (78 mg, 0.15 mmol, 38 %).

^{1}H NMR (400 MHz, Methanol-d_4) δ 7.66 (t, J = 1.7 Hz, 1H), 7.56 – 7.44 (m, 2H), 7.44 – 7.36 (m, 1H), 7.33 – 7.21 (m, 6H), 7.21 – 7.11 (m, 2H), 7.02 (dd, J = 8.6, 1.1 Hz, 3H), 2.72 (t, J = 6.1 Hz, 4H), 2.07 (t, J = 6.1 Hz, 2H), 1.35 (s, 18H).

Synthesis of 3-(5-chloro-2-((E)-2-((E)-6-((Z)-2-(5-chloro-3-(3-sulfonatopropyl)benzo[d]thiazol-2(3H)-ylidene)ethylidene)-3,4,5,6-tetrahydro-[1,1'-biphenyl]-2-yl)vinyl)benzo[d]thiazol-3-ium-3-yl)propane-1-sulfonate (**5.1a**)

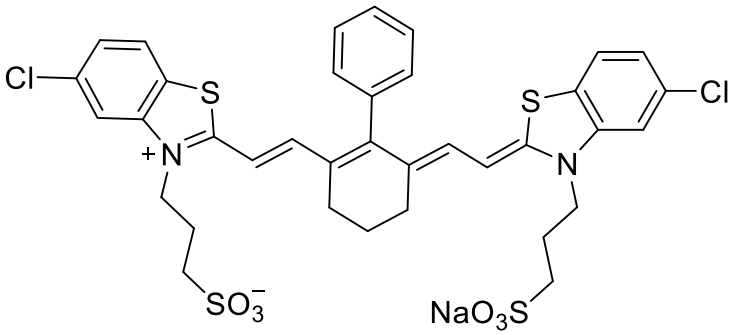

3-(5-chloro-2-methylbenzo[d]thiazol-3-ium-3-yl)propane-1-sulfonate **5** (100 mg, 0.33 mmol, 1 eq), **4a** (65 mg, 0.16 mmol, 0.5 eq), NaOAc (32 mg, 0.40 mmol , 1.2 eq) was dissolved in EtOH (6.5 mL, 0.5 M). The dark magenta solution was freeze-pump-thawed x3, then heated to 80 °C for 1h turning the solution green. The reaction was monitored by UV-Vis for the appearance of product (~800 nm) and lost of linker (~550 nm). The crude product was purified via silica gel chromatography with a gradient of 19:1 → 9:1 → 17:3 →4:1 dichloromethane: methanol to afford pure product **3-(5-chloro-2-((E)-2-((E)-6-((Z)-2-(5-chloro-3-(3-sulfonatopropyl)benzo[d]thiazol-2(3H)-ylidene)ethylidene)-3,4,5,6-tetrahydro-[1,1'-biphenyl]-2-yl)vinyl)benzo[d]thiazol-3-ium-3-yl)propane-1-sulfonate (5a)** as a shiny green brown solid (12 mg, 0.03 mmol, 9%).

^{1}H NMR (400 MHz, DMSO-d_6) δ 7.88 (d, *J* = 1.9 Hz, 2H), 7.82 (d, *J* = 8.5 Hz, 2H), 7.53 – 7.47 (m, 3H), 7.29 (dd, *J* = 8.5, 1.9 Hz, 2H), 7.24 (dd, *J* = 7.4, 2.0 Hz, 1H), 6.67 (d, *J* = 13.3 Hz, 2H), 6.58 (d, *J* = 13.4 Hz, 2H), 4.46 (t, *J* = 7.9 Hz, 4H), 2.64 (d, *J* = 7.6 Hz, 4H), 2.51 (t, *J* = 6.7 Hz, 4H), 1.93 (t, *J* = 7.4 Hz, 4H), 1.87 (t, *J* = 5.9 Hz, 2H).

*3-(5-chloro-2-((E)-2-((E)-6-((Z)-2-(5-chloro-3-(3-sulfonatopropyl)benzo[d]thiazol-2(3H)-ylidene)ethylidene)-3',5'-dimethyl-3,4,5,6-tetrahydro-[1,1'-biphenyl]-2-yl)vinyl)benzo[d]thiazol-3-ium-3-yl)propane-1-sulfonate (**5.1b**)*

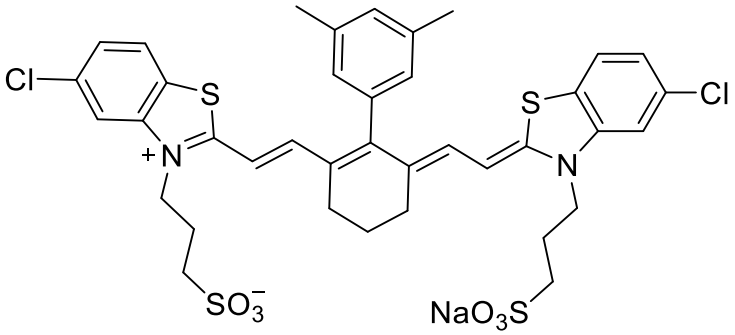

3-(5-chloro-2-methylbenzo[d]thiazol-3-ium-3-yl)propane-1-sulfonate **4** (100 mg, 0.30 mmol, 1 eq), **3b** (70 mg, 0.20 mmol, 0.5 eq), NaOAc (30 mg, 0.4 mmol, 3 eq) was dissolved in EtOH (6.6 mL, 0.5M). The dark magenta solution was freeze-pump-thawed x3, then heated to 80 °C for 1h turning the solution green.The reaction was monitored by UV-Vis for the appearance of product (~800 nm) and loss of linker (~550 nm). The crude product was purified via silica gel chromatography with a gradient of 19:1 → 9:1 → 17:3 dichloromethane: methanol to afford pure product **3-(5-chloro-2-((E)-2-((E)-6-((Z)-2-(5-chloro-3-(3-sulfonatopropyl)benzo[d]thiazol-2(3H)-ylidene)ethylidene)-3',5'-dimethyl-3,4,5,6-tetrahydro-[1,1'-biphenyl]-2-yl)vinyl)benzo[d]thiazol-3-ium-3-yl)propane-1-sulfonate (5b)** as a shiny green brown solid (45 mg, 0.10 mmol, 33%).

^{1}H NMR (400 MHz, DMSO-d_6) δ 7.88 (d, J = 1.9 Hz, 2H), 7.83 (d, J = 8.5 Hz, 2H), 7.30 (dd, J = 8.5, 1.9 Hz, 2H), 7.15 – 7.13 (m, 1H), 6.88 – 6.85 (m, 2H), 6.74 (d, J = 13.3 Hz, 2H), 6.57 (d, J = 13.4 Hz, 2H), 4.46 (t, J = 7.8 Hz, 4H), 2.63 (t, J = 6.2 Hz, 4H), 2.52 (d, J = 6.7 Hz, 3H), 2.33 (s, 6H), 1.94 (t, J = 7.4 Hz, 4H), 1.85 (t, J = 6.3 Hz, 1H).

*Synthesis of 3-(5-chloro-2-((E)-2-((E)-6-((Z)-2-(5-chloro-3-(3-sulfonatopropyl)benzo[d]thiazol-2(3H)-ylidene)ethylidene)-3',5'-diethyl-3,4,5,6-tetrahydro-[1,1'-biphenyl]-2-yl)vinyl)benzo[d]thiazol-3-ium-3-yl)propane-1-sulfonate (**5.1c**)*

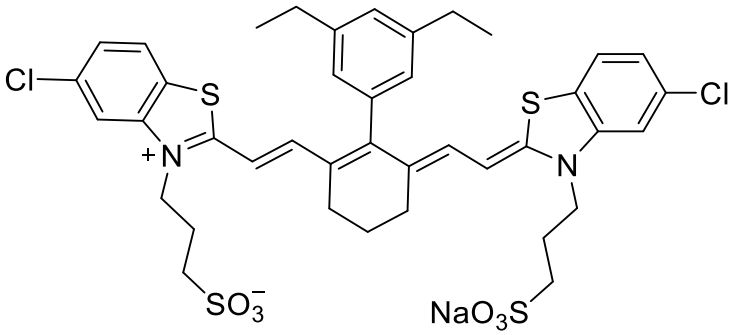

3-(5-chloro-2-methylbenzo[d]thiazol-3-ium-3-yl)propane-1-sulfonate **4** (30 mg, 0.10 mmol, 1 eq), **3c** (20 mg, 0.04 mmol, 0.5 eq), NaOAc (9 mg, 0.10 mmol, 1.2 eq) was dissolved in EtOH (2.7 mL, 0.3M). The dark magenta solution was freeze-pump-thawed x3, then heated to 80 °C for 1h turning the solution green. The reaction was monitored by UV-Vis for the appearance of product (~800 nm) and loss of linker (~550 nm). The crude product was purified via silica gel chromatography with a gradient of 19:1 → 9:1 → 17:3 dichloromethane: methanol to afford pure product **3-(5-chloro-2-((E)-2-((E)-6-((Z)-2-(5-chloro-3-(3-sulfonatopropyl)benzo[d]thiazol-2(3H)-ylidene)ethylidene)-3',5'-diethyl-3,4,5,6-tetrahydro-[1,1'-biphenyl]-2-yl)vinyl)benzo[d]thiazol-3-ium-3-yl)propane-1-sulfonate (5c)** as a shiny green brown solid (10 mg, 0.01 mmol, 12%).

^{1}H NMR (400 MHz, DMSO-d_6) δ 7.88 (d, J = 1.9 Hz, 2H), 7.82 (d, J = 8.5 Hz, 2H), 7.29 (dd, J = 8.5, 1.9 Hz, 2H), 7.18 (s, 1H), 6.91 (s, 2H), 6.79 (s, 2H), 6.57 (d, J = 13.4 Hz, 2H), 4.46 (t, J = 7.8 Hz, 4H), 2.64 (d, J = 7.6 Hz, 8H), 2.53 – 2.49 (m, 4H), 1.94 (s, 4H), 1.86 (d, J = 5.9 Hz, 2H), 1.25 – 1.18 (m, 6H).

*3-(5-chloro-2-((E)-2-((E)-3',5'-di-tert-butyl-6-((Z)-2-(5-chloro-3-(3-sulfonatopropyl)benzo[d]thiazol-2(3H)-ylidene)ethylidene)-3,4,5,6-tetrahydro-[1,1'-biphenyl]-2-yl)vinyl)benzo[d]thiazol-3-ium-3-yl)propane-1-sulfonate (**5.1d**)*

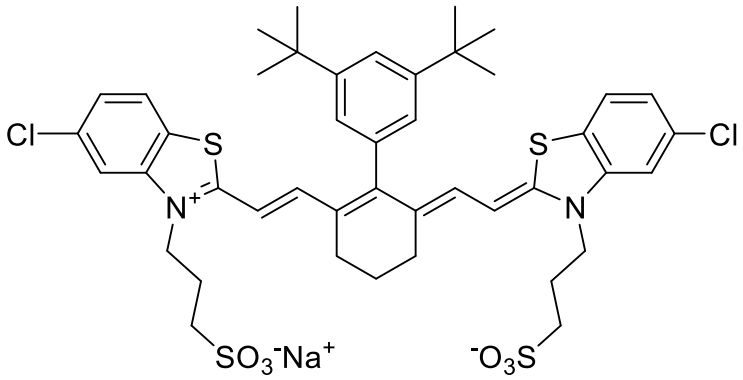

3-(5-chloro-2-methylbenzo[d]thiazol-3-ium-3-yl)propane-1-sulfonate **5** (12 mg, 0.04 mmol, 1 eq), **4d** (10 mg, 0.02 mmol, 0.5 eq), NaOAc (4 mg, 0.05 mmol, 1.2 eq) was dissolved in EtOH (0.8 mL, 0.05M). The dark magenta solution was freeze-pump-thawed x3, then heated to 80 °C for 1h turning the solution green. The reaction was monitored by UV-Vis for the appearance of product (~800 nm) and loss of linker (~550 nm). The crude product was purified via silica gel chromatography with a gradient of 19:1 → 9:1 → 17:3 dichloromethane: methanol to afford pure product **3-(5-chloro-2-((E)-2-((E)-3',5'-di-tert-butyl-6-((Z)-2-(5-chloro-3-(3-sulfonatopropyl)benzo[d]thiazol-2(3H)-ylidene)ethylidene)-3,4,5,6-tetrahydro-[1,1'-biphenyl]-2-yl)vinyl)benzo[d]thiazol-3-ium-3-yl)propane-1-sulfonate** (**5.1d**) as a shiny green brown solid (10 mg, 0.02 mmol, 54 %).

^{1}H NMR (400 MHz, DMSO-d_6) δ 7.88 (d, J = 1.9 Hz, 2H), 7.82 (d, J = 8.5 Hz, 2H), 7.49 (t, J = 1.8 Hz, 1H), 7.29 (dd, J = 8.5, 1.9 Hz, 2H), 7.06 (d, J = 1.8 Hz, 2H), 6.78 (d, J = 13.2 Hz, 2H), 6.58 (d, J = 13.4 Hz, 2H), 4.46 (t, J = 7.8 Hz, 4H), 2.64 (d, J = 5.7 Hz, 4H), 2.52 (t, J = 6.6 Hz, 4H), 1.94 (t, J = 7.5 Hz, 4H), 1.87 (s, 2H), 1.33 (s, 18H).

5.11. Microscopy information

Cryo-electron microscopy

Mesh 200 lacey formvar/carbon TEM grids from Ted Pella Inc., were plasma cleaned under a flow of H_2/O_2 by a Solarus Gatan Plasma cleaner to hydrophilize the surface. 3 μL of each aggregate was loaded onto the grids, and a Vitrobot Mark IV was used to plunge-freeze the samples in liquid ethane. The blotting conditions while freezing varied, based on which Vitrobot was used. Due to microscope availability, imaging was performed on one of two microscopes: i) FEI TecnaiG2 TF20 with a field-emission gun at 200 kV and TIETZ F415MP CCD camera, ii) Thermo Scientific Talos F200C with a filament at 200 kV and Thermo Scientific Ceta 16M camera.

Atomic force microscopy

MICA substrates were attached to a metal disk for support and tape was used to remove the top few layers, leaving a flat surface. The substrates were then cleaned in a BioForce Nanosciences UV/Ozone ProCleaner for 15 minutes. 20 μL of each aggregate was dropcast on the MICA, and allowed to evaporate. A Bruker Dimension FastScan was used in ScanAsyst mode with ScanAsyst-Air-HΠ-probes to analyze the aggregate heights. Scanning was performed at a resolution of 1 nm/pixel with a scan rate of ~1 Hz. Nanoscope Analysis was used to flatten the images, and Gwyddion was used to the minimum height to zero and correct horizontal scarring. MATLAB was used to extract the values from the grayscale image and plot the histogram of a selected region. The selected regions were chosen for containing multiple distinct layers of 2D aggregates. Gaussian fitting was performed in MATLAB to extract the heights of these layers, and the height difference between the layers were averaged. For the 1D tubular aggregate, Gwyddion was used to draw lines perpendicular to the tubes and extract their height profiles.

5.12. Linear dichroism of 5.1b J2 tubes and Frenkel exciton model

Upon learning that **5.1b** possesses a tubular morphology (J2), we employed linear dichroism to further characterize these aggregates. The information from these spectra allowed us to model the tubes and extract their chiral angle using a Frenkel exciton Hamiltonian.

$$H = \sum_{n,m} [J_{nm}|n\rangle\langle m| + \text{H. c.}] \tag{5.1}$$

Here J_{nm} is the exciton coupling strength, $|n\rangle$ represents the state where the nth dye is in its electronic excited state with all others in the ground state. We adopt a stacked-ring description for the tubular aggregates in question.[98]

Typically, the values of J_{nm} are estimated from quantum chemical calculations. Provided that the excited state wavefunctions are localized on individual molecules (no charge-transfer character), J_{nm} is given by the Coulombic interaction between the transition dipole densities of molecules n and m.[110] If the separation between the molecules is much larger than their dimensions, the coupling can be accurately approximated by truncating the multipole expansion at the first nontrivial contribution, dipole-dipole interaction, where $\vec{r}_{nm} = \vec{r}_n - \vec{r}_m$, $\hat{\mu}_n$ is the unit vector of the transition dipole moment, and μ_0 is its magnitude.

$$J_{nm} \approx \frac{\mu_0^2}{4\pi\epsilon_0}\left(\frac{1}{r_{nm}^3} - \frac{3(\hat{\mu}_n \cdot \vec{r}_{nm})(\hat{\mu}_m \cdot \vec{r}_{nm})}{r_{nm}^5}\right) \tag{5.2}$$

Given the values of J_{nm}, assuming the disorder-free limit, and taking advantage of the helical-rotational symmetry by unitarily transforming to the Bloch basis, it can be shown that there are two bright states.[89] One of them is polarized parallel to the cylindrical symmetry axis and the other perpendicular. Further assuming that the size of the tubular aggregate is smaller than the

wavelength of the corresponding optical transition, the parallel (perpendicular) bright states are given by the direct products of $k_{\parallel} = 0$ Bloch state along the axial direction and $k_{\perp} = 0\ (\pm 1)$ Bloch state along the circumferential direction. Since both bright states are of the nature of long wavelength $(k \ll 1)$, it can be readily deduced that the energy gap between them can be accurately predicted by the continuum limit of dipole-dipole interaction thanking to the cancellation of non-dipole short-range interactions.[102]

$$\Delta E = E_{\perp} - E_{\parallel} \approx \frac{1}{4\pi\epsilon_0} \cdot \frac{2\pi\mu_0^2}{r\,A_0} \sin^2\theta \tag{5.3}$$

Here r is the tube radius, A_0 is the area of each molecular site projected onto the tube surface, and θ is the angle between the transition dipole moment and the cylindrical axis.

We note that the angle θ can also be deduced by using the sum rules of linear dichroism spectra, namely the ratio between spectral weights of the two peaks where A_x is the area under the x-polarized peak. These two expressions serve to cross-check the parameters estimated.

$$\frac{A_{\perp}}{A_{\parallel}} = \tan^2\theta \tag{5.4}$$

For the **5.1b** tubular aggregate (J2), the absorption spectrum can be reasonably fitted with two Lorentzian lineshapes (shown in eq. 5).

$$I(\omega) = \left(\frac{w}{2}\right)^2 \frac{h}{(\omega - m)^2 + \left(\frac{w}{2}\right)^2} \tag{5.5}$$

Table 5.3. Spectroscopic observables from linear dichroism of **5.1b** J2 aggregates.

Absorption peak	Position m (cm^{-1})	FWHM w (cm^{-1})	Height h $(a.u.)$
Parallel	9903	137	1.15
Perpendicular	11011	741	0.19

With these parameters and eq. 2, we estimate that the chiral angle θ = 43.5 deg. On the other hand, we take the transition dipole moment of the lowest electronic transition of a Cy7 dye to be 16 Debye. This is estimated by the accepted value of 11.4 Debye for C8S3, a Cy3 dye, scaled by a factor of 1.4. that is calculated by comparing the transition dipole moments calculated using ZINDO model implemented in Gaussian electronic structure package. The tube radius can also be extracted from electron microscopy to be $r = 35\ (\text{Å})$. The dimensions of a **5.1b** molecule are estimated to be 4 Å wide and 25 Å long, giving rise to $A_0 = 100\ \text{Å}^2$. With these parameters and eq. 1 we estimate that θ = 43.6 deg, which is in excellent agreement with the estimation from the sum rule expression eq. 2. The fits from linear dichroism observables in Table 5.3 and isotropic absorbance of the **5.1b** J2 tubes are shown in Figure 5.08.

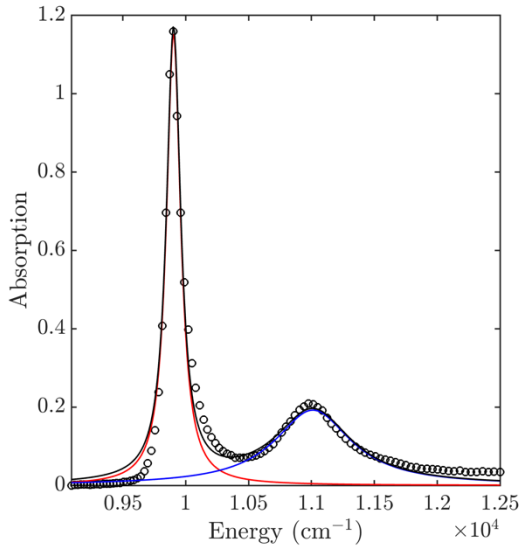

Figure 5.08. Linear dichroism of **5.1b** J2 aggregates and Lorentzian fitting. Red: Lorentzian curve fit to parallel peak. Blue: Lorentzian curve fit to perpendicular peak. Circle: experimental spectra showing the isotropic absorbance of **5.1b** J2 aggregates.

5.13. NMR spectra relevant to Chapter 5

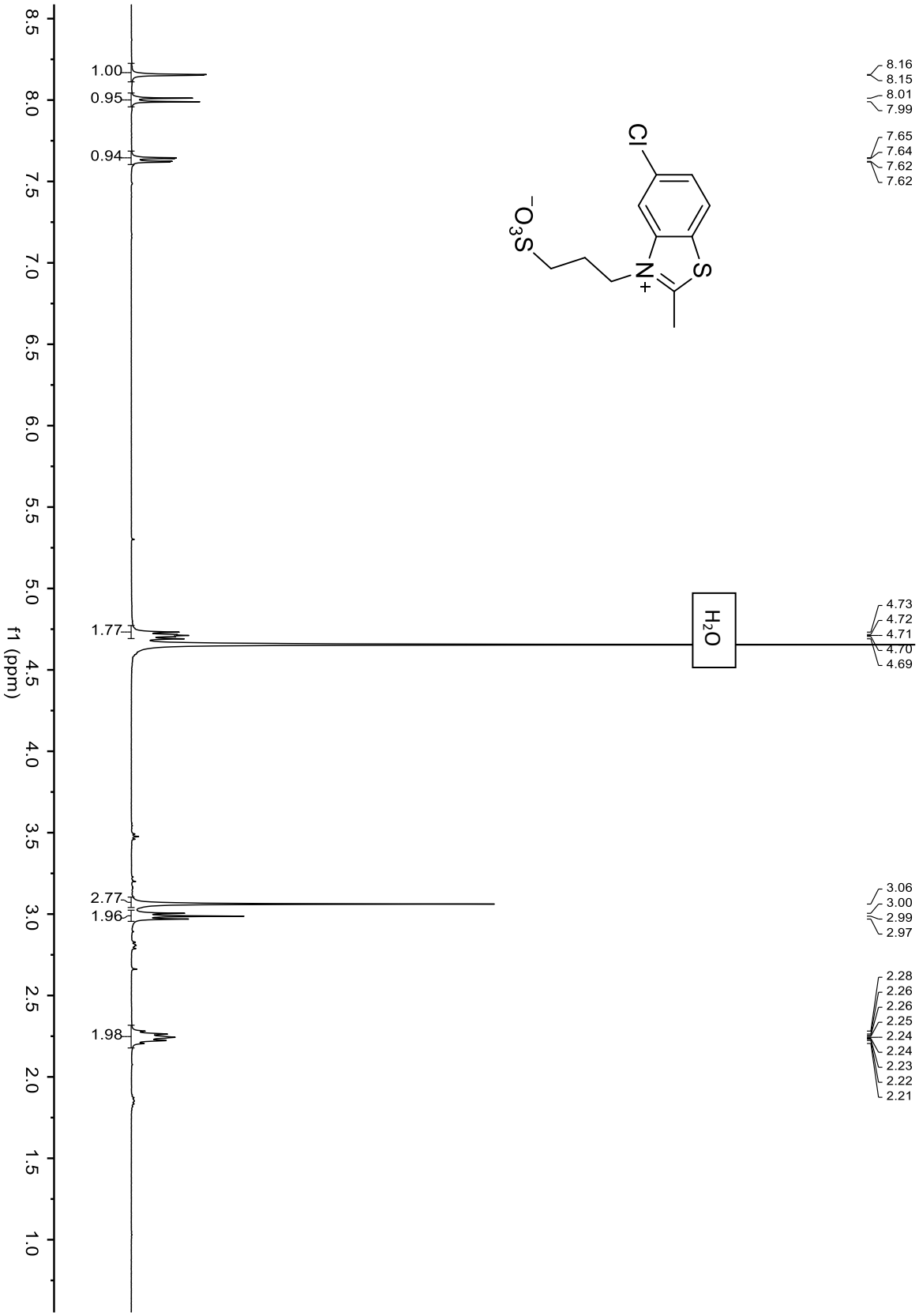
f1 (ppm)
8.5
8.0
7.5
7.0
6.5
6.0
5.5
5.0
4.5
4.0
3.5
3.0
2.5
2.0
1.5
1.0
1.00
0.95
0.94
1.77
2.77
1.96
1.98
H2O
Cl
−O3S
N+
S
8.16
8.15
8.01
7.99
7.65
7.64
7.62
7.62
4.73
4.72
4.71
4.70
4.69
3.06
3.00
2.99
2.97
2.28
2.26
2.26
2.25
2.24
2.24
2.23
2.22
2.21

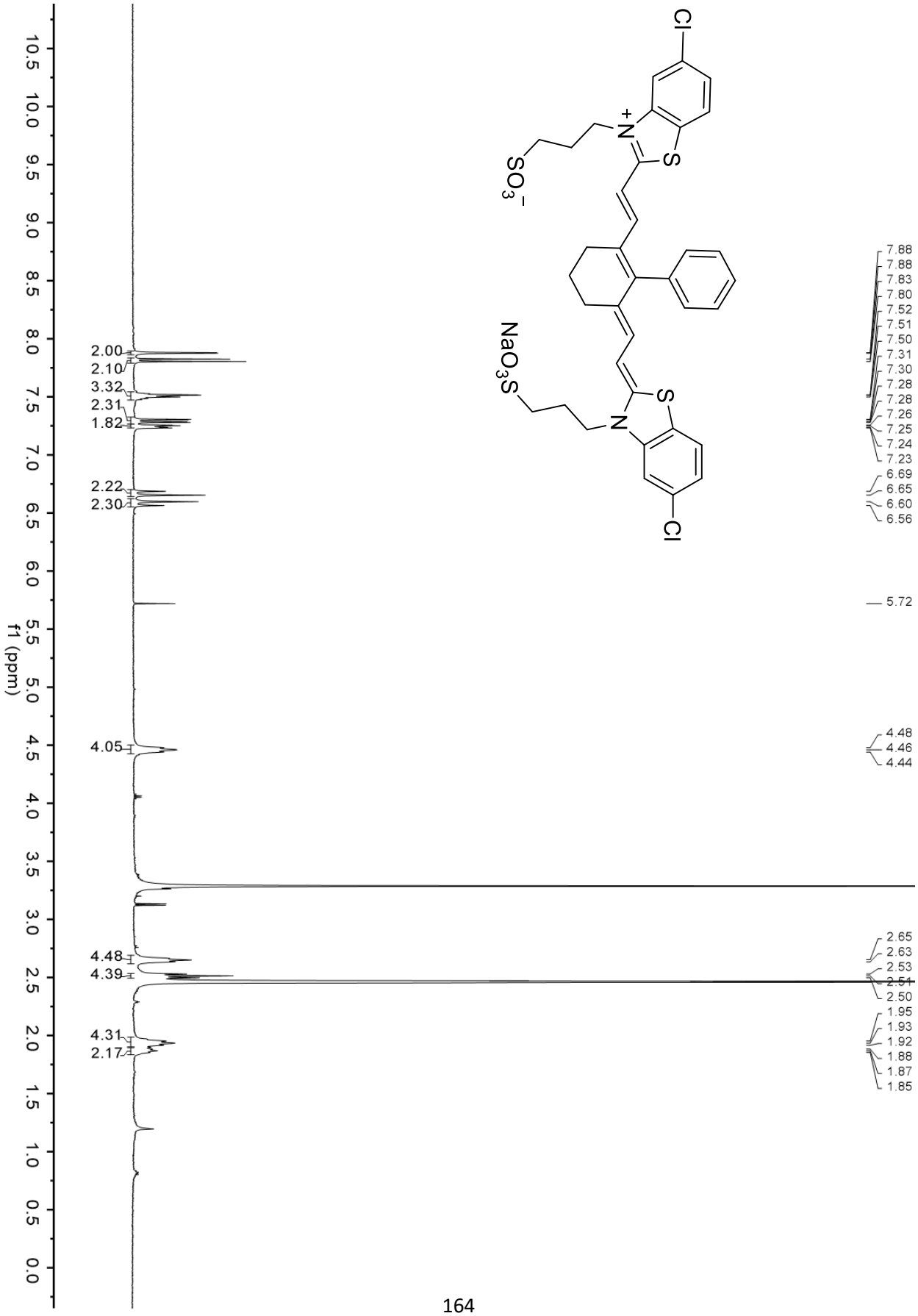
Cl
N+
S
SO3−
NaO3S
S
N
Cl
2.00
2.10
3.32
2.31
1.82
2.22
2.30
4.05
4.48
4.39
4.31
2.17
7.88
7.88
7.83
7.80
7.52
7.51
7.50
7.31
7.30
7.28
7.28
7.26
7.25
7.24
7.23
6.69
6.65
6.60
6.56
5.72
4.48
4.46
4.44
2.65
2.63
2.53
2.51
2.50
1.95
1.93
1.92
1.88
1.87
1.85
f1 (ppm)

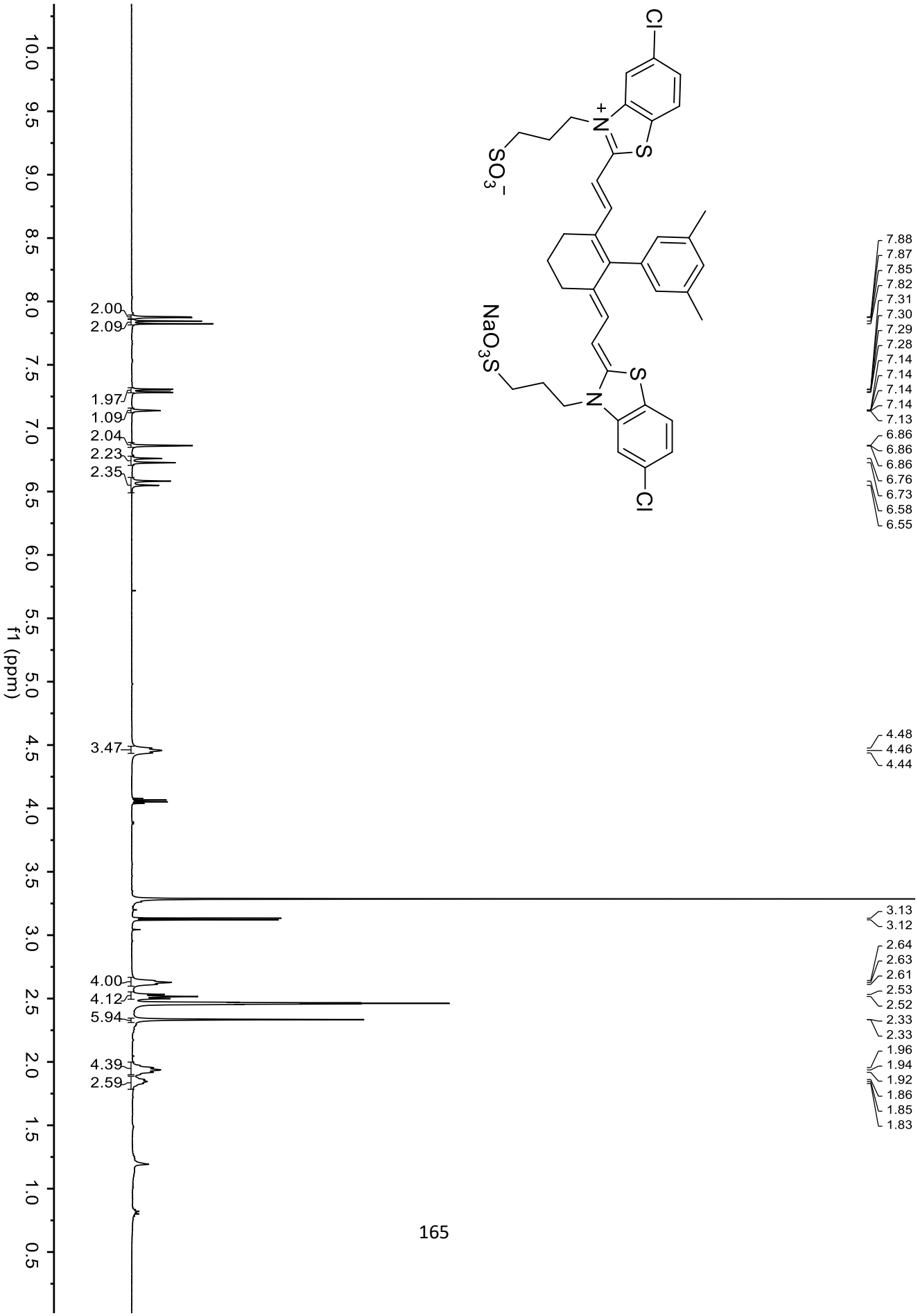
Cl
N+
S
SO3−
NaO3S
S
N
Cl
10.0
9.5
9.0
8.5
8.0
7.5
7.0
6.5
6.0
5.5
5.0
4.5
4.0
3.5
3.0
2.5
2.0
1.5
1.0
0.5
f1 (ppm)
2.00
2.09
1.97
1.09
2.04
2.23
2.35
3.47
4.00
4.12
5.94
4.39
2.59
7.88
7.87
7.85
7.82
7.31
7.30
7.29
7.28
7.14
7.14
7.14
7.14
7.13
6.86
6.86
6.86
6.76
6.73
6.58
6.55
4.48
4.46
4.44
3.13
3.12
2.64
2.63
2.61
2.53
2.52
2.33
2.33
1.96
1.94
1.92
1.86
1.85
1.83

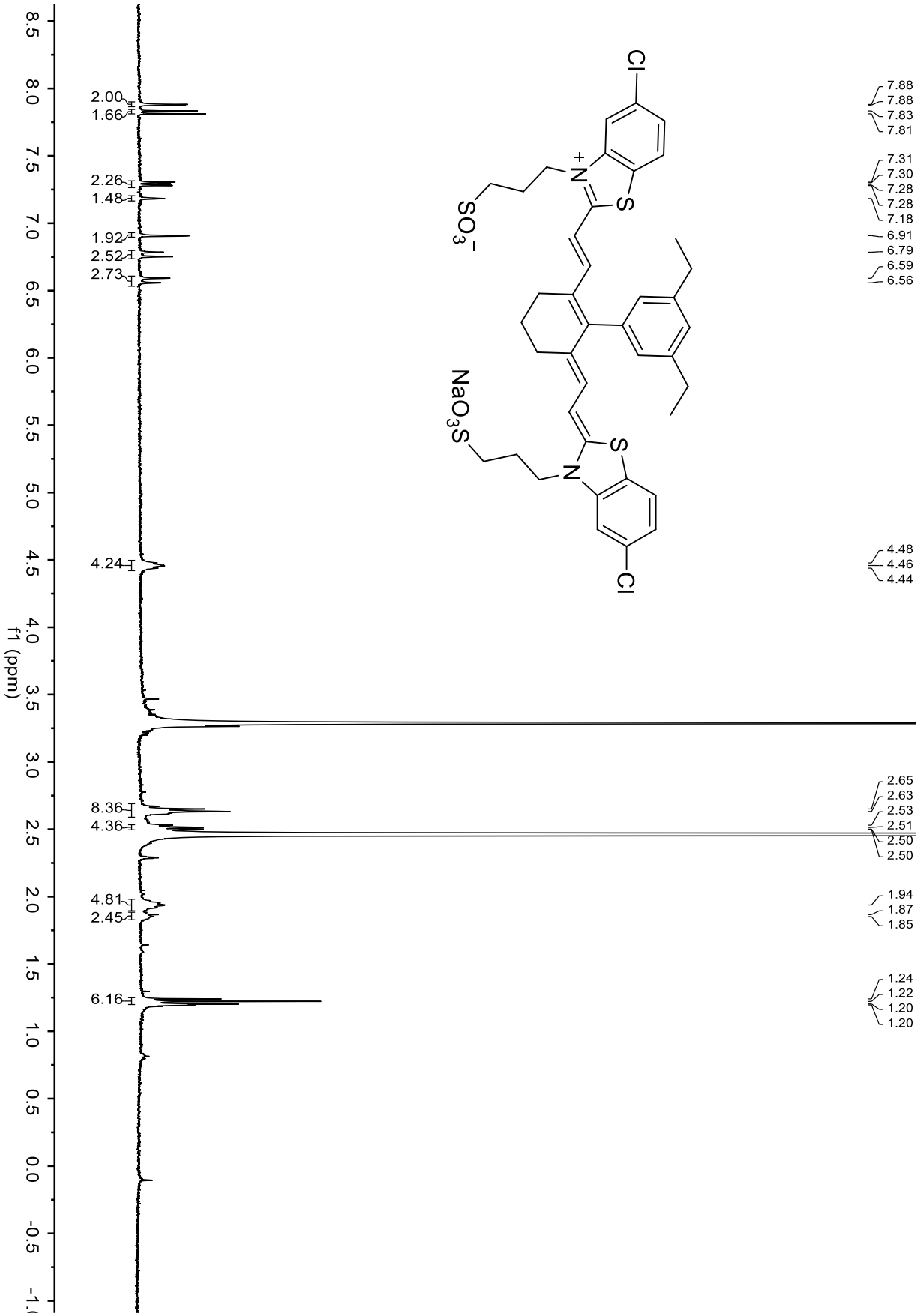
f1 (ppm)
8.5
8.0
7.5
7.0
6.5
6.0
5.5
5.0
4.5
4.0
3.5
3.0
2.5
2.0
1.5
1.0
0.5
0.0
-0.5
2.00
1.66
2.26
1.48
1.92
2.52
2.73
4.24
8.36
4.36
4.81
2.45
6.16
Cl
N+
S
SO3−
NaO3S
S
N
Cl
7.88
7.88
7.83
7.81
7.31
7.30
7.28
7.28
7.18
6.91
6.79
6.59
6.56
4.48
4.46
4.44
2.65
2.63
2.53
2.51
2.50
2.50
1.94
1.87
1.85
1.24
1.22
1.20
1.20

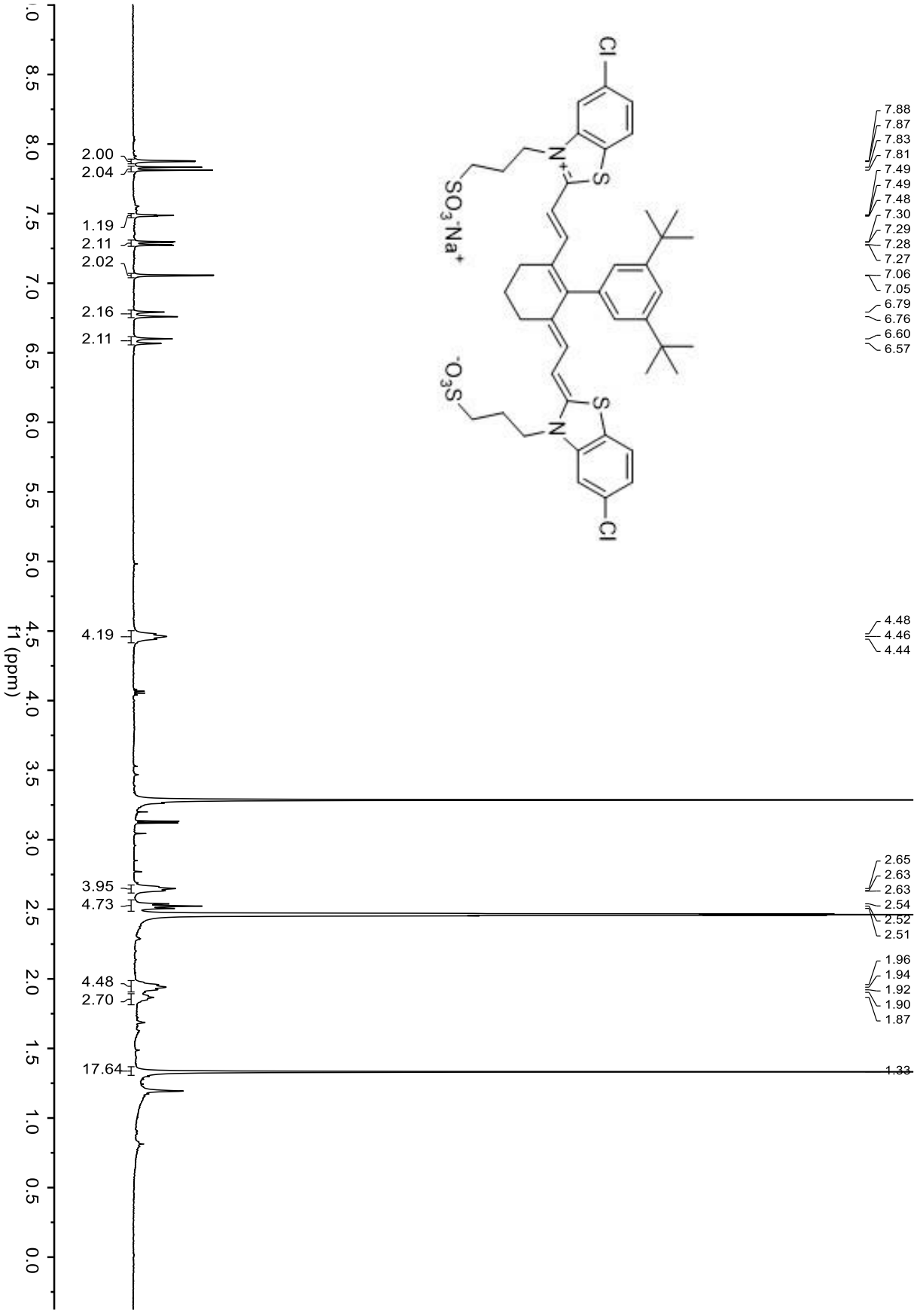
Cl
N+
S
SO3-Na+
-O3S
S
N
Cl
7.88
7.87
7.83
7.81
7.49
7.49
7.48
7.30
7.29
7.28
7.27
7.06
7.05
6.79
6.76
6.60
6.57
4.48
4.46
4.44
2.65
2.63
2.63
2.54
2.52
2.51
1.96
1.94
1.92
1.90
1.87
1.33
2.00
2.04
1.19
2.11
2.02
2.16
2.11
4.19
3.95
4.73
4.48
2.70
17.64
f1 (ppm)

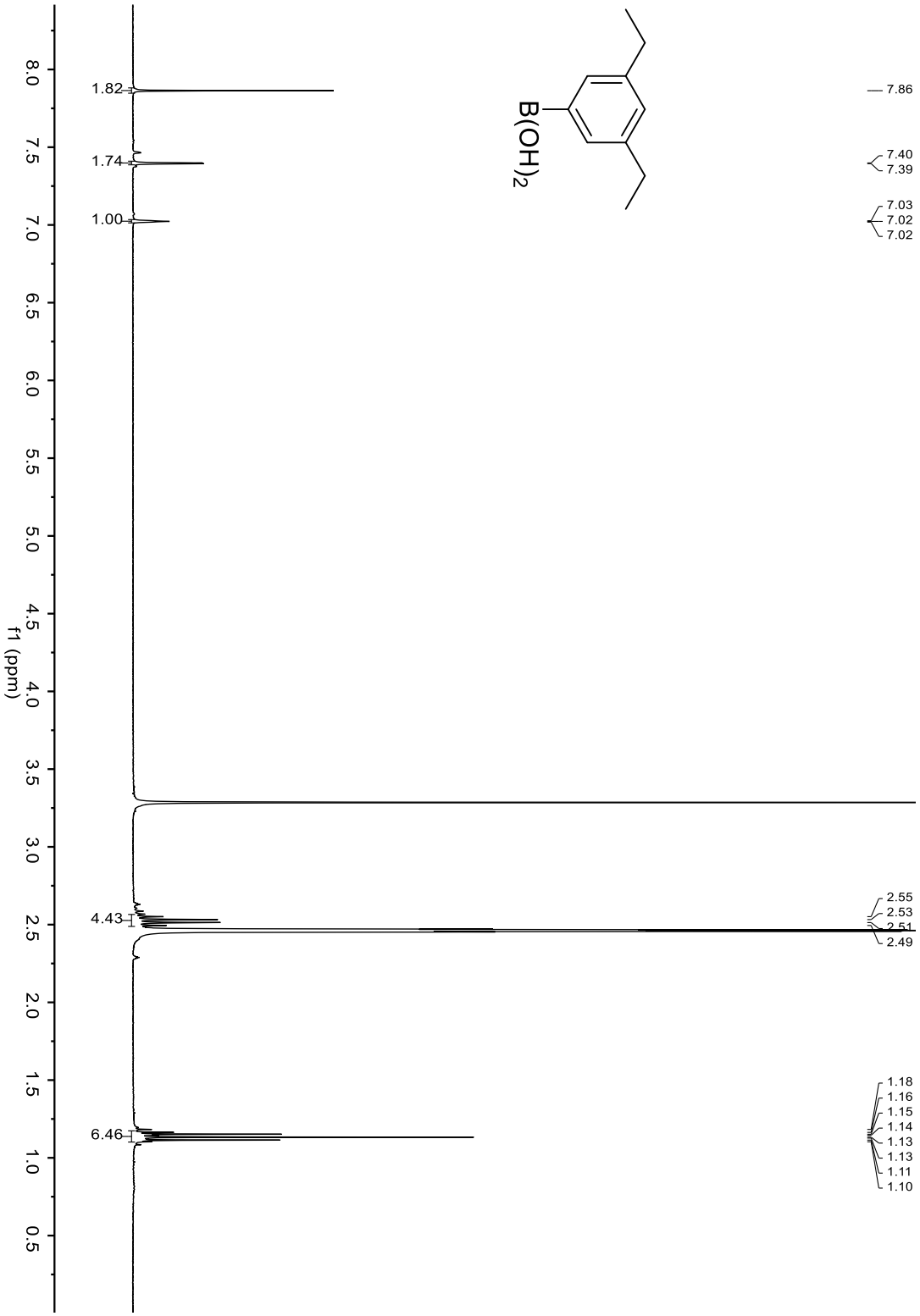
B(OH)2
1.82
1.74
1.00
4.43
6.46
7.86
7.40
7.39
7.03
7.02
7.02
2.55
2.53
2.51
2.49
1.18
1.16
1.15
1.14
1.13
1.13
1.11
1.10
f1 (ppm)

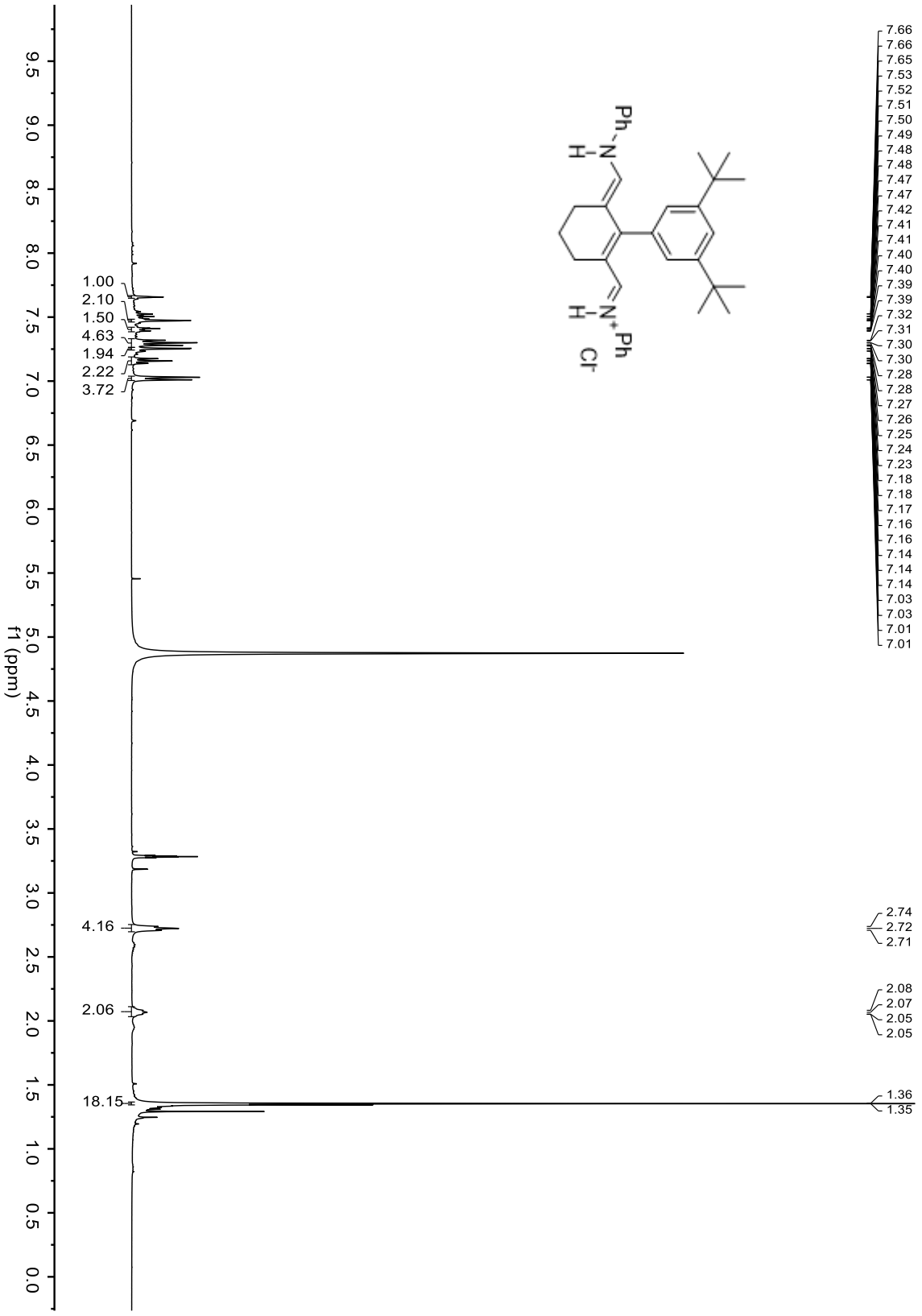
f1 (ppm)
9.5
9.0
8.5
8.0
7.5
7.0
6.5
6.0
5.5
5.0
4.5
4.0
3.5
3.0
2.5
2.0
1.5
1.0
0.5
0.0
1.00
2.10
1.50
4.63
1.94
2.22
3.72
4.16
2.06
18.15
Ph
N
H
N+
Ph
H
Cl
7.66
7.66
7.65
7.53
7.52
7.51
7.50
7.49
7.48
7.48
7.47
7.47
7.42
7.41
7.41
7.40
7.40
7.39
7.39
7.32
7.31
7.30
7.30
7.28
7.28
7.27
7.26
7.25
7.24
7.23
7.18
7.18
7.17
7.16
7.16
7.14
7.14
7.14
7.03
7.03
7.01
7.01
2.74
2.72
2.71
2.08
2.07
2.05
2.05
1.36
1.35

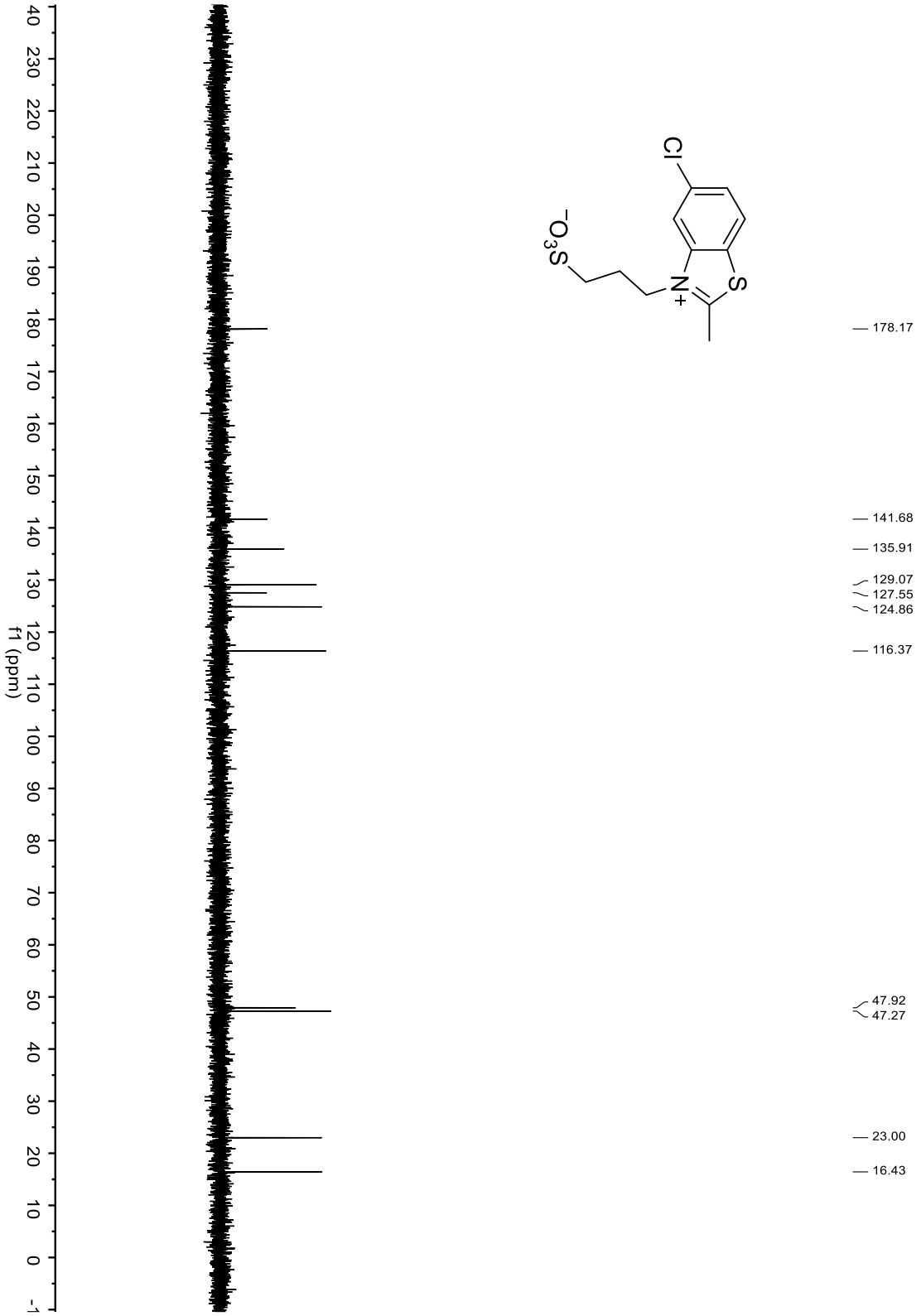
Cl
$^{-}O_3S$
N+
S
178.17
141.68
135.91
129.07
127.55
124.86
116.37
47.92
47.27
23.00
16.43
f1 (ppm)
40 230 220 210 200 190 180 170 160 150 140 130 120 110 100 90 80 70 60 50 40 30 20 10 0 -1

Chapter 6

Future Outlooks and Opportunities

In the preceding chapters, we discussed the fundamentals of J-aggregates, a high-resolution structure for a canonical J-aggregate, and several experiments that tested how particular covalent modifications to a dye monomer can affect its J-aggregation. However, many questions still remain about how chromophore structure informs self-assembly and how self-assembly can be exploited to yield desirable optical properties. Chapter six briefly summarizes two underexplored approaches with potential to provide either new methodology for studying J-aggregate structure or new chemistry that opens the application space for J-aggregate materials.

6.1. Generalized J-aggregation of polymethines using steric bulk

In Chapter 5, we discussed how the addition of the steric bulk at the 4' position of a Cy7 benzothiazole dye led to redshifting and stabilization of different morphological phases for its J-aggregates. We observed early in this work that the 4' substituent with the greatest steric bulk (i.e. 3,5-Ditertbutylphenyl) led to J-aggregation at lower salt concentrations and higher methanol ratios than the other dyes within that series. Therefore, we postulated that the use of a highly bulky linker would allow J-aggregate formation across a wide variety of dye scaffolds.

To test this, we synthesized a family of dyes from many different heterocycles with a 3,5-Ditertbutylphenyl group-based linker. The synthesis conditions and several heterocycles used for dye synthesis are shown in Figure 6.1.

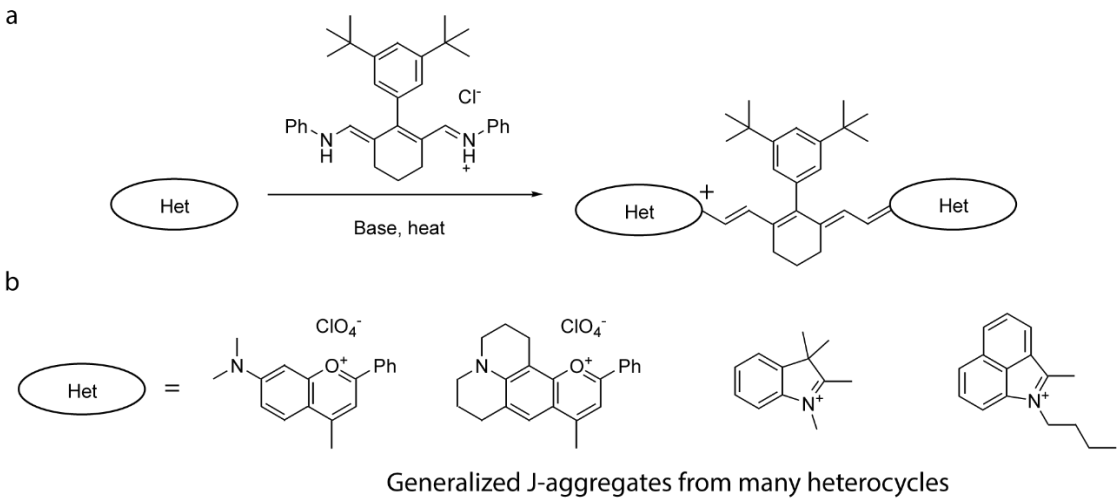

Figure 6.1. Synthesis of sterically bulky dyes for generalized J-aggregation. a) Synthetic scheme showing heterocycle, linker, and reaction conditions. b) Different heterocycle used for dye synthesis to screen for J-aggregation. Synthesis of these dyes (including Flav7-tBu) was performed by Monica Pengshung and Cesar Garcia.

Unfortunately, of the four heterocycles used for dye synthesis shown in Figure 6.1A, only one dye exhibited significant J-aggregation. The flavylium-DitBuPh dye (referred to as Flav7-tBu) J-aggregated in a mixture of 30-50% ethanol with 0.12 M NaCl brine. Because of the redshifted nature of flavylium dyes, these J-aggregates remarkably exhibited an absorption lambda max of 1361 nm. At these wavelengths, the dye absorption overlaps with the absorption of water, thereby requiring us to perform J-aggregation experiments using D_2O in place of H_2O. Absorbance of Flav7-tBu J-aggregates is shown in Figure 6.2.

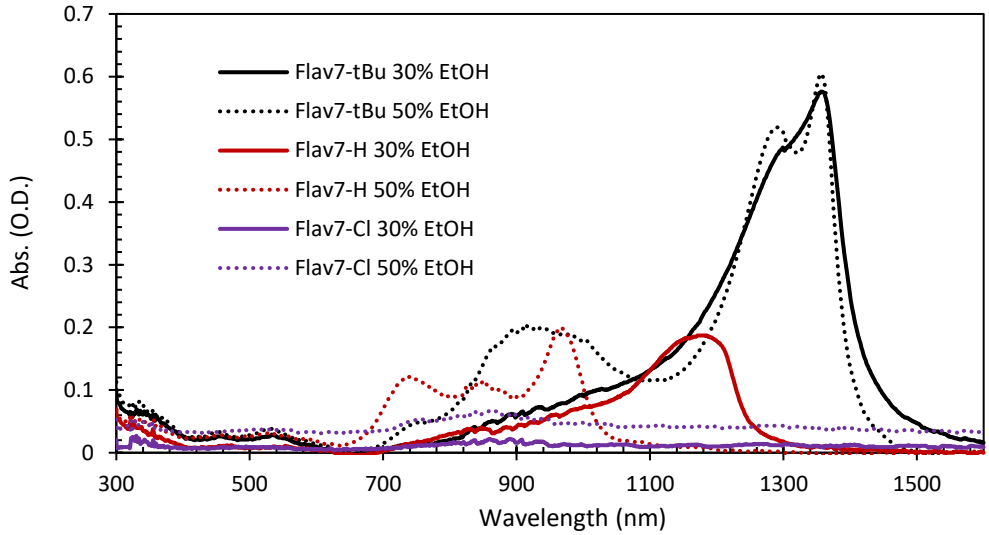

Figure 6.2. Absorbance showing J-aggregation of flavylium dyes with various 4' substituents. Aggregate absorption was measured in MeOH/D_2O with 0.12 M NaCl brine in a 1 mm cuvette approximately 24 h. after preparation. Dyes synthesized by Monica Pengshung.

Additionally, we wanted to explore to what extent the J-aggregates of Flav7 dyes were affected by their 4' substituent. That is, we wanted to understand whether flavylium-derived heptamethines J-aggregate generally, or whether the 3,5-ditertbutylphenyl substituent at the 4' position is required to induce J-aggregation. Using an identical procedure, we prepared J-aggregates of flavylium dyes with hydrogen and a chloro group as their 4' substituents. Interestingly, the chloro-derivative shows no aggregation, while the Flav7-H predominantly H-aggregates or forms broad J-aggregates. Indeed, only the Flav7-tBu showed significant J-aggregation, indicating that the 3,5-ditertbutylphenyl group was conducive towards self-assembly in a slip-stacked arrangement.

Interestingly, these J-aggregates exhibit two predominant features in their absorption (1300 and 1361 nm), separated by ~570 cm^{-1}. Based on the lineshape of other J-aggregates, these peaks may represent the parallel and perpendicular transitions of a tubular aggregate; however, a direct assignment of the nanoscale morphology would require confirmation via electron microscopy. It

should also be noted that these spectra were taken in 1 mm cuvette (typically J-aggregates at 0.1 mM concentration can be measured with optical density ~1 in a 0.2 mm cuvette), meaning that their optical density was relatively low and perhaps indicates low solubility of the dye monomer. We also examined the emission of the Flav7-tBu aggregates to explore their potential as emissive materials. Unfortunately, we found that the aggregates exhibited no fluorescence upon excitation with various wavelengths.

Because of the unique nature of these J-aggregates and their extreme redshift, it is imperative that we learn more about their morphology and photophysical properties. As mentioned previously, the development of emissive J-aggregates in the shortwave infrared could usher in a new generation of materials for information transmission faster than the current state of the art. Future experiments should include detailed screening of J-aggregation across different methanol/D_2O ratios, dye/salt concentrations, as well as an investigation regarding the kinetics of self-assembly. It may be possible to achieve emissive aggregates in this spectral window by adding additional steric bulk to the 4' position or modulating the chromophore's solubility.

6.2. Structural characterization of molecular aggregates via NMR

Chapter 3 discussed the enormous amount of structural information we obtained by reconstructing the C8S3 J-aggregate's inner wall via cryo-EM. While cryo-EM is quickly becoming one of the most prolific methodologies in structural biology, there are several other widely-used techniques for extracting structural information from biologically relevant macromolecules (e.g. proteins) that could allow researchers to further study J-aggregates. In particular, nuclear magnetic resonance (NMR) has been used extensively in structural biology but has not yet been extended meaningfully to molecular aggregate systems.

In a previous work from our lab, we used Diffusion Ordered Spectroscopy (DOSY) as a way to size small oligomers (H-aggregates) of a trimethine cyanine colloquially referred to as Cy3-Et.[105] DOSY, which is more commonly used in polymer chemistry, measures molecular diffusion coefficients using radio waves that probe nuclear spin transitions of large molecules.[111,112] This technique offers a unique approach in situations where dynamic light scattering (DLS) cannot compete due to samples either absorbing light or being too small to sufficiently scatter light. In our case, the H-aggregates and monomers of Cy3-Et were both too small to measure through light scattering, as well as absorbed light too closely to a common DLS laser line of 530 nm.

However, using DOSY, we were able to measure diffusion coefficients for both the dye monomer and its H-aggregates, then extract the hydrodynamic radii via the Stokes-Einstein equation. Figure 6.3 shows the DOSY spectrum of a Cy3-Et H-aggregates and compares their radius to that of the Cy3-Et monomer.

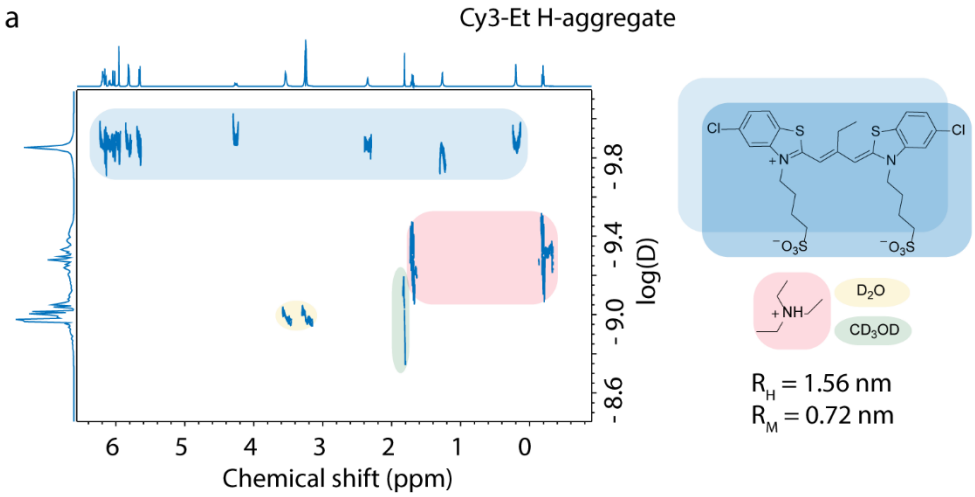

Figure 6.3. Structural characterization of Cy3-Et H-aggregate using DOSY. Adapted from Deshmukh *et al*.[105]

By taking DOSY spectra and backing out the hydrodynamic radii of the H-aggregate and dye monomer, we were able to confirm that the H-aggregate is roughly twice the size of the monomer. We therefore assumed that it represents a dimer. Our estimation of the H-aggregate's size was critical to developing a thermodynamic model of aggregation, wherein the equilibria between monomer, H-aggregate, and J-aggregates were required to be quantitative. Because of the line broadening associated with molecular aggregation, the H-aggregate samples needed to be considerably more concentrated than normal (2 mM as opposed to 0.1 mM) to obtain enough signal to complete the experiment within a several hour timeframe.

We also explored DOSY measurements of Cy3-Et J-aggregates, but found that the line broadening associated with J-aggregation resulted in a precipitous decrease of signal, ultimately preventing a meaningful measurement of the diffusion coefficient. Unfortunately, increasing the aggregate's concentration beyond 2 mM led to precipitation of the dye, which underscores the difficulty of studying aggregated materials that require specific concentration ranges. Recently a new NMR method was reported that would significantly reduce the time required for DOSY scans, which may allow researchers to measure diffusion coefficients of extended J-aggregates without forcing prohibitively long measurements.[113]

In addition to DOSY, we explored several other NMR experiments to extract structural information about J-aggregates. Nuclear Overhauser Effect Spectroscopy (NOESY) is another particularly useful multidimensional technique for studying large molecules.[114] The basic principle behind a ^{1}H NOESY experiment is that the intensity of cross peaks depends on the through-space interaction between protons. Nuclei that are spatially closer will produce a larger signal, with the largest observable distance between nuclei being approximately 5 Å.

One complication of NOESY experiments is that the net amount of signal relies heavily on the correlation time (approximately the reciprocal of the molecular tumbling rate), which is mainly determined by the molecular weight and viscosity of solvent. Because of this, small molecules (MW < 600 g/mol) exhibit positive NOE correlations, while large molecules (MW > 1200 g/mol) exhibit negative NOE correlations. For molecules between this range (most dye monomers), the NOE becomes much smaller and can theoretically be zero.[115] ROESY (Rotating frame Overhauser Effect Spectroscopy) is less sensitive to changes in molecular weight, though has a smaller dynamic range for its signal. Therefore, choosing the correct method between NOESY and ROESY may enormously expedite or increase the amount of signal in a measurement of through-space proton correlations. However, it is not clear how to exactly predict the tumbling rate of a supramolecular assembly.

Another parameter that requires optimization and complicates these experiments is the mixing time, which dictates the pause between pulses within the NOESY sequence. The duration required to maximize the NOE will depend on both the correlation time (molecular weight) as well as the distance between a particular nuclei pair. Small molecules generally yield higher NOE signals with longer mixing times (e.g. 500 ms), whereas large molecules do better with longer mixing times (e.g. 100 ms).

During our investigation of how steric bulk affects J-aggregation (Chapter 5), we found that several heptamethine cyanines from our study formed three unique aggregates that all exhibited a 2D sheetlike morphology. We briefly investigated using NOESY to probe the intermolecular interactions that could reveal differences between packing arrangements of chromophores. Figures 6.4 and 6.5 show NOESY spectra of two different sheetlike J-aggregates formed from Cy7-DiMePh.

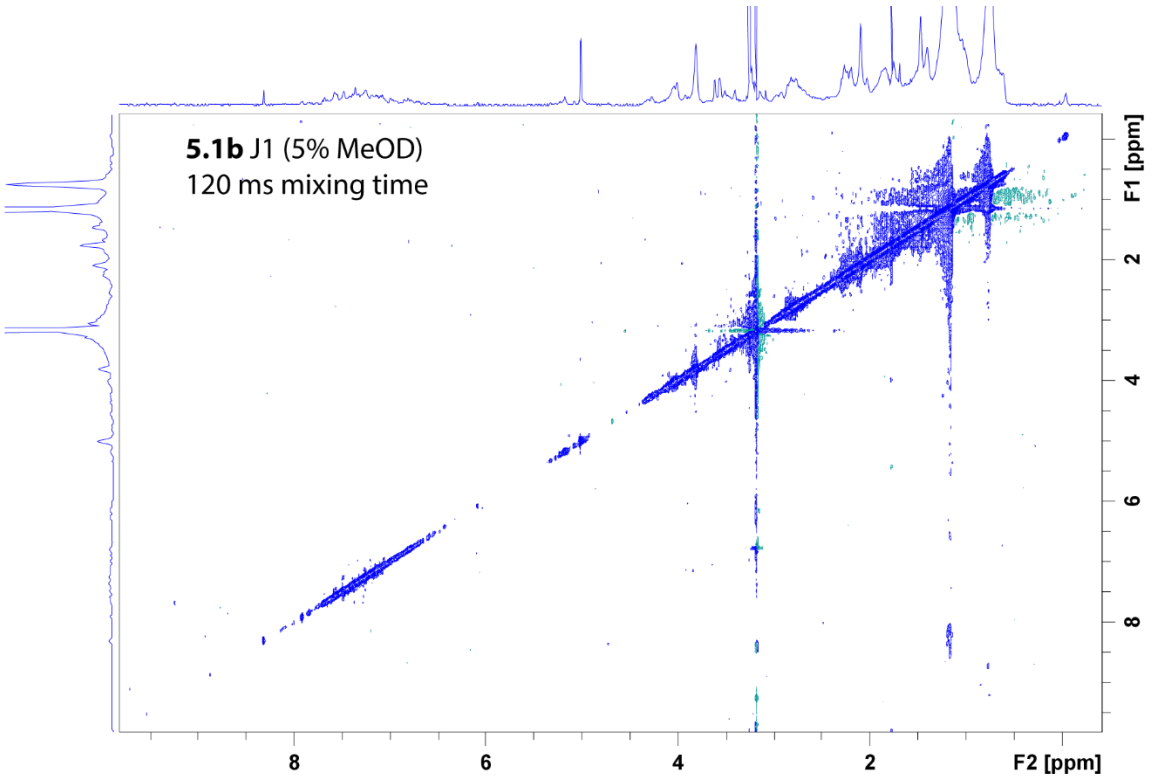

Figure 6.4. NOESY spectrum of **5.1b** J1 aggregates. Spectra taken on Bruker 800 MHz spectrometer with 120 ms mixing time. Samples were prepared in 5% MeOD/95% D_2O with 24 h. Data taken with assistance from Dr. Robert Peterson.

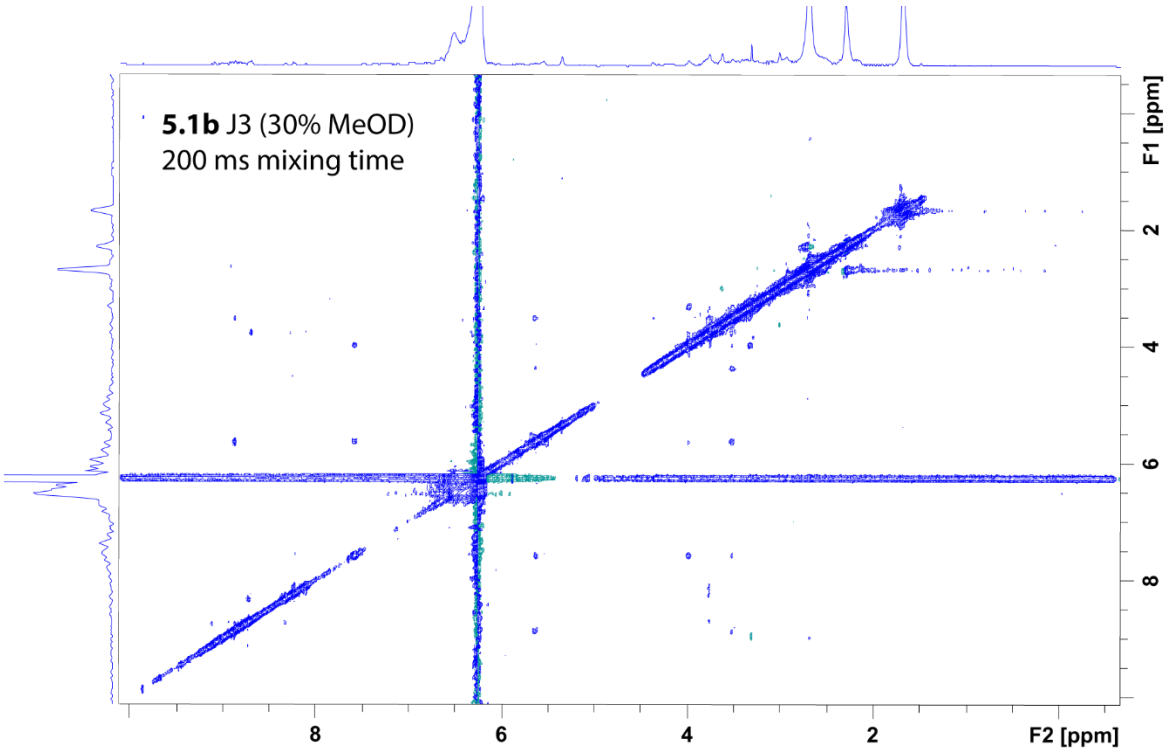

Figure 6.5. NOESY spectrum of **5.1b** J3 aggregates. Spectra taken on Bruker 800 MHz spectrometer with 120 ms mixing time. Samples were prepared in 30% MeOD/70% D_2O with 24 h. Data taken with assistance from Dr. Robert Peterson.

Comparison between Figure 6.2 and Figure 6.3 shows key differences in the magnitude and size of cross peaks. The J3 aggregate shows many cross peaks that are indicative of through-space proton interactions, while J1 shows far fewer. The analysis of these data is quite difficult because the cross peaks can originate from both proton-proton interactions within one monomer dye and from intermolecular interactions between adjacent dyes within the aggregate. While our preliminary work shows that the interactions are different between a monomer dye's NOESY spectrum and that of a J-aggregate, there needs to be more rigorous examination of this effect, preferably with a well-studied system where the molecular arrangement within the aggregate is known.

The last NMR experiment we attempted for the differentiation of sheetlike J-aggregates was to strategically label individual chromophores with fluorine atoms and use ^{19}F NMR as a way to determine their molecular arrangement within the 2D sheets. Because different arrangements of the dyes relative to one another could cause a larger distance between fluorine atoms, we hypothesized that the magnitude of the diagonal peak between these two fluorine signals could provide information that differentiates the molecular packing of otherwise identical sheets. Figure 6.6 shows the absorption spectra and molecular structure of the fluorine-labeled version of heptamethine cyanine **5.1b** (here referred to as **6.1**) that we hypothesized could be used for NOESY experiments.

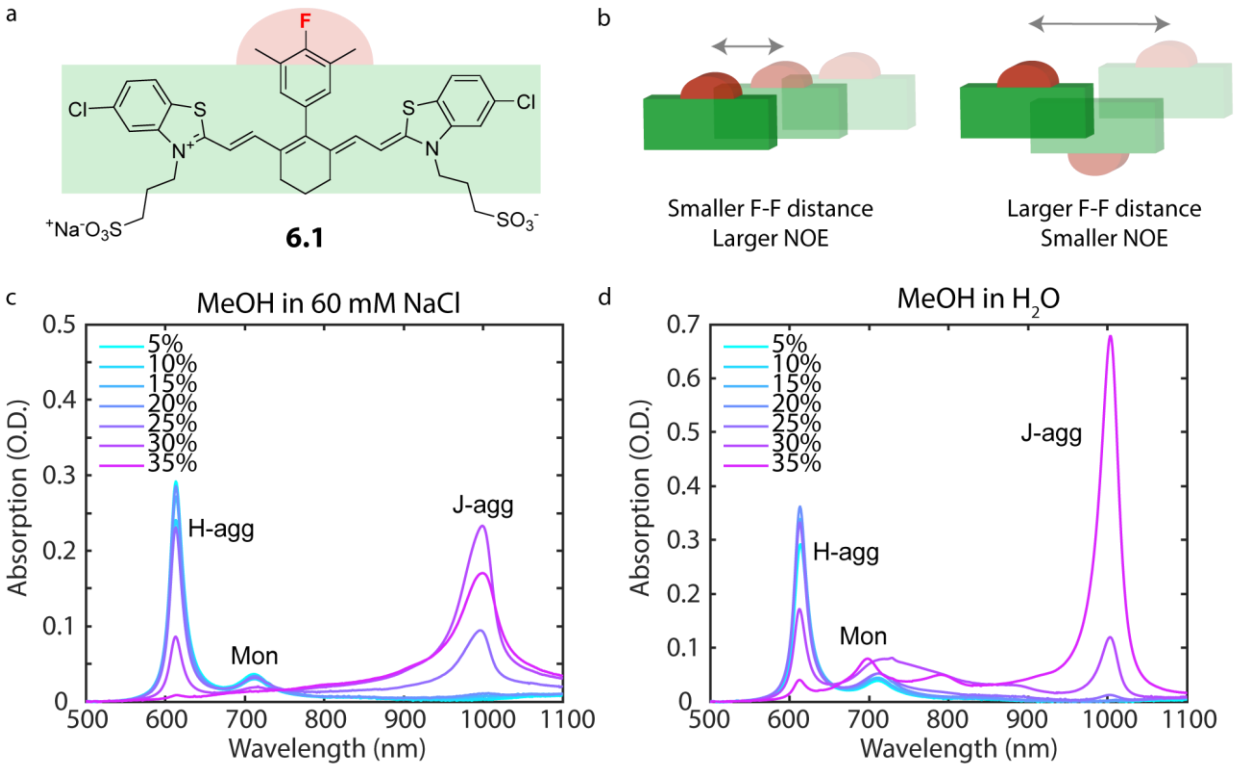

Figure 6.6. Absorption spectra and structure of **6.1** for NOESY experiments.
a,) Structure of **6.1** b) Cartoon showing different distances between fluorine nuclei for NOE experiment. c) Absorption spectra of **6.1** with 0.2 mM dye, 60 mM NaCl, 24 h. d) Absorption spectra of **6.1** with 0.2 mM dye, no salt, 24 h. Dye **6.1** synthesized by Cesar Garcia.

Unfortunately, we found that the fluorine-labeled dye **6.1** exhibited different aggregation behavior compared to its original counterpart (**5.1b**), undergoing both H- and J-aggregation even in solutions with high salt concentrations (Figure 6.5C and D). That is to say, the unique aggregation behavior we hoped to study with ^{19}F NMR was not preserved after the addition of a single fluorine atom. Although this experiment was not fruitful, it still underscores the possibility of using the method of fluorine labeling and selective NMR experimentation as a way to probe J-aggregation.

Another potentially transformative technique for studying J-aggregates is variable temperature (VT) NMR. Within the scope of VT measurements, any of the previously mentioned NMR experiments would offer structural information that has not yet been extracted for molecular aggregates. The main advantage of a VT experiment is the ability to disassemble the J-aggregate into H-aggregate and monomer parts and collect data in the various stages of decomposition. The mole fractions (obtained by temperature-dependent absorption) of these different components could then be correlated to any observable from NMR (e.g. proton-proton correlation, diffusion coefficient, chemical shift, etc.). Variable-temperature absorption data for a common trimethine J-aggregate (Cy3-Et) is shown in Figure 6.7.

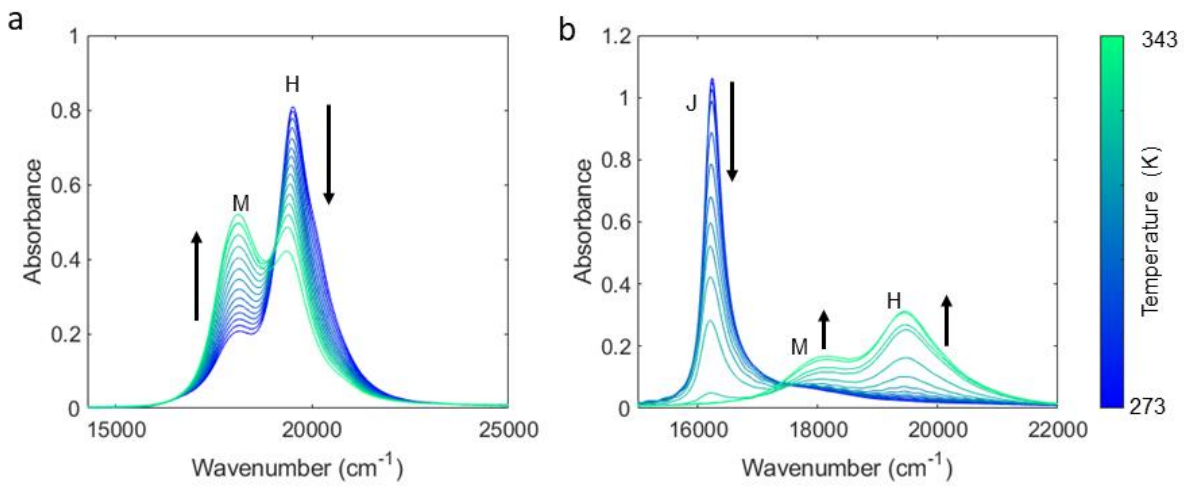

Figure 6.7. Temperature-dependent absorption of Cy3-Et J- and H-aggregates.
a) H-aggregate b) J-aggregate. Arrows indicate changes to optical density with increasing temperature. Data taken by Ray Huang and Anu Deshmukh.

Figure 6.3B shows that between 40-60 °C the Cy3-Et J-aggregates melt into an H-aggregated species and monomer, while the H-aggregates melt into primarily monomer. Viewing these transitions with simple ^{1}H NMR would allow us to understand how chemical shifts and line broadening change as a function of J-aggregation. Additional experiments such as VT NOESY or DOSY could allow us to correlate size and the magnitude of key intermolecular interactions going from the monomer to J-aggregate form.

There are several reasons why NOESY, DOSY, and variable temperature NMR measurements of molecular aggregates carry significance and require further investigation. First, there is novelty to measuring NMR of J-aggregated materials; NMR is an inexpensive, ubiquitous technique and yet the J-aggregate literature contains extremely few examples with NMR spectra beyond the requisite characterization of monomer dyes. Secondly, NMR is a much higher throughput

technique than electron microscopy that—if found to easily provide structural information about molecular aggregates—could enable facile access to structural information at high speed and low cost. Thirdly, it has been mentioned at several points in previous chapters that J-aggregates suffer from many constraints in their characterizations: limits on concentration, temperature, solvent, and solubility prevent many fundamental measurements that are standardized for similar nanomaterials. Therefore, if NMR measurements allow researchers to determine any new information about J-aggregates, these experiments will already be worthwhile.

6.3. Concluding remarks

While the fields of supramolecular chemistry and J-aggregated materials are far from solved, we have certainly made tremendous advances in our understanding of these systems in under a century. From the serendipitous discovery of J-aggregation in 1936 to the published high-resolution structure of an idyllic J-aggregate in 2023, this line of research will continue to make strides long into the future.

One broad, overarching goal I would like to conclude with is the idea of predicting how to design molecules a priori such that their interactions with one another can directly correlate to the dynamics of their supramolecular assemblies. This lofty goal would have wide-ranging impact and represent the highest possible level of our knowledge concerning these systems. Currently, that goal seems impossible. Without deep understanding concerning the exact magnitude and quantities of intermolecular forces, solvent effects, and more, that type of prediction is a fantasy. However, as we learn more and progress through supramolecular chemistry, we grow closer to that goal every year.

Our work on structure-property relationships between cyanine dyes and their monomers, elucidating the structure of molecular assemblies, and even the synthesis of new functional supramolecular materials, all take steps marching toward this goal. In the distant future, when these problems are solved, we may possess the ability to design supramolecular materials for many different types of applications such as imaging, light-harvesting, or telecommunications that far exceed our current capabilities. And while there are major challenges that must be addressed, I'm confident that these issues will continue to inspire creativity among scientists and usher them to pursue new and radical ideas for studying supramolecular systems.

References

(1) Cova, T. F. G. G.; Pais, A. A. C. C.; Seixas de Melo, J. S. Reconstructing the Historical Synthesis of Mauveine from Perkin and Caro: Procedure and Details. *Sci Rep* **2017**, *7* (1), 6806. https://doi.org/10.1038/s41598-017-07239-z.

(2) Ilina, K.; Henary, M. Cyanine Dyes Containing Quinoline Moieties: History, Synthesis, Optical Properties, and Applications. *Chemistry – A European Journal* **2021**, *27* (13), 4230–4248. https://doi.org/10.1002/chem.202003697.

(3) Williams, C. G. XXVI.—Researches on Chinoline and Its Homologues. *Earth and Environmental Science Transactions of The Royal Society of Edinburgh* **1857**, *21* (3), 377–401. https://doi.org/10.1017/S0080456800032208.

(4) Mishra, A.; Behera, R. K.; Behera, P. K.; Mishra, B. K.; Behera, G. B. Cyanines during the 1990s: A Review. *Chem. Rev.* **2000**, *100* (6), 1973–2012. https://doi.org/10.1021/cr990402t.

(5) Bricks, J. L.; Slominskii, Y. L.; Panas, I. D.; Demchenko, A. P. Fluorescent J-Aggregates of Cyanine Dyes: Basic Research and Applications Review. *Methods and Applications in Fluorescence* **2017**, *6* (1), 012001. https://doi.org/10.1088/2050-6120/aa8d0d.

(6) Tolbert, L. M.; Zhao, X. Beyond the Cyanine Limit: Peierls Distortion and Symmetry Collapse in a Polymethine Dye. *J. Am. Chem. Soc.* **1997**, *119* (14), 3253–3258. https://doi.org/10.1021/ja9626953.

(7) Pascal, S.; Haefele, A.; Monnereau, C.; Charaf-Eddin, A.; Jacquemin, D.; Guennic, B. L.; Andraud, C.; Maury, O. Expanding the Polymethine Paradigm: Evidence for the Contribution of

a Bis-Dipolar Electronic Structure. *Journal of Physical Chemistry A* **2014**, *118* (23), 4038–4047. https://doi.org/10.1021/JP501358Q.

(8) Jelley, E. E. Spectral Absorption and Fluorescence of Dyes in the Molecular State. *Nature* **1936**, *138* (3502), 1009–1010. https://doi.org/10.1038/1381009a0.

(9) Scheibe, G.; Kandler, L.; Ecker, H. Polymerisation und polymere Adsorption als Ursache neuartiger Absorptionsbanden von organischen Farbstoffen. *Naturwissenschaften* **1937**, *25* (5), 75–75. https://doi.org/10.1007/BF01493278.

(10) Hecht, M.; Würthner, F. Supramolecularly Engineered J-Aggregates Based on Perylene Bisimide Dyes. *Acc. Chem. Res.* **2021**, *54* (3), 642–653. https://doi.org/10.1021/acs.accounts.0c00590.

(11) Goswami, P. P.; Syed, A.; Beck, C. L.; Albright, T. R.; Mahoney, K. M.; Unash, R.; Smith, E. A.; Winter, A. H. BODIPY-Derived Photoremovable Protecting Groups Unmasked with Green Light. *Journal of the American Chemical Society* **2015**, *137* (11), 3783–3786. https://doi.org/10.1021/JACS.5B01297.

(12) Chan, J. M. W.; Tischler, J. R.; Kooi, S. E.; Bulović, V.; Swager, T. M. Synthesis of J-Aggregating Dibenz[a,j]Anthracene-Based Macrocycles. *J. Am. Chem. Soc.* **2009**, *131* (15), 5659–5666. https://doi.org/10.1021/ja900382r.

(13) Kasha, M. Energy Transfer Mechanisms and the Molecular Exciton Model for Molecular Aggregates. *Radiation Research* **1963**, *20* (1), 55–71.

(14) Deshmukh, A. P.; Koppel, D.; Chuang, C.; Cadena, D. M.; Cao, J.; Caram, J. R. Design Principles for Two-Dimensional Molecular Aggregates Using Kasha's Model: Tunable Photophysics in Near and Short-Wave Infrared. **2019**. https://doi.org/10.1021/acs.jpcc.9b05060.

(15) Saikin, S. K.; Eisfeld, A.; Valleau, S.; Aspuru-Guzik, A. Photonics Meets Excitonics: Natural and Artificial Molecular Aggregates. *Nanophotonics* **2013**, *2* (1), 21–38. https://doi.org/10.1515/nanoph-2012-0025.

(16) Barroso-Flores, J. Evolution of the Fenna–Matthews–Olson Complex and Its Quantum Coherence Features. Which Led the Way? *ACS Cent Sci* **2017**, *3* (10), 1061–1062. https://doi.org/10.1021/acscentsci.7b00386.

(17) Scholes, G. D.; Fleming, G. R.; Olaya-Castro, A.; Van Grondelle, R. Lessons from Nature about Solar Light Harvesting. *Nature Chemistry* **2011**, *3* (10), 763–774. https://doi.org/10.1038/nchem.1145.

(18) Balaban, T. S.; Tamiaki, H.; Holzwarth, A. R. Chlorins Programmed for Self-Assembly. In *Supermolecular Dye Chemistry*; Würthner, F., Ed.; Topics in Current Chemistry; Springer: Berlin, Heidelberg, 2005; pp 1–38. https://doi.org/10.1007/b137480.

(19) Engel, G. S.; Calhoun, T. R.; Read, E. L.; Ahn, T. K.; Mančal, T.; Cheng, Y. C.; Blankenship, R. E.; Fleming, G. R. Evidence for Wavelike Energy Transfer through Quantum Coherence in Photosynthetic Systems. *Nature* **2007**, *446* (7137), 782–786. https://doi.org/10.1038/nature05678.

(20) Caram, J. R.; Doria, S.; Eisele, D. M.; Freyria, F. S.; Sinclair, T. S.; Rebentrost, P.; Lloyd, S.; Bawendi, M. G. Room-Temperature Micron-Scale Exciton Migration in a Stabilized

Emissive Molecular Aggregate. *Nano Letters* **2016**, *16* (11), 6808–6815. https://doi.org/10.1021/acs.nanolett.6b02529.

(21) Walker, B. J.; Nair, G. P.; Marshall, L. F.; Bulović, V.; Bawendi, M. G. Narrowband Absorption-Enhanced Quantum Dot/J-Aggregate Conjugates. *J Am Chem Soc* **2009**, *131* (28), 9624–9625. https://doi.org/10.1021/ja902813q.

(22) Wang, C.; Weiss, E. A. Accelerating FRET between Near-Infrared Emitting Quantum Dots Using a Molecular J-Aggregate as an Exciton Bridge. *Nano Letters* **2017**, *17* (9), 5666–5671. https://doi.org/10.1021/ACS.NANOLETT.7B02559.

(23) Maity, P.; Gayathri, T.; Singh, S. P.; Ghosh, H. N. Impact of FRET between Molecular Aggregates and Quantum Dots. *Chemistry – An Asian Journal* **2019**, *14* (4), 597–605. https://doi.org/10.1002/asia.201801688.

(24) Pawlik, A.; Kirstein, S.; De Rossi, U.; Daehne, S. Structural Conditions for Spontaneous Generation of Optical Activity in J-Aggregates. *J. Phys. Chem. B* **1997**, *101* (29), 5646–5651. https://doi.org/10.1021/jp9708308.

(25) Rn Kriete, B.; Bondarenko, A. S.; Jumde, V. R.; Franken, L. E.; Minnaard, A. J.; Jansen, T. L. C.; Knoester, J.; Pshenichnikov, M. S. Steering Self-Assembly of Amphiphilic Molecular Nanostructures via Halogen Exchange. *J. Phys. Chem. Lett* **2017**. https://doi.org/10.1021/acs.jpclett.7b00967.

(26) Shindy, H. A. Fundamentals in the Chemistry of Cyanine Dyes: A Review. *Dyes and Pigments* **2017**, *145*, 505–513. https://doi.org/10.1016/j.dyepig.2017.06.029.

(27) Deshmukh, A.; Zheng, W.; Chuang, C.; Bailey, A.; Williams, J.; Sletten, E.; Egelman, E.; Caram, J. Near-Atomic Resolution Structure of J-Aggregated Helical Light Harvesting Nanotubes. ChemRxiv October 5, 2022. https://doi.org/10.26434/chemrxiv-2022-5m8sx.

(28) Pawlik, A.; Ouart, A.; Kirstein, S.; Abraham, H.-W.; Daehne, S. Synthesis and UV/Vis Spectra of J-Aggregating 5,5′,6,6′-Tetrachlorobenzimidacarbocyanine Dyes for Artificial Light-Harvesting Systems and for Asymmetrical Generation of Supramolecular Helices. *European Journal of Organic Chemistry* **2003**, *2003* (16), 3065–3080. https://doi.org/10.1002/ejoc.200300095.

(29) Daehne, S.; Rossi, U. D.; Moll, J. The J-Aggregation Phenomenon of Spectral Sensitizers: Structure, Spectroscopy, and Exciton Dynamics. 日本写真学会誌 **1996**, *59* (1), 250–259. https://doi.org/10.11454/photogrst1964.59.250.

(30) Spitz, C.; Knoester, J.; Ouart, A.; Daehne, S. Polarized Absorption and Anomalous Temperature Dependence of Fluorescence Depolarization in Cylindrical J-Aggregates. *Chemical Physics* **2002**, *275* (1), 271–284. https://doi.org/10.1016/S0301-0104(01)00521-3.

(31) Bednarz, M.; Knoester, J. The Linear Absorption and Pump−Probe Spectra of Cylindrical Molecular Aggregates. *J. Phys. Chem. B* **2001**, *105* (51), 12913–12923. https://doi.org/10.1021/jp012371n.

(32) Didraga, C.; Klugkist, J. A.; Knoester, J. Optical Properties of Helical Cylindrical Molecular Aggregates: The Homogeneous Limit. *J. Phys. Chem. B* **2002**, *106* (44), 11474–11486. https://doi.org/10.1021/jp026217s.

(33) Schade, B.; Singh, A. K.; Wycisk, V.; Cuellar-Camacho, J. L.; von Berlepsch, H.; Haag, R.; Böttcher, C. Stereochemistry-Controlled Supramolecular Architectures of New

Tetrahydroxy-Functionalised Amphiphilic Carbocyanine Dyes. *Chemistry – A European Journal* **2020**, *26* (30), 6919–6934. https://doi.org/10.1002/chem.201905745.

(34) Barotov, U.; Klein, M. D.; Wang, L.; Bawendi, M. G. Designing Highly Luminescent Molecular Aggregates via Bottom-Up Nanoscale Engineering. *J. Phys. Chem. C* **2022**, *126* (1), 754–763. https://doi.org/10.1021/acs.jpcc.1c09033.

(35) Cosco, E. D.; Caram, J. R.; Bruns, O. T.; Franke, D.; Day, R. A.; Farr, E. P.; Bawendi, M. G.; Sletten, E. M. Flavylium Polymethine Fluorophores for Near- and Shortwave Infrared Imaging. *Angewandte Chemie International Edition* **2017**, *56* (42), 13126–13129. https://doi.org/10.1002/anie.201706974.

(36) Bailey, A. D.; Deshmukh, A. P.; Bradbury, N. C.; Pengshung, M.; Atallah, T. L.; Williams, J. A.; Barotov, U.; Neuhauser, D.; Sletten, E. M.; Caram, J. R. Exploring the Design of Superradiant J-Aggregates from Amphiphilic Monomer Units. *Nanoscale* **2023**, *15* (8), 3841–3849. https://doi.org/10.1039/D2NR05747F.

(37) Li, W.; Li, W.; Gan, L.; Li, M.; Zheng, N.; Ning, C.; Chen, D.; Wu, Y.-C.; Su, S.-J. J-Aggregation Enhances the Electroluminescence Performance of a Sky-Blue Thermally Activated Delayed-Fluorescence Emitter in Nondoped Organic Light-Emitting Diodes. *ACS Appl. Mater. Interfaces* **2020**, *12* (2), 2717–2723. https://doi.org/10.1021/acsami.9b17585.

(38) Eisfeld, A.; Briggs, J. S. Dye Aggregates in Luminescent Solar Concentrators. *physica status solidi (a)* **2018**, *215* (2), 1700634. https://doi.org/10.1002/pssa.201700634.

(39) Kim, J. H.; Schembri, T.; Bialas, D.; Stolte, M.; Würthner, F. Slip-Stacked J-Aggregate Materials for Organic Solar Cells and Photodetectors. *Advanced Materials* **2022**, *34* (22), 2104678. https://doi.org/10.1002/adma.202104678.

(40) Sun, C.; Li, B.; Zhao, M.; Wang, S.; Lei, Z.; Lu, L.; Zhang, H.; Feng, L.; Dou, C.; Yin, D.; Xu, H.; Cheng, Y.; Zhang, F. J-Aggregates of Cyanine Dye for NIR-II in Vivo Dynamic Vascular Imaging beyond 1500 Nm. *Journal of the American Chemical Society* **2019**, *141* (49), 19221–19225. https://doi.org/10.1021/JACS.9B10043.

(41) Wang, X.; Jiang, Z.; Liang, Z.; Wang, T.; Chen, Y.; Liu, Z. Discovery of BODIPY J-Aggregates with Absorption Maxima beyond 1200 Nm for Biophotonics. *Science Advances* **2022**, *8* (48), eadd5660. https://doi.org/10.1126/sciadv.add5660.

(42) Veselovskii, I.; Kasianik, N.; Korenskii, M.; Hu, Q.; Goloub, P.; Podvin, T.; Liu, D. Multiwavelength Fluorescence Lidar Observations of Smoke Plumes. *Atmospheric Measurement Techniques* **2023**, *16* (8), 2055–2065. https://doi.org/10.5194/amt-16-2055-2023.

(43) Hilderbrand, S. A.; Weissleder, R. Near-Infrared Fluorescence: Application to in Vivo Molecular Imaging. *Current Opinion in Chemical Biology* **2010**, *14* (1), 71–79. https://doi.org/10.1016/J.CBPA.2009.09.029.

(44) Rondão, R.; Frias, A. R.; Correia, S. F. H.; Fu, L.; Bermudez, V. de Z.; André, P. S.; Ferreira, R. A. S.; Carlos, L. D. High-Performance Near-Infrared Luminescent Solar Concentrators. *ACS Applied Materials and Interfaces* **2017**, *9* (14), 12540–12546. https://doi.org/10.1021/ACSAMI.7B02700.

(45) Friedman, H.; Cosco, E.; Atallah, T.; Jia, S.; Sletten, E.; Caram, J. Establishing Design Principles for Emissive Organic SWIR Chromophores from Energy Gap Laws. *Chem* **2021**, *7*, 1–18. https://doi.org/10.26434/CHEMRXIV.14374493.V1.

(46) Bricks, J. L.; Kachkovskii, A. D.; Slominskii, Y. L.; Gerasov, A. O.; Popov, S. V. Molecular Design of near Infrared Polymethine Dyes: A Review. *Dyes and Pigments* **2015**. https://doi.org/10.1016/j.dyepig.2015.05.016.

(47) Helmerich, D. A.; Beliu, G.; Matikonda, S. S.; Schnermann, M. J.; Sauer, M. Photoblueing of Organic Dyes Can Cause Artifacts in Super-Resolution Microscopy. *Nature Methods 2021 18:3* **2021**, *18* (3), 253–257. https://doi.org/10.1038/s41592-021-01061-2.

(48) Clark, K. A.; Cone, C. W.; Bout, D. A. V. Quantifying the Polarization of Exciton Transitions in Double-Walled Nanotubular J-Aggregates. *J. Phys. Chem. C* **2013**, *117* (50), 26473–26481. https://doi.org/10.1021/jp409573h.

(49) Eisele, D. M.; Arias, D. H.; Fu, X.; Bloemsma, E. A.; Steiner, C. P.; Jensen, R. A.; Rebentrost, P.; Eisele, H.; Tokmakoff, A.; Lloyd, S.; Nelson, K. A.; Nicastro, D.; Knoester, J.; Bawendi, M. G. Robust Excitons Inhabit Soft Supramolecular Nanotubes. *Proceedings of the National Academy of Sciences of the United States of America* **2014**, *111* (33), E3367–E3375. https://doi.org/10.1073/pnas.1408342111.

(50) Martinez, V.; Henary, M. Nile Red and Nile Blue: Applications and Syntheses of Structural Analogues. *Chemistry - A European Journal* **2016**, *22* (39), 13764–13782. https://doi.org/10.1002/chem.201601570.

(51) De Mello, J. C.; Wittmann, H. F.; Friend, R. H. An Improved Experimental Determination of External Photoluminescence Quantum Efficiency. *Advanced Materials* **1997**, *9* (3), 230–232. https://doi.org/10.1002/adma.19970090308.

(52) Atallah, T. L.; Sica, A. V.; Shin, A. J.; Friedman, H. C.; Kahrobai, Y. K.; Caram, J. R. Decay-Associated Fourier Spectroscopy: Visible to Shortwave Infrared Time-Resolved

Photoluminescence Spectra. *Journal of Physical Chemistry A* **2019**, *123* (31), 6792–6798. https://doi.org/10.1021/acs.jpca.9b04924.

(53) Sillen, A.; Engelborghs, Y. The Correct Use of "Average" Fluorescence Parameters. *Photochemistry and Photobiology* **1998**, *67* (5), 475–486. https://doi.org/10.1111/j.1751-1097.1998.tb09082.x.

(54) Doria, S.; Sinclair, T. S.; Klein, N. D.; Bennett, D. I. G.; Chuang, C.; Freyria, F. S.; Steiner, C. P.; Foggi, P.; Nelson, K. A.; Cao, J.; Aspuru-Guzik, A.; Lloyd, S.; Caram, J. R.; Bawendi, M. G. Photochemical Control of Exciton Superradiance in Light-Harvesting Nanotubes. *ACS Nano* **2018**, *12* (5), 4556–4564. https://doi.org/10.1021/acsnano.8b00911.

(55) Akins, D. L. Superradiance of Aggregated Thiacarbocyanine Molecules. **1999**. https://doi.org/10.1021/jp991627a.

(56) Tsurumi, T.; Hirayama, H.; Vacha, M.; Taniyama, T. *Nanoscale Physics for Materials Science*; Taylor & Francis: Abingdon, 2010.

(57) Freyria, F. S.; Cordero, J. M.; Caram, J. R.; Doria, S.; Dodin, A.; Chen, Y.; Willard, A. P.; Bawendi, M. G. Near-Infrared Quantum Dot Emission Enhanced by Stabilized Self-Assembled J-Aggregate Antennas. *Nano Letters* **2017**, *17* (12), 7665–7674. https://doi.org/10.1021/acs.nanolett.7b03735.

(58) *Stochastically Realized Observables for Excitonic Molecular Aggregates | The Journal of Physical Chemistry A*. https://pubs.acs.org/doi/10.1021/acs.jpca.0c07953 (accessed 2022-09-05).

(59) Deshmukh, A. P.; Geue, N.; Bradbury, N. C.; Atallah, T. L.; Chuang, C.; Pengshung, M.; Cao, J.; Sletten, E. M.; Neuhauser, D.; Caram, J. R. Bridging the Gap between H- and J-

Aggregates: Classification and Supramolecular Tunability for Excitonic Band Structures in Two-Dimensional Molecular Aggregates. *Chemical Physics Reviews* **2022**, *3* (2), 021401. https://doi.org/10.1063/5.0094451.

(60) Didraga, C.; Pugžlys, A.; Hania, P. R.; Von Berlepsch, H.; Duppen, K.; Knoester, J. Structure, Spectroscopy, and Microscopic Model of Tubular Carbocyanine Dye Aggregates. *Journal of Physical Chemistry B* **2004**, *108* (39), 14976–14985. https://doi.org/10.1021/JP048288S/ASSET/IMAGES/MEDIUM/JP048288SE00023.GIF.

(61) Guthery, Scott. *A Motif of Mathematics: History and Application of the Mediant and the Farey Sequence*; Docent Press: North Charleston, SC, 2011.

(62) Chuang, C.; Knoester, J.; Cao, J. Scaling Relations and Optimization of Excitonic Energy Transfer Rates between One-Dimensional Molecular Aggregates. *J. Phys. Chem. B* **2014**, *118* (28), 7827–7834. https://doi.org/10.1021/jp4124502.

(63) Hernandez, R.; Heskamp, S.; Rijpkema, M.; Bos, D. L.; Goldenberg, D. M.; McBride, W. J.; Morgenstern, A.; Bruchertseifer, F.; Cai, W.; Boerman, O. C. Preventing Radiobleaching of Cyanine Fluorophores Enhances Stability of Nuclear/NIRF Multimodality Imaging Agents. *Theranostics* **2017**, *7* (1), 1–8. https://doi.org/10.7150/thno.15124.

(64) Lovett, W. R.; Al Hamd, A.; Casa, S.; Henary, M. Synthesis of pH-Sensitive Benzothiazole Cyanine Dye Derivatives Containing a Pyridine Moiety at the Meso Position. *Dyes and Pigments* **2021**, *190*, 109268. https://doi.org/10.1016/j.dyepig.2021.109268.

(65) Cooper, M. E.; Gregory, S.; Adie, E.; Kalinka, S. pH-Sensitive Cyanine Dyes for Biological Applications. *Journal of Fluorescence* **2002**, *12* (3), 425–429. https://doi.org/10.1023/A:1021366010681.

(66) Berezin, M. Y.; Guo, K.; Akers, W.; Northdurft, R. E.; Culver, J. P.; Teng, B.; Vasalatiy, O.; Barbacow, K.; Gandjbakhche, A.; Griffiths, G. L.; Achilefu, S. Near-Infrared Fluorescence Lifetime pH-Sensitive Probes. *Biophys J* **2011**, *100* (8), 2063–2072. https://doi.org/10.1016/j.bpj.2011.02.050.

(67) Eisele, D. M.; Cone, C. W.; Bloemsma, E. A.; Vlaming, S. M.; Van Der Kwaak, C. G. F.; Silbey, R. J.; Bawendi, M. G.; Knoester, J.; Rabe, J. P.; Vanden Bout, D. A. Utilizing Redox-Chemistry to Elucidate the Nature of Exciton Transitions in Supramolecular Dye Nanotubes. *Nature Chemistry* **2012**, *4* (8), 655–662. https://doi.org/10.1038/nchem.1380.

(68) Friedl, C.; Renger, T.; Berlepsch, H. v.; Ludwig, K.; Schmidt am Busch, M.; Megow, J. Structure Prediction of Self-Assembled Dye Aggregates from Cryogenic Transmission Electron Microscopy, Molecular Mechanics, and Theory of Optical Spectra. *J. Phys. Chem. C* **2016**, *120* (34), 19416–19433. https://doi.org/10.1021/acs.jpcc.6b05856.

(69) Renaud, J.-P.; Chari, A.; Ciferri, C.; Liu, W.; Rémigy, H.-W.; Stark, H.; Wiesmann, C. Cryo-EM in Drug Discovery: Achievements, Limitations and Prospects. *Nat Rev Drug Discov* **2018**, *17* (7), 471–492. https://doi.org/10.1038/nrd.2018.77.

(70) Biou, V. Lipid-Membrane Protein Interaction Visualised by Cryo-EM: A Review. *Biochim Biophys Acta Biomembr* **2023**, *1865* (1), 184068. https://doi.org/10.1016/j.bbamem.2022.184068.

(71) Dubochet, J. Cryo-EM--the First Thirty Years. *J Microsc* **2012**, *245* (3), 221–224. https://doi.org/10.1111/j.1365-2818.2011.03569.x.

(72) Ma, H.; Jia, X.; Zhang, K.; Su, Z. Cryo-EM Advances in RNA Structure Determination. *Sig Transduct Target Ther* **2022**, *7* (1), 1–6. https://doi.org/10.1038/s41392-022-00916-0.

(73) Tian, J.; Xie, S.-H.; Borucu, U.; Lei, S.; Zhang, Y.; Manners, I. High-Resolution Cryo-Electron Microscopy Structure of Block Copolymer Nanofibres with a Crystalline Core. *Nat. Mater.* **2023**, *22* (6), 786–792. https://doi.org/10.1038/s41563-023-01559-4.

(74) Egelman, E. H. The Iterative Helical Real Space Reconstruction Method: Surmounting the Problems Posed by Real Polymers. *Journal of Structural Biology* **2007**, *157* (1), 83–94. https://doi.org/10.1016/j.jsb.2006.05.015.

(75) Egelman, E. H. A Robust Algorithm for the Reconstruction of Helical Filaments Using Single-Particle Methods. *Ultramicroscopy* **2000**, *85* (4), 225–234. https://doi.org/10.1016/S0304-3991(00)00062-0.

(76) Egelman, E. H. Chapter Six - Reconstruction of Helical Filaments and Tubes. In *Methods in Enzymology*; Jensen, G. J., Ed.; Cryo-EM, Part B: 3-D Reconstruction; Academic Press, 2010; Vol. 482, pp 167–183. https://doi.org/10.1016/S0076-6879(10)82006-3.

(77) Deng, J.-H.; Luo, J.; Mao, Y.-L.; Lai, S.; Gong, Y.-N.; Zhong, D.-C.; Lu, T.-B. π-π Stacking Interactions: Non-Negligible Forces for Stabilizing Porous Supramolecular Frameworks. *Science Advances* **2020**, *6* (2), eaax9976. https://doi.org/10.1126/sciadv.aax9976.

(78) Hofrichter, J.; Eaton, W. A. Linear Dichroism of Biological Chromophores. *Annual Review of Biophysics and Bioengineering* **1976**, *5* (1), 511–560. https://doi.org/10.1146/annurev.bb.05.060176.002455.

(79) Nordén, B. Applications of Linear Dichroism Spectroscopy. *Applied Spectroscopy Reviews* **1978**, *14* (2), 157–248. https://doi.org/10.1080/05704927808060393.

(80) Lotya, M.; Rakovich, A.; Donegan, J. F.; Coleman, J. N. Measuring the Lateral Size of Liquid-Exfoliated Nanosheets with Dynamic Light Scattering. *Nanotechnology* **2013**, *24* (26), 265703. https://doi.org/10.1088/0957-4484/24/26/265703.

(81) Altavilla, C.; Sarno, M.; Ciambelli, P. A Novel Wet Chemistry Approach for the Synthesis of Hybrid 2D Free-Floating Single or Multilayer Nanosheets of MS2@oleylamine (M═Mo, W). *Chem. Mater.* **2011**, *23* (17), 3879–3885. https://doi.org/10.1021/cm200837g.

(82) Kriete, B.; Lüttig, J.; Kunsel, T.; Malý, P.; Jansen, T. L. C.; Knoester, J.; Brixner, T.; Pshenichnikov, M. S. Interplay between Structural Hierarchy and Exciton Diffusion in Artificial Light Harvesting. *Nat Commun* **2019**, *10* (1), 4615. https://doi.org/10.1038/s41467-019-12345-9.

(83) Krishnaswamy, S. R.; Gabrovski, I. A.; Patmanidis, I.; Stuart, M. C. A.; de Vries, A. H.; Pshenichnikov, M. S. Cryogenic TEM Imaging of Artificial Light Harvesting Complexes Outside Equilibrium. *Sci Rep* **2022**, *12* (1), 5552. https://doi.org/10.1038/s41598-022-09496-z.

(84) Patmanidis, I.; T. Souza, P. C.; Sami, S.; A. Havenith, R. W.; Vries, A. H. de; J. Marrink, S. Modelling Structural Properties of Cyanine Dye Nanotubes at Coarse-Grained Level. *Nanoscale Advances* **2022**, *4* (14), 3033–3042. https://doi.org/10.1039/D2NA00158F.

(85) Bondarenko, A. S.; Jansen, T. L. C.; Knoester, J. Exciton Localization in Tubular Molecular Aggregates: Size Effects and Optical Response. *arXiv* **2020**, *152* (19), 194302. https://doi.org/10.1063/5.0008688.

(86) Harazi, S.; Kapon, O.; Sharoni, A.; Tischler, Y. R. Direct Formation of Carbocyanine J-Aggregates in Organic Solvent. *J. Phys. Chem. C* **2019**, *123* (31), 19087–19093. https://doi.org/10.1021/acs.jpcc.9b01116.

(87) Roth, S. M.; Press, D. J.; Heyne, B.; Sutherland, T. C. Synthetic Access to Benzimidacarbocyanine Dyes to Tailor Their Aggregation Properties. *The Journal of Organic Chemistry* **2021**, *86*, 8651. https://doi.org/10.1021/ACS.JOC.1C00385.

(88) Thyrhaug, E.; Žídek, K.; Dostál, J.; Bína, D.; Zigmantas, D. Exciton Structure and Energy Transfer in the Fenna–Matthews–Olson Complex. *J. Phys. Chem. Lett.* **2016**, *7* (9), 1653–1660. https://doi.org/10.1021/acs.jpclett.6b00534.

(89) Didraga, C.; Knoester, J. Optical Spectra and Localization of Excitons in Inhomogeneous Helical Cylindrical Aggregates. *J Chem Phys* **2004**, *121* (21), 10687–10698. https://doi.org/10.1063/1.1807825.

(90) Hans von Berlepsch, *, †; Stefan Kirstein, ‡ and; Böttcher†, C. Supramolecular Structure of J-Aggregates of a Sulfonate Substituted Amphiphilic Carbocyanine Dye in Solution: Methanol-Induced Ribbon-to-Tubule Transformation. *Journal of Physical Chemistry B* **2004**, *108* (48), 18725–18733. https://doi.org/10.1021/JP046546F.

(91) Cone, C. W.; Cho, S.; Lyon, J. L.; Eisele, D. M.; Rabe, J. P.; Stevenson, K. J.; Rossky, P. J.; Bout, D. A. V. Singular Value Decomposition Analysis of Spectroelectrochemical Redox Chemistry in Supramolecular Dye Nanotubes. *Journal of Physical Chemistry C* **2011**, *115* (30), 14978–14987. https://doi.org/10.1021/JP2019457.

(92) Sorokin, A. V.; Ropakova, I. Yu.; Grynyov, R. S.; Vilkisky, M. M.; Liakh, V. M.; Borovoy, I. A.; Yefimova, S. L.; Malyukin, Y. V. Strong Difference between Optical Properties and Morphologies for J-Aggregates of Similar Cyanine Dyes. *Dyes and Pigments* **2018**, *152*, 49–53. https://doi.org/10.1016/j.dyepig.2018.01.032.

(93) von Berlepsch, H.; Regenbrecht, M.; Dähne, S.; Kirstein, S.; Böttcher, C. Surfactant-Induced Separation of Stacked J-Aggregates. Cryo-Transmission Electron Microscopy Studies Reveal Bilayer Ribbons. *Langmuir* **2002**, *18* (7), 2901–2907. https://doi.org/10.1021/la011602e.

(94) Würthner, F.; Kaiser, T. E.; Saha-Möller, C. R. J-Aggregates: From Serendipitous Discovery to Supramolecular Engineering of Functional Dye Materials. *Angewandte Chemie International Edition* **2011**, *50* (15), 3376–3410. https://doi.org/10.1002/ANIE.201002307.

(95) Pradeilles, J. A.; Zhong, S.; Baglyas, M.; Tarczay, G.; Butts, C. P.; Myers, E. L.; Aggarwal, V. K. Odd–Even Alternations in Helical Propensity of a Homologous Series of Hydrocarbons. *Nat. Chem.* **2020**, *12* (5), 475–480. https://doi.org/10.1038/s41557-020-0429-0.

(96) Baghbanzadeh, M.; Simeone, F. C.; Bowers, C. M.; Liao, K.-C.; Thuo, M.; Baghbanzadeh, M.; Miller, M. S.; Carmichael, T. B.; Whitesides, G. M. Odd–Even Effects in Charge Transport across n-Alkanethiolate-Based SAMs. *J. Am. Chem. Soc.* **2014**, *136* (48), 16919–16925. https://doi.org/10.1021/ja509436k.

(97) Arias, D. H.; Stone, K. W.; Vlaming, S. M.; Walker, B. J.; Bawendi, M. G.; Silbey, R. J.; Bulović, V.; Nelson, K. A. Thermally-Limited Exciton Delocalization in Superradiant Molecular Aggregates. *J. Phys. Chem. B* **2013**, *117* (16), 4553–4559. https://doi.org/10.1021/jp3086717.

(98) *Excitonic couplings and interband energy transfer in a double-wall molecular aggregate imaged by coherent two-dimensional electronic spectroscopy | The Journal of Chemical Physics | AIP Publishing*. https://pubs.aip.org/aip/jcp/article/131/5/054510/902111/Excitonic-couplings-and-interband-energy-transfer (accessed 2023-06-30).

(99) Jelley, E. E. Spectral Absorption and Fluorescence of Dyes in the Molecular State [1]. *Nature* **1936**, *138* (3502), 1009–1010. https://doi.org/10.1038/1381009a0.

(100) Bricks, J. L.; Slominskii, Y. L.; Panas, I. D.; Demchenko, A. P. Methods and Applications in Fluorescence Fluorescent J-Aggregates of Cyanine Dyes: Basic Research and Applications Review Related Content Nanoparticles and Nanocomposites for Fluorescence Sensing and Imaging Alexander P Demchenko-Novel Fluorescent Carboni. *Methods Appl. Fluoresc.* **2018**, *6*, 12001. https://doi.org/10.1088/2050-6120/aa8d0d.

(101) Ma, X.; Huang, Y.; Li, A.; Zeng, X.; Liu, S. H.; Yin, J.; Yang, G.-F. The Aggregates of Near-Infrared Cyanine Dyes in Phototherapy. *ChemMedChem n/a* (n/a), e202300204. https://doi.org/10.1002/cmdc.202300204.

(102) Chuang, C.; Lee, C. K.; Moix, J. M.; Knoester, J.; Cao, J. Quantum Diffusion on Molecular Tubes: Universal Scaling of the 1D to 2D Transition. **2016**. https://doi.org/10.1103/PhysRevLett.116.196803.

(103) Kaiser, T. E.; Stepanenko, V.; Würthner, F. Fluorescent J-Aggregates of Core-Substituted Perylene Bisimides: Studies on Structure−Property Relationship, Nucleation−Elongation Mechanism, and Sergeants-and-Soldiers Principle. *J. Am. Chem. Soc.* **2009**, *131* (19), 6719–6732. https://doi.org/10.1021/ja900684h.

(104) Stolte, M.; Schembri, T.; Süß, J.; Schmidt, D.; Krause, A.-M.; Vysotsky, M. O.; Würthner, F. 1-Mono- and 1,7-Disubstituted Perylene Bisimide Dyes with Voluminous Groups at Bay Positions: In Search for Highly Effective Solid-State Fluorescence Materials. *Chem. Mater.* **2020**, *32* (14), 6222–6236. https://doi.org/10.1021/acs.chemmater.0c02115.

(105) Deshmukh, A. P.; Bailey, A. D.; Forte, L. S.; Shen, X.; Geue, N.; Sletten, E. M.; Caram, J. R. Thermodynamic Control over Molecular Aggregate Assembly Enables Tunable Excitonic

Properties across the Visible and Near-Infrared. *Journal of Physical Chemistry Letters* **2020**, *11* (19), 8026–8033. https://doi.org/10.1021/acs.jpclett.0c02204.

(106) Cosco, E. D.; Arús, B. A.; Spearman, A. L.; Atallah, T. L.; Lim, I.; Leland, O. S.; Caram, J. R.; Bischof, T. S.; Bruns, O. T.; Sletten, E. M. Bright Chromenylium Polymethine Dyes Enable Fast, Four-Color In Vivo Imaging with Shortwave Infrared Detection. *J. Am. Chem. Soc.* **2021**, *143* (18), 6836–6846. https://doi.org/10.1021/jacs.0c11599.

(107) Yu, G.; Walker, M.; Wilson, M. R. Atomistic Simulation Studies of Ionic Cyanine Dyes: Self-Assembly and Aggregate Formation in Aqueous Solution. *Phys. Chem. Chem. Phys.* **2021**, *23* (11), 6408–6421. https://doi.org/10.1039/D0CP06205G.

(108) Salon, J.; Wolinska, E.; Raszkiewicz, A.; Patonay, G.; Strekowski, L. Synthesis of Benz[e]Indolium Heptamethine Cyanines Containing C-Substituents at the Central Portion of the Heptamethine Moiety. An Efficient Procedure for the Synthesis of near-Infrared Dyes 5a-d Is Described. *Journal of Heterocyclic Chemistry* **2005**, *42* (5), 959–961. https://doi.org/10.1002/jhet.5570420532.

(109) Wiedemann, T.; Voit, G.; Tchernook, A.; Roesle, P.; Göttker-Schnetmann, I.; Mecking, S. Monofunctional Hyperbranched Ethylene Oligomers. *Journal of the American Chemical Society* **2014**, *136* (5), 2078–2085. https://doi.org/10.1021/ja411945n.

(110) Krueger, B. P.; Scholes, G. D.; Fleming, G. R. Calculation of Couplings and Energy-Transfer Pathways between the Pigments of LH2 by the Ab Initio Transition Density Cube Method. *J. Phys. Chem. B* **1998**, *102* (27), 5378–5386. https://doi.org/10.1021/jp9811171.

(111) Groves, P. Diffusion Ordered Spectroscopy (DOSY) as Applied to Polymers. *Polym. Chem.* **2017**, *8* (44), 6700–6708. https://doi.org/10.1039/C7PY01577A.

(112) Li, W.; Chung, H.; Daeffler, C.; Johnson, J. A.; Grubbs, R. H. Application of 1H DOSY for Facile Measurement of Polymer Molecular Weights. *Macromolecules* **2012**, *45* (24), 9595–9603. https://doi.org/10.1021/ma301666x.

(113) Peat, G.; Boaler, P. J.; Dickson, C. L.; Lloyd-Jones, G. C.; Uhrín, D. SHARPER-DOSY: Sensitivity Enhanced Diffusion-Ordered NMR Spectroscopy. *Nat Commun* **2023**, *14* (1), 4410. https://doi.org/10.1038/s41467-023-40130-2.

(114) Sedaghat Doost, A.; Akbari, M.; Stevens, C. V.; Setiowati, A. D.; Van der Meeren, P. A Review on Nuclear Overhauser Enhancement (NOE) and Rotating-Frame Overhauser Effect (ROE) NMR Techniques in Food Science: Basic Principles and Applications. *Trends in Food Science & Technology* **2019**, *86*, 16–24. https://doi.org/10.1016/j.tifs.2019.02.001.

(115) *The Nuclear Overhauser Effect in Structural and Conformational Analysis, 2nd Edition | Wiley*. Wiley.com. https://www.wiley.com/en-us/The+Nuclear+Overhauser+Effect+in+Structural+and+Conformational+Analysis%2C+2nd+Edition-p-9780471246756 (accessed 2023-08-09).